The University Of Sheffield.

Design of multi principal component platinum group metal alloys

By:

Stavrina Dimosthenous

A thesis submitted in partial fulfilment of the requirements for the degree of Doctor of Philosophy

The University of Sheffield

Faculty of Engineering

Department of Materials Science and Engineering

27 September 2019

Abstract

Platinum group metals (PGM) (Pt, Rh, Re, Pd, Ir and Os) and their alloys have high melting points and low reactivity with oxygen, making them excellent candidates for applications at high temperatures and in aggressive environments, such as in spark plug igniters, glass manufacture and industrial chemicals processing. However, platinum group metals are classified as critical due to their low crustal abundance and the volatility of the political situation in the geopolitical areas they naturally occur in. In addition to this, PGM are also expensive, and therefore for both of these reasons, reduction in their use is desirable. Here, the extrapolation of the Hume-Rothery rules to high entropy alloys has been employed to design novel single phase platinum group metal based multiprincipal component alloys, which represents a new area of study for this type of alloy. High throughput calculation methods were combined with these guiding rules to identify 29 alloys of interest in systems based on PtRh, Ir, and Ag. The main aim of the work was to design thrifted, oxidation resistant PGM based multiprincipal component alloys for high temperature applications. Of those 29 alloy compositions, 27 alloys were manufactured at laboratory scale in 5g quantity. Results obtained from X-ray diffraction, X-ray fluorescence, scanning electron microscopy and electron dispersive X-ray spectroscopy, and electron probe microanalysis are presented showing that, of those produced and successfully alloyed, the alloys $Pt_7Rh_{23}Ni_{35}Co_{35}$, $Pt_5Rh_{20}V_5ni_{35}Co_{35}$, $Pt_5Rh_{11}V_{14}Ni_{35}Co_{35}$, $Ir_{35}Rh_{35}Co_5Ni_5Pt_{20}$ and $Ir_{12}Fe_{33}Co_{20}Ni_{30}Pt_5$ are very likely to be single phase. We identify that the pairwise enthalpy of mixing, ΔH_{AB} impacts the single phase formation to a greater extent than the multiprincipal enthalpy of mixing and we suggest the criteria that to achieve a single phase multiprincipal component alloy $-50 \leq \Delta H_{AB} \leq 0\text{kJ}\,\text{mol}^{-1}$ for all pairs in an alloy system. The ductility of the laboratory manufactured alloys is assessed for ductility at room temperature with a hammering test as the alloys need to be cold workable for industry. While this test does not give quantitative data on the ductility, it allows discrimination between an alloy with very brittle character and one that is sufficiently ductile to merit consideration for industrial casting and cold rolling trials. Further analysis by high temperature compression is not performed due to the relative ease of attempting processing trials (at the industrial partner, following the work of this thesis) compared with the access to the required equipment. Following this characterisation, those 5 alloys were chosen for industrial scale manufacture trials at 1000g scale and the success of the scale up is assessed via optical microscopy grain analysis for resistance to cracking, X-ray diffraction for identification of crystal phase, X-ray fluorescence for investigation of homogenised distribution of constituents across samples (i.e. ensuring proper manufacture), scanning electron microscopy and electron dispersive X-ray spectroscopy, and electron probe microanalysis for assessment of phase distribution and homogenisation across samples. Single phase formation still occurs at scaled up size in all 5 alloys. Vickers hardness

and elastic moduli are assessed via Vickers hardness indentation and nanoindentation and the observed behaviour without cracking indicates that all 5 alloys are ductile. Alloys were assessed using differential scanning calorimetry in an Ar environment up to 1400°C to determine the response to heating, all alloys heat well up to 1400°C and do not undergo any significant phase or state transformation. The response of these alloys to heating up in air to 1000°C and being held in air at 1000°C for 1h is assessed via thermogravimetric analysis. The results of the thermogravimetric analysis showed that the addition of V greatly impacts the oxidation of these alloys in a negative way; conversely the addition of platinum group metals to a Fe rich alloy, $Ir_{12}Fe_{33}Co_{20}Ni_{30}Pt_5$ changes oxidation resistance for the better in comparison to literature data for standard ferritic steels at 1200°C. Density Functional Theory (DFT) studies via the use of the CASTEP code are employed to test the validity of density functional theory simulations in being able to provide a good screening method prior to laboratory based manufacture to assess whether these alloys will be energetically stable as randomly ordered structures and as a means of resource management as no material will have been wasted in manufacturing. DFT simulations have been assessed as appropriate for exploring the enthalpic stability of alloys by using DFT simulations to recreate the trends seen in binary alloy phase diagrams. We employed DFT simulations to explore the enthalpic stability in 108 atom face centred cubic supercell of $Pt_7Rh_{23}Ni_{35}Co_{35}$ in disordered lattice arrangements, and short and long range ordered lattice arrangements. Density functional theory simulation trends show that $Pt_7Rh_{23}Ni_{35}Co_{35}$ tends towards mixing to a disordered lattice arrangement on a face centred cubic crystal lattice which agrees with the single phase observed in physical experiments. We show successful ground state energy simulations of 108 atom $Pt_7Rh_{23}Ni_{35}Co_{35}$ (0 0 1), (0 1 1), (1 0 1), (1 1 0) and (1 1 1) surface slabs, cleaved using the METADISE code and simulated using the CASTEP code. Results show that all planes have approximately an equal energy. Physically this means that all have an approximately equal likelihood of manifesting as the surface plane. Further work towards explaining this mixed surface plane structure could be assessed by electron backscatter diffraction imaging. We provide a methodology and parameters suitable for simulation multiprincipal component alloys up to 108 atoms using density functional theory simulations.

Acknowledgements

To my supervisors, Russell Goodall, Colin Freeman, and Ritesh Rawal, thank you, your guidance and support throughout this project has been invaluable to me.
To all the postdocs, PhD candidates, and staff in this department that have supported, helped, taught, lent an ear in times of struggle, or mentored me during the early stages of the project, throughout, and towards the end, Chris Handley, Jake Corteen, Zhaoyuan Leong, Phil Mahoney, Sarah Smythe, Tes Monaghan, thank you.
To Russell Goodall's RADIUS group members and to John Harding's MESAS group members, thank you.
To my friends and family, thank you, I could not have done this without your support.
Στα αδέλφια μου, ευχαριστώ για όλα, σας αγαπώ. Στους γονείς μου, όσο και να προσπαθήσω δεν μπορώ να εκφράσω την αμέτρητη αγαπη, ευγνωμοσύνη και εκτίμηση που έχω για εσάς. Μου παρείχατε όλα τα εφόδια που θα μπορούσε να ήθελε οποιοσδήποτε σάυτή την ζωή. Ευχαριστώ για όλα. Σας αγαπώ, Σταυρίνα.

Contents

List of Figures

List of Tables

Acronyms

at.% atomic percent content.

BCC Body-centred cubic.

BSE Backscatter electrons.

COD Crystallography open database.

DFT Density Functional Theory.

DSC differential scanning calorimetry.

EBSD electron backscatter diffraction.

EDFT ensemble density functional theory.

EDX Energy Dispersive X-ray Spectroscopy.

EPMA Electron Probe Microanalysis.

FCC Face-centred cubic.

GGA generalised gradient approximation.

H-R Hume-Rothery.

HEA High Entropy Alloy.

JMNM Johnson Matthey Noble Metals.

JMTC Johnson Matthey Technology Centre.

LDA Local-Density Approximation.

NCP norm-conserving pseudopotential.

OTF on-the-fly.

PBE Perdew-Burke-Ernzerhof.

PBEsol Perdew-Burke-Ernzerhof (PBE) for solids.

PGM Platinum group metals.

PP Pseudopotential.

ppb parts per billion.

QM quantum mechanics.

SCF self-consistent field.

SE Secondary electrons.

SEM Scanning Electron Microscope.

TGA Thermogravimetric Analysis.

USP Ultrasoft Pseudopotential.

WDS Wavelength Dispersive Spectroscopy.

wt.% weight percent content.

XRD X-ray Diffraction.

XRF X-ray Fluorescence.

Chapter 1

Introduction

Ever since the first reports on achieving multiprincipal component alloys in solid solutions, the field of High Entropy Alloy (HEA) has become increasingly attractive to researchers in metallurgy. Reasonably, whenever new science is presented to any scientific field its pursuit is inevitable. Now, 15 years since the first reports the field is ever-flourishing and this new science has only but been scratched at the surface. The discovery and exploration of new alloys is particularly attractive to industry, and companies such as Johnson Matthey Noble Metals (JMNM) for several reasons. The aim of this work was to design platinum group metal alloys for high temperature applications (also recognizing that alloys of the HEA type have been reported to have unusual and outstanding mechanical, electronic and physical properties, which may be of interest for other potential applications and could be further developed in due course, if steps can be made in establishing which alloys can be made and how they can be predicted). A key part of any industry, especially one involved in noble metals, is 'thrifting', using the least amount of material possible either due to cost or criticality of the constituent elements. Alloying noble metals with cheaper elements using HEA principles($3 \leq$ elements, 5 - 35 atomic percent content (at.%)) might produce alloys with matching qualities when compared to industry standards, at a fraction of the cost. In order to balance cost and performance, it may be valuable to explore alloys formed from several PGMs, and several non-PGMs combined. However, the multiple potential interactions here may work against the desire to achieve single phase to facilitate processing (lower strength and higher ductility). A multiprincipal component alloy in solid solution would be considered unlikely to be easily found before the advent of HEA. To a researcher, understanding why and how such an unlikely material can form is invaluable for furthering this field. In this project we develop and explore multiprincipal component alloys based on PGM alloyed with cheaper materials for high temperature uses. The design principles used in this work are based on some of the approaches which have been discussed in the literature on HEA work (which are discussed later in this thesis). These ideas are explored further and modified to reflect how PGM best alloy into multiprincipal component solid solutions. Of the 32 alloys manufactured at laboratory scale, 5 were selected to be manufactured industrially

and explored further using advance characterisation techniques. These selected alloys were all assessed to have a high likelihood of forming solid solutions, to be potentially processable with current industrial techniques and represented different areas of composition space to facilitate understanding of the behaviour of these systems. To complement the high-throughput alloy composition identification we decided to develop a method of assessing the stability of potential compositions before lab manufacture, contributing to resource management. The method is based on DFT studies of potential compositions. In the model, alloys are constructed by assigning constituent element atoms of an alloy composition of interest to loci of a selected crystal phase, at random. This way is the most suitable for exploring disordered lattice arrangements closest to reality. First, as a validation step, DFT was used to explore binary alloying by comparing DFT results for binary alloys to binary phase diagrams to confirm that DFT studies were suitable for investigating multiprincipal component alloys via DFT. Alloy $Pt_7Rh_{23}Ni_{35}Co_{35}$ was simulated using DFT to prove the suitability of the method.

Aims and objectives

Aim: Explore, identify, investigate, and develop single phase multiprincipal component alloys based on PGM for high temperature use

Objectives:

Address the criticality and cost aspects of PGM by alloying with metals of lower criticality

Identify alloy compositions of interest using high throughput methods employing the high entropy alloy extrapolated Hume-Rothery rules

Evaluate the suitability of density functional theory in simulating multiprincipal component alloys and suggest a method of pre screening compositions formed from elements which display favourable characteristics for the application (e.g. high melting point, stability in an environment with oxygen, etc).

Evaluate the stability of the compositions alloys via the use of density functional theory simulations

Suggest methods of simulating multiprincipal component alloys using density functional theory

Characterise alloys made at laboratory and determine compositions of interest to be trialled for industrial scale manufacture

Evaluate the alloys and suggest improvements to criteria for single phase multiprincipal alloy identification

Thesis structure

Chapter 2 Presents the motivations for exploring alternatives to conventional platinum group metal uses, evaluates the literature on high entropy alloys (multiprincipal component alloys), presents the theory of high entropy alloys and looks at some of the work in the field. The theory of density functional theory as a simulation tool is summarised, the feasibility of density functional theory calculations for multiprincipal component alloys summarised and some of the literature on density functional theory calculations of multiprincipal component alloys is reviewed and assessed.

Chapter 3 Introduces the methods employed in the investigation. The design of the experimental investigations is explained. The experimental equipment and characterisation methods are explained. The design of the simulation investigations and their relevance to the experimental investigations is explained and the tools used to carry out the simulations are presented, explained and assessed.

Chapter 4 Presents the results of the density functional theory investigation of phase diagrams to confirm that density functional theory can provide results that agree with experimental results. The results of the phase diagram investigation are discussed are discussed. The results of the density functional theory investigation of $Pt_7Rh_{23}Ni_{35}Co_{35}$ bulk disordered and ordered lattices, and cleaved slab surfaces are presented and discussed. The feasibility of performing large density functional theory investigations is assessed and suggestions are given on running density functional theory simulations for large multiprincipal component alloys.

Chapter 5 Presents and discusses the results of the experiments and investigations on the the alloys $Pt_7Rh_{23}Ni_{35}Co_{35}$, $Pt_5Rh_{20}V_5Ni_{35}Co_{35}$, $Pt_5Rh_{11}V_{14}Ni_{35}Co_{35}$, $Ir_{35}Rh_{35}Co_5Ni_5Pt_{20}$ and $Ir_{12}Fe_{33}C_{20}Ni_{30}Pt_5$ prepared in the laboratory and at industrial scale. An investigation on silver based alloys manufactured in the laboratory is also presented and discussed. The silver based alloys were an investigation in achieving alloying in silver, which was particularly difficult throughout this project. The investigation is based on a hypothesis for the pairwise mixing criterion, ΔH_{AB}, being important. Reasons for the difficulty, assessment of our hypothesis are discussed. Criteria based on these investigations and better assumptions following on from the assessment of results are also discussed. The laboratory alloy characterisation results are compared with the industrial scale alloy characterisation results for each alloy. The as-cast and heat treated alloys are also compared and discussed. The alloy prediction methods, the oxidation resistance, and the success of the scaling to industry are discussed and assessed. The potential applications of the 5 industrially scaled alloys are discussed.

Chapter 6 Provides brief conclusive remarks and reiterates the key discussion points.

Chapter 7 Suggest future projects and provides brief insight as to what the projects might answer that this work has not.

Chapter 2

Literature review

2.1 Platinum group metals

2.1.1 Properties and uses

PGM comprise a subset, Ru, Rh, Pd, Os, Ir, Pt, of the noble metals (inlc. Au, and sometimes Ag). PGM are extracted from the same ore and are most likely to occur, naturally, alloyed with other PGM. In rarer cases, they occur as minerals. PGM are likely to occur in areas of the world abundant in nickel and copper ore deposits, usually in the same locations or not far from them[1]. The PGM natural reserves are found primarily in South Africa (primary ore) and Russia (nickel byproduct)[2]. PGM are silvery white metals with, in general, a relatively high melting point, density and hardness, good electrical and thermal conductivities as well as good thermal stability and resistance to oxidation[3, 4]. Pt, Pd, Ir, Rh and their alloys, in particular, are easy to manufacture due to their ductility, while extensive alloying with Os and Ru would tend to make the resulting alloy unworkable. This is as Ru and Os in their elemental form have hexagonal close packed structures, while other PGM have FCC crystal structures; the alloys thus tend to form multiphase microstructures which have high strength but limited plasticity[5]. Os and Ru are, however, valuable microadditions to alloys and make very good catalysts in their elemental form[4]. However, Os and Ru are susceptible to oxidation at high temperatures, unlike the other PGM. PGM as a whole are invaluable to the catalyst industry acting as heterogeneous catalysts or cocatalysts in reactions such as the oxygen reduction reaction (ORR) and water splitting [3, 6–8].

PGM are of particular interest to industries such as automotive, medical, aerospace, chemical, sensors and electronics; of course, they are of particular value to the jewellery industry, as well [1, 3, 5, 9, 10]. PGM are important autocatalysts and are responsible for the conversion of pollution exhaust gases into CO_2in many of the worlds vehicles fitted with a catalytic converter. Similarly, PGM catalysts are used in the abatement of greenhouse gases produced in other industrial processes, such as the production of nitric acid. Other uses of PGM catalysts include, but are not limited to, fuel cell reactions and petroleum refinement. Also, Pt−Rh alloys

are used in the Ostwald process as catalyst for the conversion of ammonia to nitric acid in the ammonia oxidation step and the thermocouple industry, due to the resistance of the alloys to oxidation [4–6, 9, 11], and are particularly attractive for the purposes of water purification [12]. The value of PGM in the automotive industry is not limited to autocatalysts as Pt−Rh alloys also make excellent spark plug alloys due to their chemical stability and resistance to oxidation at high temperatures.

2.1.2 Criticality

PGM are a natural resource, and natural resources are exhaustible or unrecoverable depending on the original disposal routes. The crustal abundance (abundance in the Earth's crust) of PGM is low when compared to, for example,Si; i.e. for every 1 atom of Pt there are 10^9 atoms of Si (fig. 2.1). Gunn [13] identifies PGM as 'critical' noting that this assessment is dependent on the physical, chemical properties of the metal, supply and demand as is influenced by crustal abundance and the socio-political environment in the PGM supplying countries[14]. Gunn [13] concludes that for critical metals the responsibility falls on corporations and governments to address the criticality of materials and Gunn [1] identifies Pt and Pd as the most industrially important PGM, with Rh following. In this context, it is reported that the crustal abundance of Pt and Pd is five parts per billion (ppb), with the rest of the PGM having 0.2 times the crustal abundance of these two elements.

Further, Köhler [15] also identifies PGM as materials of high criticality, with Au and Ag being of secondary, 'critical' importance, as characterised by the uncertainty in their supply combined with their importance to technology and industry. As a specific example, the report warns against the planned obsolescence built into electronics and that the resulting disposal of the critical elements used in these devices will make the recycling and recovery of these elements difficult. The report argues, as with that above, that the responsibility falls on technology manufacturers to follow more sustainable resource management practices and that there should be no reliance on future discoveries of new resources and also stresses the need for alternative materials and to design without extensive use of resources.

Recently, a report from Grandell *et al.* [16] assessing the need for critical metals in clean technologies predicted that given current consumption rates, the cumulative consumption for Pt and Ru would reach 290% and 73% of the known reserves by the year 2050. The same report also predicts that 120% and 35% of the known resources for Pt and Ru, respectively, need to be mined by the same date. This highlights the need for discovering alternative materials and reducing the consumption of Pt. To add to the criticality of the situation, the report by Sinisalo *et al.* [2] notes that the risk to supply is increased due to minable PGM being primarily concentrated in two areas of the world. Pell *et al.* [17] applied a method for analysing the criticality of a material (the economic resource scarcity potential method) to PGM. It concluded that PGM have a higher scarcity score even than rare earth elements, which are also

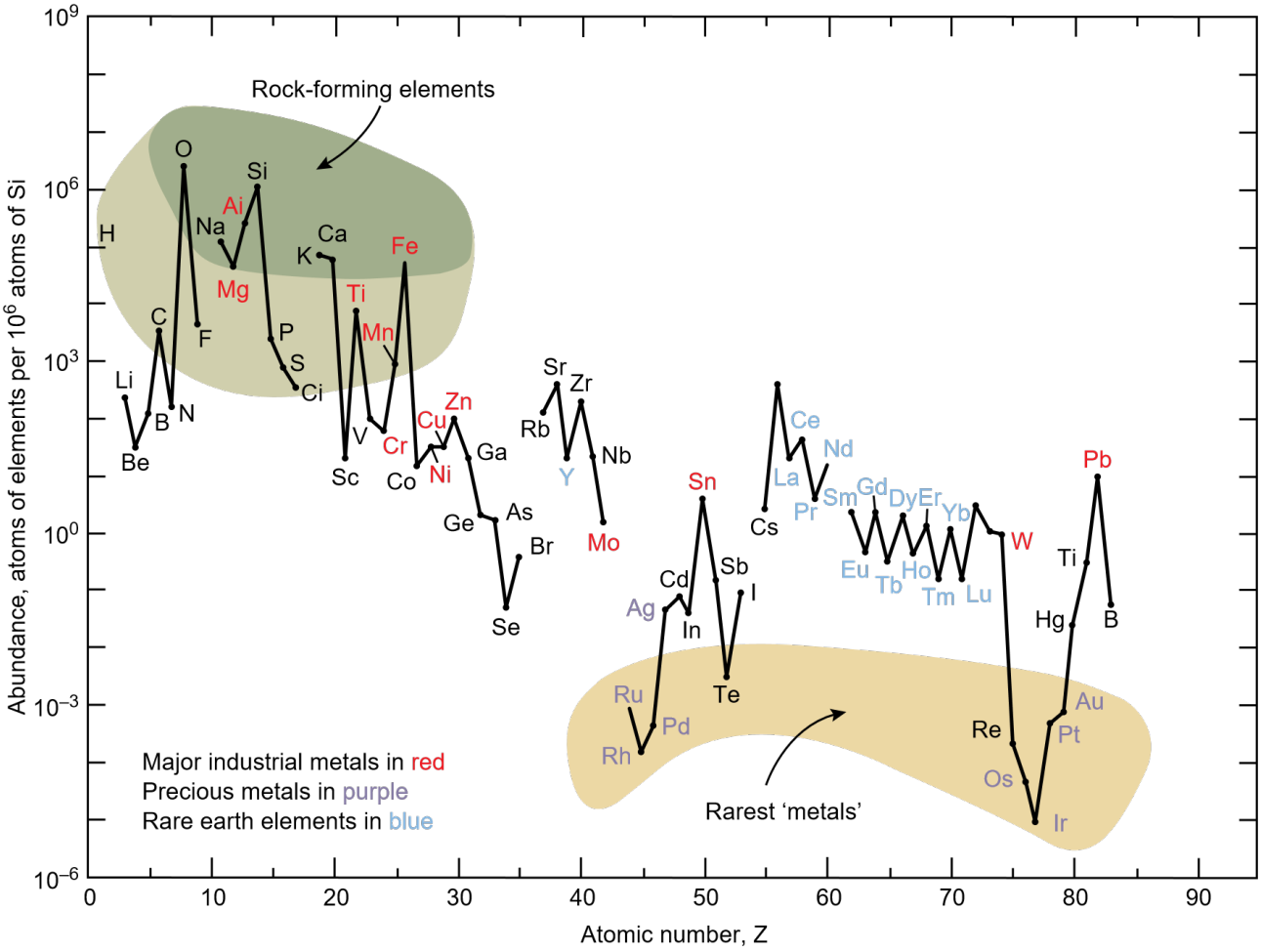

Figure 2.1: The crustal abundance of elements, arranged by atomic number, compared to 10^6 atoms of Si, i.e. there is ≈ 1 atom of Pt to 10^9 atoms of Si[13]

of high criticality, due to the rating given to the governmental system in South Africa, where there is a high concentration of reserves. Bardi *et al.* [18] concludes that mining is facing a challenge in maintaining the supply at a price that is suitable for use in mass manufacture, such as for automotive. Given the value of the metal, surprisingly little PGM is reprocessed at end of life; a 2017 press release from the World Platinum Investment Council stated that in 2012-2017 72-78% of the platinum supply came from mining, the rest coming from recycling efforts such as jewellery and spent autocatalysts.

Generally, in such works as are discussed above, the agreement is that the world needs to move away from its heavy reliance on PGM. Suggestions include finding alternative materials for current PGM uses, reducing the amount of PGM in some materials (re-design), and to improve recovery and recycling of spent PGM.

Researchers, are, of course, quick to respond to the rising costs and scarcity issues associated with PGM and the consequent economic and industrial issues. In the last few years, several reports, articles, communications, and reviews have been published on 'PGM-free', 'Pt-free', 'noble metal-free', 'sustainable' catalysts and cocatalysts [7, 8, 19–40]. Interestingly, Löffler *et*

al. [36] reports on a new use for the Cantor alloy, CoCrFeMnNi, a HEA, which is explained further in section 2.2, first reported by [41], and the first HEA to ever be reported and one of two seminal papers[41, 42] (more in section 2.2), as a suitable catalyst to replace Pt in the ORR. The report states that the Cantor alloy performs equally as Pt as a catalyst while any attempt to tune the composition by removing components does not perform nearly as well.

Considering the critical nature of PGM and the potential offered for reduced use via HEA formulations, this thesis focuses on designing alloys that are not heavily reliant on PGM for high temperature use. The current PGM alloys are very effective in terms of their properties and performance, but, as highlighted, the cost and availability of these elements mean that this use is not sustainable. As is such, recovery and recycling routes have not been assessed or considered for the purposes of this thesis.

2.2 High entropy alloys

HEA are a very attractive field of study because of the possibilities of discovery of new alloys with attractive properties and applications, and replacement alloys for conventional uses. In the simplest terms, what is referred to as a HEA is a multiprincipal component alloy. The definition of HEA, and the one informing the studies performed in this project, is that an HEA is an alloy with multiple elements ($3 \leq$), of which each has 5-35 at.%, which exhibits a single, cubic crystal phase, instead of the expected intermetallic phases. Traditionally, an HEA has $5 \geq$ components. The discovery of HEAs [41–43] not only opened up a completely new subset of metallurgy but gave rise to the focussed study of multiprincipal component alloys.

HEA are unconventional as the alloying principles counter the traditional binary alloy solvent-solute relationship, in that there is no defined solvent or solutes in HEA compositions. What was more unexpected was that HEA did alloy to single cubic phases. To explain the success in alloying elements to form multiprincipal alloys (HEA) "the entropic stabilisation of solid solutions[42], severe lattice distortion[43], sluggish diffusion kinetics[44, 45], and the [nebulous, at best] 'cocktail effect"'[46] were proposed as reasons for the stabilisation of a single cubic phase. Pickering *et al.* [46] reviewed these hypotheses and concluded that the entropic stabilisation requires further research to be a rigorous and satisfactory explanation, the severe lattice distortion effect due to the atomic size mismatch needs further work, though it might provide a satisfactory explanation as to the stabilisation of HEA. They also assessed that sluggish diffusion kinetics are more likely to be a function of the components rather than generally true across all alloys that fall within the HEA category. Also, as suggested above, the term 'cocktail effect' is unclear in terms of what it really means, despite attempts at defining and describing it[47, 48], and therefore having this as a rule or principle is probably inappropriate.

The review [46] noted that the enthalpy (eq. 2.3) is more effective as a descriptor for HEA stabilisation. In our studies this is discussed below in sections 6.5, 6.3 and 6.5.2. Similar observations that support the idea that binary mixing enthalpies have more influence on the

stabilisation of HEAs have been made by Freudenberger *et al.* [49].

Traditionally, HEAs have been defined as exhibiting a cubic single crystal phase (either FCC or Body-centred cubic (BCC)), the random arrangement of multiprincipal components on the lattice purported to suppress intermetallic phase formation. However, only a few HEAs have been reported to be single phase FCC[41, 50], or BCC[51–53] and to remain so after heat treatment. More recently, reports of alloys with a hexagonal close-packed (HCP) phase crystal structure have been published, however these alloys are not single phase[54–58]. There are numerous reports of HEA which do not fall under the strict definition of exhibiting a single phase, having the presence of intermetallic phases, instead[59–71]. Nevertheless, studies into multiprincipal component alloys have led to identifications of alloy compositions with outstanding mechanical properties[59, 72–74], even at cryogenic temperatures[75], catalytic properties[36, 56, 76–82], additive manufacturing potential[83–92], etc. It is evident that while HEAs are not exactly what they were initially purported to be that they are, nevertheless, a very exciting young field of study since the alloy identification possibilities are practically inexhaustible.

2.2.0.1 History

High-entropy alloys (HEA) first came to the forefront of alloy research in 2004[41, 42]. Two independent groups reported on the discovery of two multiprincipal component alloys which exhibited a BCC, and FCC single phase crystal structure.

HEAs have been proven to have exceptional mechanical and thermodynamic qualities. Yeh *et al.* [42] have shown that the initial alloys they synthesised mostly increase in hardness after annealing, as opposed to most conventional alloys. Also, the alloys exhibited high strength retention at high temperatures, ductility, and corrosion resistance depending on the components.

Yeh *et al.* [42] reported, primarily, $CuCoNiCrAl_xFe$ as an alloy system, together with several other alloys. Compared to conventional, commercial alloys, the HEAs synthesized in Ref.[42] exhibited resistance to softening on annealing. Some of the alloys even increased in hardness, compared to the as cast state, which may be attributed to a transformation from a metastable (kinetically stabilised, due to small sample size and rapid cooling from casting) FCC phase to a stable BCC phase, and the concomitant rise in the stress to move dislocations[93]. Along with this discovery, Yeh was the first to propose the term high-entropy alloy for this group of multiprincipal component alloys as a high configurational entropy was thought to be the reason behind the alloys exhibiting a single phase crystal structure.

Likewise, Cantor *et al.* [41] reported on a quinary, equiatomic, single phase fcc alloy CoCrFeMnNi, now referred to as Cantor's alloy or CCFN-X, for compositional variations. The Cantor group also reported on a number of six to nine multiprincipal component alloys which exhibited similar structural properties as CoCrFeMnNi, such as a primary fcc dendritic phase. It was reported that very high component number multiprincipal , equiatomic alloys were usually multiphase and brittle, but CoCrFeMnNi was primarily FCC phase which could further

support the solution of other elements such as Nb, Ge, Cu, Ti and V in it.

At this point, it is important to note that while CoCrFeMnNi is exemplary of a single-phase HEA it also decomposes and exhibits secondary phases depending on environment, temperature, and treatment. Particularly prominent is the presence of a secondary Cr-rich σ phase after very long heat treatment at temperatures ranging from 500 - 1000°C[94–97]. Also, it was shown by Otto *et al.* [98] that direct substitution of the constituents of CoCrFeMnNi with elements of similar atomic size and electronegativity that the resulting alloy is no longer single phase at room temperature. This implies that configurational entropy is not the driving factor of this single phase stability but a complementary feature once other criteria which reinforce phase stabilisation, such as solubility, are fulfilled.

2.2.1 Defining HEA

Since HEAs are such a new frontier in the research field of metallurgy, a clear definition is necessary so that HEAs can be identified properly. At the moment, an HEA is widely defined as a single phase multiprincipal component alloy at 5-35 at.% per component with a cubic crystal structure, where the solute and solvent are not distinguishable[41, 42, 99–105]. Some stress the need for an equimolar or near equimolar solution and some focus on the abundance of a metal in an alloy.

However, the field is still progressing and expanding. Can an alloy really be an HEA if it is characterised as cast or should annealing also be carried out so that a true equilibrium is reached? Are alloys which fit all the criteria for HEA but exhibit intermetallic phases, really HEA? Likewise, do multiprincipal component alloys which exhibit a single cubic crystal phase but do not fulfil all criteria for HEA fit within the HEA category?

To address the ever expanding number of interesting multiprincipal component alloys being identified Yeh *et al.* [106] introduced new categories such as low-entropy alloys (LEA), i.e. conventional alloys, and medium-entropy alloys (MEA), ternary and quaternary, characterised only by the number of components and the consequent entropic contribution (eq. 2.1)[44, 106]. Additionally, Miracle *et al.* [63] and Miracle *et al.* [107] expand the definition to multiprincipal component alloys with intermetallic phases.

Yeh *et al.* [42] proposed an initial definition for HEAs in their original paper, reporting the discovery. They define what their interpretation of an HEA is, 5-35at.% per element, high configurational entropy, 3 or more components (but not too many), single phase simple crystal structure. The paper does not emphasize the importance of the composition being equimolar but the writers are definitely in favour of equimolarity as that maximises the entropy of configuration for any given alloy, according to the definition of entropy of configuration. The writers make the case that the true configurational entropy is even higher than what is suggested by the empirical numerical formula as this disregards contributions from atomic vibrations, electron configuration and magnetic moments. It is postulated that a high entropy of

configuration is the reason for the uniformity and the random ordering of the lattice, which gives rise to a single phase. It is suggested that a large number of constituents is favourable for the single phased structure due to the higher entropy of configuration. However, it is acknowledged that alloy compositions with large heats of formation are not going to yield HEAs under this definition. Therefore, a balance must be found between a large number of components and a low enough heat of formation. To help find this balance, the writers employed certain empirically defined quantifiable criteria based on the Hume-Rothery rules. These have been built upon and refined by other workers over the last few years. New criteria have been proposed and some of the original criteria have proven not very useful. These criteria are composed of a series of formulae which are supposed to predict certain physical and electronic properties. If selection criteria are applied to these properties then the hope is to identify HEAs, whatever element combination and composition they may be found at.

Conversely, the paper by Cantor *et al.* [41] makes a case for these multiprincipal component alloys being equiatomic. Examination of CoCrFeMnNi and several other multicomponent alloys at equiatomic composition made by the group showed that the most of the alloys exhibited a single phase fcc dendritic structure as the main phase, with some segregation to the interdendritic regions, and possible formation there of other phases as a result of this concentration of certain elements. These other alloys were between 6 to 9 components. It is pointed out that very high order multiprincipal component equiatomic alloys were found to be highly brittle following several attempts at making them. The alloys were significantly below the maximum number of phases allowed by the Gibbs phase rule and further below the largest number of phases that could be expected in a material that had been subjected to non-equilibrium (i.e. real-world) solidification.

Miracle *et al.* [63] suggest that the presence of intermetallic phases in the alloys is consistent with the concept of HEAs and that the definition should be expanded to include 'HEAs' with an "intentional 2^{nd} phase" added to them. A case is made that in conventional alloys a second phase strengthening mechanism is often implemented for activation, particularly for applications requiring high strength, or strength, at high temperature through controlled particle spacing. Particle strengthening is the main reason Miracle *et al.* [63] are considering expanding the definition of HEAs past the single phase criterion. The group also attempts to introduce a new parameter in numerical empirical HEA prediction. Firstly, the report suggests, after reviewing the evidence of reported compositions, that the role configurational entropy plays in homogeneity is very weak at indicating whether alloy compositions at solid states will be homogeneous. The report suggests that the role of configurational entropy in homogeneity, and the suppression of intermetallic phases, is strongest closer to the melting point, in liquid states and at very high temperatures. They also suggest that intermetallic compounds will form in HEAs if the Gibbs free energy of a binary intermetallic is higher than the overall Gibbs free energy of the multiprincipal component system. The addition of intentional intermetallic phases to HEAs is introduced as a concept. In terms of classifying HEAs as such this deviates very

much from the revious definition introduced by Yeh *et al.* [42]. A question that arises from this, should HEAs be rigidly defined? Moreover, should we keep defining them as HEAs, or solely as multiprincipal component alloys. [63] propose the terminology of HEAs where the intent is to create a single phase, and multiprincipal component alloys or Complex Concentrated Alloys (CCAs) where the phase structure is more complex. Although these terms have begun to be used by some authors, the term HEA is still most widely used for any type of alloy where there is no single main alloying element.

A further concern is the effect processing history may have had on many of the materials reported in literature, especially in some of the early work on the subject. Characterisation in the as cast state might not be as accurate. Arc melting at small scale leads to very high cooling rates which means that alloys might be possibly frozen in a metastable state. Otto *et al.* [98] performed a study to determine whether configurational entropy really did contribute significantly to stabilising a multiprincipal component alloy at single phase. The group replaced single elements in already identified HEAs, such as CoCrFeMnNi, the premise being that if configurational entropy was preserved then the resulting alloy would be single phase, as well. However, all newly synthesized alloys were multiphase and contained intermetallics. However, what is more of interest in this case is that to prepare for the study all alloys were subjected to 3 day annealing so that they reached a state as near to an equilibrium state as possible. In annealing, only CoCrFeMnNi still exhibited a single phase microstructure, whereas every other alloy synthesized by the group exhibited multiphase microstructures. It is important to note that all synthesized alloys had single phase forming values of the entropy of mixing[98].

Similarly, Poletti *et al.* [108] annealed potential HEAs to an equilibrium state. The results revealed the importance of annealing in determining whether or not a single phase solid solution would form. Some compositions either were multiphase at equilibrium or single phase at equilibrium[108]. This is not to say that the intentional addition of intermetallic phases is not valid but there needs to be a proper procedure for characterising and, as a result, identifying HEA.

However HEA are defined, it should be clear by now why they are an exciting field offering many avenues of studying them and in the development of new materials.

2.2.2 Predictive methods for HEA

Given that the landscape of identifying HEA is vast and practically inexhaustible, efforts have been focused towards reliable identification of interesting compositions. Several methods towards prediction of phase, properties, etc. have been proposed towards tackling the problem of designing successful alloys for their intended use. The work reported here employed the predictive rules first introduced by Zhang *et al.* [109] so the following will give greater attention to those rules, while addressing the range of methods that have been used.

2.2.2.1 Hume-Rothery Rules Basis

Currently, a very widely used method for predicting the properties of a proposed HEA is the use of an empirical technique based on an extrapolation of the Hume-Rothery rules for the prediction of alloying and phase formation in binary systems.[109, 110].

Mizutani [110] summarises the rules as being powerful guides (i.e. useful but not rigorous) in designing new alloys. The rules can set some basis conditions which allow one element to dissolve in another.

The Hume-Rothery rules for single phase alloys are based on an atomic size mismatch of no more than 15% between solvent and solute for a binary solution. Similar electronegativity mismatch, $\Delta\chi$, as the higher the $\Delta\chi$, the higher the tendency of like atoms to want to group together causing segregation and intermetallic phases. Mizutani [110] also discusses the effect in terms of the valence electron concentration (VEC) as a means for crystal structure prediction which takes into account the d-band electrons. While the Hume-Rothery rule for valency states that metals should have the same, or similar, valencies to dissolve each other, VEC is used very differently in terms of HEAs in that it is used to predict whether BCC or FCC phases will be stabilised[110–112]. The reliability of VEC to predict cubic phase stabilisation is dubious.

In the following section we introduce the Hume-Rothery (H-R) extrapolation to multicomponent systems developed by Zhang *et al.* [109] (eq. 2.1, 2.4, 2.3, 2.5) and Mizutani [110] (eq. 2.6)

2.2.2.2 Predictive formulae

The H-R rules formed a basis for Zhang *et al.* [109] and Mizutani [110] to extrapolate them into multiprincipal component rules. While the H-R rules are for determining if the combination of pure metals into single phase binary alloys is viable, the set of rules has been extended into an empirical numerical model for multiple components.

The formulae are outlined below:

$$\Delta S_{mix} = -R \sum_{i}^{N} c_i \ln c_i \tag{2.1}$$

The entropy of mixing, which reduces to

$$\Delta S_{mix} = R \ln N \tag{2.2}$$

where c_i is the amount of component i in the composition. at equimolar composition. Followed by the enthalpy of mixing, adapted from Hume-Rothery,

$$\Delta H_{mix} = \sum_{j>i}^{N} 4\Delta H_{AB} c_i c_j \tag{2.3}$$

where ΔH_{AB} is the binary enthalpy of mixing for components i and j, corresponding to A and B, respectively.

The values obtained from equations 2.1 and 2.3 can be combined to calculate the Gibbs free energy like so,

$$\Delta G_{mix} = \Delta H_{mix} - T\Delta S_{mix} \tag{2.4}$$

An extension of Hume-Rothery rules for whether a single phase solid solution will form between two metals, is the atomic size mismatch for several,

$$\delta = \sqrt{\sum_{i=1}^{N} c_i \left(\frac{1 - r_i}{\sum_{i=1}^{N} c_i r_i} \right)^2} \tag{2.5}$$

where r_i is the atomic size of the i$^{\text{th}}$ component.

Calculating the VEC could, potentially, determine whether the resulting alloy has a BCC or FCC structure[113],

$$VEC = \sum_{i=1}^{N} c_i (VEC_i) \tag{2.6}$$

While the potential to predict the crystal structure of the solution is attractive, the VEC itself is not particularly useful in determining whether a single phase solid solution will form. A better alternative could be to develop an extension of the Hume-Rothery rules for $^{e}/_{a}$ similarities in the components of the solution. Mizutani *et al.* [114] discuss the importance in low ionicity in preventing the forming of intermetallic compounds. The ionicity is related to the electronegativity mismatch between two elements. In this particular study the group chose to consider the Allen electronegativity as opposed to the more widely used Pauling. This is supportive evidence for the importance of low electronegativity mismatch for resulting in a single phase solid solution. By Hume-Rothery, a similarity in electronegativity is important in determining whether or not a pair will form a single phase solid solution. An extension of the Hume-Rothery rules for single phase solid solutions leads to this formula for overall electronegativity mismatch in a multipincipal component composition,

$$\Delta\chi = \sum_{i=1}^{N} c_i \left(1 - \frac{\chi_i}{\sum_{i=1}^{N} c_i \chi_i} \right) \tag{2.7}$$

Yang *et al.* [105] proposed a combination of the factors that make up the Gibbs free energy into a simple ratio,

$$\Omega = \frac{T_m \Delta S_{mix}}{|\Delta H_{mix}|} \tag{2.8}$$

this is a very simple indicator to use in determining whether a solution will tend to a disordered structure and a single phase, as a result.

Also of interest in this project is the melting temperature of the overall composition as the

alloys are to be tested for use in high temperature applications, so a formula for approximating the melting temperature of the composition is important. Here, in common with a number of other such studies, a simple average of the component elements' melting points is used; it should be noted that this neglects the effect of any eutectics, which would depress the melting temperature below this value, or the formation of high melting point phases, which would raise the melting temperature higher.

$$T_m = \sum_i^N c_i T_i \tag{2.9}$$

In their review, Zhang *et al.* [115] state that for the formation of a solid solution the optimum search windows are $\Delta S_{mix} > 13.38\,\mathrm{J\,K^{-1}\,mol^{-1}}$, equivalent to 1.61R, $-10\mathrm{kJ\,mol^{-1}} < \Delta H_{mix} < 5\mathrm{kJ\,mol^{-1}}$ and $\delta < 4\%$. Similarly, Ye *et al.* [116] places the boundaries at $-15\mathrm{kJ\,mol^{-1}} < \Delta H_{mix} < 5\mathrm{kJ\,mol^{-1}}$ and $\delta < 5\%$, while Zhang *et al.* [117] give $\delta < 6.6\%$, also supported by Kozak *et al.* [118]. Zhang *et al.* [109] identified alloys in the range $12 < \Delta S_{mix} < 17.5\,\mathrm{J\,K^{-1}\,mol^{-1}}$, while values of ΔH_{mix} were below zero and about -10kJ mol^{-1}. This only reflects some of the literature but it is a good indicator of the thermodynamic regions where an HEA might fall into. All the literature studied so far reports that $\Omega > 1.1$ for solid solution formation. Interestingly, Guo *et al.* [119] give quite large search ranges for HEAs, even extending ΔS_{mix} to 1.32R, $11 \leq \Delta S_{mix} \leq 19.55\,\mathrm{J\,K^{-1}\,mol^{-1}}$, $-22 \leq \Delta H_{mix} \leq 7\mathrm{kJ\,mol^{-1}}$, $\delta \leq 8$.

These multiprincipal component alloy solid solution formation rules are much more constrained and rigid than the ones originally set by Hume-Rothery.

It is also possible to achieve some guidance on the phase that may be adopted. Guo *et al.* [113] state that if $VEC < 6.8$ the solution will solidify in a BCC structure and FCC is $VEC > 8$. The structure will be a combination of BCC and FCC if the VEC falls in the range range in between those two[115].

A concern is that the atomic size mismatch formula does not account for large differences between individual particles in the composition as it calculates the overall size difference across the components instead of averaging the difference between pairs of each component. Wang *et al.* [120] propose a number of alternative formulae for determining the atomic size mismatch. Of the proposed formulae, two were presented as replacements for the current formula for calculating the atomic size mismatch, α_1 and α_2. α_1 represents the total displacement of each atom in the composition from an ideal atom, an ideal atom defined as having the average radius in a random solid solution, $\bar{r}$, where $\bar{r} = \sum_i^N c_i r_i$ and α_1 is defined as,

$$\alpha_1 = \sum_i^N \frac{c_i |r_i - \bar{r}|}{\bar{r}} \tag{2.10}$$

This new parameter is based on the premise that there is a link between lattice distortion and the mismatch in atomic size. This parameter is related to local lattice distortion as Wang *et al.* [120] claim that it is important in determining whether a disordered substitutional alloy

will exhibit randomness or form ordered phases and intermetallics. However, Wang *et al.* [120] report that the parameter α_1 is not a useful parameter in distinguishing between compositions which are single phase or multiphase. This is due to the fact that it does not account for overall local lattice distortion due to neighbouring atoms and instead takes only a single atom into account.

Conversely, the authors state that α_2, as a parameter, is more successful in determining whether a single phase solid solution would form as it describes the local displacement of an atom through its interaction with neighbouring atoms in the lattice,

$$\alpha_2 = \sum_{j \geq i}^{N} \frac{c_i c_j \left| r_i + r_j - 2\bar{r} \right|}{2\bar{r}} \tag{2.11}$$

where $\frac{c_i c_j \left| r_i + r_j - 2\bar{r} \right|}{2\bar{r}}$ is a dimensionless value describing the relative displacement between pairs of atoms. Several other parameters are proposed for accounting for the local lattice distortion due to neighbouring atoms further and further away from the local atomic area of interest, which is indistinguishable from any other local atomic area of interest in the lattice. The authors conclude that α_2 is the optimal parameter in determining local lattice distortion.

Several of these prediction methods and criteria are taken into account in identifying interesting compositions in the studies performed in this work and are discussed further in sections 6.2, 6.3, 6.5 below.

2.3 Simulations of alloys

Section 2.1.2 addressed the constant rise in the demand for PGM, and the scarcity of PGM. Given the severity of the situation resulting from the interaction of these two factors, and the cost of PGM, high throughput manufacture is not the ultimate goal of this project but high throughput screening could have relevance. The high-throughput identification of interesting compositions is discussed briefly in section 2.2 and elaborated on in the methods in section 3.1.1. In this section we will discuss DFT as a possible tool for the purposes of simulating HEA. The suitability of DFT as a step in the workflow is discussed in section 3.2.1.
Note that 'computational costs' encompass CPU time, number of CPUs used, and memory (RAM) requirements.

2.3.1 Density functional theory

A material is a collection of atoms in an arrangement at a point in space-time. By this definition if we want to know the properties of a certain material then we will have the solve the time-dependent many body (atom) Schrödinger equation for that material.

There are many flavours of quantum mechanics (QM) based methods to approximating a solution to the Schrödinger equation and the work in this thesis relies on Density Functional

Theory (DFT) based methods. DFT approaches approximate a solution to the Schrödinger equation by finding the electron density, $n(\boldsymbol{r})$, of the many body system. The electron density has information about the system that is directly observable, unlike the wave function of the system that is not directly observable. Several experimental techniques allow us to observe the electron density, or the density of states for individual species or orbitals. For example, electron density maps can be constructed by combining XRD data and the density of states directly observed via scanning tunnelling microscopy[121, 122].

To begin to outline the background, let us start with the time-dependent Schrödinger equations for a single particle,

$$\hat{H}\boldsymbol{\Psi} = -i\hbar\frac{d\boldsymbol{\Psi}}{dt}, \tag{2.12}$$

in most cases we are only interested in solving for the groundstate energy, E, which is a stationary state, and lowest energy solution to the Schrödinger equation. From Merzbacher [123], if E is a real number, i.e. not complex, the time-dependent and time-independent wave functions, $\boldsymbol{\Psi}$, only differ by an oscillatory phase factor, while any physical quantity independent of time is constant. This is discussed explicitly in Merzbacher [123, chapter 4].

So, the time-dependent term drops out and we are left with the time-independent Schrödinger equation,

$$\hat{H}\boldsymbol{\Psi} = E\boldsymbol{\Psi}, \tag{2.13}$$

where the Hamiltonian operator, $\hat{H}$, has a kinetic and a potential energy term. Therefore,

$$-\frac{\hbar^2}{2\mu}\nabla^2\psi(\boldsymbol{r}) + V\psi(\boldsymbol{r}) = E\psi(\boldsymbol{r}), \tag{2.14}$$

where the first term on the left hand side represents the kinetic energy and the second term represents the potential energy, and $\psi(\boldsymbol{r})$ is the spatial part of the function.

We can begin to explain the assumptions that lead us to solving the Schrödinger equation for a many body system. QM methods rely on the adiabatic approximation developed by Born *et al.* [124]. For an atom, the mass of a proton or neutron is ≈1836 times the mass of an electron. For a nucleus in motion the electrons could be assumed to instantaneously modify their wave function according to the procession of the nucleus, therefore in relation to the electron the nucleus is stationary. Therefore the wave function can be split into two, the wave function describing the evolution of the nucleus in time and the wave function representing the electronic energy states in relation to the stationary nucleus. Effectively, nuclei are treated as classical stationary particles. Note that the Born *et al.* [124] approximation in relation to metals might not be so accurate as electrons are not bound so can move between energy shells leading to relativistic effects which can alter the electronic mass in relation to the nucleus [125]. However, Kohanoff [125] states that electronic excitations are bound to be below the Fermi region for most physical processes since we need to go beyond a few thousand degrees to begin to surpass the Fermi energy barrier.

Since we are treating the nuclei as point masses in relation to the electrons for a system of N electrons the electronic many body Schrödinger equation takes the form,

$$\left[-\frac{\hbar^2}{2m}\sum_{i}^{N}\nabla^2 - e^2\sum_{i}^{M}\sum_{i}^{N}\frac{Z_I}{|\boldsymbol{R_I}-\boldsymbol{r_i}|} + \frac{e^2}{2}\sum_{i}^{N}\sum_{j\neq i}^{N}\frac{1}{|\boldsymbol{r_i}-\boldsymbol{r_j}|}\right]\boldsymbol{\Psi} = E\boldsymbol{\Psi} \tag{2.15}$$

where, $\hbar$ is the Dirac constant, m is th electron mass, e is the charge of an electron, $\boldsymbol{R_I}$ are the coordinates of particle I, $\boldsymbol{r_i}$ are the coordinates of electron i, N is the number of electrons and M is the number of particles.

However, we are still left with the problem of having to solve for the many body wave function as treating the wave functions of electrons as interacting is too complex to calculate directly in a timely manner. An approximation that tries to simplify the many body wave function is the Hartree product, essentially, we are assuming that the electrons are not interacting with each other and separating the many body wave function into the product of a series of one-electron wave functions, each describing a single electron in the system[126–129].

$$\boldsymbol{\Psi} = \Psi(\boldsymbol{r_1},\ldots,\boldsymbol{r_N}) \tag{2.16}$$

$$\boldsymbol{\Psi} = \Psi_1(\boldsymbol{r}),\Psi_2(\boldsymbol{r}),\ldots,\Psi_N(\boldsymbol{r}) \tag{2.17}$$

The Hartree product does not provide a satisfactory simplification to the many body wave function. We need to be able to account for the antisymmetric electron 'exchange', i.e. two indistinguishable electrons exchanging coordinates, otherwise it violates Pauli's exclusion principle that no two fermions can occupy the same state, and electrons are 'labelled' and distinguishable which is counter to the quantum mechanical picture of electrons being able to occupy every orbital at any point in time. This problem was solved by Slater by the introduction of the *Slater determinant*[130]. We will not describe the Slater determinant in detail as we only want to provide an overview of DFT.

As mentioned above, the wave function cannot be directly observed so we do not know the shape of it, however the electron density is related to the Schrödinger like so,

$$n(\boldsymbol{r}) = 2\sum_{i}^{N}\Psi_i^*(\boldsymbol{r})\Psi_i(\boldsymbol{r}) \tag{2.18}$$

We apply the Hohenberg *et al.* [131] theorem which states that "the full many-particle ground state is a unique functional of $n(\boldsymbol{r})$". Therefore, we can solve for the ground state energy by starting from the electron density. Solving $n(\boldsymbol{r})$ is easier than solving the Hartree product as it only involves solving for 3 dimensions in space rather than $3N$ dimensions in space.

To simplify our treatment of the system even further and introduce a practical solution to the Hartree product, we apply the Kohn *et al.* [132] treatment to the system in that each one-electron wave function can be expressed by an energy functional and that functional is

separated into known and unknown functionals,

$$\left[-\frac{\hbar^2}{2m}\nabla^2 + V_{ion}(\boldsymbol{r}) + V_H(\boldsymbol{r}) + V_{XC}(\boldsymbol{r}) \right] \psi_i(\boldsymbol{r}) = \varepsilon_i \psi_i, \tag{2.19}$$

this is known as the Kohn-Sham equation, where $V_{ion}(\boldsymbol{r})$ is the ionic (nucleus) electron interaction potential, $V_H(\boldsymbol{r})$ is the Hartree potential, the electron-electron interaction potential, and $V_{XC}(\boldsymbol{r})$ is the electron exchange and correlation (exchange-correlation) potential. The Hartree potential describes the Coulomb repulsion of the single electron from the rest of the electron in the system. The exchange correlation potential describes all the unknowns of the system and the self-interaction of the electron being considered in the Kohn-Sham equation. NB The exchange-correlation functional, is an approximation of electron exchange and the interaction of electronic wave functions(correlation). Some of these terms can be solved explicitly analytically but are computationally costly.

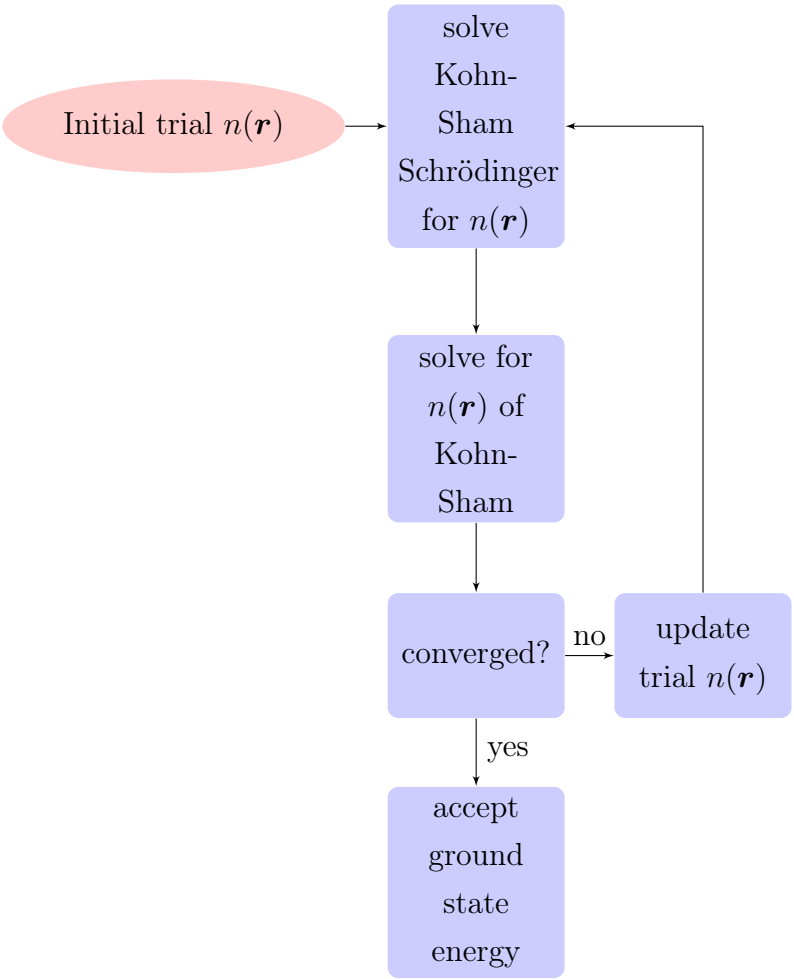

Figure 2.2: Flowchart of the SCF iterative method

The basic steps to solving for the ground state electron density, the SCF method (fig. 2.2), are as follows:

1. begin with a 'guess' for $n(\boldsymbol{r})$,

2. solve the Kohn-Sham equations for that $n(\boldsymbol{r})$,

3. solve for $n(\boldsymbol{r})$ resulting from the Kohn-Sham equations,

4. update the $n(\boldsymbol{r})$ 'guess' until $n(\boldsymbol{r})$ and the Kohn-Sham $n(\boldsymbol{r})$ converge to an appropriate tolerance

2.3.1.1 Exchange correlation functionals

In this study we employed the Local-Density Approximation (LDA), and PBE-PBE for solids (PBEsol) functionals, these are discussed below.

The exchange correlation potential, $V_{XC}(\boldsymbol{r})$, takes the form of a derivative,

$$V_{XC}(\boldsymbol{r}) = \frac{\delta E_{XC}[n(\boldsymbol{r})]}{\delta n(\boldsymbol{r})}, \tag{2.20}$$

where E_{XC} is the exchange correlation energy and a functional of the electron density. Within the LDA, E_{XC} takes the form,

$$E_{XC}^{LDA} = \int \varepsilon_{XC}(n(\boldsymbol{r}))n(\boldsymbol{r})d\boldsymbol{r}, \tag{2.21}$$

where $\varepsilon_{XC}(n(\boldsymbol{r}))$ is the exchange correlation energy per electron of a uniform electron gas and can be solved analytically (for a demonstration of this see chapter 15 of reference[133]).

LDA[132] is an exchange correlation potential based on the assumption of the uniform electron gas theory that the local density around an electron will always be the same for any electron in the system. More on the electron gas model can be found in chapter 15, page 347 of reference[133]. The assumption is made that E_{XC} is made up from the sum of volume elements which are sufficiently small to allow local variations in density to be ignored, but large enough that the many body uniform electron gas theory, where the exchange correlation energy per particle is a function of the density, can be applied.[134]. LDA works very well in describing most weakly correlated metals as the uniform electron gas model applies to the delocalised electrons in metals. However, LDA has shortcomings in describing d valence band metals[135].

LDA has been extended to include spin polarisation[136], called the local spin density approximation (LSD or LSDA), where $n(\boldsymbol{r}) = n_{\uparrow}(\boldsymbol{r}) + n_{\downarrow}(\boldsymbol{r})$. For an extensive discussion on the shortcomings of LDA and spin polarised LDA please look at pages 82-85 of reference [125].

To reiterate LDA assumes that density around every electron is homogeneous. However, there are local variations in the density around electrons in materials. The generalised gradient approximation (GGA) method addresses this local variation by expanding on the gradient and higher order derivatives of the density[125]. The exchange correlation energy takes the form,

$$E_{XC}[n(\boldsymbol{r})] = \int n(\boldsymbol{r})\varepsilon_{XC}[n(\boldsymbol{r})]F_{XC}[n(\boldsymbol{r}), \nabla n(\boldsymbol{r}), \nabla^2 n(\boldsymbol{r}), \ldots]d\boldsymbol{r}, \tag{2.22}$$

where F_{XC} is a factor that takes into account the local variation of the density.

PBE[137] type functionals are based on second order ($F_{XC}[n(\boldsymbol{r}), \nabla n(\boldsymbol{r})]$) gradient expansion that improves on local inhomogeneities in the density and retains the functional form of LDA (and spin polarised LDA).

PBEsol[138] is a revision of the PBE that is intended to improve the simulation of the equilibrium properties of solids with densely packed structures and surfaces. The electronic topology in metals is described by the uniform electron gas model and PBEsol expands LDA. As a result, we can accurately simulate a range of solid packings, including FCC, BCC and even multiphase structures. Therefore, PBEsol is a suitable functional for simulating the FCC HEA we are interested in in the present work.

2.3.1.2 Pseudopotentials

In this study we employed NCP and USP pseudopotentials, these are discussed below.

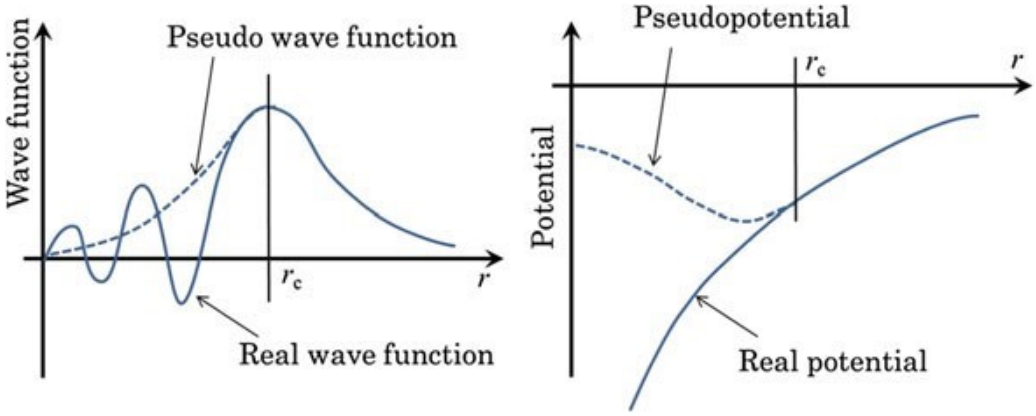

Figure 2.3: All-electron (solid) and pseudo (dashed) wave functions and potentials inside and outside the core radius, r_c[139]

Atomic interactions, chemical bonding and processes are governed by the electrons in the outermost shells (valence). The V_{ion} term can be solved analytically but that is computationally costly. To describe the electronic interactions in materials we can adopt the 'frozen core approximation' and only treat the valence electrons. It is important to note that this approximation does not reflect the reality that all electrons are indistinguishable and exchange states. Nevertheless, we define a pseudopotential which prevents valence electrons from interacting with the core of the atom and acts to give repulsive forces on a short range, but attractive over a longer range[140]. In pseudising wave functions, the core interacting part of the wave function is smoothed to a nodeless plane wave, past the core radius the wave function retains its all electron shape.

NCP were introduced by Hamann *et al.* [141] to address accuracy and applicability to a range of systems. In constructing norm-conserving pseudopotentials there are 4 key properties to adhere to, the energy of the pseudopotential must agree with the real all electron potential, the pseudo wave function and all electron wave function must be the same beyond the 'core

radius', the charge density of the pseudopotential and the all electron potential must agree within the core radius, and as must the logarithmic derivatives and first energy derivatives of both the real and pseudo wave functions beyond the 'core radius'. Essentially, a core region is defined and beyond the core region the wave function and potential are treated as all electron.

To further optimise calculations and cut down on computational costs, Vanderbilt [143] proposed the USP scheme. In comparison to NCP, the only requirement for USP is to agree with the all-electron wave function and potentials outside of the core radius. This allows for the defined core radius to be larger than in NCP[139] and has significant impact on computational costs associated with large atoms.

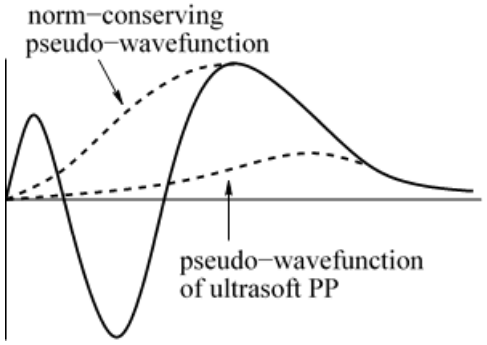

Figure 2.4: Comparison of the NCP and USP wave functions to the all-electron [142]

NB This section was written with all cited materials and informed by references [125, 129, 144–146].

2.3.2 DFT for alloys

The processing power of modern computers has made memory intensive DFT calculations more feasible, and deliverable at a shorter time scale. In recent years, several studies have been published on the use of DFT to simulate HEA. Usually, DFT is used complement or validate physical experiments, or vice versa, or as a purely computational study[147–149].

Most studies have used PBE exchange correlation functionals for the calculations[104, 147, 148, 150–163], USP[104], NCP[163], projector augmented wave (PAW) pseudopotentials[150, 152, 155–158, 161, 162], non Kohn-Sham DFT[164], no DFT at all[147]. These choices are dependent on the valence electrons (i.e the size of the atoms), what software is available, and the desired properties they want to calculate. Many studies use the special quasi-random structure model (SQS) of Zunger *et al.* [165], citing the computational cost of DFT calculations on large supercells with many atom species[151, 155, 156, 159, 160, 166]. A caveat of SQS is that it might impose long range order, however most studies that employed SQS as a means to cut down on computational costs used DFT before moving on to atomistic scale simulations where large supercells can be used without large computational costs[150, 151, 153, 155–161, 166].

Studies have focused on the use of DFT to calculate elastic properties[147, 155, 156, 163], magnetic properties[154, 158, 159, 164], phase transitions[150, 154], and to explore entropy[149, 161], and more.

Anand *et al.* [149] found that phase stability is dependent on configurational entropy, i.e. the randomness in the arrangement of the atoms on the lattice, and temperature, when the enthalpic stabilisation was fulfilled. Conversely, Schön *et al.* [161] saw that the influence of entropy on phase stabilisation is very small. Calvo-Dahlborg *et al.* [159] employed DFT to confirm that CoCrNiFe(Mn)-like alloys fit within an FCC phase, they reproduced experimental data, probed complexity of magnetic properties and showed that magnetic properties could be fine-tuned via alloying, even at large concentrations. Similarly, Zuo *et al.* [158] showed that alloying alters the crystal phase stabilisation at room temperature which alters Fermi level and as a result the magnetic properties. Körmann *et al.* [167] combined DFT with other techniques to predict magnetic properties of known HEA and validated the results of those simulations. Bonny *et al.* [148] used DFT to design and fit the interatomic potential of a quinary HEA providing a useful framework for interatomic potential methods.

Chapter 3

Methods

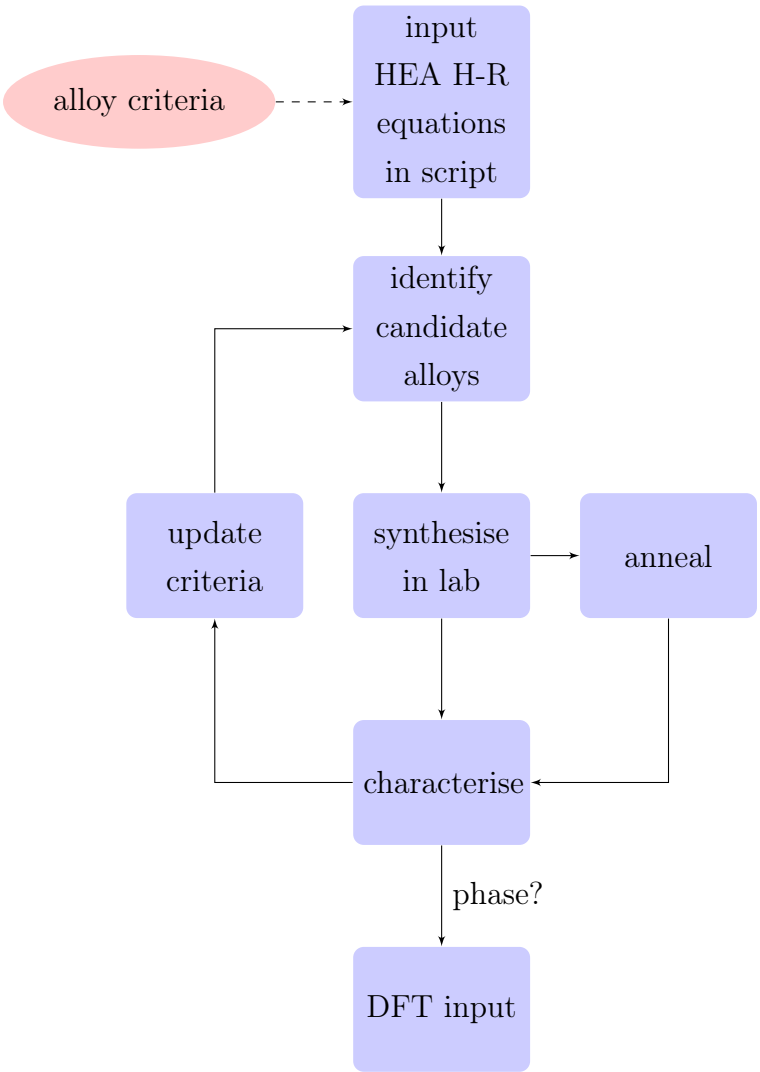

Figure 3.1: Overview flowchart of the project methodology

3.1 Experimental methodology

The scope of the project was to explore, identify, and investigate interesting multiprincipal component alloys with potential for high temperature applications. The general investigation methodology is illustrated in figure 3.1. The elements considered in this project are in table 3.1 and were chosen primarily due to their melting point. We explored quaternary and quinary compositions in a range of 5-35 at.% per component, summing up to 100 at.%, having consulted the literature and determined that for a single phase alloy that is multiprincipal it is a suitable area to explore. A simple combinatorial exercise using equation 3.1 shows that we would have 1820 and 4368 unique element combinations per alloy for quaternary and quinary, respectively. These numbers are before we even assign at.% values the sum of which is equal to 100% to each element.

$$\frac{n!}{r!(n-r)!} \tag{3.1}$$

where n is the number of types (elements) and r is the number of elements per combination in which every combination is unique, not repeatable and order of types in each combination does not make the combination unique. If we were to multiply the number of element combinations with the number of ways in which those elements could be added together to amount to 100 at.%, for quaternary that is 1820×11462 and for quinary it is 4368×553401. Given, that the total number of compositions this project could potentially explore were $\approx 440 \times 10^9$ before we apply any screening criteria, so we adopted a high-throughput approach to identifying interesting alloys.

3.1.0.1 Selection of metals

The primary purpose of this project is to explore noble metal multiprincipal component alloys and design, investigate and develop alloys for JMNM.

For the purposes of the project JMNM was consulted on which combinations of elements were interesting to them. We decided on PtRh, Ir and IrRh as bases for the compositions to investigate. Raykhtsaum [9] revealed that binary alloys of platinum and nickel are common. The primary criterion for selection is melting temperature, secondary criteria are toxicity, manufacturability (ductility) and alloying compatibility with noble metals. Ruthenium and osmium were excluded from the pool of noble metals, due to being hard to manufacture and toxic, respectively.

The elements presented on table 3.1 were chosen as candidate elements. In the initial stages of screening, melting temperature, atomic size, VEC, valence and Pauling electronegativity were considered for each element[113, 168]. Ultimately, once melting temperature and toxicity were screened, we proceeded to explore the full landscape of alloys that could be produced from the elements in table 3.1.

Atomic Number	Symbol	Atomic Size(Å)	Melting Temperature (K)	Boiling Temperature (K)	Pauling electronegativity	VEC	Crystal Structure
23	V	1.316	2183	3680	1.63	5	BCC
24	Cr	1.249	2180	2944	1.66	6	BCC
26	Fe	1.241	1811	3134	1.66	6	BCC
27	Co	1.251	1768	3200	1.88	9	HEX
28	Ni	1.246	1728	3186	1.91	10	FCC
29	Cu	1.278	1357	3200	1.90	11	FCC
41	Nb	1.429	2750	5017	1.60	5	BCC
42	Mo	1.363	2896	4912	2.16	6	BCC
45	Rh	1.345	2237	3968	2.28	9	FCC
46	Pd	1.375	1828	3236	2.20	10	FCC
47	Ag	1.445	1235	2435	1.93	11	FCC
74	W	1.367	3695	5828	2.36	6	BCC
75	Re	1.375	3459	5869	1.90	7	HCP
77	Ir	1.357	2739	4701	2.20	9	FCC
78	Pt	1.387	2041	4098	2.28	10	FCC
79	Au	1.442	1337	3129	2.54	11	FCC

Table 3.1: List of chosen elements and the relevant properties

3.1.1 Alloy identification

3.1.1.1 High-throughput method

A set of all possible combinations of 5-35% adding up to 100% for quaternary and quinary systems was set up in a text file. A code was written to screen all compositions and combinations of compositions. The code combines elements of interest and combined them into alloy compositions until every possible non-repeatable combination is exhausted. Each combination of each composition is put through the HEA H-R formulae and the result is compared against the chosen criteria. The primary criteria to be met are the enthalpy of mixing as defined in eq. 2.3, ΔH_{mix}, and the atomic size mismatch as defined in eq. 2.5, δ. Criteria were modified per alloy identification and manufacture cycle, informed by the directly previous cycle, and each modification is outlined in sections 6.2, 6.3, and 6.5 for PtRh, Ir, and Ag, respectively.

3.1.1.2 Alloys selected

Composition	δ	ΔH_{mix}	Reason for selection
$Pt_9Rh_{35}Ni_{21}Cu_{35}$	0.03555	-0.1820	ΔH_{mix} close to zero
$Pt_7Rh_{23}Ni_{35}Co_{35}$	0.03883	-0.0168	ΔH_{mix} close to zero
$Pt_{35}Rh_5Ni_5Ag_{25}$	0.03551	2.9900	low ΔH_{mix}
$Pt_5Rh_{25}Ni_{35}Cu_{35}$	0.03429	-1.1600	low ΔH_{mix}
$Pt_5Rh_{25}Ni_{35}Co_{35}$	0.03770	0.4600	ΔH_{mix} close to zero
$Pt_{35}Rh_{35}V_{22}Ag_8$	0.02685	-21.5672	very low δ and ΔH_{mix}
$Pt_{35}Rh_{35}V_5Ag_{25}$	0.02978	-2.1600	combination of very low δ and low ΔH_{mix}
$Pt_5Rh_{20}V_5Ni_{35}Co_{35}$	0.03651	-3.6500	combination of low δ and ΔH_{mix}
$Pt_5Rh_{15}V_{35}Ni_{10}Cu_{35}$	0.02680	-9.8100	very low δ
$Pt_5Rh_5V_{31}Cr_{24}Mo_{35}$	0.03481	-9.9892	interest in the addition of Mo
$Pt_5Rh_5V_{35}Cr_{20}W_{35}$	0.03385	-9.4800	interest in the addtion of W
$Pt_5Rh_{20}V_5Ni_{35}Cu_{35}$	0.03320	-0.7100	very low ΔH_{mix}
$Pt_{21}Rh_{34}V_5Ag_{32}Cu_8$	0.03850	-0.0012	extremely low ΔH_{mix}
$Pt_{17}Rh_{30}V_{14}Ag_{30}Re_9$	0.03410	-8.8800×10^{-16}	ΔH_{mix} virtually zero
$Pt_5Rh_{11}V_{14}Ni_{35}Co_{35}$	0.03415	-9.5864	combination of low δ and ΔH_{mix}; variation on other compositions
$Pt_{35}Rh_{35}V_5Ag_{20}Cu_5$	0.03245	-3.8100	combination of low δ and ΔH_{mix}; variation on other compositions
$Pt_5Rh_{10}V_{15}Cu_{35}Co_{35}$	0.02954	-3.9700	combination of low δ and ΔH_{mix}; variation on other compositions

Table 3.2: List of compositions selected using the criteria summarised in section 6.2

PtRh

Composition	δ	ΔH_{mix}	Reason for selection
$Ir_{35}V_{14}Fe_{16}Cu_{35}$	0.03317	-5.4152	inclusion of Fe
$Ir_{32}V_{10}Co_{34}Cu_{24}$	0.03440	-5.1232	combination of Cu and Co since it did not work previously; test whether the new criterion outlined in section 6.3 might help with alloying homogeneously
$Ir_{32}Fe_{9}Ni_{35}Cu_{24}$	0.03772	0.2824	low PGM content
$Ir_{35}Fe_{10}Pd_{22}Pt_{33}$	0.03041	-0.8992	inclusion of Fe and Pd
$Ir_{35}V_{15}Fe_{10}Cu_{35}Ag_{5}$	0.03790	-3.6200	inclusion of Ag
$Ir_{12}Fe_{33}Co_{20}Ni_{30}Pt_{5}$	0.03618	-4.4956	low PGM content
$Ir_{13}Nb_{5}Pd_{26}Re_{35}Pt_{21}$	0.01051	-7.0508	inclusion of Nb and Re; alloy was not manufactured
$Ir_{35}Rh_{28}Pd_{27}Pt_{5}Au_{5}$	0.01608	4.6028	inclusion of Au
$Ir_{35}Rh_{28}Pd_{27}Ag_{5}Pt_{5}$	0.01647	4.5528	inclusion of Ag
$Ir_{35}Rh_{35}Co_{5}Ni_{5}Pt_{20}$	0.02702	-1.1100	combination of PGM with elements that worked well previously
$Ir_{35}Rh_{35}Fe_{5}Pt_{25}$	0.02266	-1.8400	inclusion of Fe
$Ir_{35}Rh_{35}Pd_{20}Pt_{10}$	0.01039	2.6100	high PGM content

Table 3.3: List of compositions selected in the Ir IrRh investigation

Composition	δ	ΔH_{mix}	Reason
$Ag_{30}Pd_{35}Pt_{35}$	0.02125	-2.3800	small δ, negative ΔH_{mix}
$Ag_{35}Pd_{30}Au_{35}$	0.02208	-5.8800	small δ, negative ΔH_{mix}
$Ag_{25}Cu_{5}Pd_{35}Pt_{35}$	0.02747	-3.5400	small δ, negative ΔH_{mix}
$Ag_{35}Pd_{5}Pt_{25}Au_{35}$	0.01900	-2.2800	small δ, negative ΔH_{mix}

Table 3.4: List of silver based compositions compositions selected in the Ag investigation

3.1.2 Manufacture

3.1.2.1 Argon arc melting

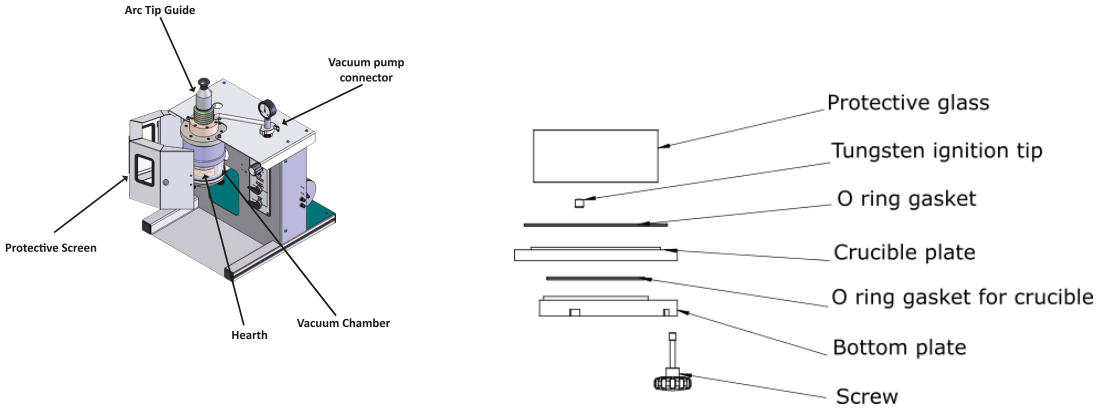

(a) Overview of the Arc Melter **(b)** Schematic of the melting tip-hearth set up

Figure 3.2: The Edmund Bühler Compact Arc Melter MAM-1 [169]

Argon arc melting was chosen as the preferred method for alloy manufacture in lab and at JMNM.

Argon arc melting works by passing a current through a cathode, in this case the arc melter tip, which concentrates the electrical current to a thin high temperature beam. The circuit is completed by the arc meeting the material to be melted and the hearth.

The laboratory is kitted with a Bühler Compact Arc Melter MAM-1 (MAM-1) (Fig. 3.2) and JMNM has industrial scale equipment. The alloys comprise of high melting point elements, argon arc melting is suitable for high melting point elements, the MAM-1 can melt up to 3500°C[169] with similar capacity at JMNM. In both cases the capability exceeds the melting points of the elements comprising the alloys. Additionally, control over the direction of the arc by the user provides enhanced homogeneity as the arc can be moved in a stirring motion. The list of metals considered for the project is on table 3.1, all melting temperatures for the metals are well within what is possible to melt for the arc melters.

3.1.2.2 Melting procedure

In the laboratory, 5g of raw materials were prepared per alloy sample made. The balance used to measure the material has a precision of 0.00005g. Each element was cut into small pieces following weighing out and constituent elements were mixed together to further ensure homogeneity when melting. Given the lower pressure used in the argon arc melter the melting and boiling points of elements would be lower than at atmospheric pressure. Certain compositions contained elements where the melting point of one and the boiling point of another would overlap. To ensure minimal vapourisation due to melting-boiling point overlap the melting

procedure was modified to account for this. The bottom of the hearth is water cooled so the elements would be layered in the crucible in such a way that the low melting point elements would be in the cooler part of the furnace. This would tend to reduce, and possibly eliminate the time at which the lower melting point materials were at temperatures above their boiling point, by seeing the greatest heating intensity applied to the higher melting point elements. The possibility of the loss of certain elements was however recognised, and the composition of the key alloys explored in the work was verified after manufacture. All constituents used were elemental metals of at least 99.95% purity, foil was preferred for ease of use but some elements were supplied in grain form.

The tip of the arc is ground to a point to ensure a thin and concentrated arc. The arc melter is fitted with a removable bottom water cooled copper crucible. The crucible comprises 7 cavities in which the alloy can be melted, and a vacuum sealant gasket. A glass collar is placed around the crucible before placing into the hearth to protect the outer glass of the hearth. The air in the hearth is vacuumed until the pressure drops below 1.0×10^0 torr. The hearth is then flushed with argon gas. This procedure is repeated a further 3 times to remove all air from the hearth. A good vacuum to reach to insure that the hearth is depleted of air is 6.0×10^5 torr and lower. The arc is then filled with argon gas to a pressure of 0.7bar to operate.[170]

Raw materials were melted into a solid mass for no more than 30 seconds so as not to overheat the hearth. The sample was flipped and remelted. The flipping and melting procedure was repeated 5 times to further ensure homogeneity.

3.1.2.3 Heat treatment

Cooling rates in small scale argon arc melters tend to be high which could lead to alloys being 'frozen' in a metastable state or be inhomogeneously mixed. Also, we wanted to know whether the alloys remained in single phase when tending to a thermodynamically stable state.

Alloys were heat treated at 700°C post laboratory manufacture and 1000°C post industrial manufacture according to the standard practice within JMNM. Laboratory manufactured alloys were heated to 700°C in an argon atmosphere and maintained at 700°C for 72 hours and left to cool inside the furnace.

The choice of 700°C is based on observations on CoCrFeMnNi by Pickering *et al.* [94] where precipitation of a Cr-rich phase was observed after prolonged heat treatment at 700°C. As will be explained in section 5 no significant change was observed in the heat treated laboratory manufactured alloys in comparison to their as-cast counterparts. In the industrial manufacture, heat treatment was performed to be as close to JMNM standards, therefore 1000°C was chosen.

3.2 Computational experiments

In section 2.3.2 there is mention of the computational costs involved with large DFT calculations. Depending on the parameters used, calculations can take between 1-192h using 4-32

CPU cores. The computational time and cost is not trivial, we were able to perform these calculations thanks to our two dedicated high performance computing clusters provided to researchers of the University of Sheffield.

An aim of this project was to provide a reliable predictive procedure for determining whether potential alloys are manufacturable. DFT was selected as a screening method post the high-throughput alloy identification described in section 3.1.1.

In this study of HEAs there were a few questions we wanted to attempt to answer. Are the alloys that mix homogeneously in manufacture truly homogeneous or in a metastable state due to the cooling rate associated with argon arc melting, can we prove that the alloys are in thermodynamic equilibrium via DFT? Can we investigate how readily these alloys oxidise and compare with experimental data to find trends?

To confirm the simulation results are significant in a physical world DFT simulations would be investigated concurrently with the manufacture of certain selected alloys which are likely to be single phase to inform and update the high-throughput + DFT study methodology. We need to sample a randomised lattice, $3 \times 3 \times 3$ atomic cells were constructed with an FCC lattice arrangement (108 atoms), this unit cell is large enough to prevent long range ordering and small enough for calculations to be performed on in a practical time frame.

The study was designed as follows

1. Determine the suitability of DFT for this study via the DFT investigation of known phase diagrams

2. Simulate alloys manufactured in this study and probe the thermodynamic stability of random (mixed) vs. ordered lattice arrangements

3. Design a method of performing surface calculations reliably and robustly on HEA systems

NB: A combination of CASTEP 16 and CASTEP 18 [171–176] was used for simulations in this study.

3.2.1 Suitability of density functional theory

There is strong evidence to show that DFT is a very reliable study route for the investigation of PGM. Specifically, DFT is used to investigate PGM heterocatalysts and as adsorption substrates[177–183].

3.2.1.1 Phase diagram DFT investigation

We set up an investigation to determine whether DFT was suitable for providing physically significant results because simulating metals at room temperature is computationally intensive and slow. A study of known binary phase diagrams was constructed to show that DFT provided results that aligned with the binary phase diagrams.

Since Pt, Rh and Ni are prevalent in most of the alloys (tables 3.2, 3.3) selected for synthesis using the method described in section 3.1.1, the phase diagrams of PtRh(figure 3.3) and PtNi(figure 3.4) are shown. Notably, both systems form ordered phases across the at.% gamut at 0°C.

For this study the CASTEP[171] code for first principles electronic structure calculation (DFT) was used with NCP (discussed in section 2.3.1) [184] LDA functionals and a Pulay density mixing scheme [185, 186] (this latter is a standard method available for updating the electron density at the end of a self consistent step) for geometry optimisation. The systems were treated as metallic (delocalised electrons). Across the range of combinations of Pt and Rh, and Pt and Ni, one cell was constructed per combination. For the ordered phases 30 different cells were constructed where the elements were arranged randomly on the lattice sites. All cells constructed were based on the FCCRh structure defined by Moshopoulou *et al.* [187] obtained from the Crystallography open database (COD) [188–192]. Cells of ordered phases were constructed from the crystal structure of the prototype taken from the COD, Ni_3Pt was constructed from the $AuCu_3$ prototype characterised by Wyckoff [193] and NiPt was constructed from the AuCu prototype characterised by Johansson *et al.* [194].

The results of this study are presented and discussed in section 4.1.

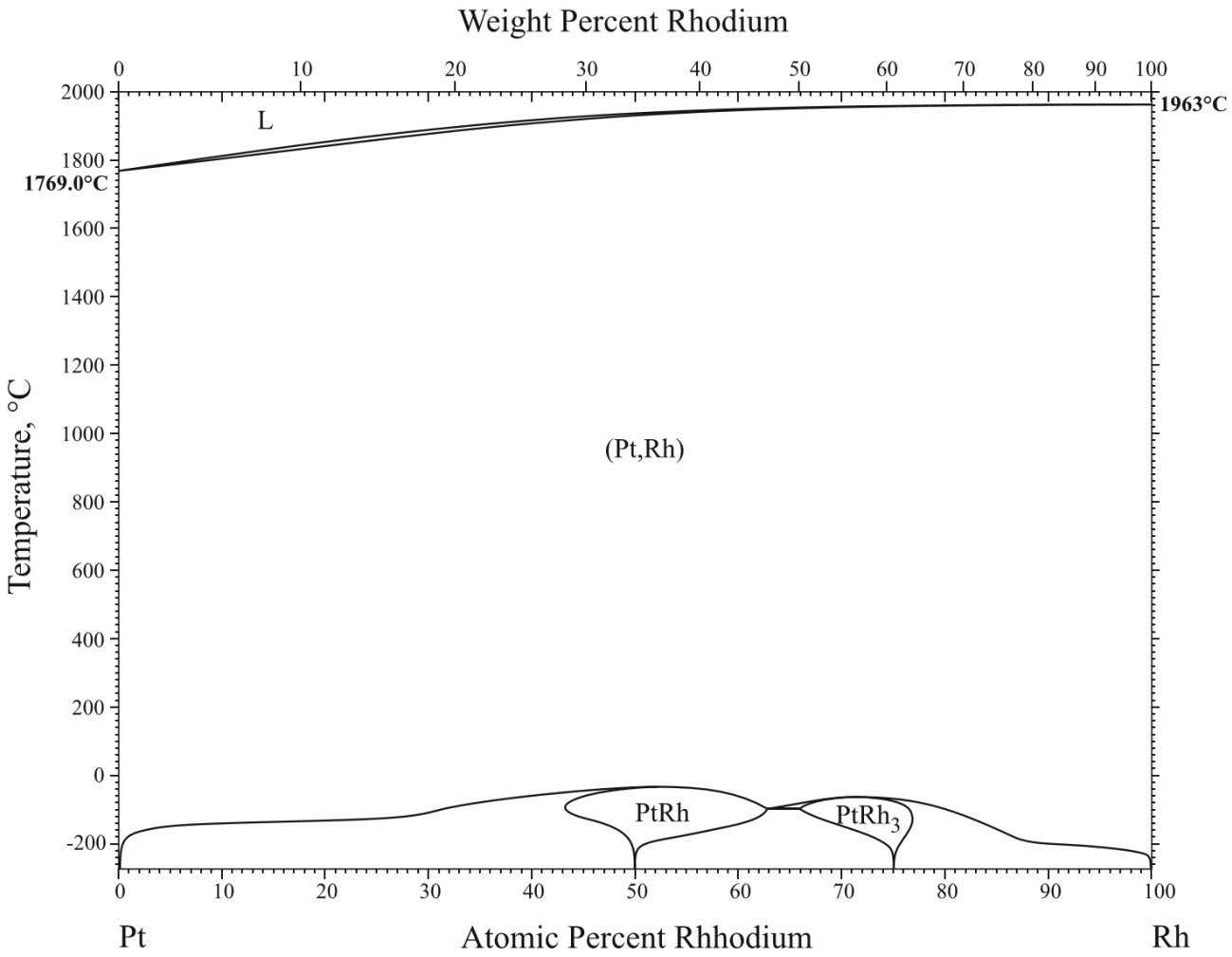

Figure 3.3: Phase diagram of Pt−Rh[195]

Phase	at.%Rh	Pearson symbol	Space group	Prototype
(Pt,Rh)	0 - 100	*cF4*	$Fm\bar{3}m$	Cu
PtRh	43 - 63	*cf**		
$PtRh_3$	66 - 77	*tI8*	*I4/mmm*	Al_3Ti

Table 3.5: Pt-Rh crystal structure data[195]

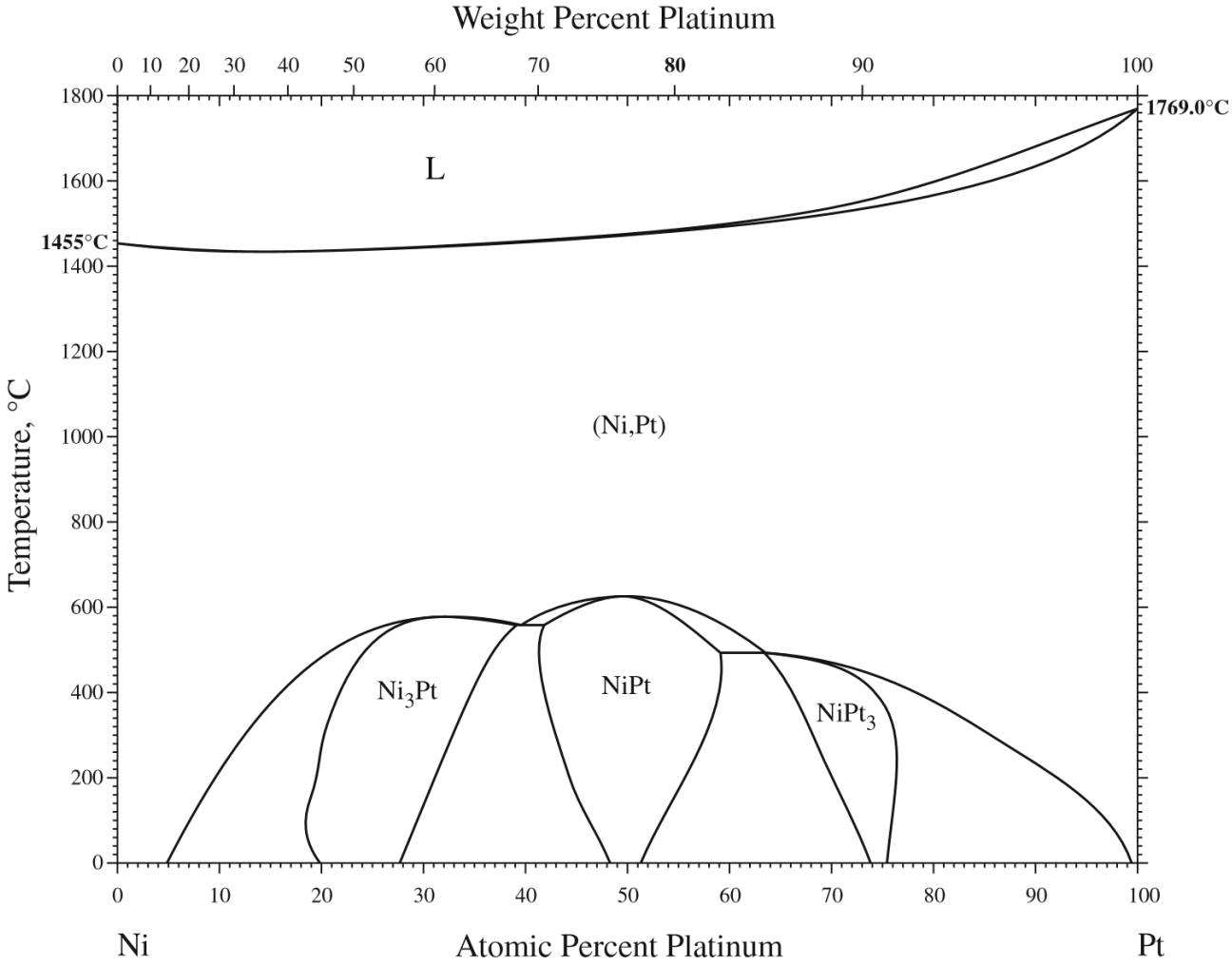

Figure 3.4: Phase diagram of Pt−Ni[196]

Phase	at.%Pt	Pearson symbol	Space group	Prototype
(Ni,Pt)	0 - 100	*cF4*	$Fm\bar{3}m$	Cu
Ni_3Pt	∼25	*cP4*	$Pm\bar{3}m$	$AuCu_3$
NiPt	∼50	*tP4*	*P4/mmm*	AuCu
$NiPt_3$	∼75	*cP4*	$Pm\bar{3}m$	$AuCu_3$

Table 3.6: Pt-Ni crystal structure data[196]

3.2.2 HEA simulations

For simulating HEA a similar method to solutions was used as in section 3.2.1.1. Geometry optimisations were performed on structures employing Lee [184] NCP pseudopotentials within LDA using Pulay [185] density-mixing optimisation. The systems were treated as metallic. The alloy system simulations were performed on $Pt_7Rh_{23}Ni_{35}Co_{35}$. 30 randomly arranged structures were prepared using a CASTEP `.cell` input cell generation Python 2.7 script, written by

Stavrina Dimosthenous derived from code by Dr. Christopher M. Handley (Dept. of Materials Science and Engineering, University of Sheffield). Random structures maintained the same fractional coordinates in space, elemental positions were randomised using the shuffle function of the Python random module. Structures were checked for uniqueness against other structures in the group during the random position generation. Cells were based on the Rh FCC cell by Moshopoulou *et al.* [187] obtained from the COD.

The systems were treated as spin-polarised with respect to Co (`SPIN = 3`). Suggestions on treating systems with spin are provided in section 4.5.

NB: Suggestions of simulating HEA using modern CASTEP on-the-fly (OTF) NCP and USP pseudopotentials within LDA and PBEsol schemes are provided in section 4.5. The suggestions are based on calculations performed on other systems comparing combinations of solution parameters.

3.2.3 HEA surface simulations

When investigating oxidation of materials via DFT the oxygen adsorption investigation is performed on cleaved surfaces of the bulk cell. We wanted to develop a method of investigating oxygen adsorption on HEA surfaces via DFT. The first step to the development of such a method was to develop a method of optimising these slab geometries of different orientation. A $Pt_7Rh_{23}Ni_{35}Co_{35}$ geometry optimised cell calculated using the procedure described in section 3.2.2 was used as our initial cell and prototype in this study. A geometry optimised cell is produced at the end of each CASTEP geometry optimisation if the user sets up the run to produce it, otherwise a cell can be produced via the CASTEP `.check`, `.castep_bin` or `.cst_esp` files using the c2x code to convert the information into a readable `.cell` file [197]. Surfaces of the lowest energy geometry optimised structure were cleaved from the `.cell` file resulting from the calculation using the METADISE code [198]. Surface slabs of [0 0 1], [1 1 0], [1 0 1], [1 1 1], and [0 1 1] exposed surfaces were cleaved from the optimised cell. METADISE will cleave as many surfaces as there are atoms, 108 in our case, so 30 cleaved surface slabs were chosen at random from the ones produced by METADISE. Singlepoint energy calculations were performed on each of the 30 surface slabs per miller plane. For the singlepoint energy calculation CASTEP 18 was use along with OTF NCP Pseudopotential (PP) within an LDA scheme and an ensemble density functional theory (EDFT) optimization procedure, which improves the convergence to the ground state energy[199].

The lowest energy $Pt_7Rh_{23}Ni_{35}Co_{35}$ original cell was treated with the same procedure to allow for the calculation of the surface energies. Ramamoorthy *et al.* [200] define the surface energy, E_{surf} as,

$$2E_{surf} = E_{slab} - nE_{tot} \tag{3.2}$$

a simple rearrangement gives,

$$E_{surf} = \frac{E_{slab} - nE_{tot}}{2} \tag{3.3}$$

for E_{surf}, where E_{slab} is the 'bulk' slab groundstate energy after a singlepoint calculation, E_{tot} is the groundstate energy of the bulk cell. In this study, $n = \frac{n_{slab}}{n_{bulk}}$ is, where n_{slab} is the number of atoms in the slab supercell and n_{bulk} is the number of atoms in the bulk supercell. The METADISE slab generation module will usually keep $n_{slab} \equiv n_{bulk}$ so that reduces the number of steps in the calculation.

3.3 Characterisation

Laboratory manufactured samples were prepared as described in section 3.1.2.2. Each sample produced was approximately 1cm in diameter depending on the density of the comprising elements.

The main aim in the laboratory scale manufacture was to produce single phase multiprincipal component alloys. To save on resources visual inspection of the alloys produced was important. If alloys displayed inhomgeneity visible to the naked eye then they were immediately excluded from any further characterisation analyses.

Phase analysis was performed via XRD, element distribution on prepared sample surfaces was investigated via XRF and energy dispersive X-ray spectroscopy (EDX) via scanning electron microscopy. To further confirm homogeneity and single phase, alloys which were found to be single phase via these techniques were sent to Johnson Matthey Technology Centre (Johnson Matthey Technology Centre (JMTC)) for analysis via electron probe microanalysis (EPMA). Alloys of interest were subject to a crude ductility trial to investigate manufacturability.

Industrially manufactured samples were prepared on site at JMNM. 1kg of charge was prepared from the wt.% of each component element, pre-melting. Characterisation samples were cut from the resulting ingots of alloys (≈15cm×6cm).

For the industrial scale manufacture, it was important to ensure that the results for the phase composition and microstructure scaled with the quantity of material being alloyed. The same visual inspection was used upon cooling and the cut-off samples were inspected for visual inhomogeneous mixing, as well. The same spectroscopic techniques of XRD, XRF, EDX, and EPMA were used to perform phase analysis and confirm homogeneity. We chose nanoindentation, Vickers hardness indentation, grain size optical analysis, and thermogravimetric analysis (TGA) as techniques for mechanical property and thermal property evaluation, respectively. To fully understand the alloys' response to TGA, differential scanning calorimetry (DSC) was used to investigate the response of the alloys to heating in an inert atmosphere.

It is important to note that all samples were manufactured from materials where the noble metal content was provided on loan from JMNM. The arrangements for this loan limited the total amount of metal value which could be held at the University of Sheffield at any one time, due to insurance terms. Due to the high value of some of the elements used, strategic decisions had to be made to return samples before the end of the project, in order to release value with which further supplies of pure metals could be borrowed. As a result, not all samples were

retained long enough for repeat measurements to be made, and in some instances this resulted in optimisation of the techniques and settings for the sample characterisation being refined after some samples were no longer available.

3.3.1 Sample preparation

The following procedure was used to prepare samples for characterisation. Samples were mounted in clear resin for the first round of alloy design and development, subsequent samples were mounted in conductive bakelite. Both mounting procedures were conducted with a Buehler Simplimet 1000 automatic mounting press using the mounting procedures advised by the suppliers.

A Buehler EcoMet automatic grinder-polisher fitted with a Buehler AutoMet power head was used to grind and polish samples to a planar, mirror finish. Grinding was performed at 200-250 rpm for the grinding plate and 39-49 rpm for the power head. Polishing was performed at 100-125 rpm for the grinding plate and 39 rpm for the power head. The back of the mounted samples was ground flat using P240 silica grit paper for the case of nanoindenter measurements. When mounted in bakelite there is an air gap between the sample and the bakelite. To ensure maximum force transfer through the sample for accurate determination of the reduced modulus during nanoindentation the back of the mounted sample was ground to the point where the underside of the sample was well exposed and planar. Care was taken to indent the prepared sample surface over the area that was directly exposed on the underside.

Samples were ground flat using P400, P800, P1200, P2500 and P4000 grades of SiC grit paper. Samples were washed between each paper grade and the grinding plate was cleaned between each paper grade to prevent any fallout particulates from scratching the sample.

Samples were then polished using 6µm diamond water based suspension and Buehler TexMet C polishing cloth followed by 1µm diamond water based suspension and Buehler MicroCloth polishing cloth. Samples were washed with isopropyl alcohol, dried using hot air, then washed with isopropyl alcohol and dried with hot air between each grade of diamond suspension. The power head was also washed between each grade of diamond suspension, and finally a protective cup was placed on top of each sample until required for characterisation.

3.3.2 X-ray diffraction

X-ray diffraction (XRD) is a well known phase analysis technique. The goal of using XRD in this project is to identify phases present in the alloys, and therefore to determine whether the alloys are a single cubic phase, ideally FCC, or not.

Due to the small wavelength of X-rays, they are able to penetrate solids, and diffract through the lattice planes, forming a diffraction pattern. Analysis of these patterns allows the identification of the size and shape of the unit cell, the number of atoms, electrons and the lattice configuration.

For example, Bragg's law, figure 3.5, gives us a way of determining the lattice spacing, d, by knowing the angle the diffracted X-ray exits the sample,

$$n\lambda = 2d\sin\theta \tag{3.4}$$

where n is an integer related to the order of the reflection, (λ) is the wavelength of the incident X-rays, d is the spacing of the particular diffracting planes and (θ) is the angle of diffraction. [201, 202].

In this project, a Siemens/Bruker D5000 diffractometer and a Bruker D2 Phaser were used for pattern collection. As a standard both the diffractometers have a Cu anode target and a Ni $k\beta$ filter, without a bean monochromator so the beam has both CuKα1 and CuKα2 radiation. Samples were ran at different ranges in 0 - 120° 2θ depending on prior XRD traces. All alloys are unique to this project, but the latest ICDD PDF-4+ [203] databases and the COD[188–192] were used to index and analyse the XRD scans for any matches against known compositions using the Bruker DIFFRAC.SUITE EVA software.

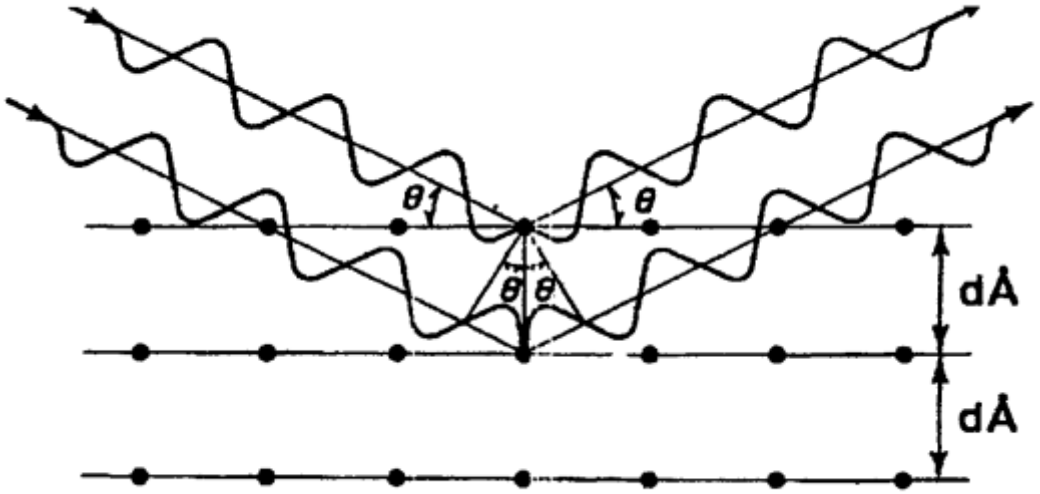

Figure 3.5: Bragg's law representation of the path of X-rays diffracting through a crystal[202]

XRD data were analysed using the Bruker DIFFRAC.SUITE EVA software, peaks were identified and manually indexed using Bragg's Law and with a procedure outlined in ref. [204] and in this [205] tutorial by Dr. Nik Reeves-McLaren from the Department of Materials Science & Engineering at the University of Sheffield, an illustration (fig. 3.6). The peaks were indexed manually using the relationship in equation 3.4. Since the diffractometer has a Cu anode target we know that λ in equation 3.4 is 1.5406Å [206]. For a cubic system,

$$\frac{1}{d^2} = \frac{(h^2 + k^2 + l^2)}{a^2} \tag{3.5}$$

where $[h\,k\,l]$ are the indices defining the lattice plane of diffraction and a is the lattice parameter. For a cubic system a is a single value (i.e. all lattice parameters are the same as the unit cell is a cube) and we know from our diffractometer that λ is constant. We reach this relationship for calculating the lattice plane,

$$\sin^2\theta = \frac{n^2\lambda^2}{4a^2}(h^2+k^2+l^2) \tag{3.6}$$

The $\sin^2\theta$ values can be calculated and compared to find a common factor, which can then be compared to possible values resulting from the combination of h, k and l to index each peak.

An example of the process to index the peaks is displayed in figure 3.6. The ratio values displayed are the ratio of the $\sin^2\theta$ of the first peak and every subsequent peak is multiplied by $1, 2, 3\ldots$ until all ratios are integers. Each ratio is equal to $h^2+k^2+l^2$, which we can determine the lattice plane from.

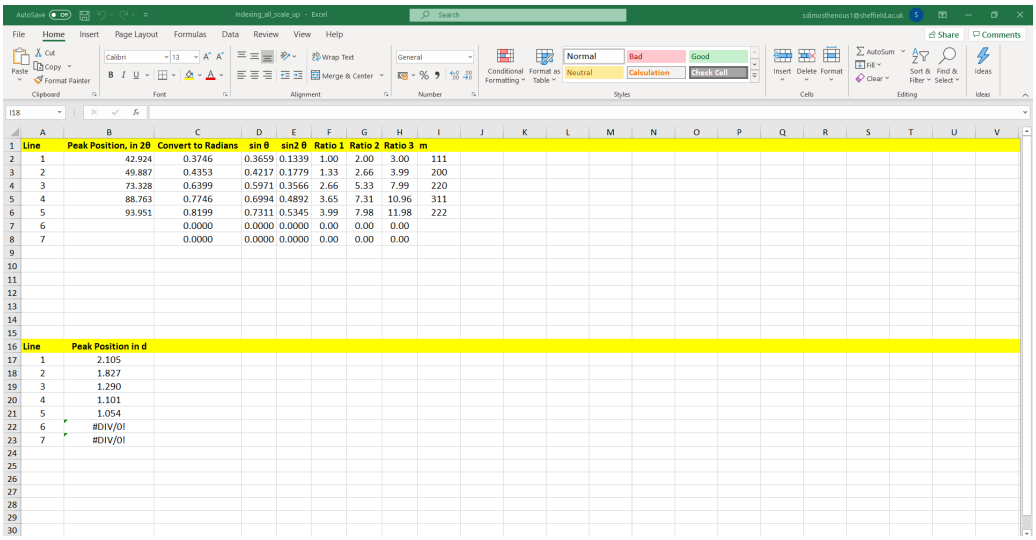

Line	Peak Position, in 2θ	Convert to Radians	sin θ	sin2 θ	Ratio 1	Ratio 2	Ratio 3	m
1	42.924	0.3746	0.3659	0.1339	1.00	2.00	3.00	111
2	49.887	0.4353	0.4217	0.1779	1.33	2.66	3.99	200
3	73.328	0.6399	0.5971	0.3566	2.66	5.33	7.99	220
4	88.763	0.7746	0.6994	0.4892	3.65	7.31	10.96	311
5	93.951	0.8199	0.7311	0.5345	3.99	7.98	11.98	222
6		0.0000	0.0000	0.0000	0.00	0.00	0.00	
7		0.0000	0.0000	0.0000	0.00	0.00	0.00	

Line	Peak Position in d
1	2.105
2	1.827
3	1.290
4	1.101
5	1.054
6	#DIV/0!
7	#DIV/0!

Figure 3.6: Illustration of the manual indexing analysis performed on one of the XRD data sets presented in figures 6.2a

3.3.3 X-ray fluorescence

XRF is a widely used quick analysis technique for qualitative and quantitative assessment of materials. XRF was used in this project to identify the local composition at different points on the surface of the sample to determine whether the elements are distributed homogeneously across the bulk of the synthesized alloy.

XRF is a spectroscopic technique that relies on analysing the fluorescent (or secondary) X-rays emitted by a sample that has been bombarded by an X-ray source. The interaction resulting in fluorescence is illustrated in figure 3.7, as is evident, there are more ways in which X-rays can interact with matter and most XRF machines will have accounted for these interactions and the resulting radiation. The most common way to produce incident X-rays is by an X-ray tube which produces X-rays from decelerated electrons (Bremsstrahlung radiation) [207–209].

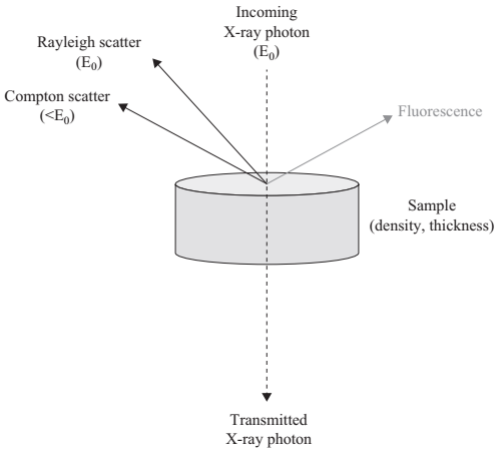

Figure 3.7: X-ray beam interactions with matter [209]

The machine used for XRF analysis is a Malvern PanAlytical Zetium which utilises X-ray tube technology and wavelength dispersive detection. The standard calibration procedure was followed before every measurement session, where gain correction and Drift standards are ran and tested against the factory measurements of the standards. This is done to account for the aging of the X-ray tube over time and ensuring that the quantification is accurate[210]. Apertures ranging over 6mm - 12mm were used for the surface exposed to the X-rays, depending on the size of the sample. The data is presented as the wt.% of the material present on the surface bombarded with X-rays. Since the data collected by the software is also presented in weight percent content (wt.%) we convert to at.% to compare the data to the expected composition. The formula for converting from wt.% to at.% for an alloy with N components is presented in eq 3.7.

$$at.\%_i = \frac{{}^{wt.\%_i}/_{m_i}}{{}^{wt.\%_i}/_{m_i} + {}^{wt.\%_j}/_{m_j} + \ldots + {}^{wt.\%_N}/_{m_N}}, \tag{3.7}$$

where m_i is the atomic mass of component i.

XRF was performed on the alloys as a means to gauge homogeneity in mixing across the sample. Due to the scale over which the assessment is made, a stronger indicator for homogeneous mixing during manufacture in this study is the similarities across samples of the same composition.

XRF data was collected once per sample imaged. We chose the largest aperture the sample size could accommodate. The error quoted is the absolute error associated with the measurement as calculated by the data processing software of the Zetium. For some samples it was not possible to give these data, as the values were not originally recorded, and the samples were returned for reprocessing.

3.3.4 Scanning electron microscopy

The microstructure of samples was investigated via the use of a scanning electron microscope (SEM). A sample is placed in the vacuum chamber of the SEM and bombarded with accelerated electrons. There are numerous ways in which the bombarded (imaged) surface can interact with those electrons, figure 3.8. Of concern in this study are the interactions producing Secondary electrons (SE), sample electrons that are emitted from the sample in response to the incident

gun electrons, and BSE, electrons originally from the gun that have been deflected by the nucleus of an atom in sample, likelier with 'heavier' atoms which means that images produced from BSE will be brighter in regions of the imaged surface where the material is composed of elements with a larger number of electrons, and X-ray photon emission, produced by the interaction of an incident electron with a core-shell electron[211]. SEM typically have detectors for SE and BSE as is illustrated in figure 3.9.

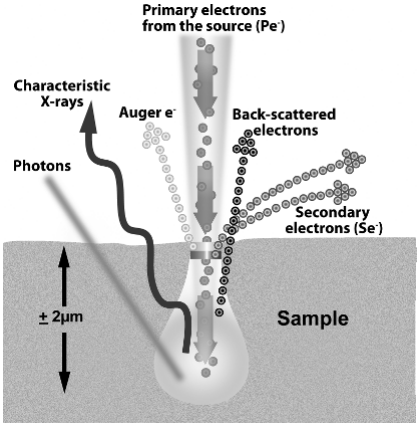

Figure 3.8: Representations of electron-surface interactions [212]

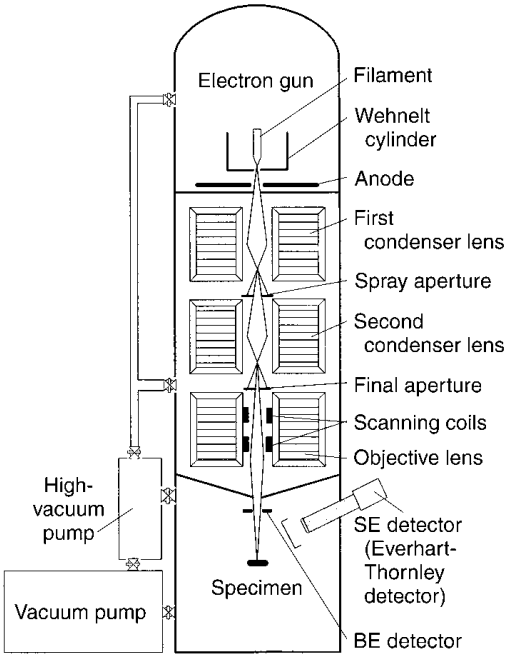

Figure 3.9: Schematic of a typical SEM illustrating the positions of SE and BSE detectors[213]

The SEM used was an FEI Inspect F and F50 at the Sorby research centre at the University of Sheffield. A Zeiss EVO MA 10 was used at JMNM. For the purposes of data collection during this project, an accelerating voltage of 20keV and a spot size of 3 - 5 were used (conditions developed to allow good imaging and data collection for EDX, described below). Both SE and BSE imaging modes were used, the former for imaging the sample surface, similar to optical microscopy, and the latter for identifying segregation.

3.3.4.1 Energy dispersive X-ray spectroscopy

Energy dispersive X-ray spectroscopy (EDX or EDS) relies on the collection of the characteristic X-rays emitted by the elements on the surface of the sample in the surface - beam interaction mentioned in the above section (3.3.4) and illustrated in figure 3.8. This allows for qualitative chemical analysis of the surface and further investigation of segregation at the surface. The EDX detector used was an Oxford Instruments X-Max 80mm^2 silicon drift detector for analyses conducted at the Sorby Centre at the University of Sheffield and at JMNM. After several trial and error data collections using a range of accelerating voltages, we chose to operate the electron gun at 20keV of accelerating voltage with a spot size ranging between 4-5. EDX chemical composition maps were constructed by the soft-

ware to investigate the elemental homogeneity across the prepared sample surface. Areas where segregation was suspected during BSE visual inspection were subject to point spectrum analysis.

While SEM coupled with EDX analysis was able to illuminate the homogeneity of the sample and provide qualitative analysis there was an overlap of the elemental peak positions in the spectra due to the nature of the alloy constituents. Given usage time constraints and the volume of samples to be characterised SEM-EDX was utilised as a fast way of assessing whether the distribution of elements throughout the sample was, to a first approximation, uniform and that areas of very significant segregation did not exist within the sample. This fast scanning involved taking an EDX element analysis map measurement for 5 minutes using 20keV accelerating voltage and a spot size of 4. The choice of measurement parameters were a result of trial and error to identify the most suitable parameters for these particular measurements.

3.3.5 Electron probe microanalysis

Electron probe microanalysis (EPMA) of samples was conducted by Dr. Gareth Hatton at JMTC, Sonning Common, UK. Dr. Hutton produced at.% distribution maps of imaged surfaces at low and high magnification which resolved the distribution of elements on the imaged surface, the homogeneity in mixing, ultimately the degree to which an alloy exhibited a single phase or multiple phases.

The EPMA used was a Jeol JXA-8500F electron probe microanalyzer, operated at an accelerating voltage of 20keV for 100ms/pixel where each pixel was of side length 1.5µm (low magnification) and 0.5µm (high magnification) and was carried out on prepared polished surfaces of various alloy specimens. The EPMA is fitted with 5 wavelength dispersive spectrometers and one silicone drift diode EDX detector. The EPMA can therefore analyse up to 5 elements simultaneously via wavelength dispersive techniques suitable for the analysis of the alloys designed in this project [214].

The EPMA functions similarly to SEM with EDX functionality, able to perform chemical analysis of the imaged surface to about 0.5µm interaction volume, in this study. The minimum area that can be imaged varies depending on composition. Also, EPMA can map the distribution of elements in the area imaged to a good level of precision, making it extremely beneficial for confirming homogeneity. When comparing the EPMA and EDX, the primary benefit of EPMA is the higher resolution and accuracy involved with EPMA due to the use of wavelength dispersive technology.

Like EDX, Wavelength Dispersive Spectroscopy (WDS) relies on collecting the characteristic X-rays emitted by the sample after bombardment by an electron gun. The energy dispersive spectrometer detects the energy of the characteristic X-ray as emitted by the excited electron returning to its ground state. In contrast WDS relies on Moseley's law which states that the square of the frequency of the characteristic X-ray is directly proportional to the atomic number

of the emitting element.

While WDS offers a higher resolution in comparison to EDX it can only detect a certain number of elements at a time. Since wavelength dispersive detectors are built to detect within certain ranges, several detectors are needed to cover the spectrum of wavelength ranges. Depending on the wavelength dispersive detector there might also be significant overlap in the elements detected. Also, the emitted X-ray might not be within the detection range of the wavelength dispersive detector. In contract EDX detectors can collect all energies and detect all elements simultaneously, however the resolution is much lower in comparison to WDS and we cannot quantify the elemental distribution on the imaged surface.

Of particular concern with EDX is the overlap of the spectra of the PGMs, the wavelength dispersive spectroscopy, utilised by EPMA, can address the issue of spectrum overlap and is more suitable for mapping and quantitative analysis. Also, since the maximum number of elements in any alloy we had was 5 the EPMA provided to us in this study was suitable for collecting data for at.% elemental distribution maps.It was observed that it can reveal segregation as low as 1 at.%.

3.3.6 Manufacturability hammer trial

At an early stage of the experimental work on the alloys, it was decided that a quick discrimination between alloys that were highly brittle (and therefore not suitable for manufacturing processes such as wire drawing) and those with some ductility would be useful. To do this a very basic hammer trial was developed, which was only performed on the first cycle of successfully alloyed laboratory manufactured alloys, e.g. the PtRh-based series of experimental alloys. Each sample was placed in a cylindrical cavity of 6mm diameter kitted with a snug fitting punch, flat at both ends. The punch was placed on top of the sample. A hammer was used to hit the punch. Each trial consisted of 20 impacts, attempting to make each of comparable energy, samples were inspected after every 5 impacts for shattering. Despite not being accurate and only providing qualitative data, the hammering trial can give a fair indication about how a material will perform when being manipulated at room temperature and helped in making decisions about which alloys to schedule for industrial scale up trials.

3.3.7 Vickers hardness

Vickers hardness indentation is a widely used technique in academia and industry. The method was developed by Smith *et al.* [216] with hardness defined as the load needed to create an impression of a particular size (though in the modern embodiment the load is normally set and the size of indent measured). A Vickers hardness test is performed on a sample at constant load using a square-based pyramidal shaped diamond indenter, with the hardness determined from measurements of the diagonals presented in figure 3.10. The Vickers hardness number (HV) is the applied load on the sample divided by the surface area of the resulting

indentation[215].

Vickers hardness microindentation was performed at Johnson Matthey Noble Metals on a Future Tech Corporation Model: FM-100 (FM-100) and at the Department of Materials Science and Engineering at the University of Sheffield on an EMCOTEST DuraScan 70 G5 (DuraScan). The usual practice at JMNM is to indent with 300gf (HV 3), equivalent to 2.94N converted using 1kgf $\approx$ 9.806N equivalency. The samples were indented in a diagonal direction across the polished surface of the sample to cover the longest length across the sample and space the indents as far apart as reasonably possible so that they do not interfere with neighbouring indents. The FM-100 is manually driven so indents are performed by the user on manually focused on areas. The best care was taken to take a diagonal across the sample, 16 - 18 readings were taken. On the DuraScan each sample was indented with 9 - 10 indents equally spaced by the software to account for sample surface size differences. Indent size analysis was performed by the software once the length of the indent diagonals was confirmed by the user. An HV number was given per indent and an average was calculated over all the indents per sample.

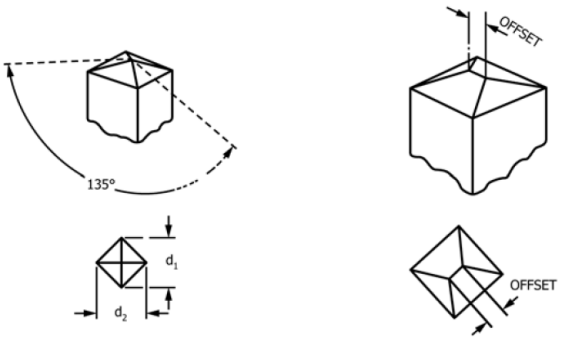

Figure 3.10: Vickers indenter tip schematic showing the tip diagonals[215]

3.3.8 Nanoindentation

Nanoindentation was performed on a Hysitron TI Premier in the Department of Materials Science and Engineering at the University of Sheffield under the guidance of Dawn Bussey. Nanoindentation was used to investigate the elastic modulus and the hardness of the alloys. Both these qualities are important in informing how a material will respond to mechanical processing, and potentially in service.

As a standard, a grid of 49 indents were taken per sample with a load of 100mN per indent. 100mN is a relatively high load in the context of nanoindentation, this was to try to imitate a microindenter. A high load transducer was used to facilitate that the load as we are interested in macroscale modulus and hardness. The 49 indent pattern can be seen on figure 3.11. A dwell time of 30s was used to ensure proper depth penetration. This dwell time ensures that any time-dependent deformation processes have proceeded to a negligible level, and that the hardness and modulus recorded will be correctly representative of the sample. A grid pattern of 49 indents was obtained. The number of indents is sufficient for analysis of the mean reduced modulus once outliers are excluded.

The analysis procedures used for the nanoindentation data are those introduced by Oliver *et al.* [217].

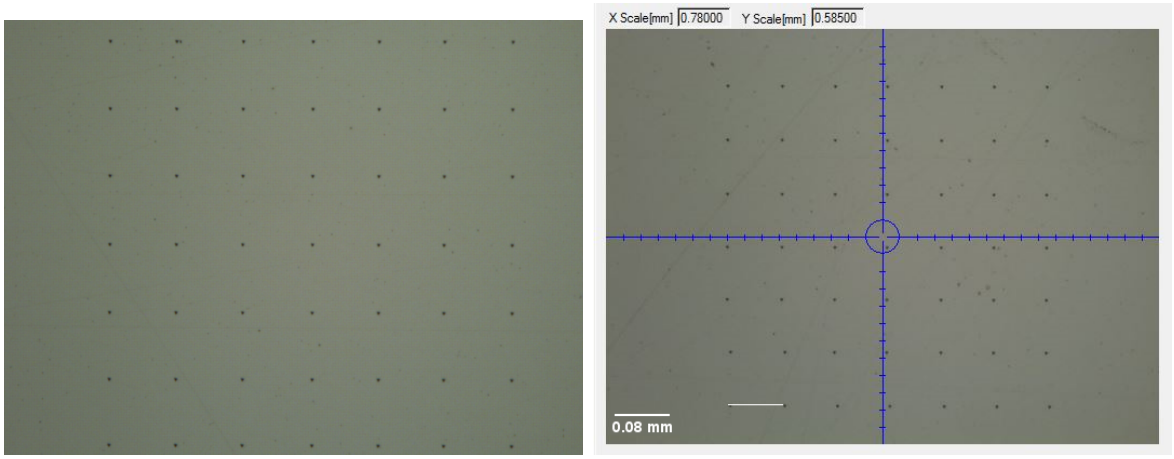

(a) $Pt_5Rh_{11}V_{14}Ni_{35}Co_{35}$ **(b)** $Pt_5Rh_{20}V_5Ni_{35}Co_{35}$

Figure 3.11: 49 indent grid pattern

3.3.9 Differential Scanning Calorimetry

Differential Scanning Calorimetry (DSC) was performed by Dr. Oday Hussein at the Department of Materials Science and Engineering at the University of Sheffield. The instrument used was a TA Instruments SDT-Q600. DSC was performed in argon and a 20°C min^{-1} up to 1400°C. Readings were taken from the start of heating to the sample reaching room temperature post-heating. Once 1400°C was reached the heating system was turned off and the sample was left to cool in the argon atmosphere. DSC was performed to investigate thermal stability of samples at the range of 1000°C and 1200°C before thermogravimetric analysis (TGA).

The solidus temperature for each alloy was determined from the heat flow vs. temperature plot of the results. Tangent lines are extrapolated from the steady state part of the curve, and from the rising/peaking part of the curve. The horizontal axis value of the point at which the two lines intersect is the solidus temperature.

3.3.10 Thermogravimetric analysis

The investigation of the alloy samples was informed by the investigation carried out in Migas *et al.* [218] with consultation from Dr. Claire Utton at the Department of Materials Science and Engineering, University of Sheffield. Samples of known geometry, 3mm × 3mm × 3mm, were made by electrical discharge machining (EDM), where possible, otherwise care was taken to cut the samples as close to the geometry of the ED machined samples as possible. A sample was placed in an alumina crucible and left in a NETZSCH STA 449 F3 Jupiter to heat up at a rate of 5°C min^{-1} in air until 1000°C was reached.

Each measurement was checked intermittently for mass gain. If the sample was stable in the heating up stage then the temperature was held at 1000°C for 1h or until significant mass gain was observed when the measurement was checked; if the sample was not stable in air then the analysis was halted.

Analysis of the results investigates mass gain during the measurement in air and is informed by visual inspection in comparison to how the sample looked before the measurement.

3.3.11 Etching and optical microscopy grain size analysis

Etching reveals the underlying microstructure that might not be visible otherwise. A chemical reagent attacks the surface of a ground and polished sample and reveals, for example, the grain structure (if the etchant and the procedure are appropriate). The grain structure depends on a number of factors such as cooling and mechanical processing so can be manipulated to suit the intended use of a metal.

As-cast and annealed industrially manufactured samples were electrolytically etched using a standard procedure for PGMs at JMNM. Samples were etched in a 10%HCl saturated with NaCl solution. The current was varied between 0.2A - 1.0A judged according to the sample's response to the AC etch. The etched sample was then washed and dried.

Optical images of each sample were taken to examine the revealed microstructure.

$$\sigma_y = \sigma_0 + k_y d^{-1/2} \tag{3.8}$$

Etching is primarily important in this project as it reveals the alloy grains and presents another avenue to investigate the mechanical properties of our alloys. Generally, the smaller the grain size the stronger the metal, due to the increase in barriers to dislocation motion as slip planes do not continue across grain boundaries[219]. The Hall-Petch relationship in equation 3.8 describes an inverse proportionality between the average grain diameter, d, and the yield strength, σ_y of a metal if σ_0 and k_y, which are quantities characteristic to a certain material, are known. This is assuming that the grains are approximately similar in size and not at either extreme of size.

Since we do not know the quantities σ_0 and k_y it is reasonable to assume that a small enough d coupled with variable crystallographic orientations does point to a strong metal.

Chapter 4

Simulation results and discussion

4.1 Phase diagram DFT simulations

4.1.1 Phase diagram study

The phase diagrams presented in section 3.2.1.1 are presented here as they are referred to extensively below.

4.1.1.1 PtNi

For the data presented in figure 4.3 and figure 4.7 the parameters outlined in section 3.2.1.1 were employed. Both sets of data were handled in the same manner so the following outline of the method applies to both PtNi and PtRh; for brevity we only refer to PtNi. PtRh is presented in section 4.1.1.2. The final energy of the geometry optimised random lattice ordered 108 atom FCC structure was compared against the enthalpy obtained from

$$expected = c_{\mathrm{Ni}} E_{\mathrm{Ni}} + c_{\mathrm{Pt}} E_{\mathrm{Pt}} \tag{4.1}$$

where c_{Ni} and c_{Pt} are the at.% of Ni and Pt, respectively, calculated from the proportion of the number of atoms of each species in the 108 atom lattice, and E_{Ni} are E_{Pt} the energy for the geometry optimised 108 atom single species Ni and Pt lattices, respectively. The expected energy was subtracted from the calculated energy.

Across the plot we can see that as the alloy tends to more equiatomic proportions that mixing is more favourable. Of course, this was only performed on one lattice arrangement with the assumption that this lattice arrangement is representative of a lattice which is fully mixed with any particualr atom having equal probability of occupying any random atom site. More random arrangements are needed for each different proportion of atoms of interest to be able to draw a complete conclusion.

In the Pt−Ni phase diagram we can see that the ordered phases PtNi and $PtNi_3$ have a lower energy than the random lattice arrangements. While the random lattice arrangements

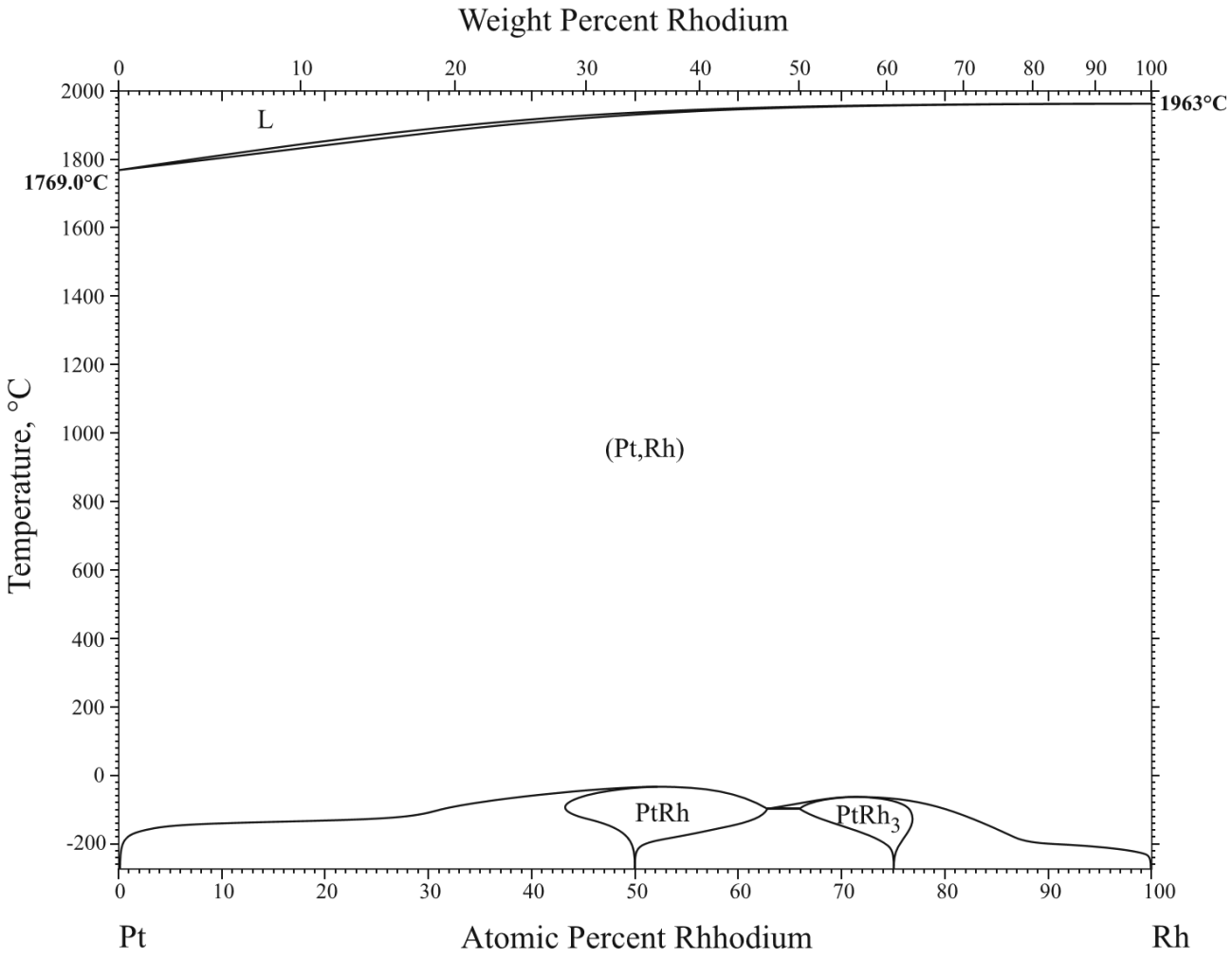

Figure 4.1: Phase diagram of Pt−Rh[195]

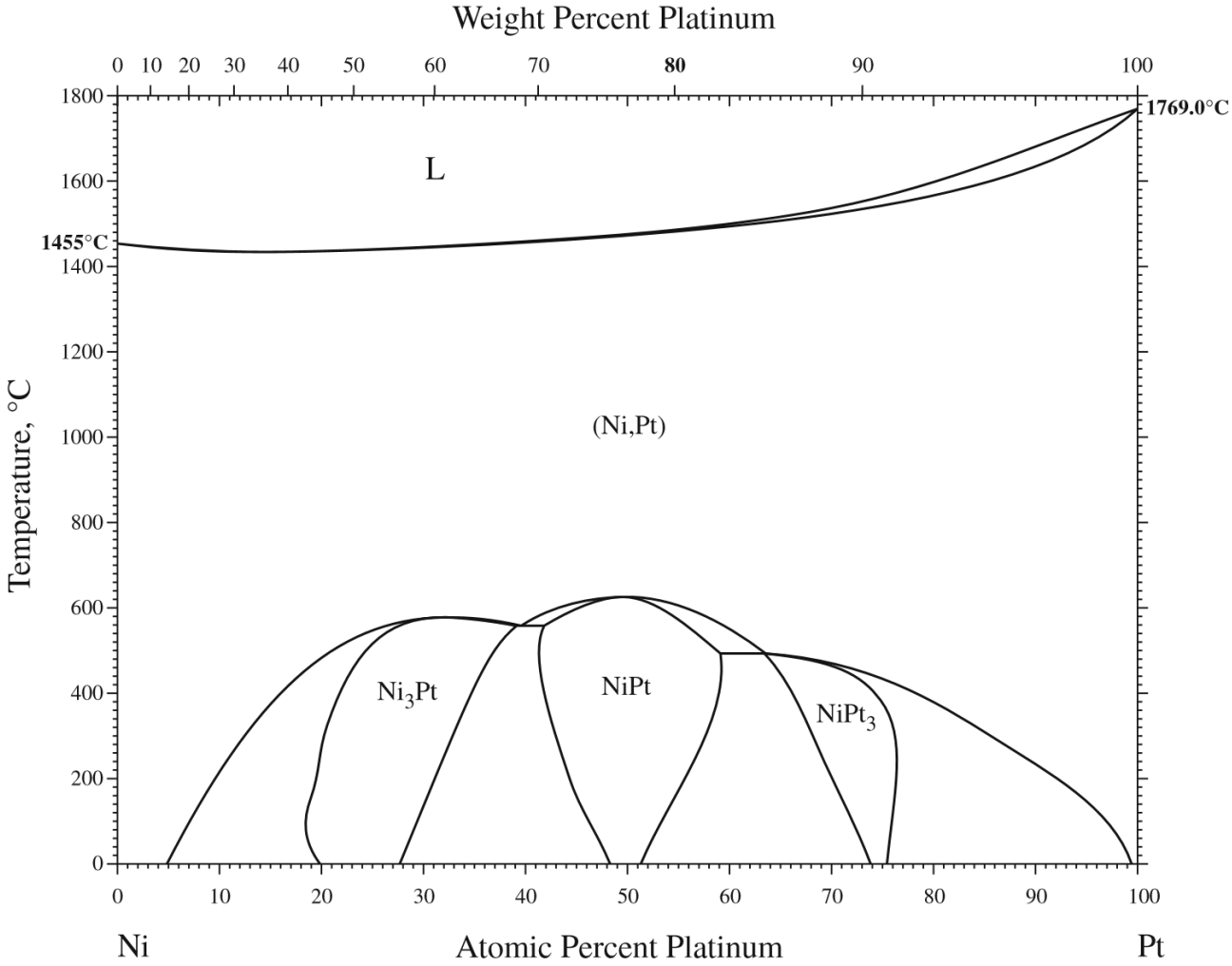

Figure 4.2: Phase diagram of Pt−Ni[196]

are energetically viable it is evident the ordered lattices are the favoured arrangements. With the current methods we can identify ordered phases that would be favourable from the point of view of reduced energy only if we know they are there. This method could be expanded upon via the use of high throughput computational structure searching techniques as a future project.

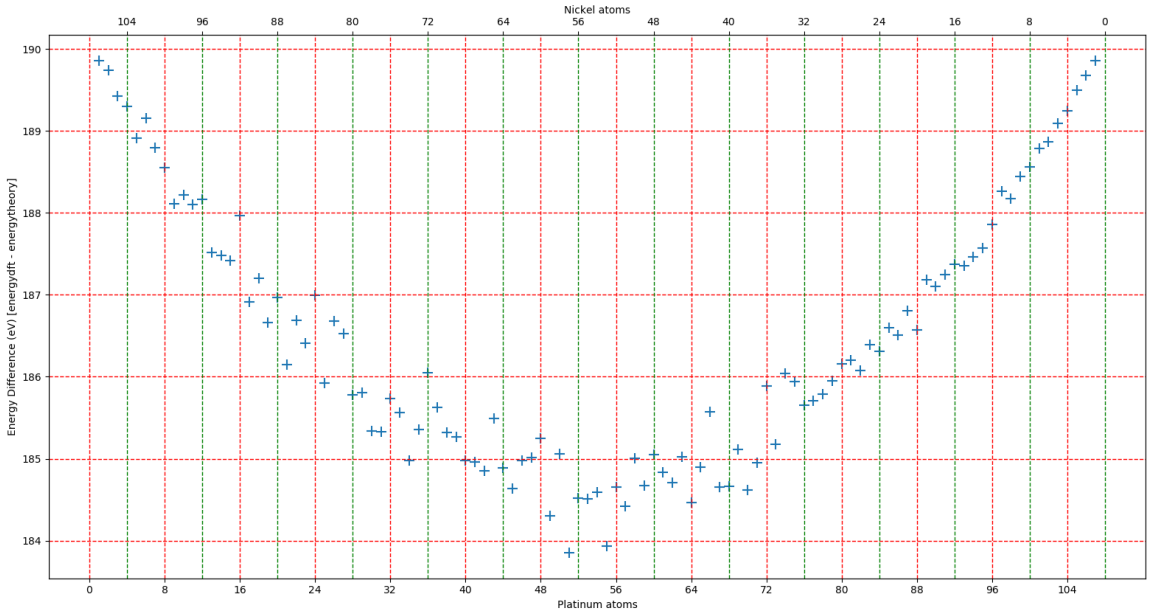

Figure 4.3: Enthalpy of DFT calculations with subtracted expected enthalpy of an ideally mixed pair system of PtNi across a range of at.% in 108 atom randomly arranged FCC cells

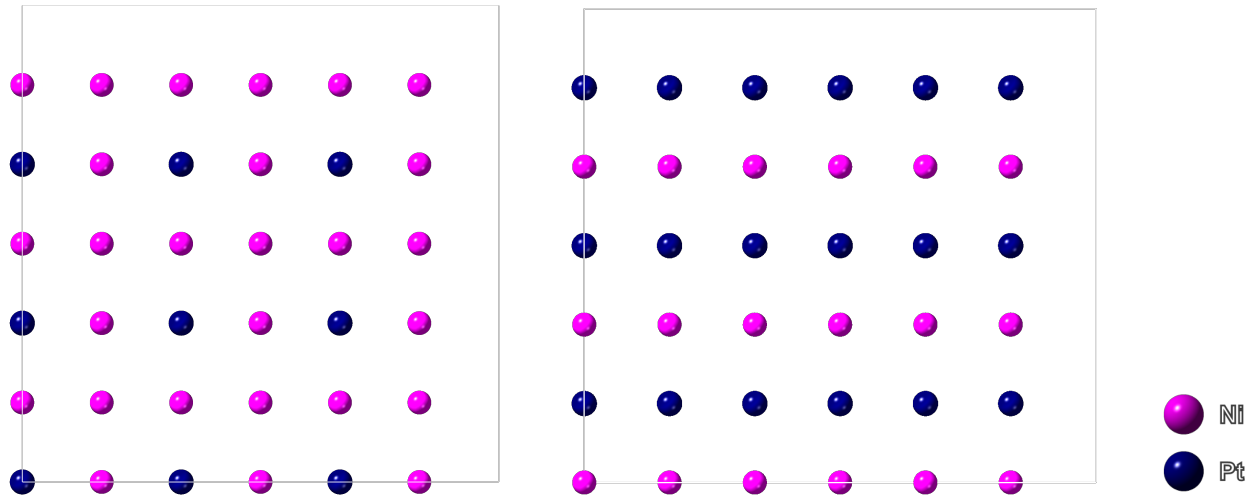

(a) Ni_3Pt **(b)** NiPt **(c)** key

Figure 4.4: Graphical representation of the arrangement of two PtNi ordered structures as shown in figure 4.2

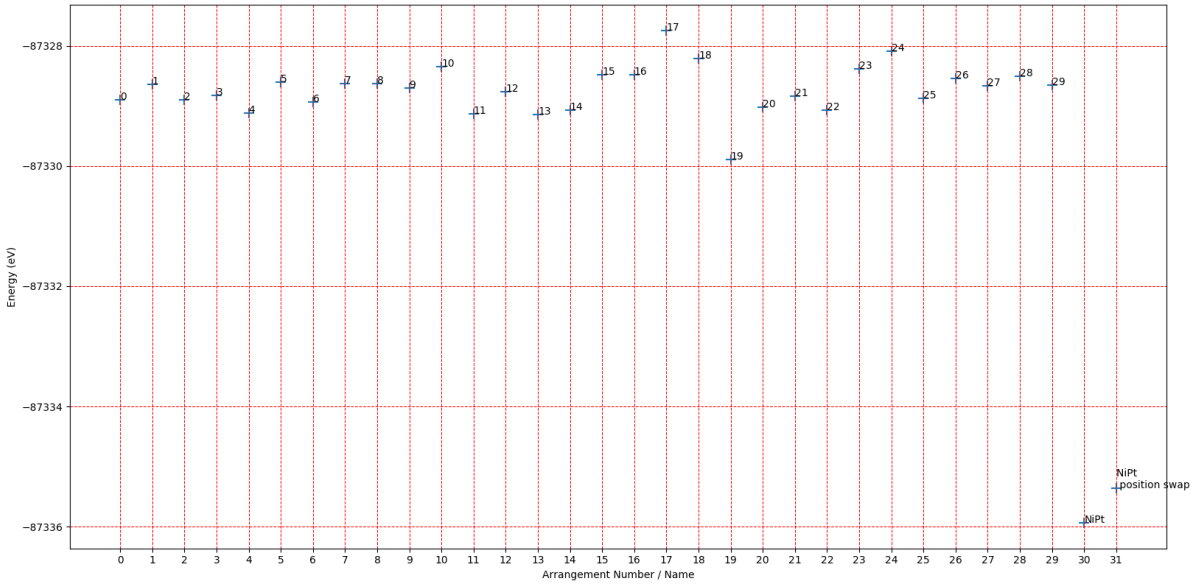

Figure 4.5: Groundstate energy of 30 relaxed 108 FCC cells of $Pt_{50}Ni_{50}$ compared against a relaxed 108 atom cell of the phase NiPt (Tab. 3.4b)

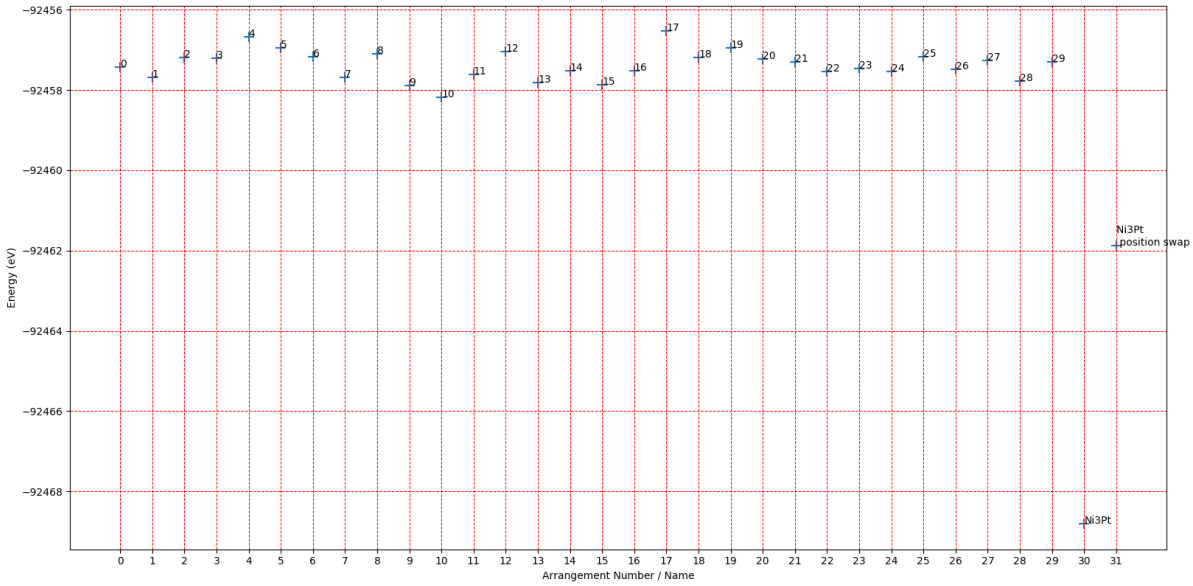

Figure 4.6: Groundstate energy of 30 relaxed 108 FCC cells of $Pt_{25}Ni_{75}$ compared against a relaxed 108 atom cell of the phase Ni_3Pt (Tab. 3.4b)

4.1.1.2 PtRh

As with PtNi (fig. 4.3) the compositions tend to have a lower enthalpy relative to the expected enthalpy, considering the system to follow ideal mixing, as they tend towards equiatomic

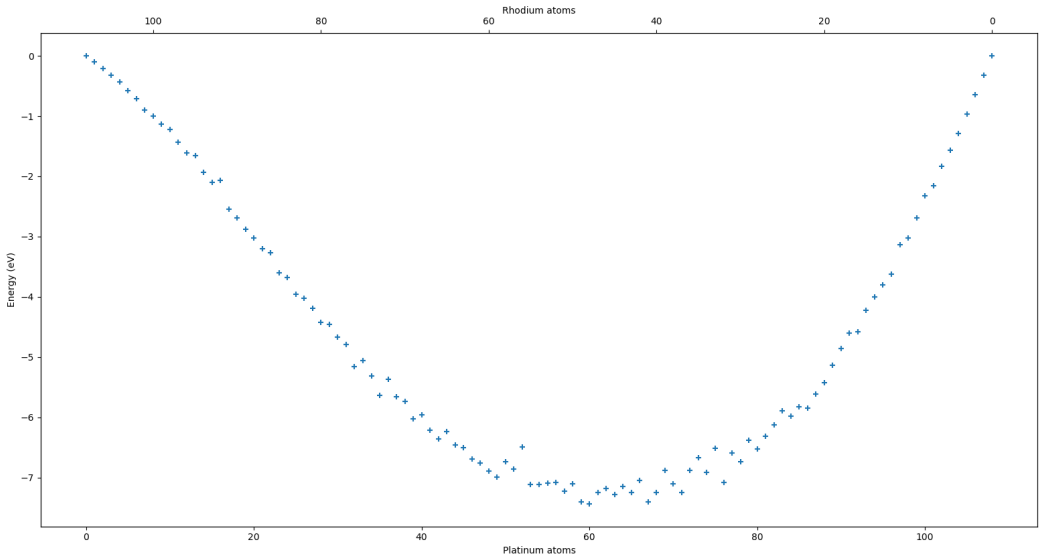

Figure 4.7: Enthalpy of DFT calculations with subtracted expected enthalpy of a pair system of PtRh across a range of at.% in 108 atom randomly arranged FCC cells

ratios with a slight favourability towards a higher number of Pt to Rh atoms. Comparing these results with the phase diagram (also based on calculations, rather than extensive experimental investigation) in figure 3.3 it does agree as above 0°C full mixing is energetically favourable as the equilibrium state. To further confirm this, the energy of a larger number of different random arrangements per Pt to Rh ratio could be calculated to create a plot, as in figure 4.7 of the mean enthalpy per atomic ratio.

Both figure 4.4b and figure 4.7 show that compositions of varying at.% of Pt:Rh and Pt:Ni are energetically viable as randomly ordered distributions of the elements concerned on an FCC crystal lattice. However, with PtNi, figures 4.5 and 4.6 show that the ordered phases of NiPt and Ni_3Pt which are assessed in this work are favoured. This is comparable to the phase diagram presented in figure 4.2. We would expect this to be the case if the phase diagram were generated from a similar study of comparing the ordered phases which could possibly be present to a randomly ordered phase of the same composition was performed. It is noteworthy if the phase diagram of Pt-Rh is examined at low temperatures (below 0°C) some ordered phases are seen. These do not appear to have been observed in experimental work in the literature (which is limited) and the current modelling, which does not directly assess these ordered systems, neither supports nor refutes the existence of these phases.

We have shown that with DFT as a tool we can explore, computationally, trends in how alloys mix and identify whether the arrangement will tend to order or disorder in real life.

4.2 HEA DFT screening

To construct a method for treating large cells of multi species alloys (HEA), the $Pt_7Rh_{23}Ni_{35}Co_{35}$ was used as a test composition. LDA functionals were used with the norm-conserving pseudopotentials constructed in Ref. [184]. 30 randomly arranged 108 atom site lattices of the composition were constructed on the same loci with the same lattice parameter, the method is described in more detail in section 3.2.3. The 30 randomly arranged lattices were compared against manually ordered arrangements of the same composition.

In figure 4.8 we compare the ground state energy of 30 random FCC lattice arrangements (e.g. figure 4.9d) for composition $Pt_7Rh_{23}Ni_{35}Co_{35}$ to ordered lattice arrangements. The ordered lattice arrangements that calculations were performed on are shown in figures 4.9a, 4.9b, 4.9c. It is evident from figure 4.8 that the ordered compositions labelled '1' and '2' have significantly higher energy than the 30 randomly arranged compositions and ordered composition '3' which tends to group the Co and Ni and Pt and Rh atoms together. We cannot conclusively say that the alloy composition tends to disorder however that appears to be the trend, with the low level of ordered composition '3' suggesting that compositions with some separation of Ni-Co together and Pt-Rh together would also be possible to attain. Further analysis of this using the methods suggested in section 4.5 is required to strengthen the confidence in the trend, especially since the ordered composition '3' falls in the energetically favoured category. To ensure that the ordered alloys have a high degree of ordering at the level of the atomic nearest neighbours the average number of the nearest neighbours of each species to each other species was computed. CASTEP can output the nearest neighbours for all atoms in a lattice. A code was written to compute the mean nearest neighbours of each species to a different species in the composition. It was found that the mean number of nearest neighbours of like atoms was much higher in ordered lattices '1' and '2' in comparison to the lower energy structures. Ordered lattice '3' had a mean number of nearest neighbours to species similar to the numbers in the randomly arranged structures, showing it was, in fact, a less highly ordered arrangement than '1' or '2'. The results of the mean nearest neighbours calculations are in Appendix A, section A.1.

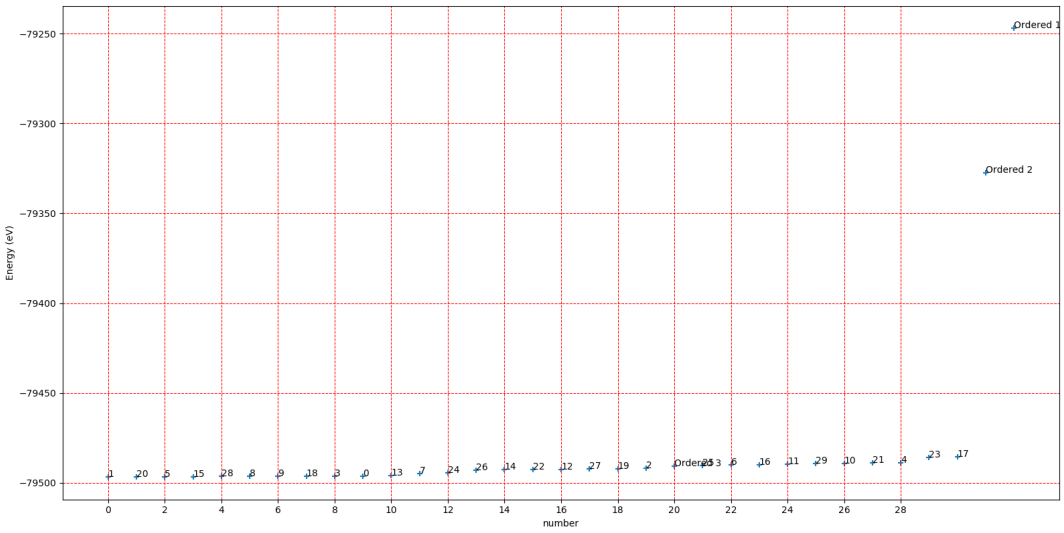

Figure 4.8: $Pt_7Rh_{23}Ni_{35}Co_{35}$ simulations arranged in order of ascending enthalpy

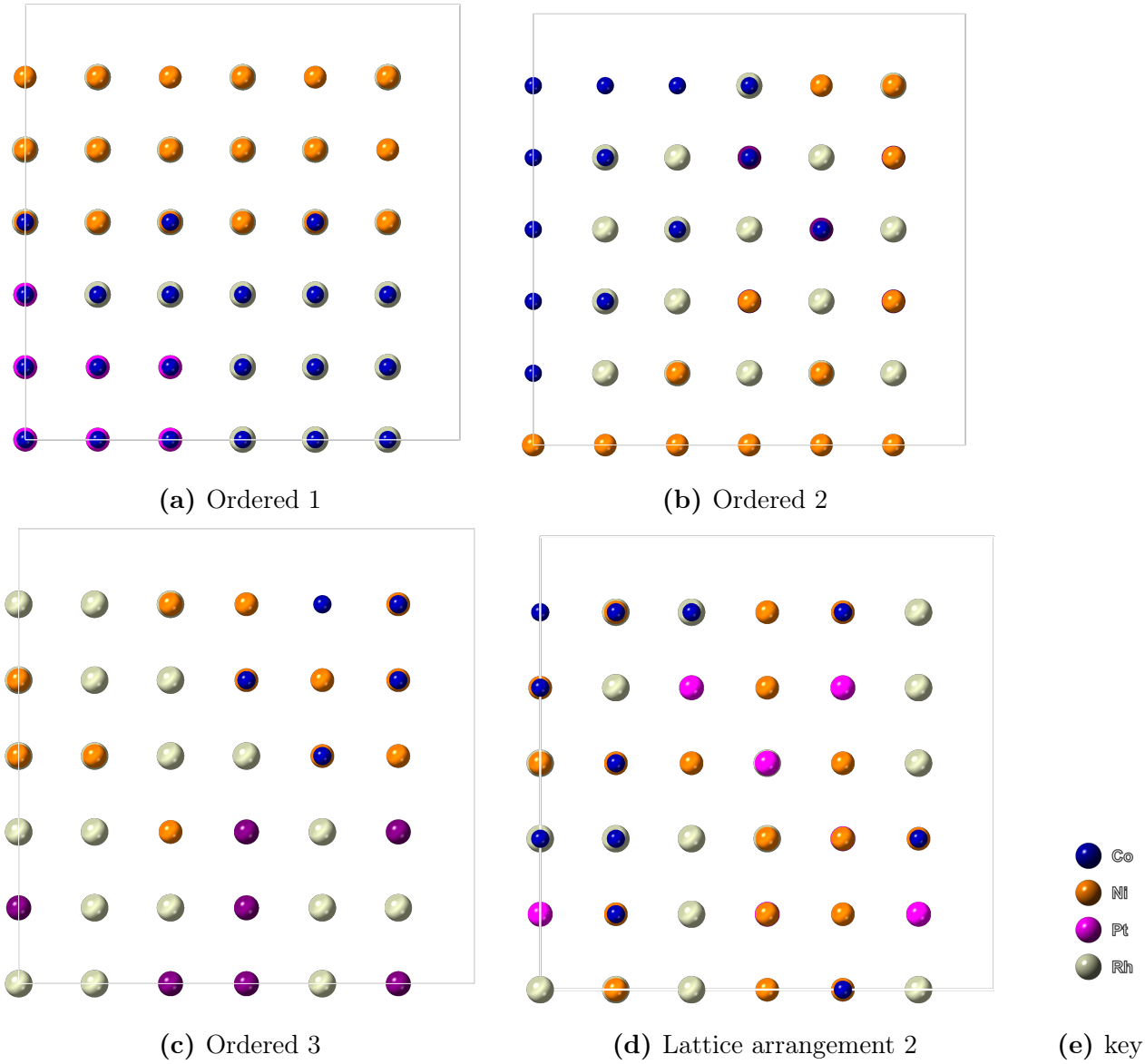

(a) Ordered 1 **(b)** Ordered 2

(c) Ordered 3 **(d)** Lattice arrangement 2 **(e)** key

Figure 4.9: Ordered lattice arrangements and an example of a random lattice arrangement that were simulated

4.3 Surface slabs

To assess which the lowest energy plane(s) is (are) we devised a series of steps outlined below, the results of which are also discussed.

Of the $Pt_7Rh_{23}Ni_{35}Co_{35}$ randomly arranged lattices, the lattice labelled '2' was chosen after the geometry optimisation, to be cleaved into surface slabs for Miller plane surface analysis. Surfaces were cleaved in the (0 0 1), (0 1 1), (1 0 1), (1 1 0), and (1 1 1) planes. Metadise[198] cuts as many surface slabs as there are atoms in a lattice. Since, there are 108 atoms in the lattice 108 surfaces were generated, of those 108 surfaces per Miller plane 30 were chosen at random per Miller plane.

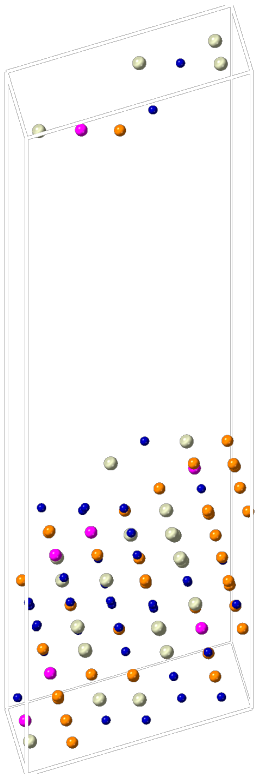

(a) (1 1 1) surface slab, label 72

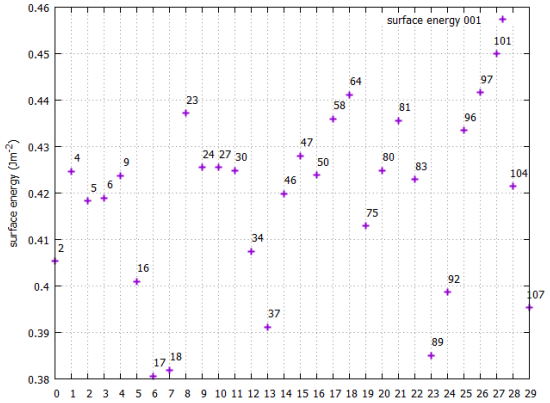

(b) (0 0 1)

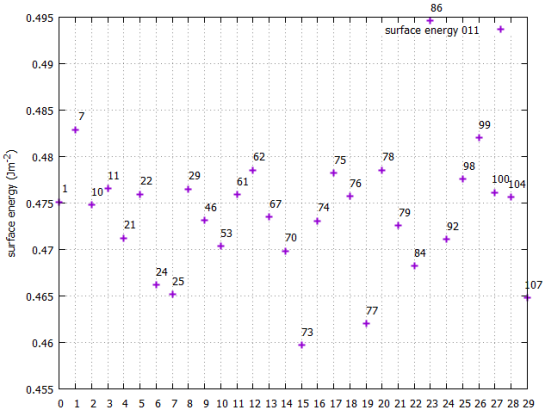

(c) (0 1 1)

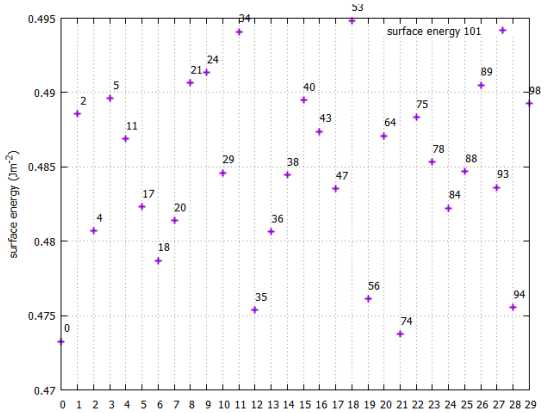

(d) (1 0 1)

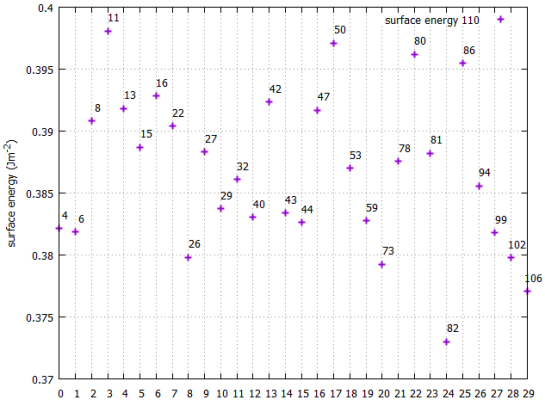

(e) (1 1 0)

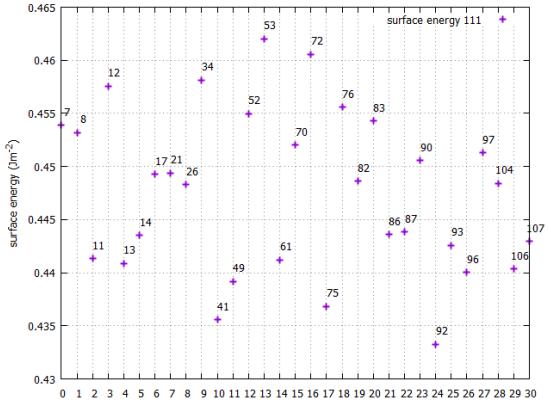

(f) (1 1 1)

Figure 4.10: Energies of exposed plane surface slabs

The of the single point energy calculation were manipulated to get the surface energy as described in section 3.2.3. The geometry of the planes was not optimised.

The results of the cleaved surface slab calculations are displayed in figure 4.10 as a comparison of the surface energy of each slab. All the surface energies of the generated slabs are fairly similar across all cleaved planes and the surface energy difference in any set of planes is small, the largest difference being $\approx 0.09\text{eV}\,\text{Å}^{-2}$. This indicates that there is unlikely to be any significantly favoured plane, from energetic concerns, and that a surface would be equally likely to display any of the considered planes (and by extension, quite probably other planes not explicitly calculated here). However, the results are inconclusive and more work is needed to confirm this mixed plane manifestation and whether it it would continue to be the predicted outcome when we simulate annealing. Extensions of this technique are discussed in chapter 8

The study should be taken further firstly by optimising the geometry of the structures and comparing it to the bulk lattice in a similar way, the results should then be compared to the single point calculations. Secondly, the method should be scaled to molecular dynamics potential based methods or lattice dynamics potential based methods where annealing can be simulated following energy calculations on the as-cast structure. In this way, we would able to, we can gauge whether such a phenomenon of mixed surface planes manifests for annealed structures. The study should also be repeated for larger systems of atoms (e.g. $4 \times 4 \times 4$). This was not conducted in this work, as the simulation of crystal structures above was of greatest relevance to understand the experimental results. Should there be further development looking as surface sensitive processes, such as catalysis or oxidation (which may be important in possible applications of these materials if they are found to be processable), then the surface modelling explored here would become of greater focus for its ability to make predictions relevant to these behaviours.

Finally, electron backscatter diffraction (EBSD) could be used to investigate the planes that manifest on a cut surface of the manufactured alloy, when allowed to relax to a stable state (e.g. by prolonged heating in a stable atmosphere to cause faceting) as a means to experimentally verify the results.

4.4 Discussion

Overall, DFT has provided results which align with data observed physically and independent of this project as it explored in section 4.1. Proceeding with investigations in alloy $Pt_7Rh_{23}Ni_{35}Co_{35}$ we can see that the random lattice arrangements of the alloy are all at a similar energy and energetically favourable. The random lattice arrangements are more energetically favoured compared to the ordered lattice arrangements, which indicates that in a physical investigation the alloy will tend to mix homogeneously, as is evident in the physical data. This contrasts with the data we have obtained for the known binary alloys as at certain ratios the binary alloys have an ordered lowest energy lattice structure. So a there could be a difference

going from binary to multi component in that multiple components tend to disordered lattice arrangements. The study does suggest that atoms will want to randomly arrange themselves at atomic scale, for $Pt_7Rh_{23}Ni_{35}Co_{35}$.

The surface plane energies suggest that the physical manifestation of the similarity in energy will be a surface structure with many different planes being presented. This could be further investigated in the future via geometry optimisation of the cleaved slabs concurrently with EBSD analysis of physical samples.

We have shown that we can simulate the surface slabs of the $Pt_7Rh_{23}Ni_{35}Co_{35}$ HEA for 108 atoms. We can see that some surfaces are of lower energy than others, generally. However, as mentioned above experimental investigation of the approach would be needed to be able to compare to physical results.

In devising a good investigation we must also be able to explore negatives. In the way that we showed that $Pt_7Rh_{23}Ni_{35}Co_{35}$ will tend to a random arrangement on an FCC crystal lattice and not a highly ordered arrangement, it can also be shown that certain alloys will favour order. The same procedure that was used to explore the favoured arrangements of $Pt_7Rh_{23}Ni_{35}Co_{35}$ can be used to explore alloy compositions that did not work in the experimental trials (discussed in the following chapters). In this study, however, we chose to focus our resources on building a method for simulating HEAs via DFT simulations by studying the alloy $Pt_7Rh_{23}Ni_{35}Co_{35}$ which did work, thus meaning our simulations had potential value in understanding the real alloys that were being explored.

4.5 Suggestions on simulating large HEA systems

The calculations used in this investigation were carried out as benchmark tests on simulating 108 atom FCC lattices which consist of multiple elements, using a number of different approaches to assess their effectiveness for such a purpose. Both LDA and PBEsol work well and the choice between them depends on the data required. OTF USP is highly effective, especially for the large atoms (e.g. Pt) we are simulating. Spin polarisation is turned on for the whole system rather than explicitly stated per atom. EDFT is used for fast convergence. Pulay density mixing works well too depending on the system, however it requires 100s of SCF iterations, which is wasteful of memory, also even after ≈100 - 300 cycles the ground state energy calculation might not converge; usually the iteration values will tend to oscillate around convergence instead of converging so the suggestion is system, and convergence criteria dependent. OTF NCP are generally too rigorous to provide results in < 168h and without multiple restarts of the calculation. The simulations work well for 16-32 CPU cores. For further simulation of multicomponent alloys, of the type experimentally investigated here, PBEsol or LDA exchange correlation functionals, and USP would be recommended, in order to give a suitable balance between time of calculation, and suitable accuracy to be of assistance in alloy design.

Chapter 5

Experimental Exploration of Alloys and Physical Properties

This chapter outlines the alloys designed for experimental exploration in a number of key systems, with similarities to current alloys used for applications. Results are presented for the mechanical properties and the high temperature oxidation resistance for all alloys, and this will be followed in the next chapter (ch. 6) by focussing on the main alloys explored in detail and discussing their phase formation and microstructure. In the next chapter results for each alloy will be presented for laboratory scale manufacture and industrial scale manufacture.

As will be discussed below, of the alloys in the PtRh cycle of design $Pt_7Rh_{23}Ni_{35}Co_{35}$, $Pt_5Rh_{20}V_5Ni_{35}Co_{35}$ and $Pt_5Rh_{11}V_{14}Ni_{35}Co_{35}$ were selected for industrial scale up. There are several reasons for alloys not being selected for this further stage after the initial experimental exploration in the laboratory; either they did not alloy, i.e. did not mix in the melted state in the hearth or were visibly not homogeneously mixed when the samples were prepared for characterisation, were not manufacturable, or did alloy but when assessed were not single phase. All compositions that contained Ag in the PtRh cycle of design did not alloy, i.e. mix when melted in the hearth. Given the criteria used all alloys were expected to alloy into single phase structures, therefore a new criterion outlined in section 6.3 was devised. The criterion was devised by inspecting the three successful alloys in this cycle. Further discussion of the updated criteria can be found in and section 6.5 and 6.6

5.1 Presentation of results

This chapter discusses the mechanical criteria used for each of the alloy production cycles and briefly discusses why the alloys were chosen from these for further industrial scale trials. The chapter is then divided into results presentation followed by discussion. Below there are some more detailed comments with regard to the presentation of results for several specific techniques. The results for the mechanical properties are presented and discussed together for

all alloys at both laboratory and industrial scale. The thermal analysis results are presented and discussed in the same section for all alloys.

Below follows some considerations on the manufacture procedure and the subsequent characterisation techniques and procedures.

Discussion of the alloy microstructure supported by data from XRD, XRF, SEM, EDX, and EPMA is found in the following chapter (ch. 6).

Before the presentation of the mechanical properties and of the characterisation of the microstructure in the next chapter (ch. 6) the alloys selected for industrial scale manufacture and testing are presented on table 5.1. Several alloys made in the laboratory manufacture stage were not considered for industrial scale manufacture due to visual inspection of the cross-section revealing a speckled macroscopic structure, which was taken as a rapidly-observable sign that there was macroscopic segregation in the manufactured alloy, and therefore that the alloy was less likely to be suitable for further investigation, as it did not apparently form a well-mixed alloy readily. Some results obtained from the alloys not selected are presented and discussed briefly in section 5.2, giving additional details of why these example alloys were not considered suitable for further investigation. These are, fig. 5.1 which is an SEM-EDX map of the alloy $Pt_9Rh_{35}Ni_{21}Cu_{35}$, XRD data for alloy $Pt_5Rh_5V_{31}Cr_{24}Mo_{35}$ are presented in figure 5.3a, and an SEM-EDX map of $Pt_5Rh_{25}V_5Ni_{35}Cu_{35}$ is presented in figure 5.2. The figures are accompanied by explanation of why the alloys were not chosen for industrial trials.

As well as these initial observations, backed up by the investigation of particular example alloys were not the only criteria applied in deciding which alloys should be examined further in the work, and a number of other considerations were involved in the selection of alloys for industrial scale trials. The reasons for selection or rejection are briefly described in table 5.1. While there were a number of alloys that could have been taken forward for further trials, there was capacity for up to 5 alloys to be trialled under industrial conditions, and so some selection was necessary.

5.2 Initial screening of alloys

Table 5.1 summarises the characterisation for each alloy made at laboratory scale. Characterisation at laboratory scale involved assessing whether the alloy melted homogeneously in the arc melter, whether there was macroscopic homogeneity in the sample, XRD, the EDX map and a ductility test conducted as a hammer test. A check (✓) signifies that the characterisation step was passed successfully, while a cross (✗) signifies that the characterisation step was not passed successfully, consequently, the characterisation of the alloy was halted. Certain alloys are accompanied by notes indicating why they were chosen or not. The alloy compositions selected for industrial scale trials are indicated in bold.

Alloy	Homogeneous melt	Macroscopic homogeneity	XRD	EDX Map	Hammer test	Notes
$Pt_9Rh_{35}Ni_{21}Cu_{35}$	✓	✓	✓	✗	✓	Fig. 5.1
$Pt_7Rh_{23}Ni_{35}Co_{35}$	✓	✓	✓	✓	✓	Generally suitable properties, significant PGM reduction from existing alloys
$Pt_{35}Rh_{35}Ni_5Ag_{25}$	✗					
$Pt_5Rh_{25}Ni_{35}Cu_{35}$	✓	✗				
$Pt_5Rh_{25}Ni_{35}Co_{35}$	✓	✓	✓	✓	✓	Similar to $Pt_7Rh_{23}Ni_{35}Co_{35}$
$Pt_{35}Rh_{35}V_{22}Ag_8$	✗					
$Pt_{35}Rh_{35}V_5Ag_{25}$	✗					
$Pt_5Rh_{20}V_5Ni_{35}Co_{35}$	✓	✓	✓	✓	✓	Comparable with $Pt_7Rh_{23}Ni_{35}Co_{35}$ with V addition, V desirable to explore in high temperature applications
$Pt_{35}Rh_{35}V_5Ag_{20}Cu_5$	✗					
$Pt_5Rh_{10}V_{15}Cu_{35}Co_{35}$	✓	✗				
$Pt_5Rh_{15}V_{35}Ni_{10}Co_{35}$	✓	✗				
$Pt_5Rh_{11}V_{14}Ni_{35}Co_{35}$	✓	✓	✓	✓	✓	Comparable with $Pt_7Rh_{23}Ni_{35}Co_{35}$, higher V addition than $Pt_5Rh_{20}V_5Ni_{35}Co_{35}$
$Pt_5Rh_5V_{31}Cr_{24}Mo_{35}$	✓	✓	✗	✓	✗	Fig. 5.3a
$Pt_5Rh_{25}V_5Ni_{35}Cu_{35}$	✓	✓	✓	✗		Fig. 5.2
$Pt_{21}Rh_{34}V_5Ag_{32}Cu_8$	✗					
$Pt_{17}Rh_{30}V_{14}Ag_{30}Re_9$	✗					
$Ir_{35}V_{14}Fe_{16}Cu_{35}$	✗					
$Ir_{32}V_{10}Co_{34}Cu_{24}$	✗					
$Ir_{32}Fe_9Ni_{35}Cu_{24}$	✓	✗				
$Ir_{35}Fe_{10}Pd_{22}Pt_{33}$	✓	✗				
$Ir_{35}V_{15}Fe_{10}Cu_{35}Ag_5$	✗					
$Ir_{12}Fe_{33}Co_{20}Ni_{30}Pt_5$	✓	✓	✓	✓		Very low PGM content, compable with some existing Fe-based alloys with PGM additions
$Ir_{35}Rh_{28}Pd_{27}Pt_5Au_5$	✗					
$Ir_{35}Rh_{28}Pd_{27}Ag_5Pt_5$	✗					
$Ir_{35}Co_5Ni_5Rh_{35}Pt_{20}$	✓	✓	✓	✓		Similar to some existing Ir-Rh alloys
$Ir_{35}Fe_5Rh_{35}Pt_{25}$	✓	✓				Alloy less attractive for scale up due to high PGM content, characterisation was halted
$Ir_{35}Rh_{35}Pd_{20}Pt_{10}$	✓	✓				Alloy less attractive for scale up due to high PGM content, characterisation was halted
$Ir_{35}Co_{17}Ni_{13}Rh_{35}$	✓	✓				Alloy less attractive for scale up due to high PGM content, characterisation was halted

Table 5.1: Alloys for both PtRh and Ir alloy series manufactured in the laboratory and the reasons for their selection for industrial scale manufacture and testing, compositions indicated in bold are the alloys subsequently selected for industrial scale trials

The EDX map of alloys $Pt_9Rh_{35}Ni_{21}Cu_{35}$ and $Pt_5Rh_{20}V_5Ni_{35}Cu_{35}$ are shown in figures 5.1

and 5.2, respectively, to show why the alloy was not chosen for industrial scale trials. Additionally, the XRD data for the alloy $PtrRh_5V_{31}Cr_{24}Mo_{35}$ are not consistent with an FCC crystal structure.

The 5 alloys chosen for industrial scale manufacturing trials were $Pt_7Rh_{23}Ni_3Co_{35}$ for how it performed in the laboratory scale characterisation. The two low and medium content V alloys, $Pt_5Rh_{20}V_5Ni_{35}Co_{35}$, $Pt_5Rh_{11}V_{14}Ni_{35}Co_{35}$, were chosen due to interest from industry for assessing V containing alloys for high temperature applications. Furthermore, there would be a direct comparison between the wo alloys due to the components being the same with a the content being different. The addition of Fe in an alloy for high temperature applications together with low PGM content was of interest to industry so alloy $Ir_{12}Fe_{33}Co_{20}Ni_{30}Pt_5$ was chosen for industrial scale manufacturing trials. Finally, a high PGM content alloy was chosen, $Ir_{35}Rh_{35}Co_5Ni_5Pt_{20}$.

These 5 alloy samples, as made up in the laboratory, were then taken forward for further tests at industrial scale. The scalability of the alloys at industrial level was assessed by comparing the results of the characterisation employed at laboratory scale with the equivalent at industrial scale. The mechanical properties were assessed by nanoindentation and Vickers hardness, DSC, TGA and oxidation resistance.

Figure 5.1 shows the EDX map of alloy $Pt_9Rh_{35}Ni_{21}Cu_{35}$ at 6000x magnification.

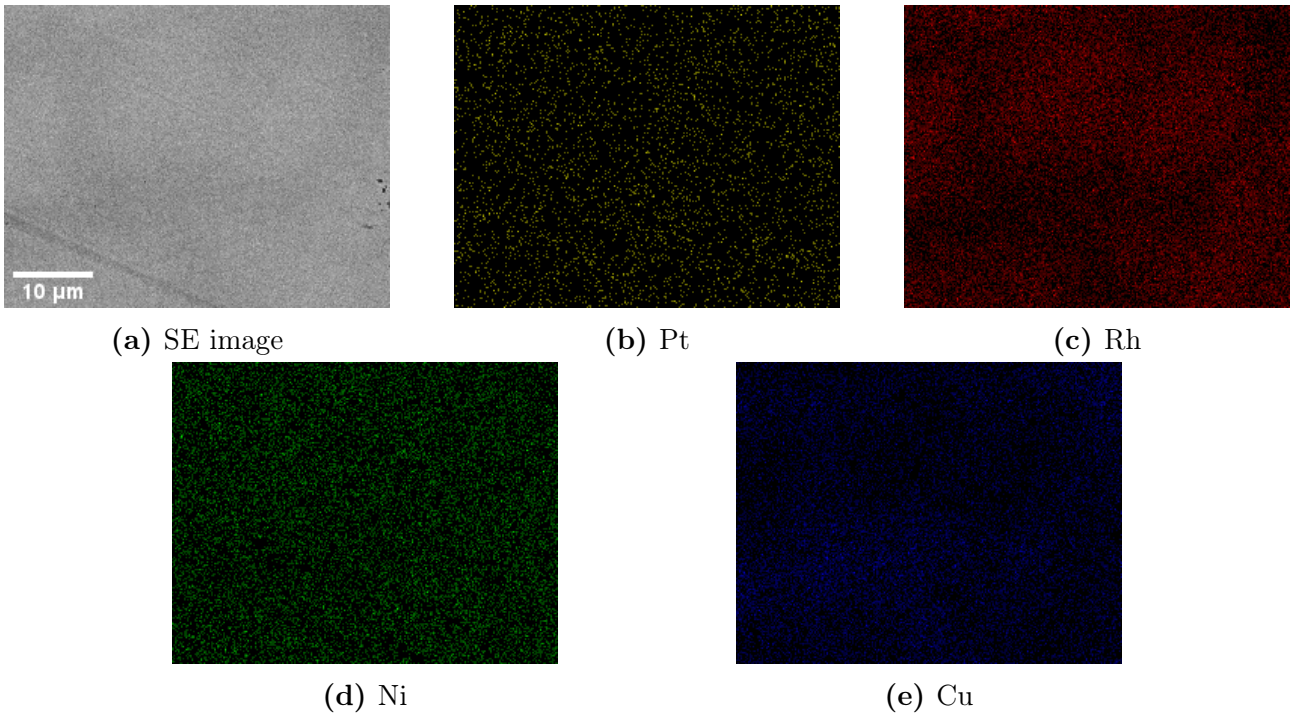

(a) SE image **(b)** Pt **(c)** Rh

(d) Ni **(e)** Cu

Figure 5.1: EDX map of $Pt_9Rh_{35}Ni_{21}Cu_{35}$ at 6000x magnification

We see from the map that despite there being uniform distribution across the sampled area that there is segregation. The segregation is particularly noticeable in Pt, Rh, and Cu. This is a reason why $Pt_9Rh_{35}Ni_{21}Cu_{35}$ was not selected for industrial scale trials. Another reason for

not selecting the alloy is that other alloys were of higher interest to industry.

Figure 5.2 is an EDX map of $Pt_5Rh_{20}V_5Ni_{35}Cu_{35}$ taken at 6000x magnification. Note that there is no data for Cu.

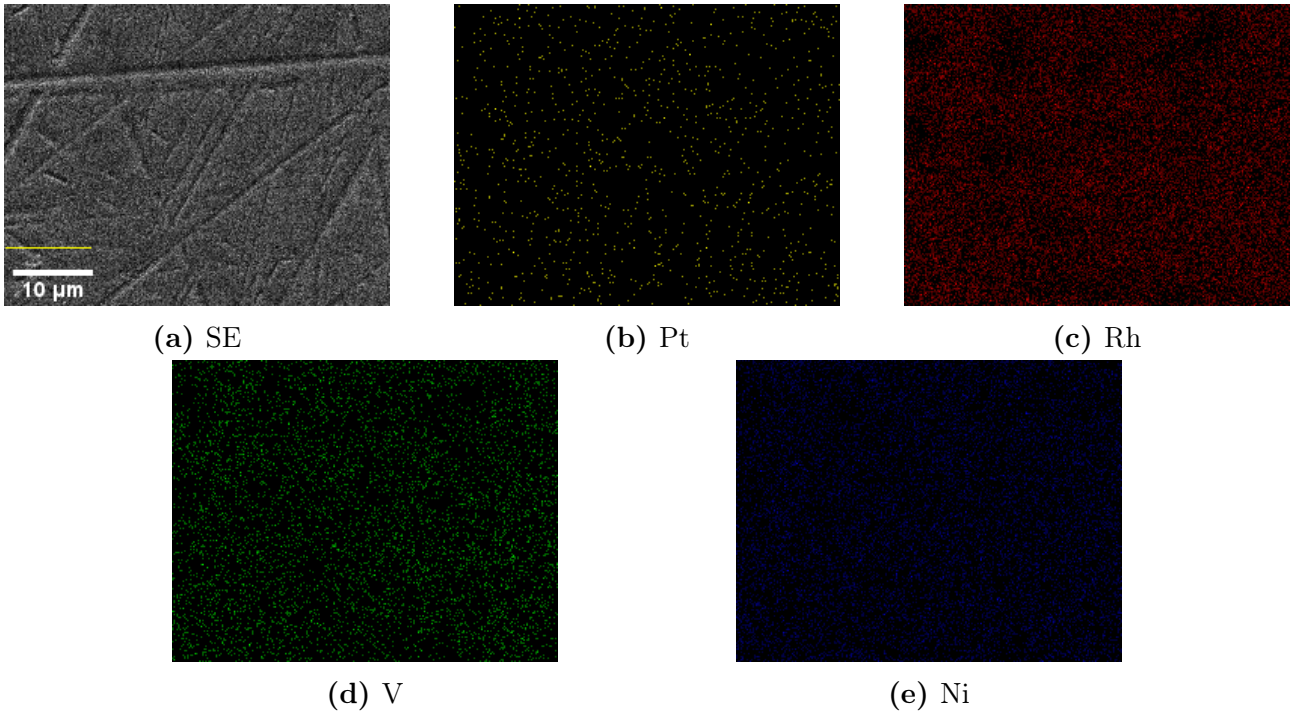

(a) SE **(b)** Pt **(c)** Rh

(d) V **(e)** Ni

Figure 5.2: EDX map of $Pt_5Rh_{20}V_5Ni_{35}Cu_{35}$ at 6000x magnification

There is some noticeable segregation in figure 5.2, particularly in Rh. More noticeable is the low content of Pt which is lower than would be expected. There is no data for Cu as no Cu was detected in the sampled area. An interpretation of the data would be that Pt and Cu are segregating from the other constituent elements. This is why this alloy was not selected for industrial scale trials.

Displayed on figure 5.3a is the XRD data collected for alloy $Pt_5Rh_5V_{31}Cr_{24}Mo_{35}$.

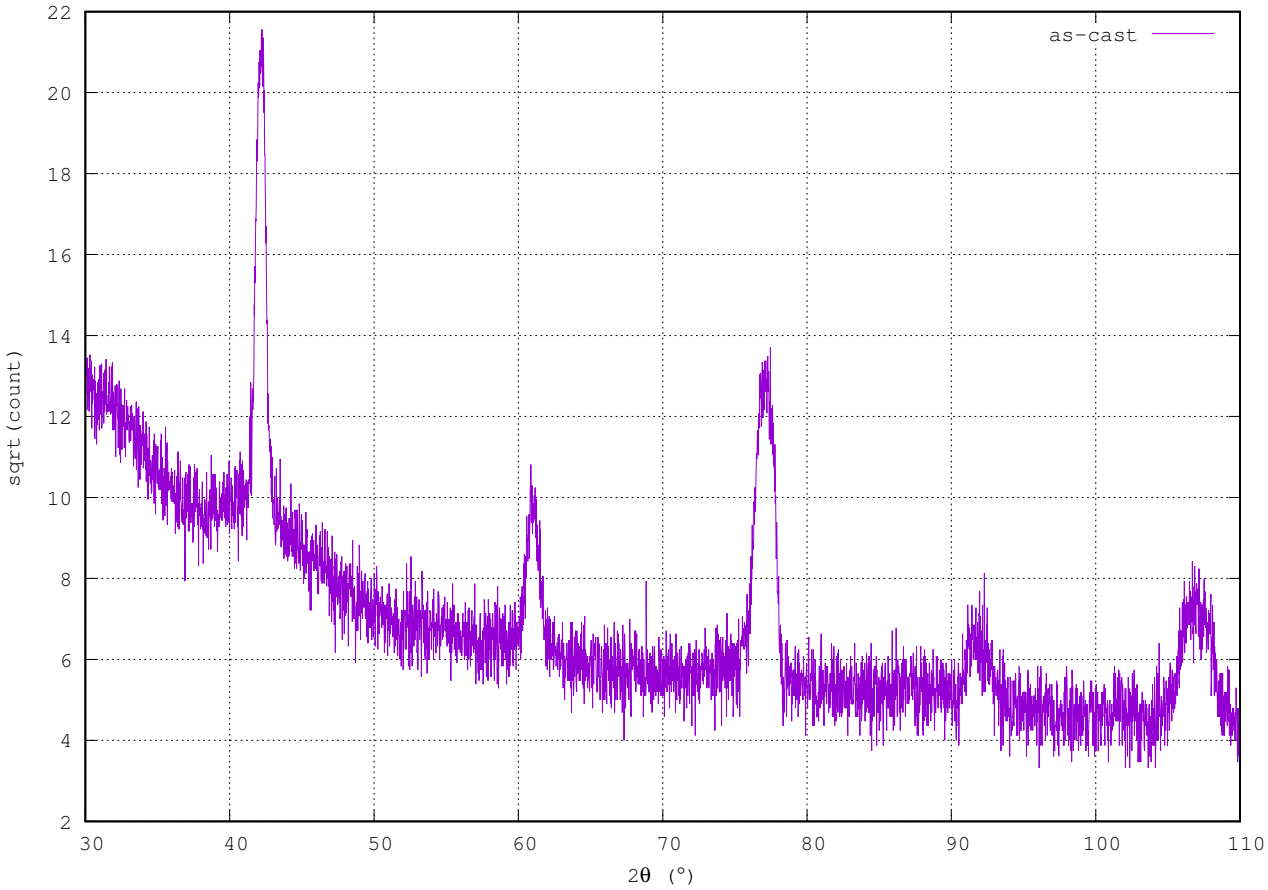

(a) XRD data for $Pt_5Rh_5V_{31}Cr_{24}Mo_{35}$

We see from the peak positions that the XRD data displayed in figure 5.3a are not consistent with an FCC crystal structure. This, together with the brittleness exhibited in the alloy made it an unsuitable candidate for industrial scale trials as manufacturability of the alloys is very important.

5.3 Mechanical properties

To assess the laboratory manufactured alloys from the PtRh cycle of manufacture a simple hammer test was devised and performed. The test was intended to provide a rapid indication of ductility and deformation behaviour at room temperature. The details of the hammer test are summarised in section 3.3.6 in the Methods (sec. 3) and in the section below, 5.3.1. The results for the PtRh alloys chosen to be trialled for industrial manufacture are presented in section 5.3.1 followed by a short discussion. The hammer test was not performed on the alloys from the Ir laboratory manufacture cycle due to time constraints and industrial manufacture trial expedition.

Nanoindentation and Vickers Hardness indentation were performed on all industrially manufactured alloys to obtain more quantitative information on the mechanical behaviour. The results are presented and discussed briefly below in section 5.3.2.

5.3.1 Manufacturability test

A crude manufacturability trial was performed on the single phase candidate alloys from the laboratory manufacture cycle focusing on PtRh based alloys. The Ir based alloys were not subjected to the same hammering test due to the expedition of the industrial manufacturing trials, and a reduced set of alloys which needed to be selected from.

While the hammer test performed on these alloys is a qualitative technique, the results were obtained rapidly and gave good indication of the desired properties, with a good capability to identify alloys which would not show enough plasticity to be suitable for deformation processing, as was necessary at the time. A rigorous and quantitative test for this behaviour would be tensile testing or three point bend testing. However, the material available from the single button arc melted casts made for first exploration of alloying was insufficient to manufacture trial samples of a suitable size (not withstanding the fact that multiple samples to allow repeats in these tests to get reliable values) for either technique.

The results of the manufacturability trial are summarised on table 5.2.

	Initial		After 20 hammerings	
Sample	Thickness (mm)	Diameter(mm)	Thickness (mm)	Diameter(mm)
$Pt_5Rh_{11}V_{14}Ni_{35}Co_{35}$	5.76	11.45	5.26	11.65
$Pt_5Rh_{20}V_5Ni_{35}Co_{35}$	4.53	11.27	3.82	11.54
$Pt_7Rh_{23}Ni_{35}Co_{35}$	5.78	10.77	5.11	10.79

Table 5.2: Laboratory scale manufacturability trial results on single phase candidate samples after 20 hammerings

All candidates performed well in the trial and deformed smoothly without any cracking. This indicates that all candidates are likely to be ductile and capable of being cold worked, at least to some extent.

5.3.2 Indentation

Data for the nanoindentation results of the alloys and the Vickers Hardness results of the alloys are presented below.

The values obtained via nanoindentation give the reduced modulus which is related to the Young's modulus via

$$E = (1 - \nu^2) \Bigg/ \left(\frac{1}{E_r} - \frac{(1 - \nu_i^2)}{E_i} \right) \tag{5.1}$$

where E is the Young's modulus, E_r is the reduced modulus of the sample, E_i is the Young's modulus of the indenter, ν is the Poisson's ratio of the material and ν_i is the Poisson's ratio of the indenter[220]. From the formula we can see that the reduced modulus value which is

measured results from the deformation of the sample being indented and the deformation of the indenter (which is a substantial amount less for most materials, as the indenter is diamond) combined, being a function of both. The diamond indenter tip is assumed to be perfect in its material properties (although a calibration for the indenter shape and the deviation from the ideal Berkovitch three sided pyramid is regularly carried out), given that the repeated indentations will not have caused any significant damage below the surface, with a Poisson's ratio of, $\nu_i = 0.07$, and a Young's Modulus of, $E_i = 1140$GPa. For alloys a good approximation, given that the Poisson's ratio of PGM is usually in range 0.3-0.4, is assumed to be $\nu = 0.32$.

The calculated, "rule-of-mixtures" (ROM) elastic modulus arises from doing a simple atomic ratio elastic modulus summation for the alloy, i.e.

$$E = \sum_{i}^{N} c_i E_i \tag{5.2}$$

where c_i is the atomic percentage of the alloying constituent i and E_i is the respective elastic modulus for each component.

5.3.2.1 Nanoindentation

Alloy	State	Reduced Modulus (GPa)	Elastic Modulus (GPa)	ROM Elastic Modulus (GPa)	ROM Reduced Modulus (GPa)	ROM Elastic Modulus (XRF data)
$Pt_7Rh_{23}Ni_{35}Co35$	As cast	202.96±0.97	221.40	218.16	200.51	214.13
	Annealed	197.70±1.14	214.47			214.46
$Pt_5Rh_{20}V_5Ni_{35}Co_{35}$	As cast	215.17±0.45	237.80	212.95	196.54	209.96
	Annealed	221.14±0.84	245.98			209.92
$Pt_5Rh_{11}V_{14}Ni_{35}Co_{35}$	As cast	212.45±0.71	234.11	199.72	186.32	Inconclusive XRF data
	Annealed	226.56±0.96	253.50			197.35
$Ir_{35}Rh_{35}Co_5Ni_5Pt_{20}$	As cast	299.63±1.27	364.21	335.10	281.57	348.51
	Annealed	300.89±1.09	366.29			353.97
$Ir_{12}Fe_{33}Co_{20}Ni_{30}Pt_5$	As cast	202.74±0.89	221.11	243.19	219.11	242.94
	Annealed	207.97±0.98	228.08			240.20

Table 5.3: Reduced and elastic modulus results, both experimental from nanoindentation, and also predicted by the Rule of Mixtures (ROM) for the nominal and XRF measured compositions.

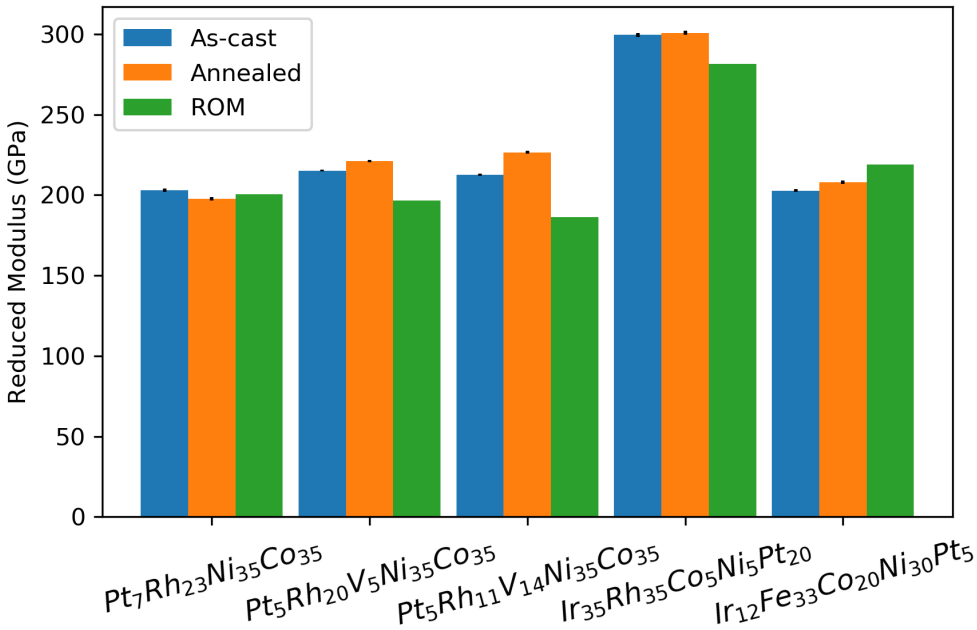

(a) Full scale graph

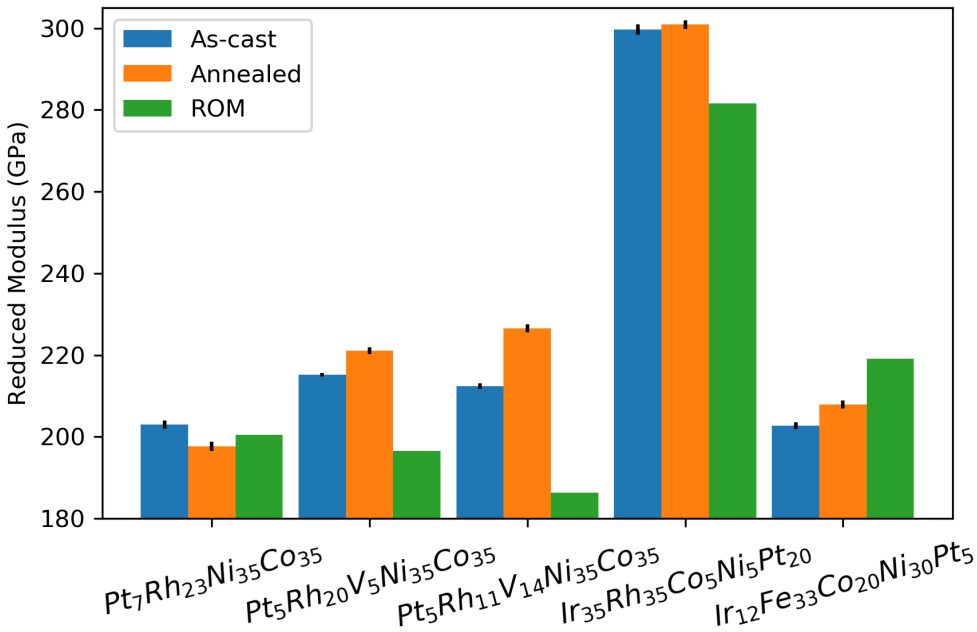

(b) Scaled graph to show error associated with measurement

Figure 5.4: Comparison of the reduced moduli obtained experimentally (nanoindentation) for as-cast and annealed alloys compared to the ROM elastic modulus converted to a reduced modulus from table 5.3. As the experimental error in the data is so low, a scaled graph is also included to allow this level to be seen.

The errors for the data presented in figure 5.4 are the standard error associated with each set of measurements performed on a particular sample. The standard error is the standard

deviation, σ, divided by the square of the number of data points, N.

$$err = \frac{\sigma}{\sqrt{N}} \tag{5.3}$$

where the σ is

$$\sigma = \sqrt{\frac{\sum_{i=1}^{N}(x_{-}\bar{x})^2}{N-1}} \tag{5.4}$$

In most cases, the elastic modulus obtained via nanoindentation is $\lessapprox 15\%$ different from the value obtained via the ROM (atomic ratio summation). Of course, ROM for Young's modulus is a very rough estimation, which can be confounded by many factors, such as the formation of more than one phase, but it is a type of assessment that is easily carried out and highly appropriate to apply in the type of alloy design procedures used to predict the modulus prior to the creation of alloys.

Overall, the results from the nanoindentation of the alloys for as-cast and annealed samples are consistent in comparison to each other across all alloys given what we know about changes in the modulus of elasticity with heat treatment. However, some unexpected effects, such as the moduli increasing post heat treatment are discussed below. This evidences the homogeneity in the mixing of the alloys. The elastic moduli extrapolated from the reduced moduli, along with the hardness results from the nanoindentation of $Pt_7Rh_{23}Ni_{35}Co_{35}$, $Pt_5Rh_{20}V_4Ni_{35}Co_{35}$, and $Pt_5Rh_{11}V_{14}Ni_{35}Co_{35}$ are consistent with the deformation behaviour exhibited in the laboratory samples (section 5.3.1).

We can see in table 5.3 that the difference in reduced modulus between as-cast and annealed is very small, in most alloys, although this converts to a larger difference in the modulus of elasticity, although the changes are in fact still very small. In the results for $Pt_7Rh_{23}Ni_{35}Co_{35}$ the reduction in modulus after heat treatment are which is indicated may be due to the relief of residual stresses, present in the samples as the result of dimensional change during the solidification process. Such stresses could contribute to the resistance to elastic deformation in the as-cast state and then be relieved by the heat treatment.

The results for $Ir_{35}Rh_{35}Co_5Ni_5Pt_{20}$ show that there was no change in the sample after heat treatment, this again might be due to the uncontrolled nature of the cooling, both in the hearth and after heat treatment in the furnace.

We observe an increase in the modulus of $Pt_5Rh_{20}V_5Ni_{35}Co_{35}$, $Pt_5Rh_{11}V_{14}Ni_{35}Co_{35}$, $Ir_{12}Fe_{33}Co_{20}Ni_{30}Pt_5$. While small, this could result from changes in the grain structure of the samples. The majority of metallic materials show elastic anisotropy in the cystalline form, so if there was a preferred grain orientation or texture, as may result from growth in casting, it could be that a preferential orientation in the sample presented lower resistance to the elastic deformation caused by the indenter. Changes to the grains during heat treatment, such as recrystallisation or simple grain growth, might alter this and so change the effect. This process

could result in an apparent modulus increase, or decrease as observed earlier, depending on the orientation of the texture in the sample, of the test, and how the sample structure evolved.

Comparing the results for the change in modulus with data for binary PGM alloys obtained from the PGM Database, there is some evidence for an increase in the modulus of PGM alloys post annealing[221]. However, the as-cast modulus falls within ranges that also include the modulus after annealing. Likewise, sometimes annealing does not affect the modulus. Also, we do not know what the annealing parameters were in this literature database. Control of the modulus of an alloy via annealing is a very intricate process depending on a lot of parameters and for this study we did not try to control for these parameters. Rather, heat treatment was utilised as a homogenisation procedure after casting. It must also be remembered that, although the differences between samples pre and post anneal were greater than the standard error found in the experiments, the absolute differences are not great and indicates that any changes are only minor effects.

Finally, nanoindentation is a nanoscale technique and as such is potentially subject to the influence of local variations and defects in the material. Larger samples (which could be obtained in further work from the industrially-cast ingots) would allow the machining of specimens suitable for tensile testing, which would give a better measure of this behaviour at a scale more appropriate for the likely applications.

5.3.2.2 Hardness

The Vickers Hardness indentation procedure is outlined in section 3.3.7. The Vickers Hardness indentation results, presented on table 5.4, show changes in the macroscale hardness of the alloys post heat treatment. Such results are to be expected given that, in general, it is likely that heat treatment changes the microstructure and defect structure of the alloy, however, more data are needed across many samples to be able to conclusively link the changes to specific developments of microstructural features.

Alloy	State	Nanoindentation Hardness (GPa)	Vickers Hardness (HV)	HV converted to Hardness (GPa)
$Pt_7Rh_{23}Ni_{35}Co35$	As cast	2.85±0.02	178.00	1.75
	Annealed	2.93±0.02	166.00	1.63
$Pt_5Rh_{20}V_5Ni_{35}Co_{35}$	As cast	3.50±0.01	200.46	1.97
	Annealed	3.76±0.01	183.30	1.80
$Pt_5Rh_{11}V_{14}Ni_{35}Co_{35}$	As cast	4.45±0.02	231.20	2.27
	Annealed	5.02±0.01	257.00	2.52
$Ir_{35}Rh_{35}Co_5Ni_5Pt_{20}$	As cast	5.34±0.04	309.90	3.04
	Annealed	5.30±0.02	256.00	2.51
$Ir_{12}Fe_{33}Co_{20}Ni_{30}Pt_5$	As cast	3.28±0.02	231.20	1.65
	Annealed	3.41±0.01	257.00	1.61

Table 5.4: Vickers hardness and nanoindentation hardness results

The hardness of $Pt_7Rh_{23}Ni_{35}Co_{35}$ increases after heat treatment, in one measurement (which is the same trend seen in the changes in the modulus), while it decreases in the Vickers hardness. This, and the relatively small differences in each case suggest that there is no major change in the hardness in this alloy; the heat treatment time and temperature are probably not enough to induce any major changes in the microstructure, at least to the extent that it contributes to strength. For $Ir_{35}Rh_{35}Co_5Ni_5Pt_{20}$ the hardness also remains approximately the same, to 0.1, although there is a decrease in Vickers hardness, to a relatively large extent. The hardness and Vickers Hardness of $Pt_5Rh_{11}V_{14}Ni_{35}Co_{35}$ and $Ir_{12}Fe_{33}Co_{20}Ni_{30}Pt_5$ both increase after heat treatment, which suggests evolution in the structure. Grain growth, and reduction in dislocation density are likely with heat treatment at sufficient temperature, but both of these would lead to reductions in hardness. It could be that there is the formation of fine second phases, or ordering in the structure, which would see hardness increases, or even, in this kind of alloy, that a more even distribution of the elements (i.e. the removal of segregation) may see improved solid solution strengthening throughout the material. In $Pt_5Rh_{20}V_5Ni_{35}Co_{35}$ the hardness increases but the Vickers Hardness decreases after heat treatment, these changes are both relatively small, and may not indicate an underlying real change in the material.

While, nanoindentation and Vickers Hardness indentation provided an insight to the characteristics of the alloys and how the alloy changes after heat treatment there are better characterisation techniques to assess the modulus of elasticity. Other complementary techniques would be tensile testing and three-point beam bending.

5.4 DSC, TGA and oxidation resistance

5.4.1 DSC

Figure 5.5 shows scatterplots of DSC data obtained for all 5 alloys. Positive heat flow corresponds to exothermic processes and the opposite direction for endothermic.We see that all DSC plots follow a similar heating pattern where there is steady heat flow up to 1100 - 1300°C followed by a rapid rise in heat flow, indicating the start of a phase transition. The heating stage was only carried out up to 1400°C due to the capabilities of the equipment, which is why the phase transition was not completed in the results shown. As expected from the compositions, these alloys evidently have a high liquidus temperature.

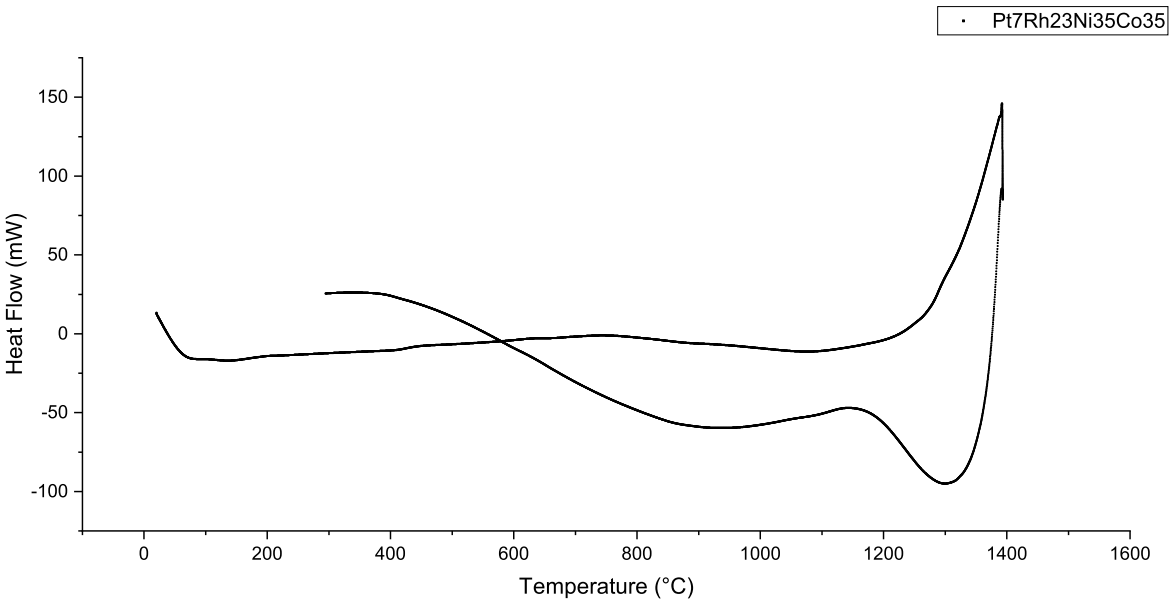

(a) $Pt_7Rh_{23}Ni_{35}Co_{35}$

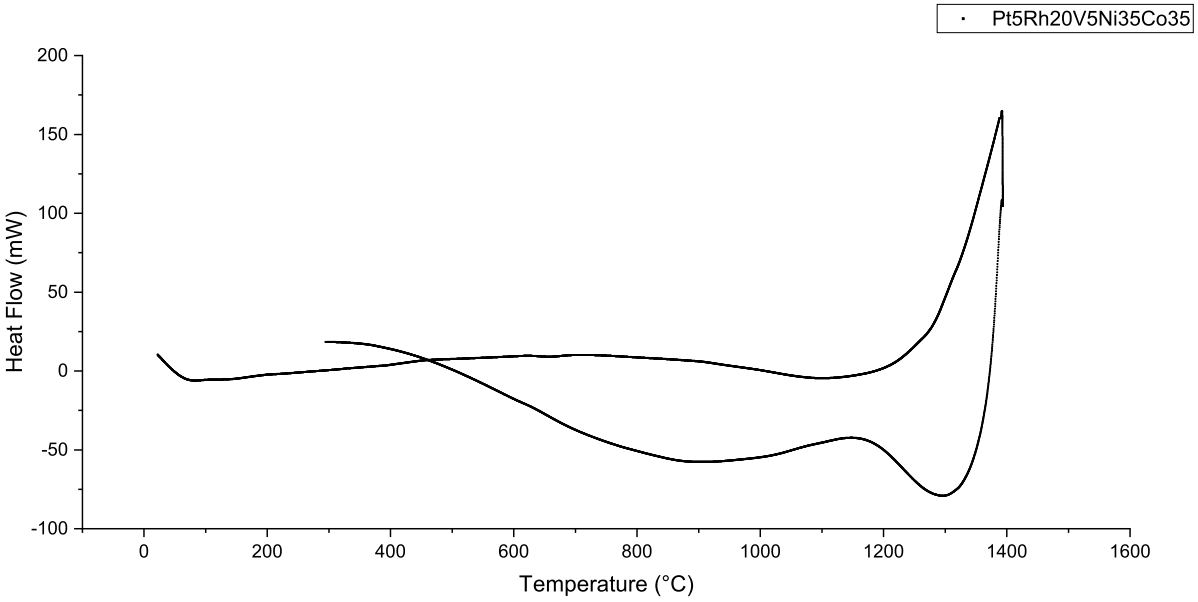

(b) $Pt_5Rh_{20}V_5Ni_{35}Co_{35}$

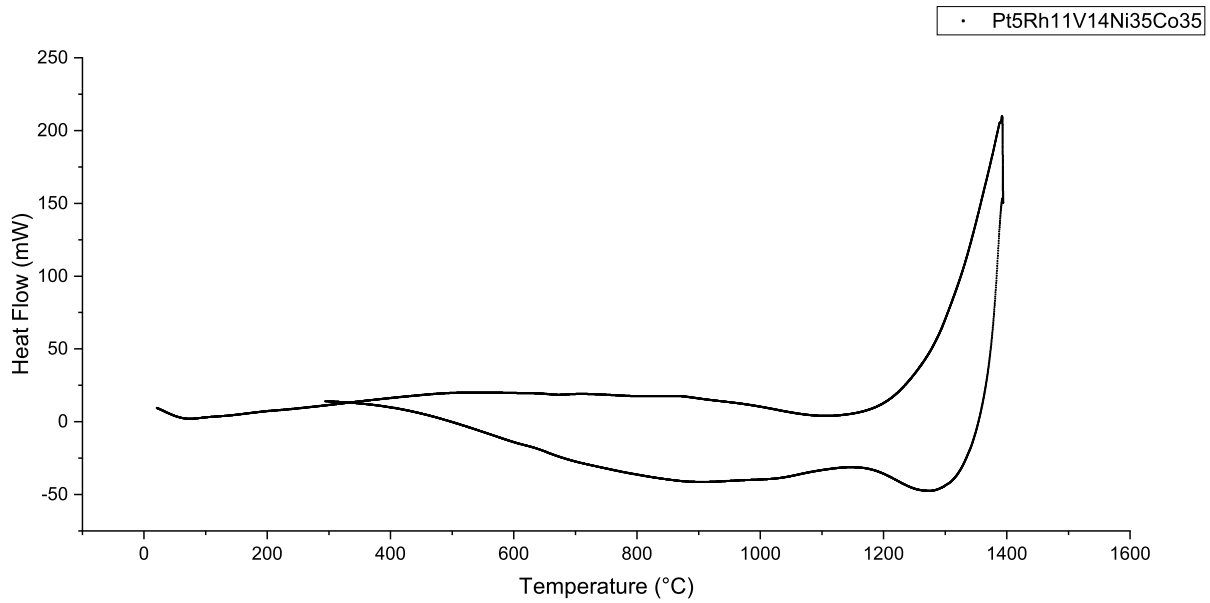

(c) $Pt_5Rh_{11}V_{14}Ni_{35}Co_{35}$

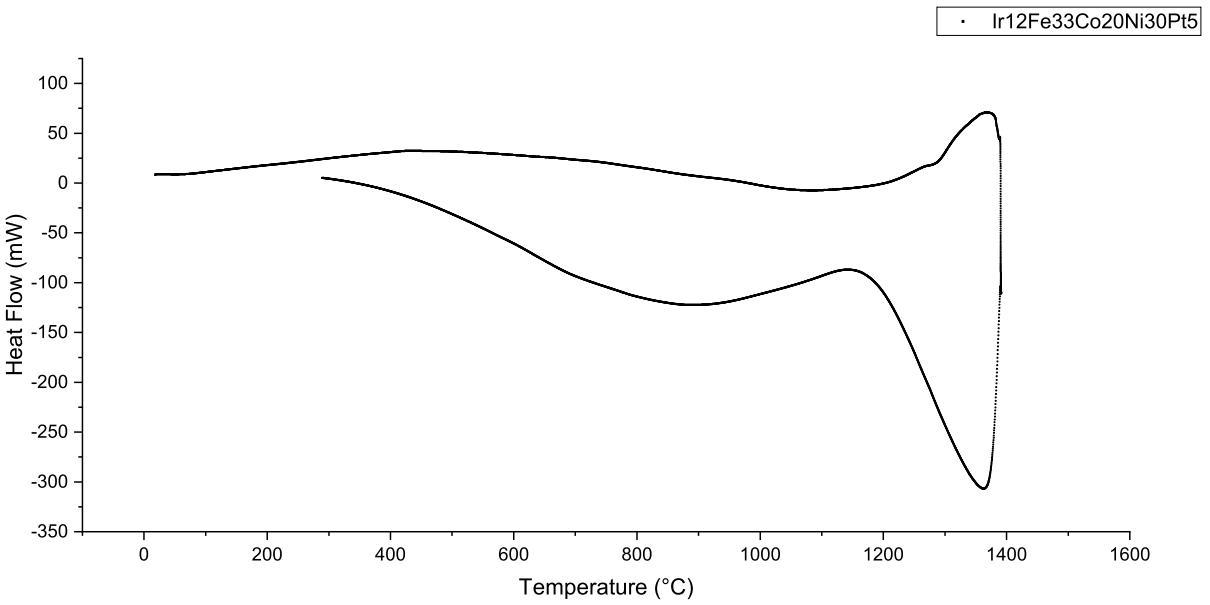

(d) $Ir_{12}Fe_{33}Co_{20}Ni_{30}Pt_5$

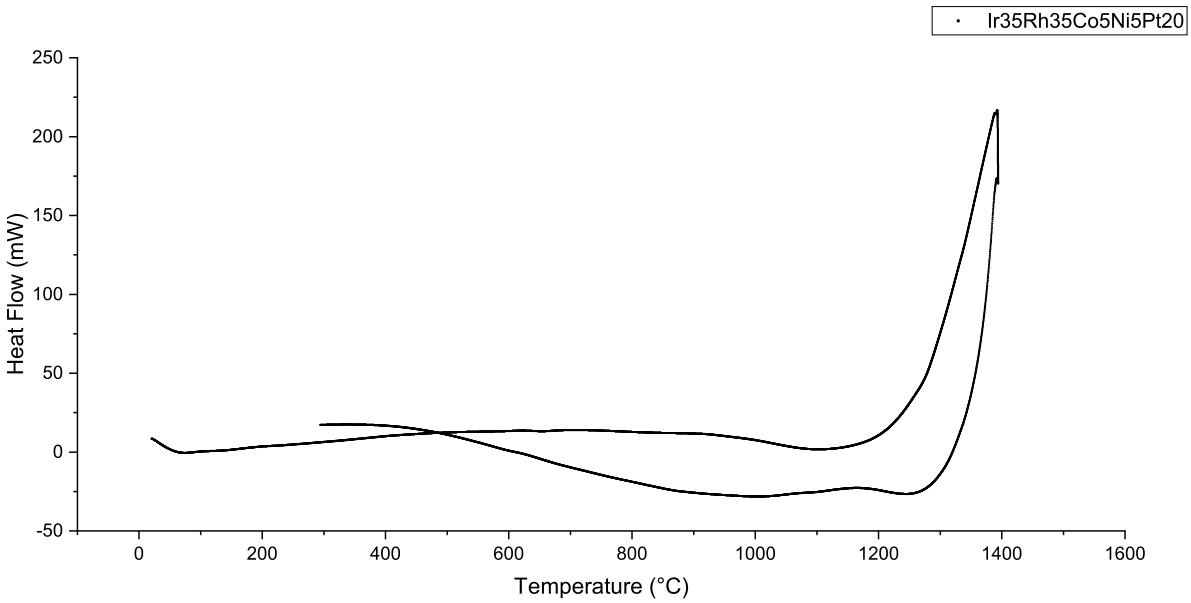

(e) $Ir_{35}Rh_{35}Co_5Ni_5Pt_{20}$

Figure 5.5: DSC of all 5 industrially manufactured alloy samples

In the heating phase there are no notable phase transitions observed and any deviations from linearity in heat flow are small and most likely due to the lag between the temperature reached by the calorimeter and the temperature the sample would be at. Alloys $Ir_{35}Rh_{35}Co_5Ni_5Pt_{20}$, $Pt_5Rh_{11}V_{14}Ni_{35}Co_{35}$, $Pt_5Rh_{20}V_5Ni_{35}Co_{35}$ and $Pt_7Rh_{23}Ni_{35}Co_{35}$ have similar responses to heating, a partial phase transition is observed between 1200°C and 1400°C (which is the highest temperature possible in the DSC used), leading to the assumption that a full phase transition would take place if the samples were heated further. It is likely that this transition is melting, and the part captured corresponds to the lower part of the melting range (the solidus and the lower part of the solid-liquid tow phase region).

DSC was performed in an inert atmosphere of argon to determine the response of the industrially manufactured alloys to heating and give limits to set the conditions on how to perform the TGA study. The range of interest for TGA is 1000°C - 1200°C, temperatures typical for the applications PGM alloys are used at. It is also important to study the alloys' oxidation behaviour in the solid state, not when molten, and study of the DSC curves indicates that the onset of melting (i.e. the solidus) is, for all of the alloys, above 1000°C.

For the intents of the study we can see that the alloys are stable, conservatively, up to at least 1000°C, informing the temperature at which to perform TGA. The measured solidus (table 5.5) for all alloys is approximately 1250°C. The exothermic peak, machine cut-off, and dip observed at 1400°C indicates, as discussed above, that melting begins at a temperature below 1400°C, but completes at some point thereafter. While we cannot determine the liquidus, the calculated solidus and the exothermic peak continuing beyond 1400°C indicates that the liquidus will be closer to the melting points of the pure constituent elements.

Alloy	Solidus (°C)
$Pt_7Rh_{23}Ni_{35}Co35$	1265
$Pt_5Rh_{20}V_5Ni_{35}Co_{35}$	1266
$Pt_5Rh_{11}V_{14}Ni_{35}Co_{35}$	1264
$Ir_{35}Rh_{35}Co_5Ni_5Pt_{20}$	1250
$Ir_{12}Fe_{33}Co_{20}Ni_{30}Pt_5$	1266

Table 5.5: Values for the solidus for each alloy calculated from the DSC curves

5.4.2 TGA

Data of the % mass gained per sample and the mass gained per unit surface area per sample is plotted against at.% for V and PGM content (fig. 5.7). Figures 5.6a and 5.6b show the mass gain during heating to 100°C and when held at a constant temperature of 1000°C for 1h.

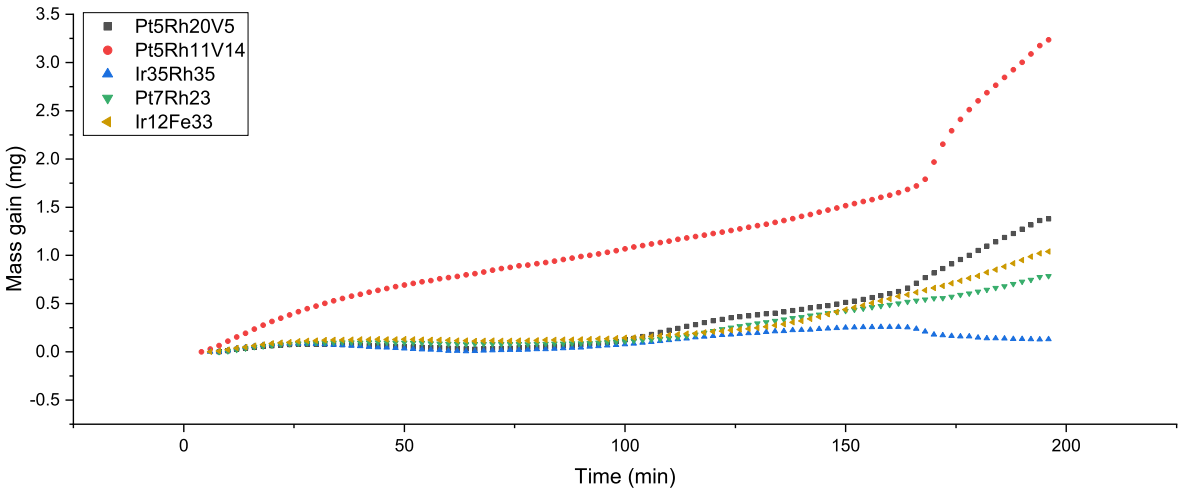

(a) Thermogravimetric Analysis (TGA) of alloys up to 1000°C

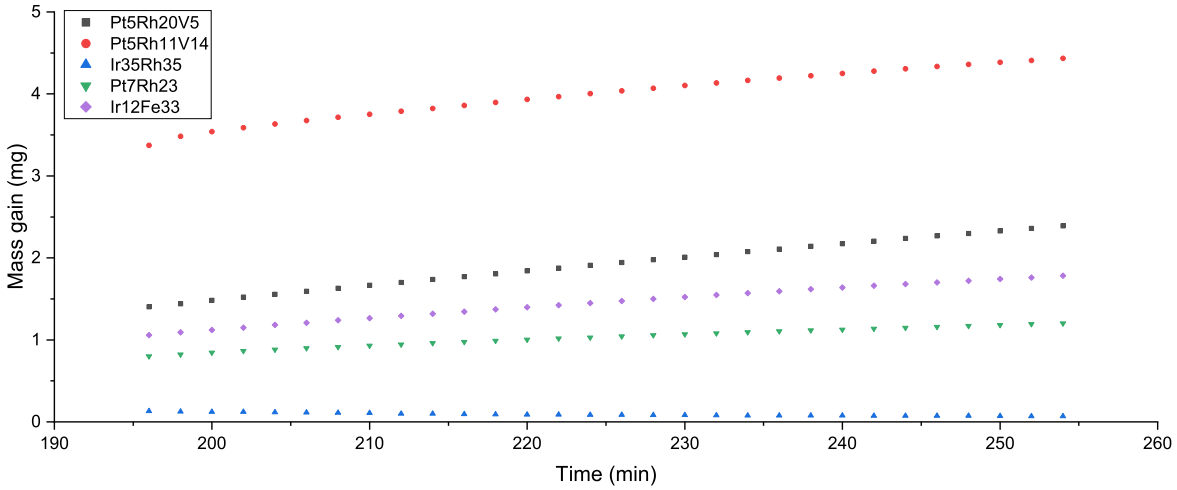

(b) Thermogravimetric analysis of alloys kept at 1000°C for 1 hour

Figure 5.6: TGA of alloys heated to 1000°C (a) and held (b) for 1 hour

The plots show that the greater the V content at at.% then the greater the mass gained. The alloy with the highest V content begins readily oxidising during ramp, whereas a lower V content in $Pt_5Rh_{20}V_5Ni_{35}Co_{35}$ means that the oxidation does not begin until around 100 min. The alloy containing a high at.% of Fe, $Ir_{12}Fe_{33}Co_{20}Ni_{30}Pt_5$ performs better than the V containing alloys; although Fe is more susceptible to oxidation than the PGMs, inspection of an Ellingham diagram shows that vanadium has a more favourable reaction with oxygen. It is therefore logical that this component, when present in high amounts, dominates the oxidation behaviour.

It is clear that the absence of V in $Pt_7Rh_{23}Ni_{35}Co_{35}$ and the high PGM content of $Ir_{35}Rh_{35}Co_5Ni_5Pt_{20}$ make them more suited to high temperature uses in air as the mass gain is minimal.

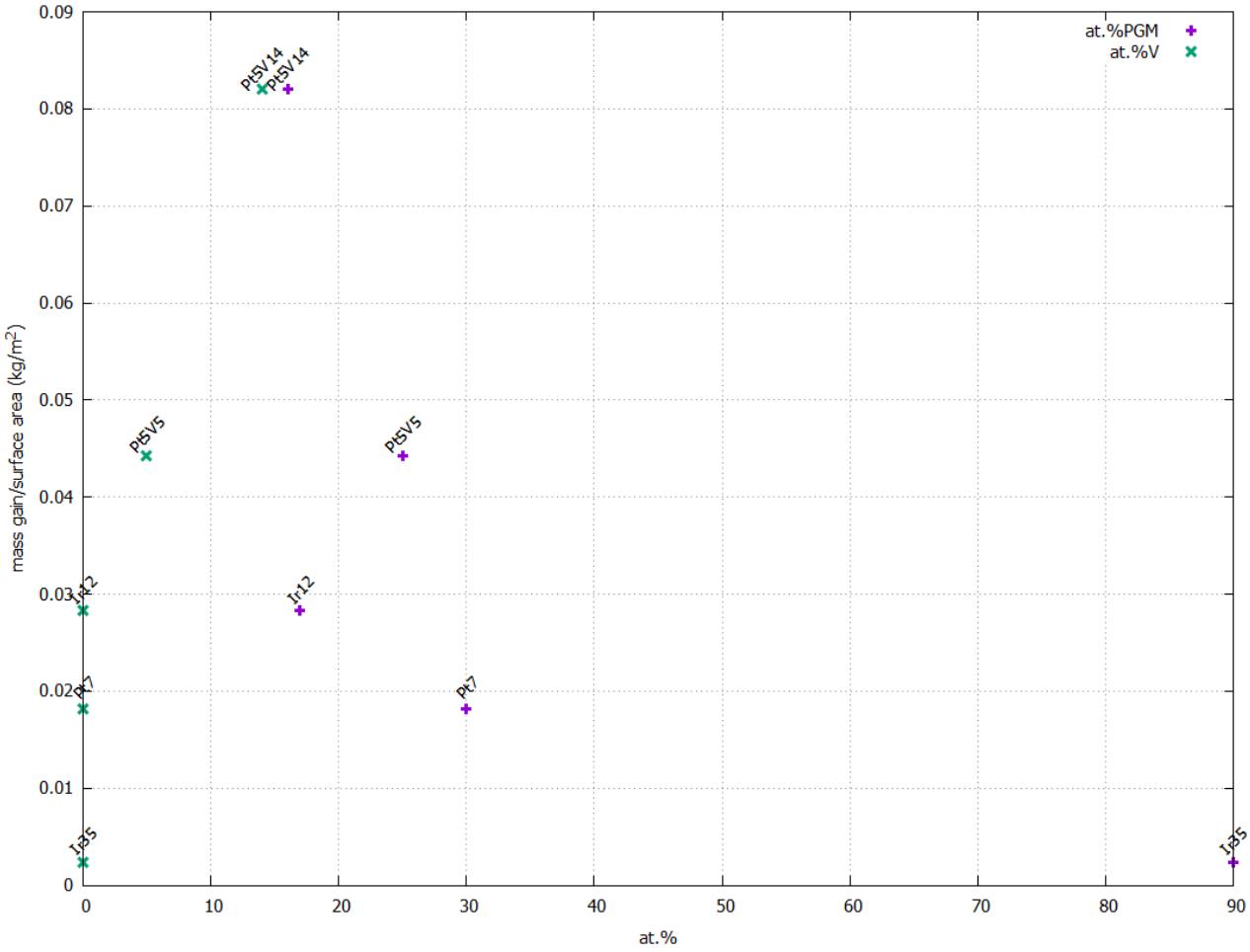

Figure 5.7: Mass gained per surface area during TGA trials with respect to V and PGM at.% content

As it displayed mid-range oxidation resistance, had a relatively low PGM content (just 17 at %), and had a sufficiently high solidus, we studied the mass gain of $Ir_{12}Fe_{33}Co_{20}Ni_{30}Pt_5$ heated to 1200°C, held at 1200°C for 22h. Both the higher temperature and increased time made this a more demanding test of the oxidation resistance of the alloy. The mass gain in this study was ≈19mg with a mass gain of ≈14mg gained during the heating stage. The data are displayed in figure 5.8.

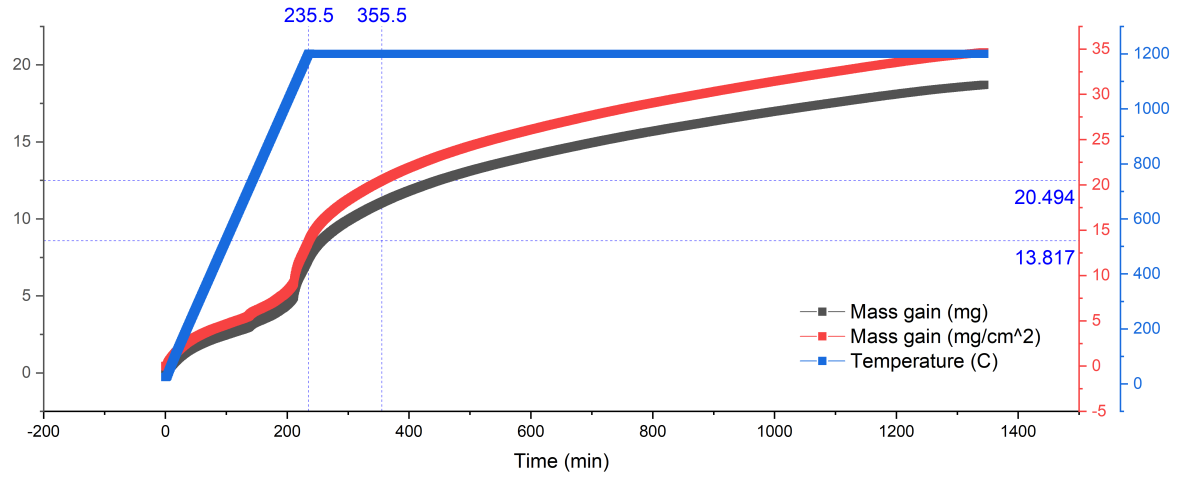

Figure 5.8: Mass gain, mass per unit area gain and temperature against time for $Ir_{12}Fe_{33}Co_{20}Ni_{35}Pt_5$ up to 1200°C

5.4.3 Discussion

The calculated solidus temperatures of the annealed alloys indicate that all alloys would be good candidates for conventional high temperature applications and would remain solid. However, for certain high temperature applications the atmosphere of operation would affect the suitability of an alloy.

Analysis of the TGA results will help determine which alloys are suitable for operation under potentially oxidising conditions. It is very clear that the V addition greatly influences mass gain during heating in air (fig. 5.7), in that it increases the mass gained at high temepratures in air. We have 3 alloys of increasing V content, $Pt_7Rh_{23}Ni_{35}Co_{35}$, $Pt_5Rh_{20}V_5Ni_{35}Co_{35}$ and $Pt_5Rh_{11}V_{14}Ni_{35}Co_{35}$. $Pt_7Rh_{23}Ni_{35}Co_{35}$ gained $0.0182 kg\,m^{-2}$, while $Pt_5Rh_{20}V_5Ni_{35}Co_{35}$ gained $0.0443 kg\,m^{-2}$ which is more than double from $Pt_7Rh_{23}Ni_{35}Co_{35}$ just with the addition of 5% V, and $Pt_5Rh_{11}V_{14}Ni_{35}Co_{35}$ $0.0820 kg\,m^{-2}$ which is more than 4 times the mass per area gained by $Pt_7Rh_{23}Ni_{35}Co_{35}$. When held at 1000°C the V containing alloys continue to gain mass at a faster rate than the other alloys. $Ir_{12}Fe_{33}Co_{20}Ni_{30}Pt_5$ has comparable PGM content to $Pt_5Rh_{11}V_{14}Ni_{35}Co_{35}$, 17% vs. 16%, respectively, even with a high Fe content, $Ir_{12}Fe_{33}Co_{20}Ni_{30}Pt_5$ gained less than half of the mass per unit area than $Pt_5Rh_{11}V_{14}Ni_{35}Co_{35}$, and less mass per unit area than $Pt_5Rh_{20}V_5Ni_{35}Co_{35}$, despite $Pt_5Rh_{20}V_5Ni_{35}Co_{35}$ having 25% PGM content. Interestingly, when heated to 1200°C, $Ir_{12}Fe_{33}Co_{20}Ni_{30}Pt_5$ performs comparably to standard ferritic stainless steels SUS430, B443NT and B445J1M. The stainless steels were placed in an already hot TGA furnace and heated for 120min to 1200°C) in an analysis performed by Cheng *et al.* [222]. During the isothermal stage of the TGA at 1200°C $Ir_{12}Fe_{33}Co_{20}Ni_{30}Pt_5$ gains $6.677 mg\,cm^{-2}$ (fig. 5.8) in 120 minutes while SUS430, B443NT and B445J1M gain $\approx 80 mg\,cm^{-2}$, $\approx 18 mg\,cm^{-2}$ and $\approx 6 mg\,cm^{-2}$, respectively[222]. So $Ir_{12}Fe_{33}Co_{20}Ni_{30}Pt_5$ could be a good alternative for applications requiring steel like alloys. Of course, the PGM content here is low and

the Ir and Pt are minor additions, with the dominant elements being Fe, Ni and some Co; it is not therefore surprising that the behaviour is comparable to some steels, as the highest alloying levels in some stainless steels can approach these ratios of elements (though it would be rare for the iron content of a steel overall to be so low). Also, increasing PGM content has an inverse relationship to mass gain per unit area as we can see in figure 5.7. $Ir_{35}Rh_{35}Co_5Ni_5Pt_{20}$ gains minimal mass per unit area during heating and virtually zero during the isothermal stage of the analysis. While $Pt_7Rh_{23}Ni_{35}Co_{35}$ does gain some mass per unit area it also performs well at the isothermal stage of the analysis, at 1000°C. As expected, PGM content is correlated with good oxidation resistance, though it is noteworthy that $Ir_{12}Fe_{33}Co_{20}Ni_{30}Pt_5$ with a relatively low PGM content still shows reasonable resistance to oxidation. In this alloy it may be that the generally well mixed nature of the alloy, and the fact that where there is microsegregation where Fe is accompanied by Ir and Ni by Pt, allows the beneficial effect of the PGM to be seen. It should also be noted that the Ni content of the alloy is high and that this can be correlated with oxidation resistance in alloys.

Chapter 6

Microstructure and Phase formation of Selected Alloys

6.1 Presentation of results

The alloys that the thesis is focused on are then presented in this chapter including the results obtained by XRD, XRF, optical images after etching, SEM and EDX, and EPMA. For each technique the section is divided into results at the laboratory scale and results at the industrial scale. Results are explained and discussed briefly in each results section, for the purpose of understanding the phase makeup, origin and stability of the microstructures in each of these alloys. Discussion is presented with each set of results followed by a short overall discussion about the alloy.

The simulation results, which included findings related to one of these alloys, were presented in the simulation results chapter 4.

Also included in this chapter are the results obtained in a short manufacture cycle exploring novel alloys from the general systems of interest with significant content of silver. We present results and discussion on trialling a criterion for identifying single phase multiprincipal component alloys based on silver within the HEA design criteria, as in the work to be discussed, the presence of silver was found to confound the parameters used for initial selection.

Discussion and evaluation of the alloy prediction methods used is also given, followed by a comparison of the alloys at laboratory scale and industrial scale. The chapter ends with a discussion on the potential fields of application for these alloys.

6.1.0.1 Industrial scale manufacture results

Note that the alloy samples presented here, which are described as being the results of industrial scale up trials have been manufactured at JMNM in a procedure outlined in section 3.1.2.1. Samples were cut from 1kg ingots, the annealed samples were heat treated after being cut rather than the whole ingot being heat treated.

6.1.1 XRD

At the laboratory scale XRD analysis was performed on all alloys that appeared to have alloyed homogeneously. For $Ir_{35}Rh_{35}Co_5Ni_5Pt_{20}$ and $Ir_{12}Fe_{33}Co_{20}Ni_{30}Pt_5$ only data for the as-cast alloys were collected due to expediting the industrial manufacture trial part of the project.

The background signal for the patterns on most of these alloys varies due to the mounting medium being changed and the use of 2 different machines to collect data during downtime on the main machine. Each case contributes differently to the amount and shape of the background, but nevertheless the main peaks in the pattern due to the crystalline metallic structure can be distinguished as a crystalline phase of FCC structure (due to the systematic position of the peaks and the absences when these are indexed), however, there are a small number of peaks that are not consistent with these patterns, and that might be secondary phases, mounting medium artifacts, preparation inconsistencies and inadequacies, or environmental factors or interferences; of these, the presence of some other crystalline phases in relatively small amounts in the region of analysis is the most likely.

XRD results for all alloys, as-cast and annealed, are presented for the industrial scale manufactured alloys. No direct comparison phases were identified. All alloys are consistent to some degree with an FCC crystal phase; as is expected, when manually indexed, most alloys are, in fact, FCC as they present all the peaks indicative of an FCC crystal phase. An example of the indexing can be found on figure 3.6.

6.1.2 XRF

At the laboratory scale XRF analysis was only performed on PtRh alloys. The two cycles of alloy design were performed several months apart. Two alloys of potential interest for applications were selected from the Ir-cycle for industrial scale up trials. XRF analysis on the Ir alloys was deemed unnecessary as the SEM and EDX data of laboratory manufactured $Ir_{35}Rh_{35}Co_5Ni_5Pt_{20}$ (fig. 6.45, 6.46) and $Ir_{12}Fe_3Co_{20}Ni_{30}Pt_5$ (fig. 6.56) indicated that the alloys had mixed uniformly with some segregation between the dendrites and that there were no areas of segregation on a large scale, or to a large extent.

The results for all alloys show some contrast in the wt.% analysed by XRF, but overall the change in wt.% is not so stark that it would be considered that a good level of mixing had not occurred in alloying. It is important to note that the area analysed is dependent on the aperture chosen so we cannot conclude that the wt.% distribution on the surface is exactly as presented. We can, however, conclude that the surface prepared for analysis is overall fairly homogeneous and close to the intended composition to be manufactured.

At the industrial scale XRF results are presented for all alloys made at JMNM for as-cast and annealed samples. XRF was used to determine homogeneity and consistency in composition across samples from the same ingot. The part of the sample and the overall area analysed ultimately depends on the shape of the sample as that informs the aperture used. XRF data

collected might be affected by a number of factors such as sample preparation, and cleanliness.

Overall, we see that the as-cast and heat treated samples of each alloy are very similar to each other, with no large differences in the wt.%. There are some bigger differences in alloys $Pt_5Rh_{11}V_{14}Ni_{35}Co_{35}$, $Ir_{35}Rh_{35}Co_5Ni_5Pt_{20}$, and $Ir_{12}Fe_{33}Co_{20}Ni_{30}Pt_5$, around 3-4wt.%. Still, the results do indicate homogeneity in the region of the ingot which they came from for all samples.

6.1.3 Optical microscopy

Optical microscopy images were obtained of etched as-cast and annealed samples of each industrially manufactured alloy. The samples were etched using the procedure described in section 3.3.11. Depending on how the etchant attacked the surface some grains are visible, some are not. Dimensions of some of the visible grains are provided for illustrative purposes of how the microstructure responded to heat treatment. However, there are insufficient data to provide reliable information about the approximate grain size, to an extent where statistical methods can be usefully employed.

6.1.4 SEM and EDX

While SEM-EDX is a very powerful technique that is able to produce high resolution atomic distribution maps on imaged surfaces, in this study it was used in a manner to provide a quick technique to be able to determine which samples would be of interest to industry, i.e. which samples appeared to have a uniform elemental distribution across the imaged surface, and to aid with microstructure interpretation, by indicating which elements tended to be found associated with each other, and which were more likely to separate. Due to the large number of samples that needed to be assessed for each manufacture cycle, data was collected for approximately 5min for each sample. It is recognised that this is a low collection time, and that as a result the amount of counts recorded for each spot on the image will be low. As a result, it is not appropriate to use the images presented here for high confidence or quantified assessments of composition distribution.

For the laboratory manufactured alloys SEM and SEM-EDX were performed on 3 different machines, depending on what was available at which site (Sheffield, JMNM) so there are inconsistencies in the style in which the data are displayed due to differences in software used to acquire the data on different machines. SEM data are displayed per alloy, where data is available, for both as-cast and annealed. For laboratory produced $Ir_{35}Rh_{35}Co_5Ni_5Pt_{20}$ and $Ir_{12}Fe_{33}Co_{20}Ni_{30}Pt_5$ only as-cast data was obtained due to the need for expediting the industrial manufacture trials.

Secondary and backscatter electron SEM images are displayed per alloy followed by SEM-EDX maps of that alloy for as-cast and annealed, where data are available. Where alloys have been etched, the corresponding data and some grain size and dendrite size analysis are provided, depending on how the etchant attacked the surface. It is important to note that where

grains and dendrites are analysed the goal is not to reach a conclusion about the crystal growth in these alloys since insufficient data have been collected and applications would not require particular as-cast microstructures as most would involve significant mechanical deformation in shaping. Showing the appearance of the microstructure, however, will provide an appreciation of it.

Overall, the alloys appeared to be well mixed and the elemental distribution appeared uniform and homogeneous at the scales investigated across the prepared surfaces of the samples for all alloys imaged. Do note, however, that the penetration depth in this form of imaging is strongly correlated to the accelerating voltage. The accelerating voltage for most of these analyses was 20kV, while the penetration depth depends on many factors, among them the composition of the material, it is important to consider there could be a tendency to homogenise compositions over the depth of the analysis penetration mapped via EDX, nevertheless, little difference is seen in lateral measurements on this length scale.

The SEM-BSE images are presented to give an idea of the microstructure and cooling behaviour of these alloys. In most alloys, the dendrite structure changes or disappears post heat treatment, as would be expected if the temperature and time have reached levels high enough to cause significant atomic motion. All alloys appear fairly uniform under SEM-BSE.

EDX maps are displayed below, accompanied by an SEM-BSE photo, per alloy per heat treatment state. The spot size varied from 4-5 and an accelerating voltage of 20kV was used.

The maps show a very homogeneous distribution of elements across the areas imaged, although the peak positions in the spectra do overlap for some constituent elements, e.g. Pt and Ir, and Ni and Co.

The overlapping spectra do show that the fast EDX does not possess the appropriate resolution to resolve these particular elements to a good degree of accuracy, due to the short data collection time, so the apparent homogeneity might also be due to the incorrect element being detected.

6.1.5 EPMA

Below we present results for EPMA performed on the laboratory scale manufactured PtRh based alloys. All EPMA data collection and analysis was performed by Dr.Gareth Hutton at JMTC. Each EPMA section is split into alloys with low and high magnification data per alloy per heat treatment state. Overall, the laboratory scale alloys appear very homogeneous with only a small degree of segregation observed, ≈1-2 at.% per alloy. Also, it appears that heat treatment helps further homogenise the alloy and the dendrite growth appears more regular and uniform.

In the industrially manufactured alloys the distribution of elements in the alloys appears very homogeneous with only a small degree of segregation observed, ≈1-2 at.% per alloy in $Pt_7Rh_{23}Ni_{35}Co_{35}$ and $Pt_5Rh_{20}V_5Ni_{35}Co_{35}$, slightly more segregation is observed in $Pt_5Rh_{11}V_{14}Ni_{35}Co_{35}$

compared to the laboratory scale alloy, probably due to differences in the mixing in the arc melter and the quantity of the material used and made. The Ir alloys are homogeneous in wt.% across the area analysed. However, there is more segregation than expected, $\approx 1-5$at.%in the as-cast and post heat treatment analyses of the Ir alloys. This could be for a number of reasons, but the primary cause may be the manufacture and homogenisation procedures. In comparison to the laboratory scale manufacture, it seems that 1000°C works better in homogenising the alloy.

6.2 PtRh criteria and alloys chosen

The PtRh binary is the basis of a number of commercial PGM alloys. For the identification of novel alloys based on containing PtRh at any at.%, the criteria of $\delta \leq 4\%$, $-20\text{kJ}\,\text{mol}^{-1} \leq \Delta H_{mix} \leq 10\text{kJ}\,\text{mol}^{-1}$ and $-10\text{kJ}\,\text{mol}^{-1} \leq \Delta H_{mix} \leq 5\text{kJ}\,\text{mol}^{-1}$ were used. The reason for choosing a tighter range for ΔH_{mix} within the first quoted wider range was to identify alloys that possessed a ΔH_{mix} value near zero which might not have been clearly identified within the wider range . We wanted to explore enthalpies that ranged from the very negative to fairly positive and around zero to investigate the effect, if any this would have on the resulting alloy when manufactured. Since the alloys were to be based on PtRh, the compositions would be the form PtRhXY and PtRhXYZ, for quaternary and quinary, respectively, were X, Y and Z are placeholders for any of $\{\text{V}, \text{Cr}, \text{Co}, \text{Ni}, \text{Cu}, \text{Mo}, \text{Ag}, \text{W}, \text{Re}\}$, which was the full list of considered elements, the total possible number of compositions screened in this case was 36×11462 and 84×553401, for quaternary and quinary respectively, $\approx 47 \times 10^6$. We explored all possible at.% combinations within the range 5-35at.% per component and did not choose compositions based on a lower limit for ΔS_{mix}, where $1.5R$ is sometimes considered to be the lowest threshold for ensuring random ordering within the resulting alloy, arising from the entropy of mixing, ΔS_{mix}, for a composition with equiatomic constituents[44]. Alloys were selected based on those having a good chance of forming under these criteria, having similarities to current commercial alloys in some respects, and also to explore alloys with similarities to each other to give a change of systematic learning. The alloys selected using these criteria and the reasons for the choice are in table 3.2.

6.3 Ir and IrRh criteria and alloys chosen

In the PtRh investigation, Ag containing compositions did notalloy well (in most cases seen by the elements not mixing in the liquid state); the reasons for this are discussed further in section 6.5. For the Ir and IrRh investigation the search ranges for the criteria were kept the same. Permutations were IrWXY(Z) and IrRhXY(Z) for [V, Cr, Fe, Co, Ni, Cu, Nb, Pd, Ag, Re, Pt, Au], table 3.3. An additional criterion was explored with the limits set as $c_k c_l \Delta H_{CD} - c_i c_j \Delta H_{AB} \leq 2\text{kJ}\,\text{mol}^{-1}$ for every pair of elements a composition contained. The

choice for the criterion was informed by examining the ΔH_{mix} of alloys that mixed successfully and homogeneously from the study outlined in section 6.2 (tab. 3.2). The criterion, however, was not successful in predicting single phase alloys and compositions suffered from the same problems encountered in the PtRh investigation. What was observed from both investigations was that alloys which appeared to be single phase had a small difference in the ΔH_{AB} across pairs in the composition, all of which had negative or very small positive ΔH_{AB} values.

Alloys $Ir_{35}Rh_{35}Co_5Ni_5Pt_{20}$ and $Ir_{12}Fe_{33}Co_{20}Ni_{30}Pt_5$ were chosen for industrial scale manufacture due to being assessed as single phase and being of mixtures of elements that were, from availability, cost and handling requirements, of interest to industry. Ag containing alloys did not alloy completely during manufacture. Also, the rate of success was lower than the previous cycle of alloy identification and selection; several alloys appeared single phase but there were small but significant degrees of segregation observed in several alloys that alloyed homogeneously during manufacture.

The results of this cycle informed a further consideration to take into account when trying to design single phase HEA. If we consider the ΔH_{AB} of pairs, i.e. binary alloys, which fully alloy substitutionally, if we alloy elements which alloy as binaries successfully then we would increase the likelihood of designing a single phase multiprincipal component alloy. An investigation was designed based on the incorporation of Ag into HEA alloys of this type, and is expanded in section 6.5.

6.4 Alloy results & discussion

Note that the amorphous phase showing in the $30 - 40^{\circ}$ range in some of the XRD data which is presented in this section of the chapter is due to the mounting medium which was clear resin.

6.4.1 $Pt_7Rh_{23}Ni_{35}Co_{35}$

6.4.1.1 XRD

XRD patterns are displayed in figures 6.1 and 6.2. The lattice parameters obtained from the XRD data are presented in table 6.1. The average lattice parameter and the lattice parameters for ordered structures obtained from simulations are displayed on table 6.2.

Manufacture scale	As-cast (Å)	Annealed (Å)
Laboratory	3.628	3.604
Industry	3.647	3.644

Table 6.1: Lattice parameter for $Pt_7Rh_{23}Ni_{35}Co_{35}$ obtained from XRD data sets at different stages of manufacture and processing

	Lattice parameter (Å)
Average from DFT	3.606
Ordered 1	3.661
Ordered 2	3.625
Ordered 3	3.616

Table 6.2: Lattice parameter for $Pt_7Rh_{23}Ni_{35}Co_{35}$ obtained from averaging over the lattice parameters obtained from geometry optimisations on the randomly arranged lattices compared to geometry optimisations on the ordered lattices (sec. 4.2, fig. 4.9)

Figures 6.1 and 6.2 show the XRD data collected for the laboratory manufactured samples and industry manufactured samples, respectively. Both figures display the individual data for as-cast and annealed samples and a normalised comparison of the two. Generally, all data is consistent with a pattern characteristic of an FCC crystal structure.

Laboratory scale

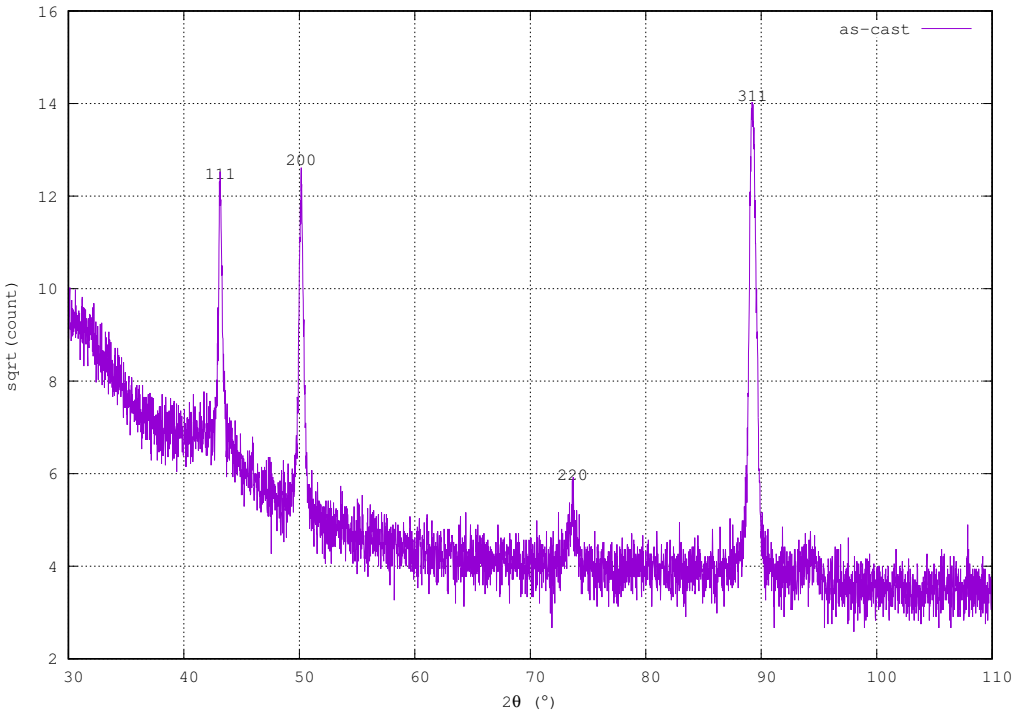

(a) as-cast

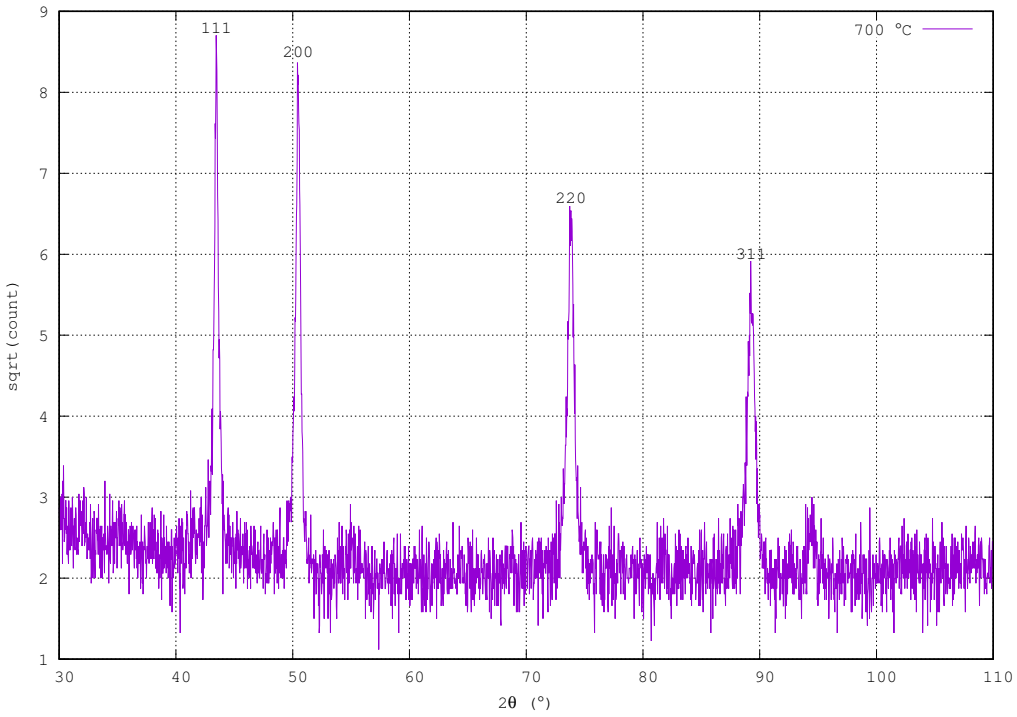

(b) annealed @ 700°C

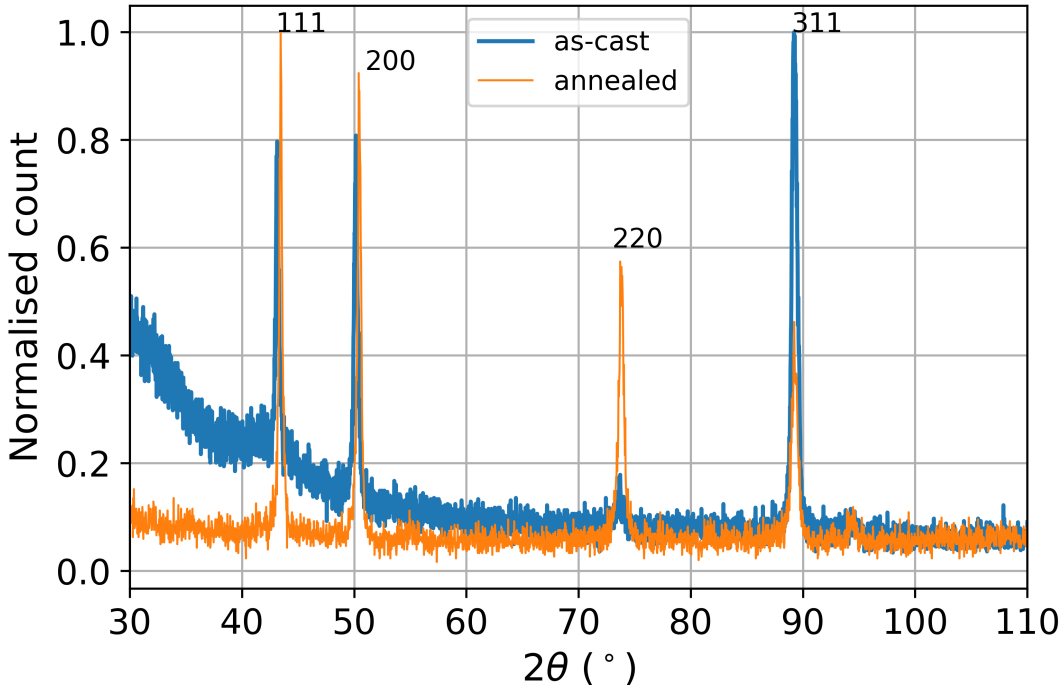

(c) Comparison of normalised XRD data for as-cast and annealed samples

Figure 6.1: XRD of laboratory manufactured $Pt_7Rh_{23}Ni_{35}Co_{35}$

For the laboratory manufactured samples, the XRD patterns before and after heat treatment match, indicating the alloy solidified into an equilibrated, or close to equilibrated, state, to the

resolution of the patterns collected. On appearance, patterns appear to match the relative peak positions which result from an FCC crystal structure. The peaks are strong which can indicate that the alloy is in a form with a strong regular (i.e. crystalline) arrangement. The lattice parameters obtained from indexing the XRD peaks show that the lattice parameter is consistent up to 0.1Å. The data are from two different samples, manufactured independently of each other so there is a consistency in lattice parameter.

Comparing the lattice parameters obtained from the laboratory samples and the industrially manufactured samples we can, again, see a consistency at 0.1Å. However, the industrially manufactured samples are consistent with each other to an even higher degree of precision, 0.01Å. The industrially manufactured samples were obtained from the same 1kg ingot so the consistency across the lattice parameter indicates that there is consistency and homogeneity across the ingot.

Observing the normalised data in figure 6.1c we can see that the peak intensity for the (1 1 1), (2 0 0) and (2 2 0) become sharper, which may be due to a decrease in localised residual strains from casting, or due to a reduction in segregation in the phase.

Industrial scale

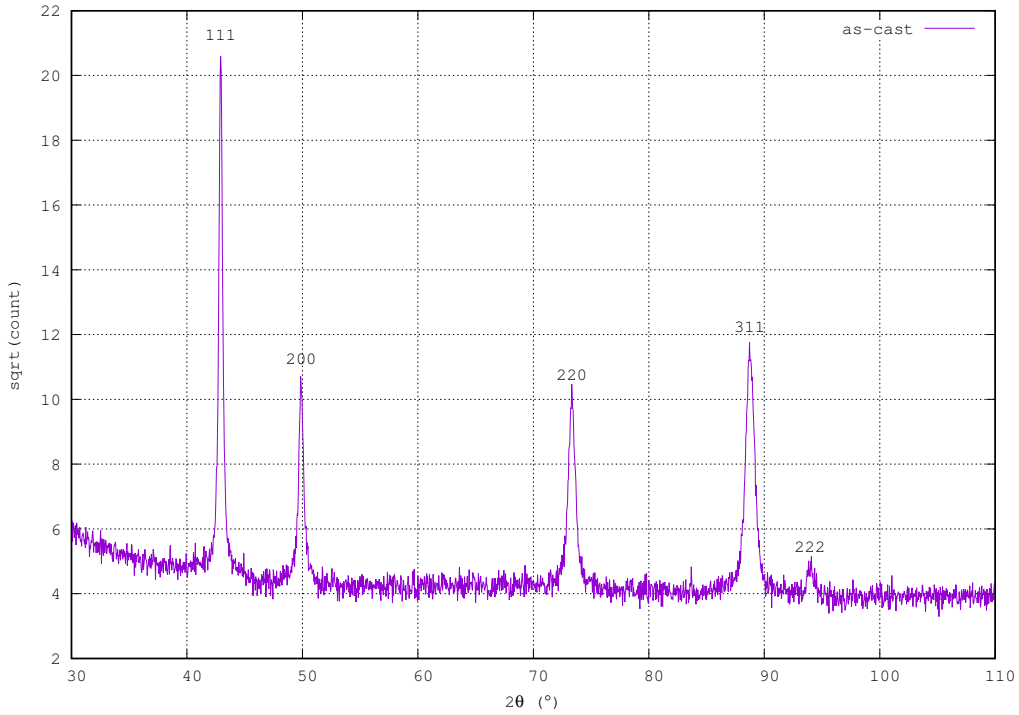

(a) as-cast

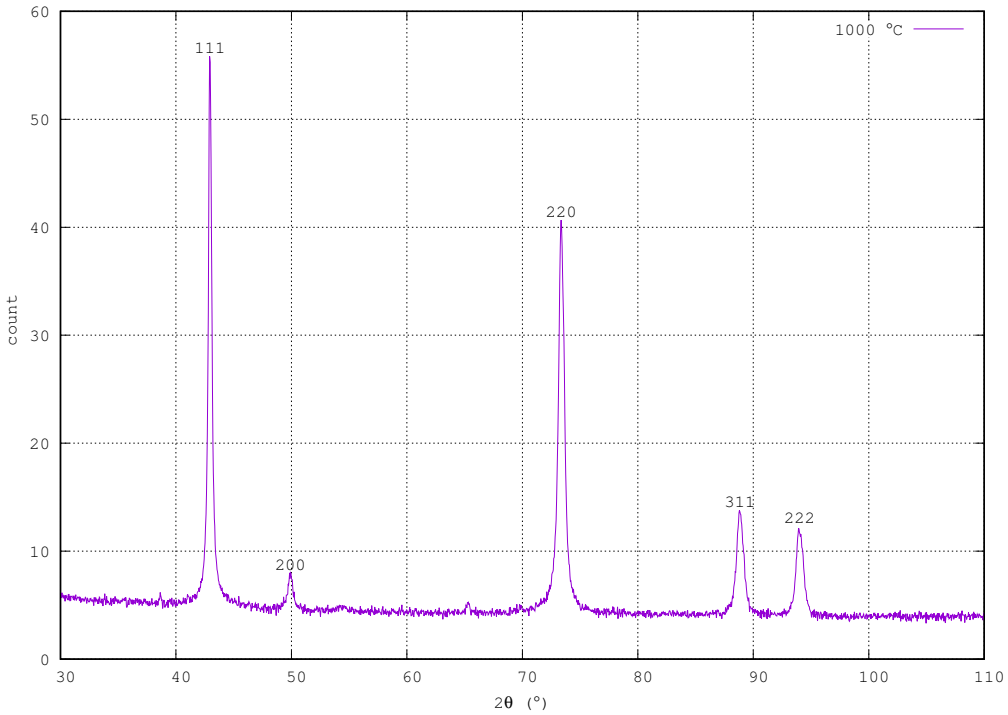

(b) annealed @ 1000°C

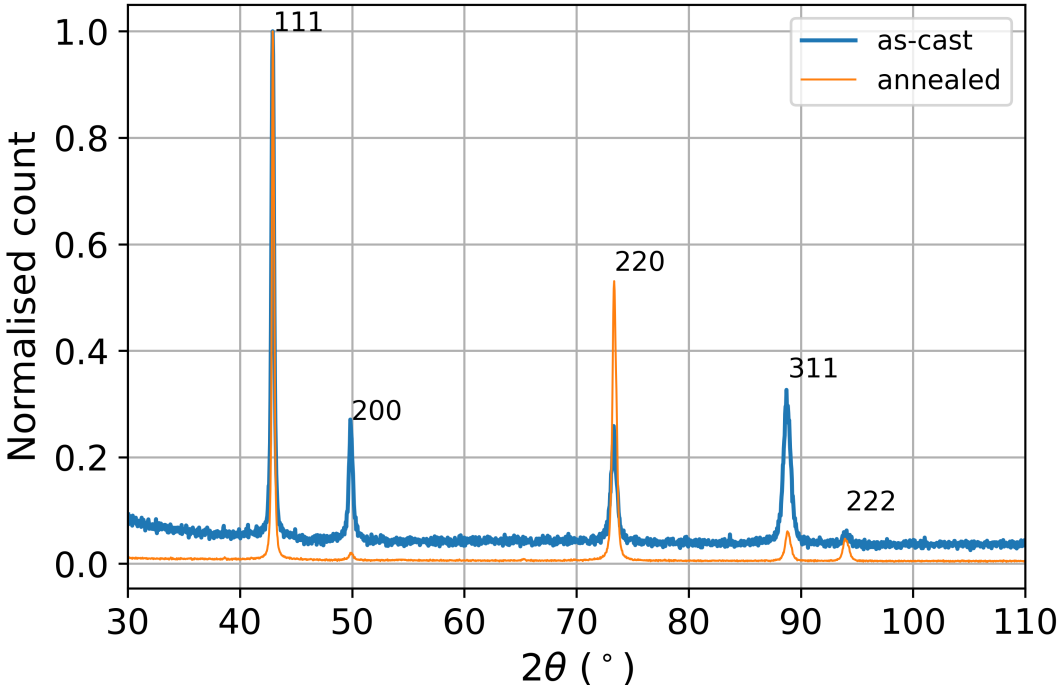

(c) Comparison of normalised XRD data for as-cast and annealed samples

Figure 6.2: XRD of $Pt_7Rh_{23}Ni_{35}Co_{35}$ manufactured @ JMNM

Discussion

The XRD data between the as-cast and annealed industrially manufactured samples seem

to agree as peaks are present in the same positions for the patterns in both samples. The XRD data for the industrially processed samples are also in agreement with the laboratory scale data, especially noting the higher degree of noise in the data from the laboratory processed samples, in comparison with the industrial scale data.

In figure 6.2c we can see that the peaks for (1 1 1) planes maintain the same appearance and general shape following heat treatment whereas the peak corresponding to (2 2 0) becomes sharper and more intense, which may indicate an increase in grain size, reduced strain, or segregation following heat treatment. Conversely, peaks (2 0 0), (3 1 1) and (2 2 2) become smaller and wider indicating a decrease in grain size following heat treatment. It could be that there are some uneven and irregular changes in grain size, leading to complex changes in sample response. In particular, it is likely that the grain size is quite large in both as cast and heat treated conditions, and therefore the XRD assessment probably only samples a relatively limited number of grains; changes in the specific orientation of these grains, as may result from changes in overall grain size, or even from random sample-to-sample variation, could result in changes to peak intensity from differences in the bias of the orientations sampled.

Figures 6.1a and 6.2a look different but the peak positions and identified planes are identical. There are a few possible reasons for the differences. Firstly, the amorphous peak due to the resin mounting medium of the sample measured for figure 6.1a might be overlapping with the signal from the (1 1 1) plane. Also, the amorphous XRD trace might be contributing to the increase of the baseline of the scan above zero. The measurements taken for the industrial scale alloys were over a longer period of time with a longer dwell time at each data point which would result in a higher resolution XRD graph. It is also possible that the differences in the sampled grain population discussed above may be a cause.

Additionally, we also have to consider the differences in the scale of the samples and the contribution this has on the cooling rate, both for as-cast and for the heat treated samples. For these reasons we would expect the granularity of the samples to vary across the 4 different types of sample preparations. Given that the samples have a consistent crystal structure across them as indicated by the identified peaks and that the lattice parameters are fairly consistent between laboratory scale and industrial scale, the alloy $Pt_7Rh_{23}Ni_{35}Co_{35}$ was scaled successfully (i.e. did not show any significantly different phase formation behaviour between the two sets of samples), according to XRD data.

Accounting for all the above mentioned factors there is consistency in the composition across laboratory scale and industrial scale as indicated by XRD. The peaks share the same positions and indicate a FCC crystal phase. XRD data indicates that the composition is a stable FCC crystal phase, at least across the manufacture and heat treatment conditions explored; while not covering every set of conditions, the range which is explored indicates a good probability that the phase seen is a stable one, at least as the majority phase of the alloy.

6.4.1.2 XRF

The quantitative XRF data for the laboratory manufactured alloys are given in tables 6.3a and 6.3b in the as-cast and annealed states, respectively. Likewise, the XRF data for the industry manufactured alloys are presented in figure 6.4a and b.

Laboratory scale

	XRF (.wt%)	at.%	at.%→wt.%
Pt	18.22±0.9	7	17.40
Rh	23.11±1.0	23	30.15
Ni	25.77±0.7	35	26.17
Co	28.5±0.8	35	26.28

(a) As-cast

	XRF (.wt%)	at.%	at.%→wt.%
Pt	20.39	7	17.40
Rh	24.20	23	30.15
Ni	28.52	35	26.17
Co	26.89	35	26.28

(b) Annealed (no absolute error)

Table 6.3: XRF of laboratory scale manufactured $Pt_7Rh_{23}Ni_{35}Co_{35}$

The quantitative XRF data, given in tables 6.3a and 6.3b, show some minor differences in the wt.% distribution across the surfaces measured with XRF, approximately 1-2.5% across all samples. This suggests that there is homogeneity across different samples given the proximity of the wt.% between as-cast and annealed, indicating that the alloy samples solidify homogeneously. However, there are some differences between the intended, nominal composition and the measured composition. This suggests that there might be areas of segregation in the as-cast alloy, or that there may be some loss of certain elements during the manufacturing process (though none of these is expected to display high volatility). The same is observed in the annealed sample, which may indicate that 700°C might not be a high enough temperature to adequately homogenise the sample. Additionally, the lower than expected presence of Rh and the higher than expected presence of Ni is also observed in areas of segregation in the data obtained from EPMA (fig. 6.9, 6.10) where areas of high Ni are lower in Rh in the interdendritic matrix.

However, the distribution of elements is overall consistent across as-cast and heat treated samples. This indicates that the sample solidifies to a stable crystal structure which agrees with the observations made from the XRD data.

Industrial scale

	XRF (.wt%)	at.%	at.%→wt.%
Pt	19.42±0.3	7	17.40
Rh	23.09±0.4	23	30.15
Ni	26.59±0.2	35	26.17
Co	30.64±0.3	35	26.28

(a) As-cast

	XRF (.wt%)	at.%	at.%→wt.%
Pt	19.30±0.3	7	17.40
Rh	23.76±0.4	23	30.15
Ni	26.66±0.2	35	26.17
Co	30.07±0.3	35	26.28

(b) Annealed

Table 6.4: XRF of industrial scale manufactured $Pt_7Rh_{23}Ni_{35}Co_{35}$

Discussion

The agreement of industrial scale XRF wt.% data across the samples characterised is very strong, which is to be expected given that the samples came from the same 1kg ingot, and that the mixing of the elements within this larger ingot should be better than in the smaller scale laboratory melts. The presence of a higher than expected level of Co and lower than expected Rh is inconsistent with the data found from EPMA (fig. 6.11, 6.12), however both areas sampled would have been different and there might be variations in elemental distribution across relatively large distances across the sample. However, there is agreement of laboratory scale and industrial scale results, especially considering that the laboratory scale alloys are two different samples and the ingot cut-offs are the same sample this is further evidence to homogeneous solidification being a feature of this alloy.

6.4.1.3 Optical micrographs

Optical micrographs from this point are presented for the industry manufactured alloys in the as-cast and annealed states. Samples were prepared and etched as described in sections 3.3.1 and 3.3.11, respectively.

Optical micrographs for $Pt_7Rh_{23}Ni_{35}Co_{35}$ are presented in figure 6.3a and b, respectively. In table 6.5 we present a grain size analysis of the visible grains for figures 6.3a and b, respectively.

Note that figures 6.3a and b were obtained using different data acquisition equipment and software, hence the variation in image quality, resolution and magnification.

The grains in figures 6.3 take on a generally elongated shape both in the as-cast and annealed samples.

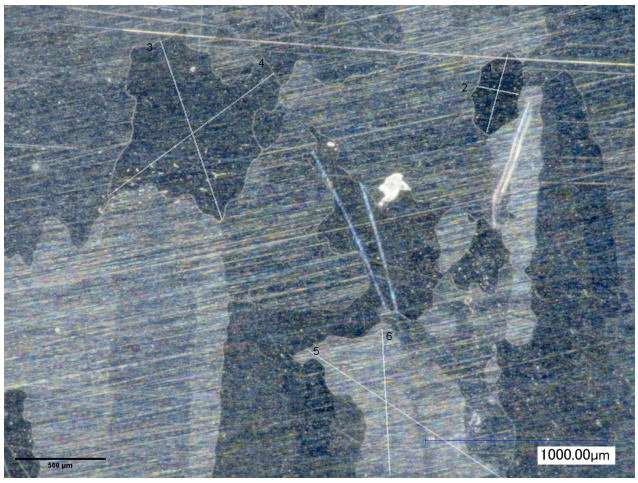

(a) As-cast etched sample optical image taken with a digital optical microscope @ JMNM

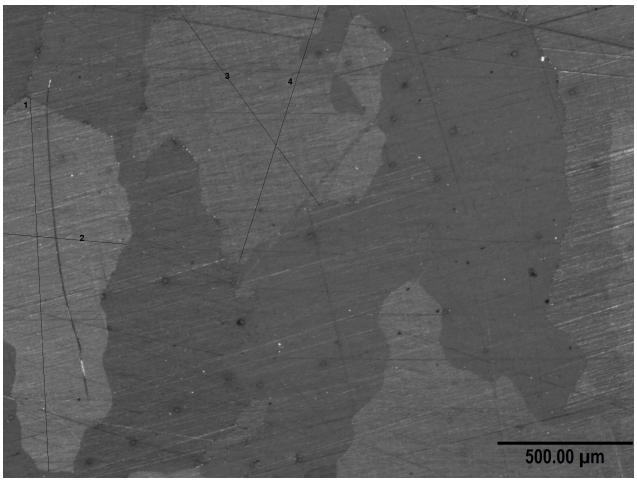

(b) Annealed sample optical image at 5x magnification taken at Sheffield

Figure 6.3: $Pt_7Rh_{23}Ni_{35}Co_{35}$ optical images of industrial scale manufactured as-cast and etched and annealed and etched samples

	Length (µm)
1	203
2	106
3	474
4	521
5	586
6	369

(a) Figure 6.3a grain analysis

	Distance (µm)
1	1381
2	452
3	864
4	986

(b) Figure 6.3b grain analysis

Table 6.5: Grain sizes for the optical micrographs of industrially manufactured $Pt_7Rh_{23}Ni_{35}Co_{35}$

The optical micrographs (fig. 6.3) show that the alloy solidifies with a conventional crystal structure; the as cast grains are columnar, perhaps indicating that the barrier to nucleation is fairly high, or at least that the melt is clean. The annealed grains maintain their size and take on a more equiaxed appearance. However, the grains appear to not be in a consistent configuration across any of the samples, likely to be a result of the inhomogeneous cooling rate, and a non uniform structure as would be expected in any cast ingot.

While the data are not sufficient to draw any conclusions, we can see some evidence that the grain size increases after heat treatment. This would be expected as there is no indication from DSC of any phase changes, and the diffusive motion of atoms at the annealing temperature could permit grain boundary motion and the growth of larger, lower energy grains. The larger grain size after heat treatment is also consistent with the increased sharpness of some peaks in the data presented for XRD. However, in XRD we observed grain size variation according to

the peak widths. While we see that the grains after heat treatment are larger we can also see a high variation in grain size across the samples.

It must be noted that we have insufficient data from optical microscopy, comparing the data we have we can understand the microstrutures presented and what general microstructure the alloy samples and the preparation tend to.

6.4.1.4 SEM-EDX

The SEM data for the laboratory and industrially manufactured alloys are displayed in figures 6.4, and figures 6.5 and 6.6,respectively. The EDX data for the industrially manufactured alloys can be found in figures 6.7 and 6.8, for the as-cast and annealed states, respectively.

Laboratory scale Figure 6.4a is a backscatter image of the s-cast laboratory manufactured $Pt_7Rh_{23}Ni_{35}Co_{35}$, the image shows no distinguishing features however some degree of contrast is noticeable. While figure 6.4b is a secondary electron image of the same alloy and after annealing and etching which shows a "crocodile skin"-like cellular dendritic structure.

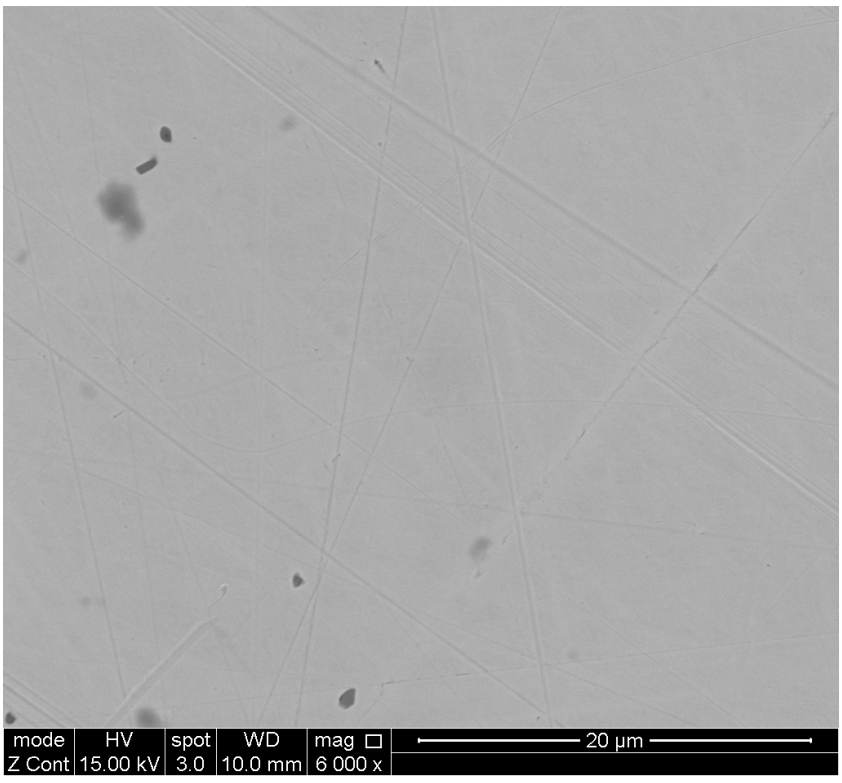

(a) BSE image of as-cast $Pt_7Rh_{23}Ni_{35}Co_{35}$ at 6000x magnification

(b) SE image of etched and annealed $Pt_7Rh_{23}Ni_{35}Co_{35}$ at ≈500x magnification taken at JMNM by Harry Macpherson

Figure 6.4: SEM micrographs of laboratory manufactured $Pt_7Rh_{23}Ni_{35}Co_{35}$ at different surface preparations

	Distance (µm)	approximate dendrite size(µm)
1	315	35
2	190	32
3	174	28
4	161	27

Table 6.7: Figure 6.4b dendrite analysis

Comparing figure 6.4b with the data from EPMA measurements (fig. 6.10) we can see that the intercellular matrix is rich in Nii, which would therefore likely to have been rejected in front of the growing solid. The cellular dendritic structure exposed from the etching will be due to the etchant attacking the Ni rich region of the sample to a greater, i.e. the material with higher levels of Ni, and less of the other elements, is more susceptible to the etchant. Comparing the at.% distribution of the of the constituent elements as shown in the EPMA data, the interdendritic matrix is Ni rich whereas the cell-like dendrites are richer in Pt and Rh, Co is more present in the dendrite matrix but the difference in at.% between dendrite and matrix is only $\tilde{2}$%. Comparing the data with the as-cast EPMA data, the information is similar, i.e. Ni rich matrix, Pt and Rh rich dendrite cells and fairly uniform distribution of Co.

The resolution of the EDX map data collected was not of appropriate degree to reveal anything in addition to or complementary to the EPMA data show below in figures 6.9 and 6.10 so the data has been omitted.

Industrial scale

In figure 6.5 we see two BSE images of as-cast industry manufactured $Pt_7Rh_{23}Ni_{35}Co_{35}$ taken at 100x and 1000x magnification. The dendritic structure in figure 6.5a is mixed into regions of laminar, cellular and 'tree-like' dendrites, whereas the region imaged in figure 6.5b is a very uniform cellular structure.

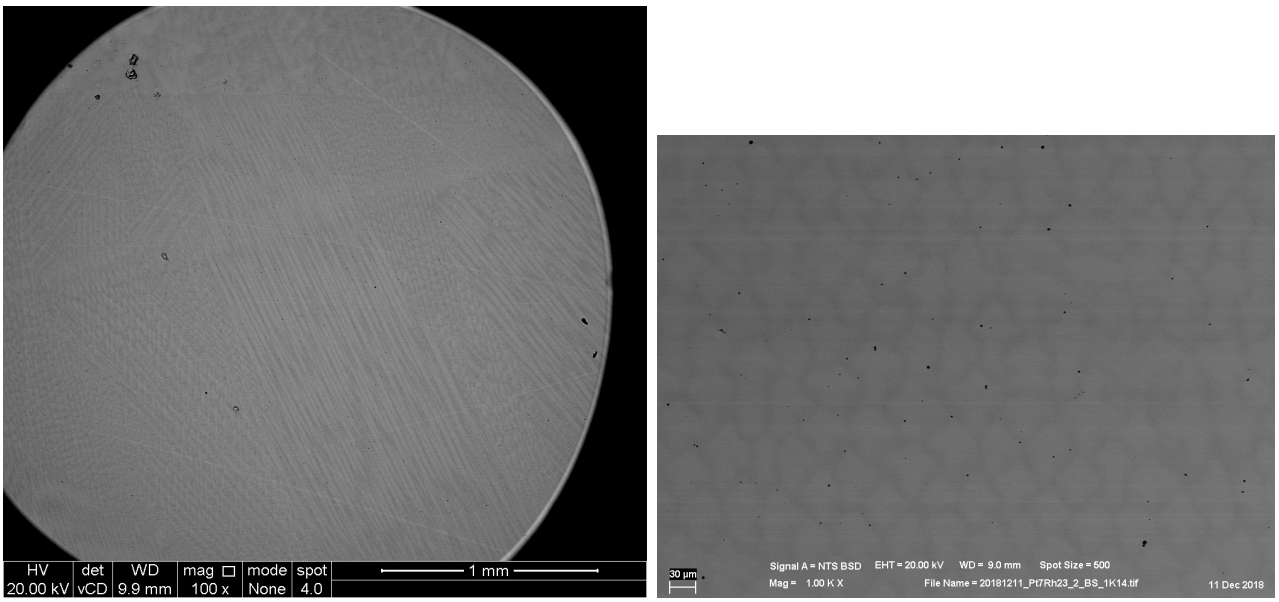

(a) 100x magnification **(b)** 1000x magnification

Figure 6.5: As-cast BSE images of industrially manufactured $Pt_7Rh_{23}Ni_{35}cO_{35}$

The SEM BSE images of the annealed industry manufactured $Pt_7Rh_{23}Ni_{35}Co_{35}$ samples are displayed in figure 6.6. We can see a generally uniform and equiaxed grain structure and some contrast in figure 6.6a, conversely, while smaller grains are noticeable in the area imaged in figure 6.6b they are generally more uniform.

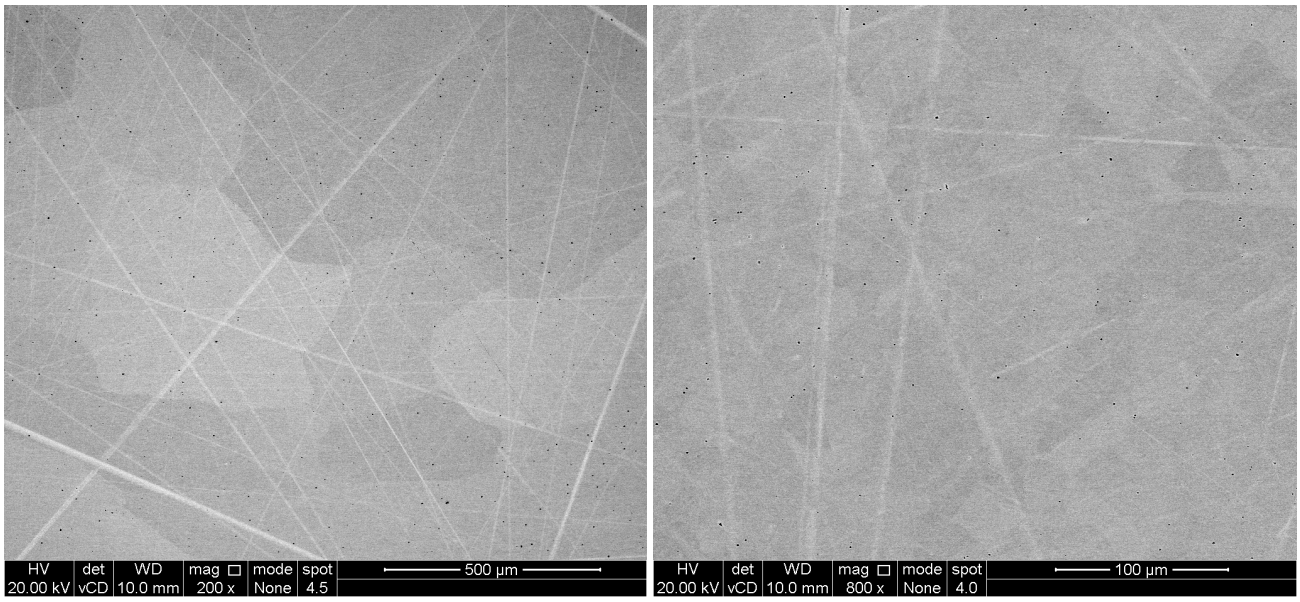

(a) 200x magnification **(b)** 800x magnification

Figure 6.6: Annealed BSE images of industrially manufactured $Pt_7Rh_{23}Ni_{35}cO_{35}$

Comparing the as-cast with the annealed SEM images we can see that heat treatment has apparently removed the cellular dendritic structure that was visible. The as-cast microstructure is composed of large, laminar, grains with varying dendritic structure inside them. It appears that heat treatment might not have affected the grain size particularly, but the grains in the annealed sample do appear to be more equiaxed. Given that the choice of measurement area was not controlled the differences in grain structure might be due to the measurement being performed in a different area of the sample. Furthermore, there may not be a consistent grain size throughout the sample, which might mask changes in the grain size or shape. An inconsistent grain size might be the result of the uneven and uncontrolled cooling inside the furnace after heat treatment. Nevertheless, the cellular dendritic structure with segregation was seen throughout the as cast sample, and is absent in the images of the heat treated sample, indicating that the conclusion that these features are removed by the thermal exposure is robust.

Generally, the elemental distribution in figures 6.7 and 6.8 is uniform with no observable segregation in any of the elements.

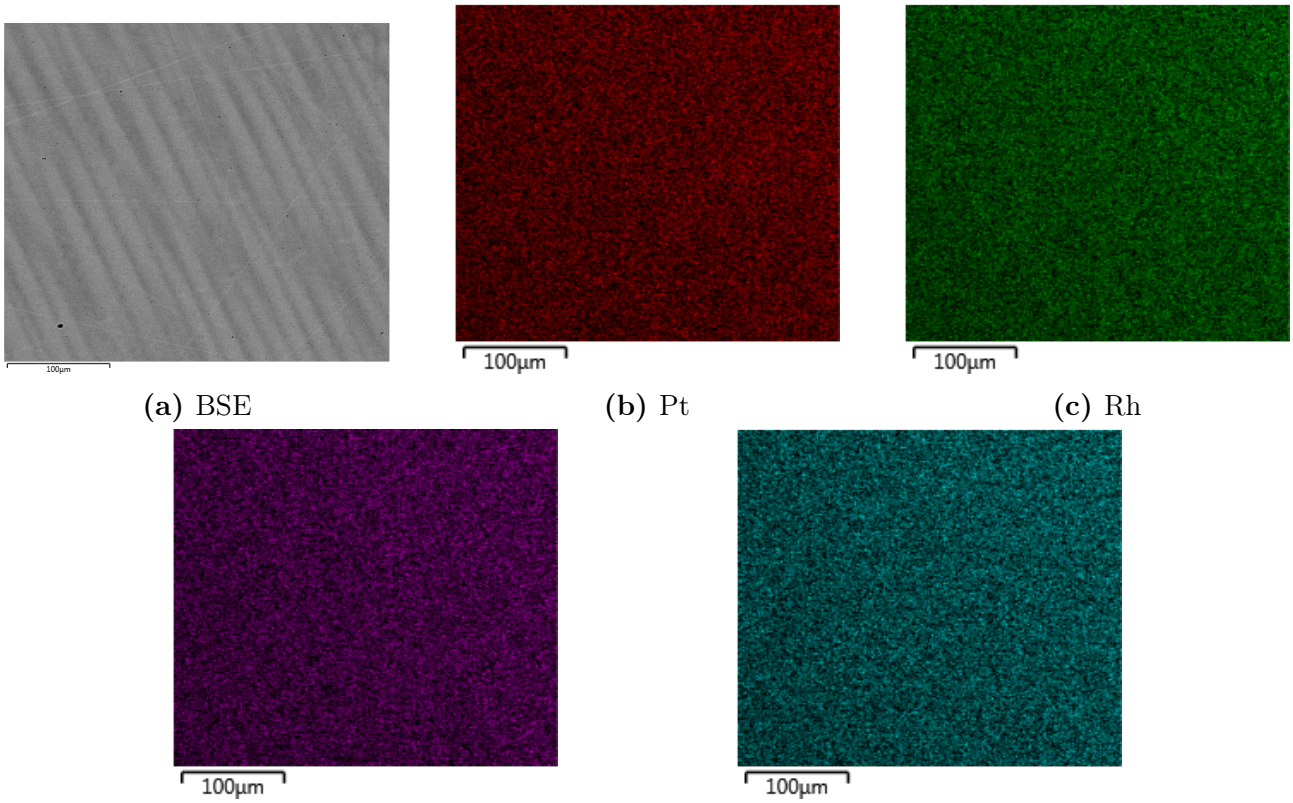

(a) BSE **(b)** Pt **(c)** Rh

(d) Ni **(e)** Co

Figure 6.7: 800x magnification EDX map of as-cast $Pt_7Rh_{23}Ni_{35}Co_{35}$

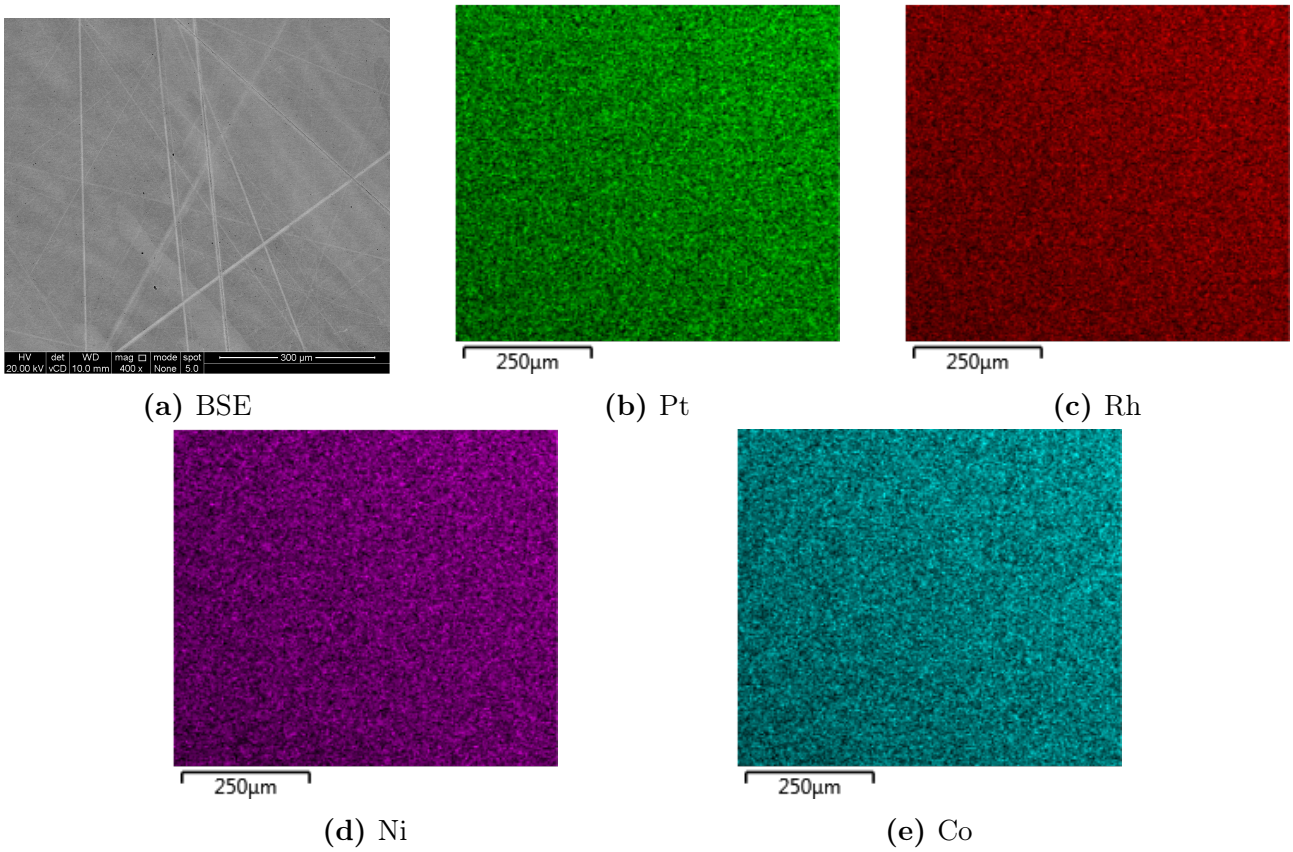

(a) BSE **(b)** Pt **(c)** Rh

(d) Ni **(e)** Co

Figure 6.8: 400x magnification EDX map of annealed $Pt_7Rh_{23}Ni_{35}Co_{35}$

The elemental distribution maps in figures 6.7 and 6.8 show a very uniform distribution of elements across the area imaged, with some small areas of segregation. This contrasts with the BSE images that accompany them as the images would appear to clearly show areas of lighter element concentration and heavier element concentration in the dendrites. It is likely that these differences do exist, but the rapid nature of these maps means that the noise level in the elemental maps is not low enough for the changes in composition to be discerned. The BSE images reveal that there is some segregation across the elemental distribution of the sample.

Comparing the observations with the EPMA data in figures 6.11 and 6.12 we can see that Ni is in fact once again segregating from Pt and Rh, which is not observed in the EDX data, for the reasons discussed above.

6.4.1.5 EPMA

EPMA data for the as-cast and annealed samples of the laboratory and industry manufactured alloys are displayed on figures 6.9 and 6.10, and 6.11 and 6.12.

Laboratory scale

There is noticeable minor segregation in all elements in both as-cast and annealed samples of the laboratory manufactured alloys. We see that there is a uniform distribution in Co and that Ni is visibly segregating from Pt and Rh in the industrially manufacture samples.

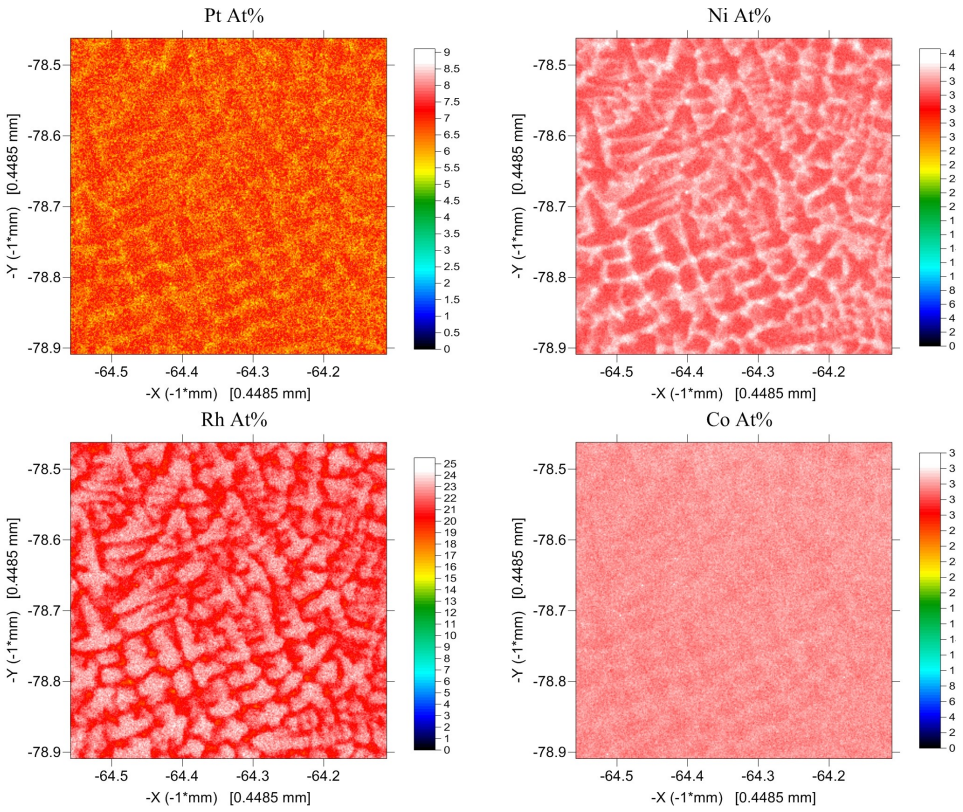

(a) Low magnification

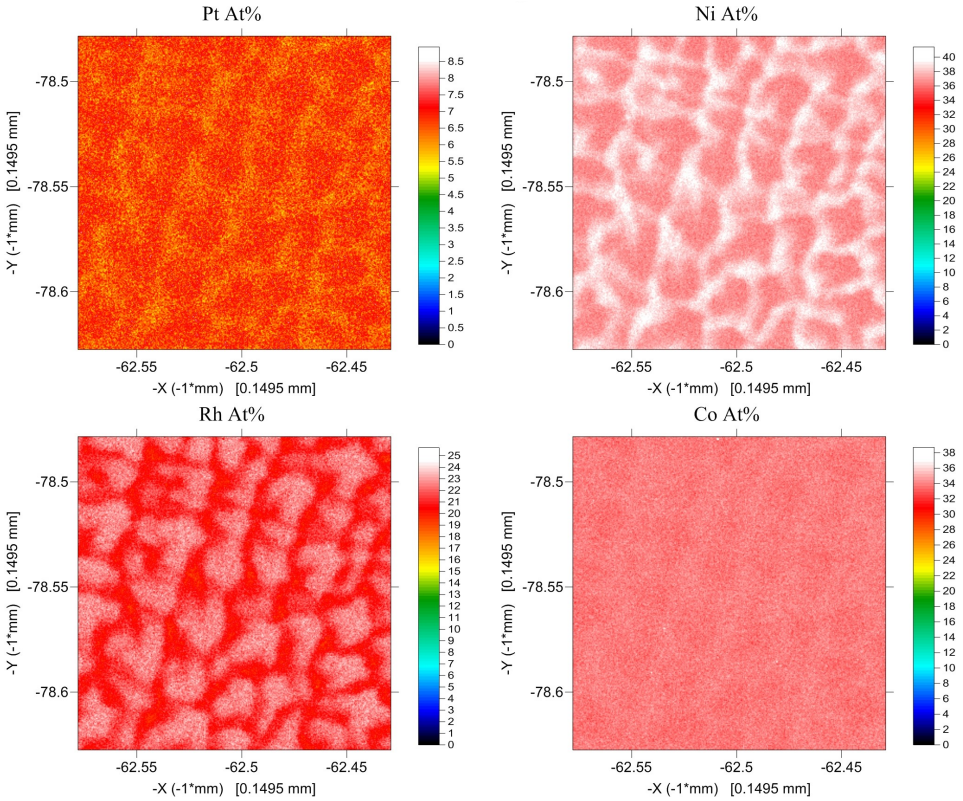

(b) High magnification

Figure 6.9: EPMA of as-cast $Pt_7Rh_{23}Ni_{35}Co_{35}$

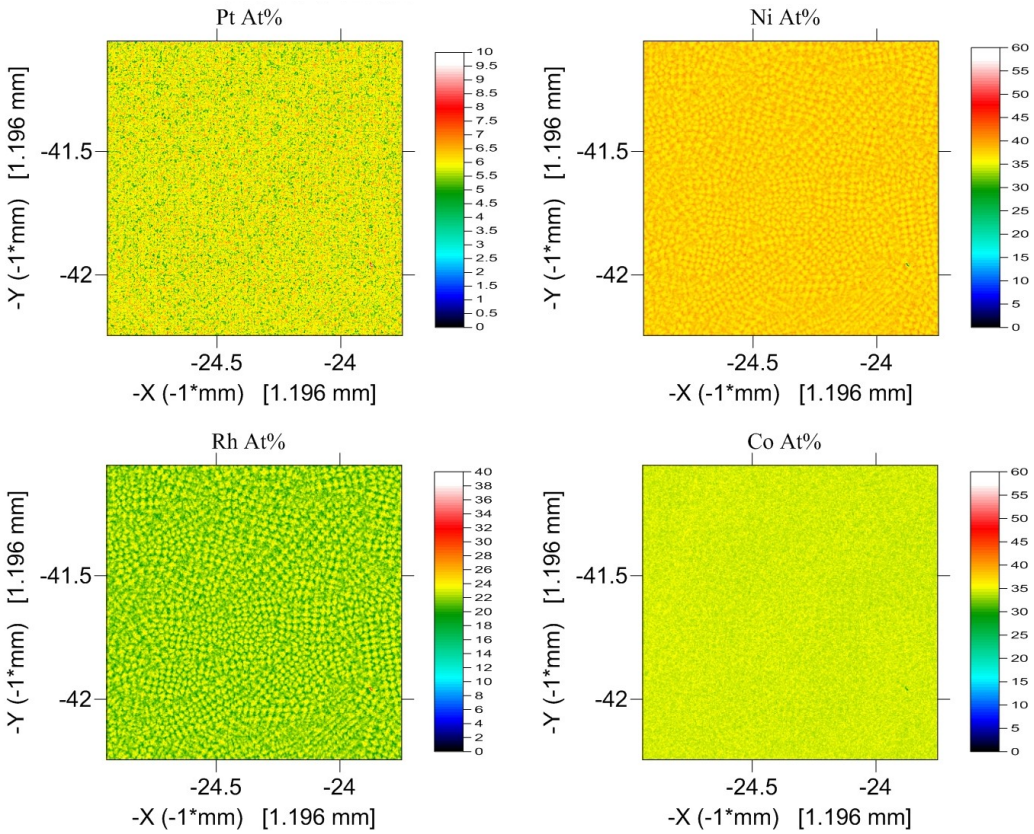

(a) Low magnification

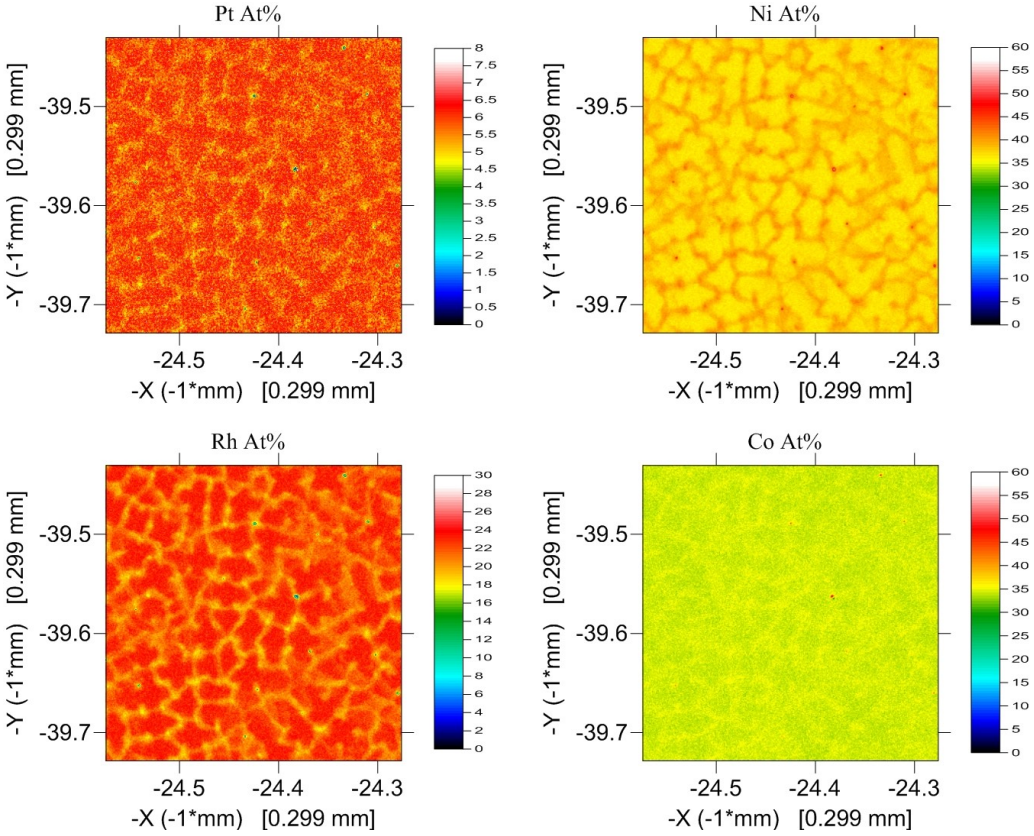

(b) High magnification

Figure 6.10: EPMA of annealed $Pt_7Rh_{23}Ni_{35}Co_{35}$

The EPMA results presented in figure 6.9 show that there is a small degree of segregation of $\approx 2-3\%$ where Ni is segregating away from Pt and Rh. Co appears to be uniformly distributed with a small indication of segregation. The EPMA results for the annealed alloy in figure 6.10 show the Ni and Co to be more even and homogeneous across the alloy. There is strong evidence for the presence of a small PtRh phase although it is not, however, as strong as in the as-cast sample. Overall, the annealed alloy is more homogeneous, as is expected.

Industrial scale

In figure 6.11 we see that Ni is visibly segregating from Pt and Rh, Co, however is uniformly distributed across the imaged area. Similarly, in figure6.12 we see that Ni is segregating from Pt and Rh, there is a small degree of non uniformity in the distribution of Co compared to the as-cast sample.

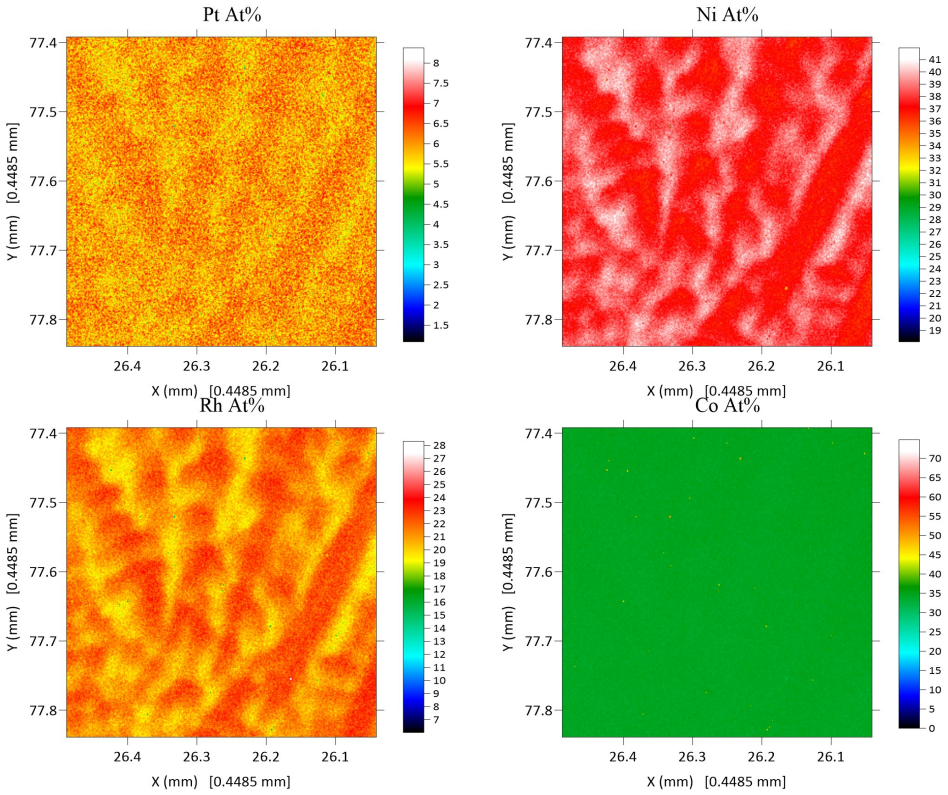

(a) Low magnification

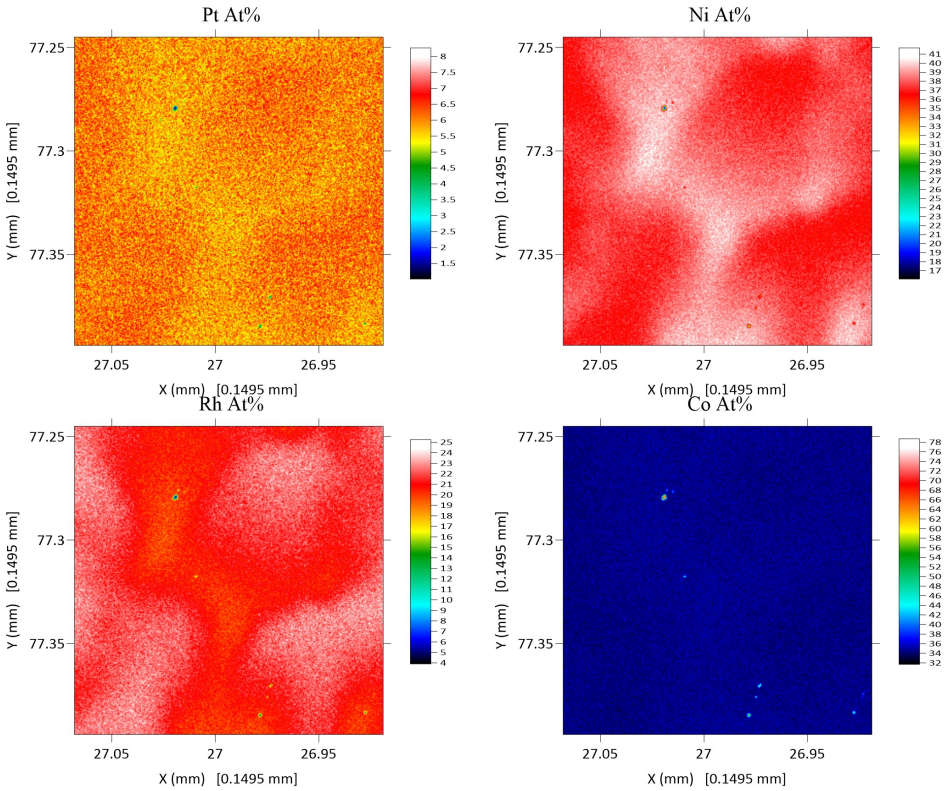

(b) High magnification

Figure 6.11: EPMA of as-cast $Pt_7Rh_{23}Ni_{35}Co_{35}$, samples taken from a 1kg ingot

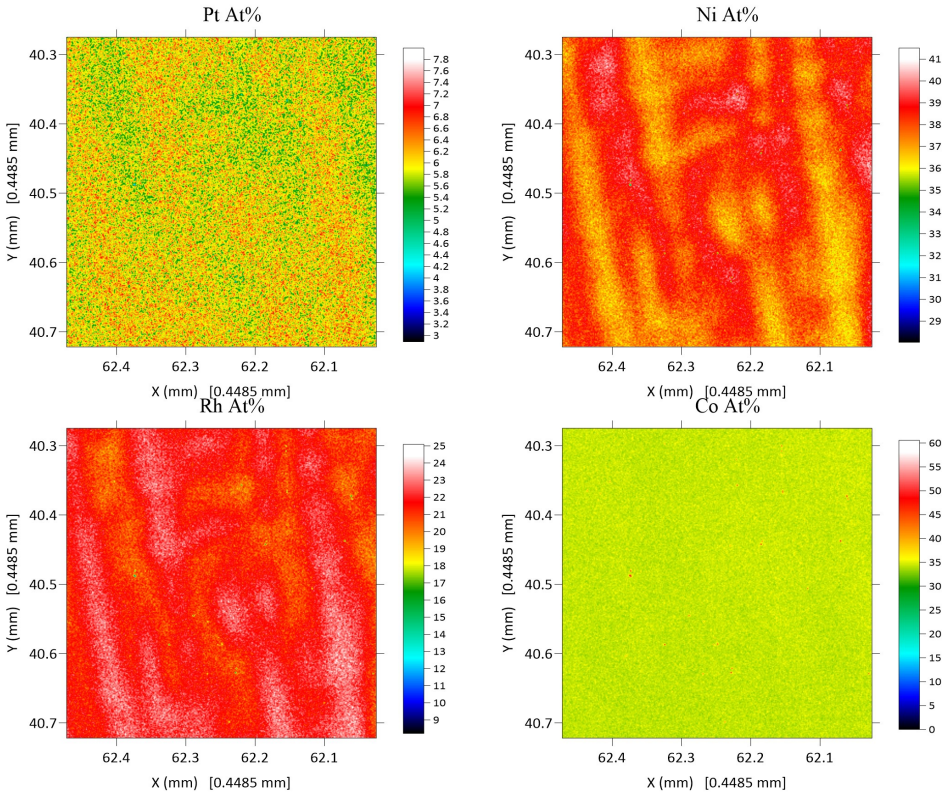

(a) Low magnification

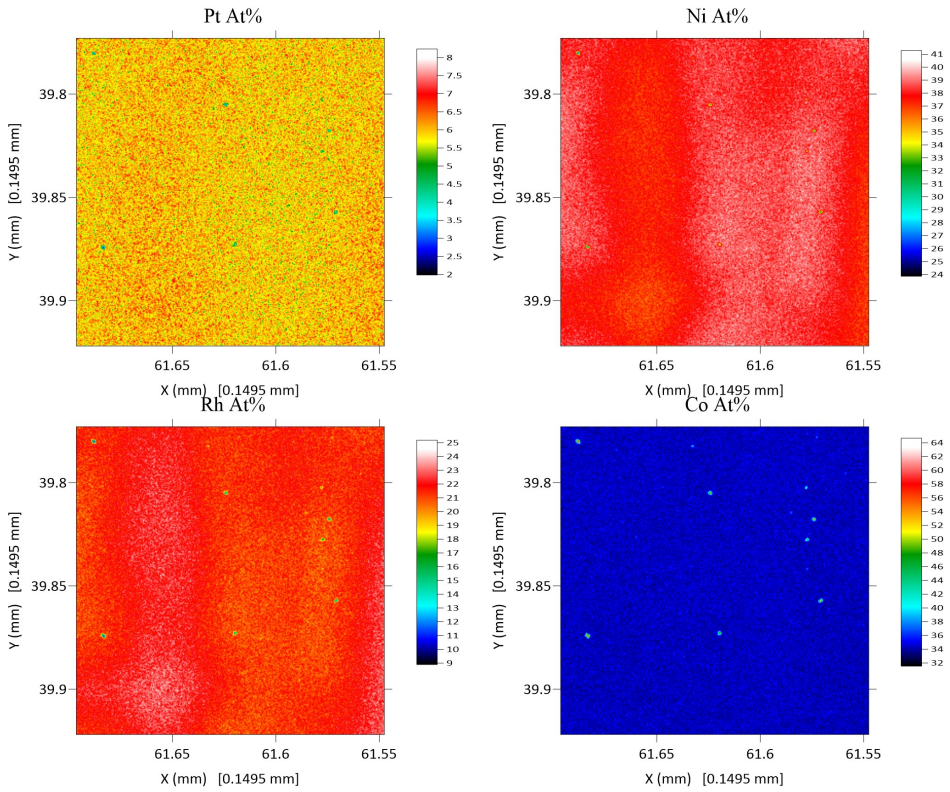

(b) High magnification

Figure 6.12: EPMA of annealed $Pt_7Rh_{23}Ni_{35}Co_{35}$, samples taken from a 1kg ingot

Discussion

EPMA results for the as-cast sample (fig. 6.11) are similar to what was observed in the laboratory scale characterisation, with an evident PtRh segregation into the dendrites, however, Ni is also present at some level in the dendrites. An interaction of what is observed in the laboratory scale data and what is observed here might indicate that the dendrites have a higher content of PtRhNi while Co is very evenly distributed across the samples during cooling and crystallisation. This is not the case for the heat treated samples which are in better agreement with the laboratory scale data, expected as the two alloys will have different casting conditions, but the heat treatment is the same, meaning they should be converging on the same state. A weak PtRh phase separating from Ni, Pt does appear to be distributed more evenly, though.

Evident from figure 6.12, the heat treatment appears to have homogenised the alloy as the range in the distribution of Rh and Ni across the area imaged appears to have decreased after heat treatment. This is not observed in the laboratory scale data. As a result, heat treatment at 1000°C would further promote homogenisation in an industrial setting.

6.4.1.6 Further Discussion of Alloy Structure

Concerning XRD indexing via database match search the alloys do not match any structures from the PDF4+[203] or the COD so the phases are unique to the alloy. The alloys appear to form as a stable FCC crystal structure. The segregation to the interdendritic regions, and its

diminishing extent on heat treatment is suggestive of solidification-induced microsegregation, rather than the formation of distinct phases. Heat treatment at a higher temperature, 1000°C, promotes homogeneity better than at a lower temperature.

Simulation results, discussed earlier support what is observed, that the composition favours a disordered arrangement, as is displayed in figure 4.8. The lattice parameter obtained from averaging over all the lattice parameters obtained for the simulations on disordered structures matches the lattice parameters obtained from physical data to 0.1Å. We can see that DFT calculations can predict a lattice parameter close to values obtained from physical data, which is further evidence that they are able to accurately capture reality in alloys of this type. Additionally, we have to consider that the DFT calculations explored structures where the lattice positions were disordered in the way it would ideally manifest in the real world. However, we have seen from characterisation data that the mixing in the real alloys (at least in the as-cast forms) is far from ideal and we observe areas of segregation. Inspecting the lattice parameters obtained from the ordered structures we can see that they vary across a range of 0.5Å. We obtained a larger lattice parameter from the more highly ordered structure 1. As the order in the ordered structures decreases the lattice parameter tends closer to what is obtained for the ideal mixing case. Given observations of the physical lattice parameter we can see that all the lattice parameters obtained from DFT data match the lattice parameters obtained from real data to 0.1. This might be another indication that our real alloy might follow the ideal mixing case.

Also, surface slab simulations reveal that no particular plane is significantly more favoured than another, which would be consistent with the observation of the mixed grains on the surface of the alloy but further characterisation, such as EBSD along with very careful development of an equilibrium surface, required to confirm this. Simulation results for $Pt_7Rh_{23}Ni_{35}Co_{35}$ have been discussed in sections 4.2 and 4.3.

The differential scanning calorimetry (DSC) of the annealed alloy suggests that the melting point is somewhere above 1400°C and a phase change might be happening between $\approx 1250°C - 1400°C$. TGA suggests that $Pt_7Rh_{23}Ni_{35}Co_{35}$ will not readily oxidise in the presence of O_2 in air, unless exposed to temperatures above 1200°C. When kept at a constant temperature of 1000°C for an hour there is minimal mass gain observed. Where oxidation does occur, O is probably binding to Ni, this can be investigated via XRD, and the simulation methods outlined in section 4.5 and chapter 8. The nanoindentation (tab. 5.3) and Vickers microhardness indentation (tab. 5.4) results suggest a ductile material as the material indents with ease no cracking is observed. Also, this interpretation of the data is in agreement with the qualitative data from the hammering test performed on the laboratory scale as-cast alloy. The mechanical property data across the samples are in agreement which is further evidence for homogeneity across the samples.

6.4.2 $Pt_5Rh_{20}V_5Ni_{35}Co_{35}$

6.4.2.1 XRD

The lattice parameters calculated from the XRD data presented in figures 6.13 and 6.14 are presented in table 6.8.

Manufacture scale	As-cast (Å)	Annealed (Å)
Laboratory	3.627	3.623
Industry	3.647	3.647

Table 6.8: Lattice parameter for $Pt_5Rh_{20}V_5Ni_{35}Co_{35}$ obtained from XRD data sets at different stages of manufacture and processing

Discussion

Comparing the lattice parameters obtained from both scales of manufacture we can see consistency across same scale samples. This evidences that the samples solidify in a stable FCC crystal structure; this is seen to be stronger for the industrially manufactured alloy since it was heat treated at a higher temperature than the laboratory manufactured alloy, 700°C vs. 1000°C. The lattice parameter determined for the industrially manufactured alloy has about a 0.02Å difference from the laboratory manufactured alloys. From this good agreement and unchanging nature of both the structure type and the lattice dimensions, we can see that the alloys solidify to a stable crystal structure. The lattice parameter seems to be closer to the lattice parameters of the FCC constituent elements than the lattice parameters of the BCC constituent elements[223]], which would be expected as the structural arrangement of similar size atoms into a BCC structure will alter the lattice parameter compare to that of an FCC arrangement.

Figures 6.13 and 6.14 show the XRD data collected for the laboratory manufactured samples and industry manufactured samples, respectively. Both figures display the individual data for as-cast and annealed samples and a normalised comparison of the two. We see that the data generally agree with FCC crystal structures with some noticeable minor peaks in all the data. Particularly, in figure 6.13a all peaks have a close double. In general, alloys tend to share the same peak positions in both as cast and industry manufactured.

Laboratory scale

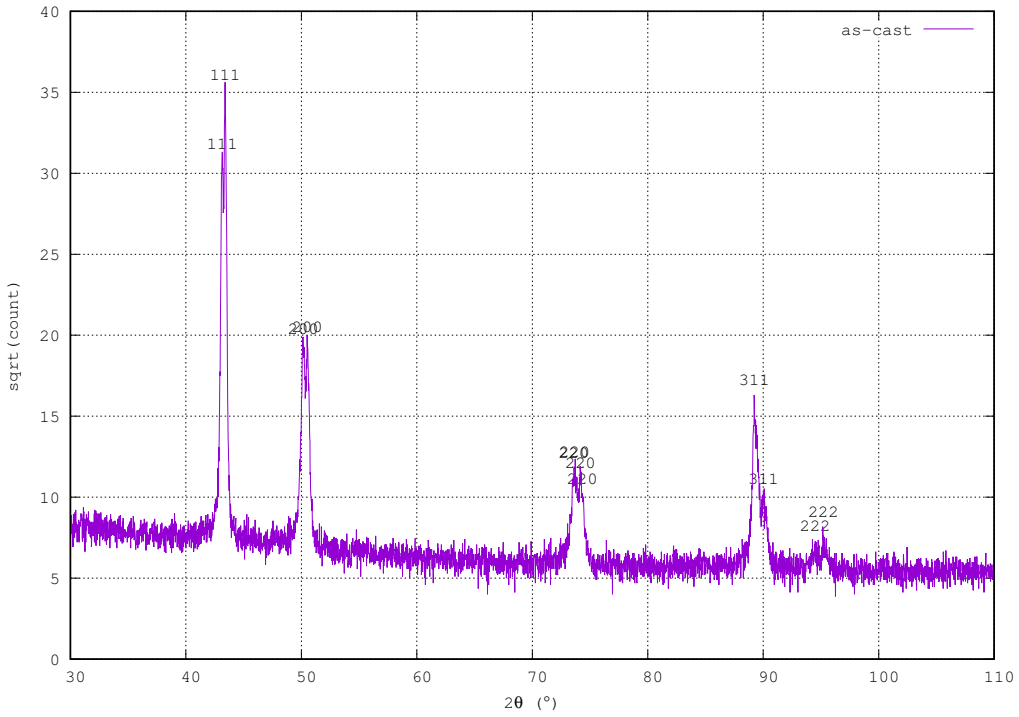

(a) as-cast

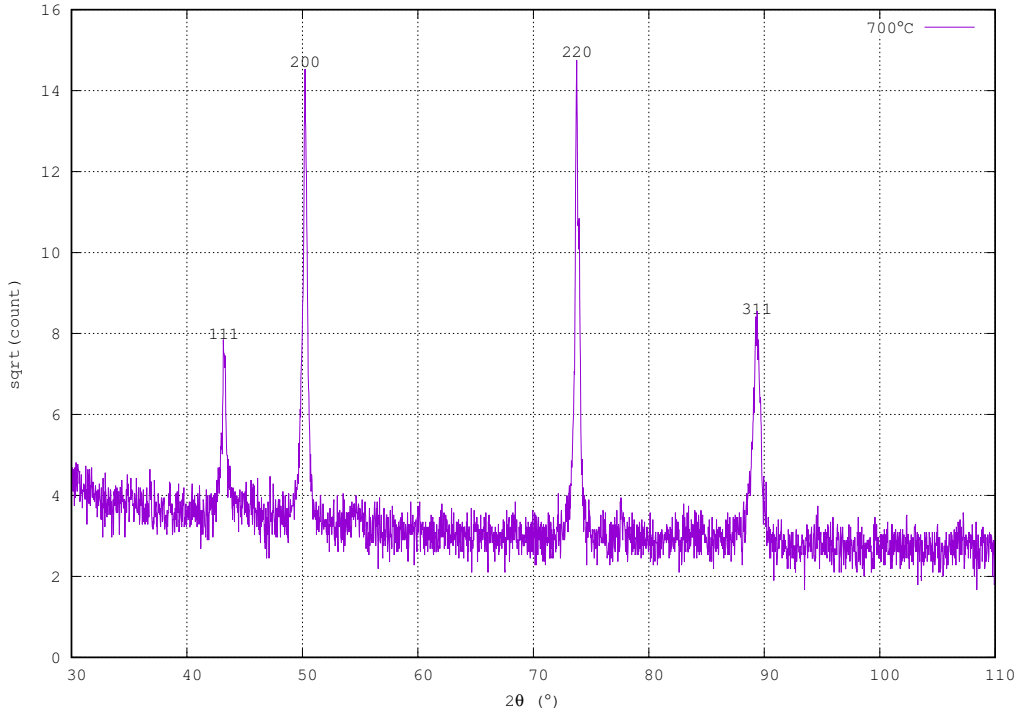

(b) annealed @ 700°C

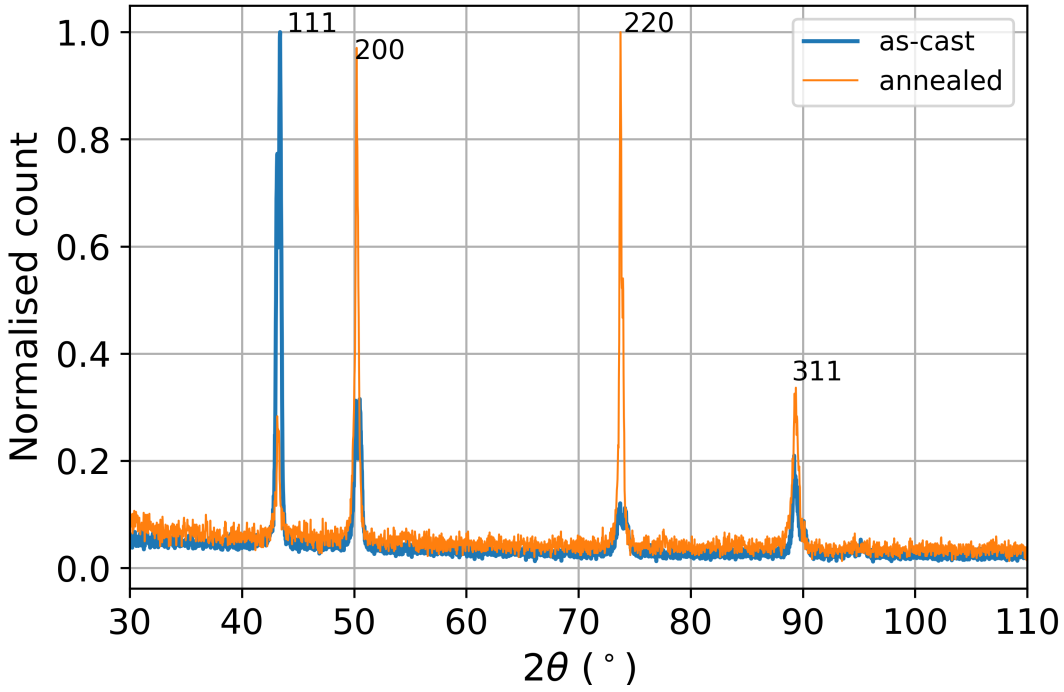

(c) Comparison of normalised XRD data for as-cast and annealed samples

Figure 6.13: XRD of laboratory manufactured $Pt_5Rh_{20}V_5Ni_{35}Co_{35}$

Discussion

The indexed XRD data show that in the as-cast state there are two distinct, but very close peaks for each set of lattice planes and 4 distinct, yet very close peaks for lattice place (2 2 0). The reason for the peaks could be a very similar secondary phase. This could result if certain elements are strongly segregated from the growing phase on solidification, and the phase-separate structure is retained on further cooling. The observations could indicate that the different phases are present in different quantities or regions of different size as the peaks are distinct but vary in height (although no further analysis of this has been performed). These additional phases are not observed in the annealed sample which would imply that annealing homogenised the sample chemically.

Comparing the normalised peak heights between as cast and annealed we can see that there is a change in peak height and width for all planes. This may reflect underlying preferred orientations in the region of the material being analysed, with different orientations dominating in each case, either due to the presence of large grains, or to there being an overall preferred orientation. While it is not possible to say conclusively, either or both of these factors could be affected by heat treatment, although the differences could be simply due to the location where the measurements were made and the material thus sampled. Note that as-cast and annealed samples examined to reach these conclusions are not from the same original cast sample in this case, though the processing of each (except for the heat treatment) used the same conditions.

Industrial scale

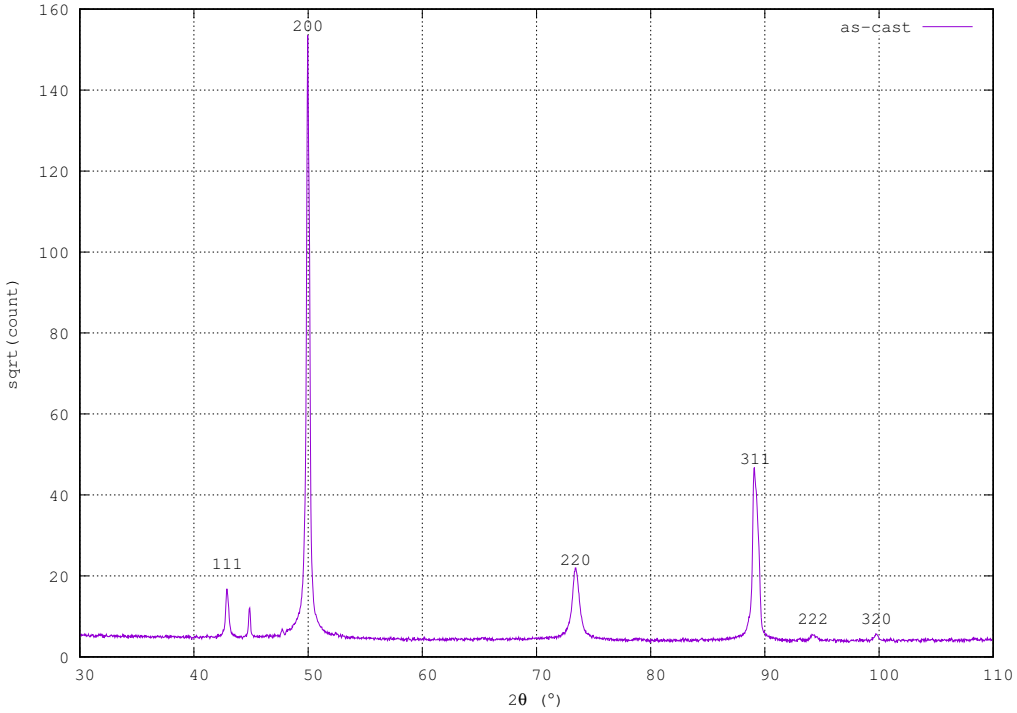

(a) as-cast

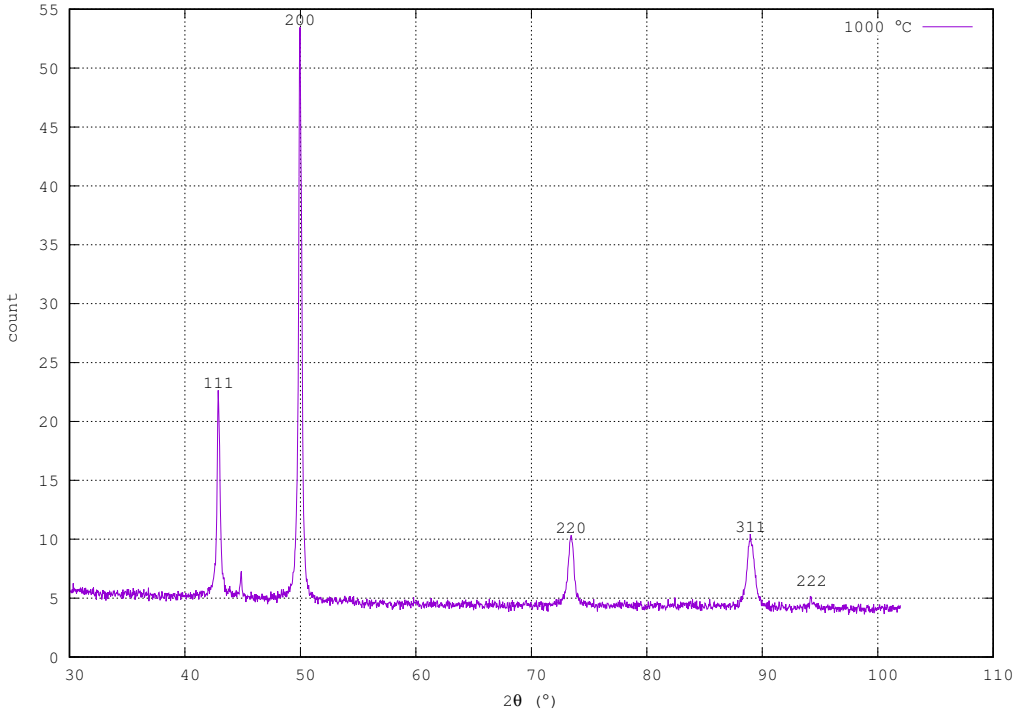

(b) annealed @ 1000°C

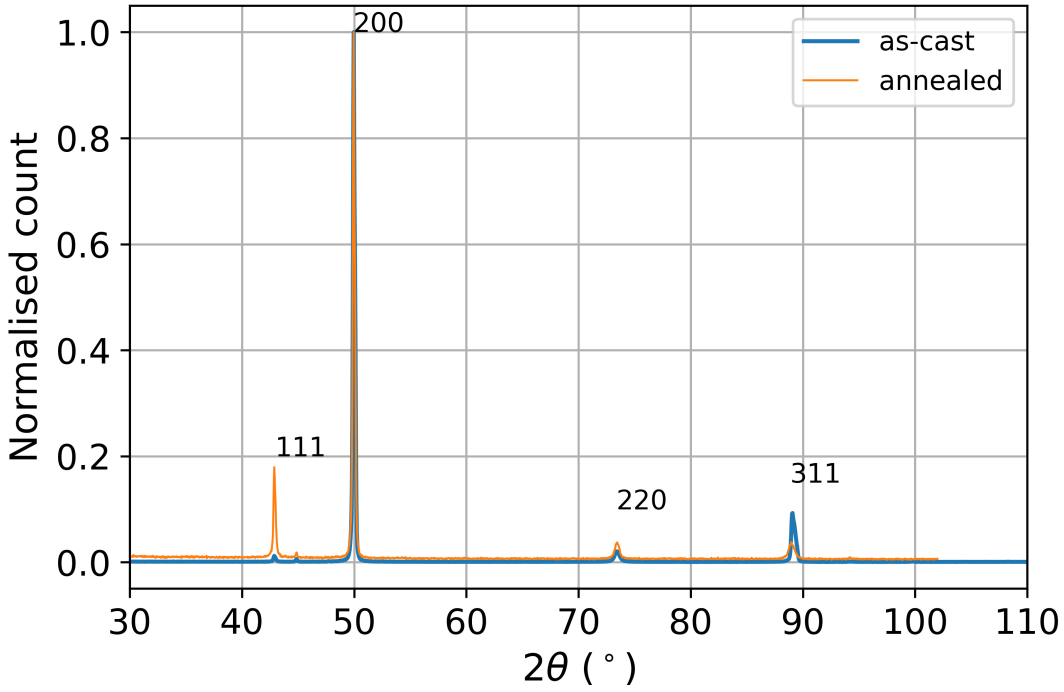

(c) Comparison of normalised XRD data for as-cast and annealed samples

Figure 6.14: XRD of $Pt_5Rh_{20}V_5Ni_{35}Co_{35}$ manufactured @ JMNM

Discussion

The XRD data for as-cast and annealed conditions in this alloy appear very similar. Both exhibit an unidentified peak which does not appear to part of the main (indexed) series of peaks in the patter. This peak is located at approximately 44°. This could be due to a very weakly present secondary phase or an impurity carried over from the manufacturing procedure. From the indexed peaks, the lattice parameter calculated is the same for these two samples, which is to be expected due to the samples being from the same 1kg ingot.

The modulus of elasticity (tab. 5.3) increases after heat treatment, although only by a very small degree, which (although distinguishable with the calculated error for the tests) is probably not a significant change. The hardness (tab. 5.4) decreases, as would be generally expected after a heat treatment, giving the opportunity for grain growth and reduction of dislocation density.

The intensity of different peaks varies in the normalised XRD patterns, which probably relates to changes in the overall texture of the microstructure examined, either from sampling location to sampling location, or possibly of the material on a more global scale, due to the heat treatment.

6.4.2.2 XRF

The quantitative XRF data for the laboratory manufactured alloys are given in tables 6.9a and 6.9b in the as-cast and annealed states, respectively. Likewise, the XRF data for the

industry manufactured alloys are presented in figure 6.10a and b.

Laboratory scale

	XRF (.wt%)	at.%	at.%→wt.%
Pt	15.36	5	13.17
Rh	20.59	20	27.8
V	3.06	5	3.44
Ni	29.50	35	27.74
Co	31.26	35	27.85

(a) As-cast (no absolute error)

	XRF (.wt%)	at.%	at.%→wt.%
Pt	14.64	5	13.17
Rh	21.86	20	27.8
V	2.97	5	3.44
Ni	30.05	35	27.74
Co	30.48	35	27.85

(b) Annealed (no absolute error)

Table 6.9: XRF of laboratory scale manufactured $Pt_5Rh_{20}V_5Ni_{35}Co_{35}$

Industrial scale

	XRF (.wt%)	at.%	at.%→wt.%
Pt	14.96±0.3	5	13.17
Rh	21.29±0.3	20	27.8
V	3.06±0.1	5	3.44
Ni	28.28±0.2	35	27.74
Co	32.11±0.3	35	27.85

(a) As-cast

	XRF (.wt%)	at.%	at.%→wt.%
Pt	14.79±0.3	5	13.17
Rh	21.49±0.3	20	27.8
V	3.19±0.1	5	3.44
Ni	28.29±0.2	35	27.74
Co	32.23±0.3	35	27.85

(b) Annealed

Table 6.10: XRF of industrial scale manufactured $Pt_5Rh_{20}V_5Ni_{35}Co_{35}$

Discussion

The XRF data across as-cast and annealed for both scales of manufacture is presented in tables 6.9 and 6.10. The data are consistent with each other, varying only slightly in wt.% measured for each element. This implies that the composition scales well and that in both scales the resulting alloys are fairly homogenous in the as-cast state.

In both scales of manufacture and both as-cast and heat treated states we observe a higher wt.% in Ni and Co and a lower wt.% in Rh than the nominal, designed composition. Comparing this with EPMA results in figures 6.25, 6.25b and 6.26b we can see that areas of higher Ni presence, i.e. the interdendritic matrix, are complemented by areas of lower Rh presence. Likewise, there is a higher concentration of Rh and a lower Ni concentration in the dendrites. However, the same observation cannot be made about Co concentration, which is very uniformly distributed across the area imaged, and it would in any case not be expected that these very small scale differences, seen over the order of microns in the EPMA, would have an influence on the XRF results, where the examined zone is of the order of millimetres.

Overall, we observe a consistent elemental distribution across different samples. However, we can see that it is quite different from the expected elemental distribution. The difference in expected elemental distribution and measured might be due to macrosegregation across the scale of the sample, or possibly due to loss of certain elements during the manufacturing process. This could occur in a relatively consistent manner by volatilisation of the elements with higher vapour pressure for example. Elements that are less prone to evaporation would in the process become enriched in the final alloy.

6.4.2.3 Optical micrographs

Optical micrographs for $Pt_5Rh_{20}V_5Ni_{35}Co_{35}$ are presented in figure 6.15a and b, respectively. In table 6.11 we present a grain size analysis of the visible grains for figure 6.15a and b, respectively.

Note that figures 6.15a and b were obtained using different data acquisition equipment and software, hence the variation in image quality, resolution and magnification.

The grains look elongated and similar in size across both images.

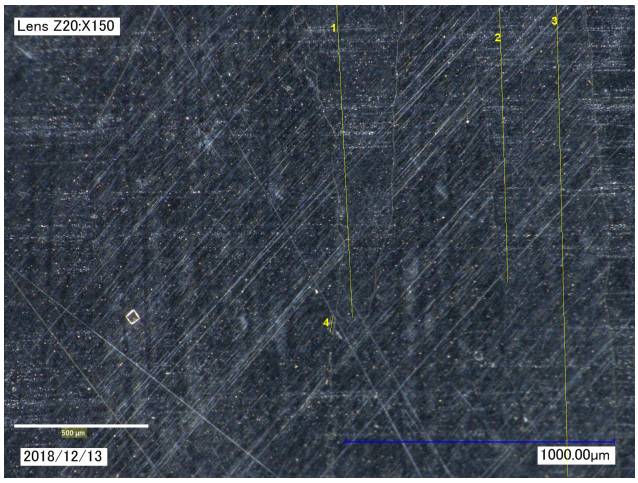

(a) As-cast etched sample optical image taken with a digital optical microscope @ JMNM

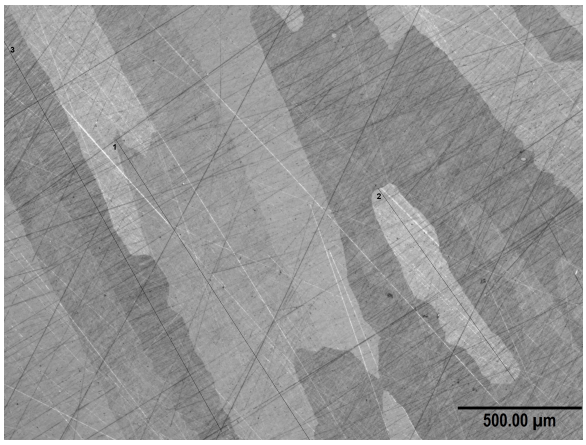

(b) Annealed sample optical image at 5x magnification taken at Sheffield

Figure 6.15: $Pt_5Rh_{20}V_5Ni_{35}Co_{35}$ optical images of as-cast and etched and annealed and etched samples

	Length (µm)
1	1166
2	1021
3	1757
4	57

(a) Figure 6.15a grain analysis

	Distance (µm)
1	1440
2	953
3	1802

(b) Figure 6.15b grain analysis

Table 6.11: Grain sizes for the optical micrographs for industrially manufactured $Pt_5Rh_{20}V_5Ni_{35}Co_{35}$

Discussion

Optical microscopy data shows that the heat treatment did little to change the grain structure or alignment. In both as-cast and annealed states the grains are elongated but have an irregular orientation in reference to other grains.

As for other alloys, there are some changes in peak intensity in the XRD traces, which are likely to be due to differences in the particular grains being assessed in each case; the structure on the other hand remains the same on heat treatment, consistent with the absence of any observed change in the microstructure. There is a slight, and probably not significant, change in the elastic modulus, which is also in line with this alloy being largely unaltered by the heat treatment performed.

Of course, we do not have enough optical micrograph data to be able to draw firm conclusions from. However, comparing with data from XRD and nanoindentation we can see what the microstructure might tend to, and that it is broadly stable under the conditions explored.

6.4.2.4 SEM-EDX

The SEM backscatter data for the as-cast and annealed laboratory manufactured alloys are displayed in figures 6.16a and b, and figures 6.18a, and b, respectively. For the industrially manufactured alloys, the SEM backscatter image data are displayed in figures 6.20 for the as-cast sample and 6.21 for the annealed sample.

The EDX data for the laboratory manufactured alloys can be found in figures 6.17 and 6.19, for the as-cast and annealed states, respectively. EDX data for the industry manufactured alloy are displayed in figures 6.22 and 6.23 for as-cast and annealed, respectively.

Laboratory scale

In figure 6.16a we see a bse image of as-cast $Pt_5Rh_{205}Ni_{35}Co_{35}$ with some visible dendrites which take on a cellular structure. Figure 6.16 is quite uniform without any distinguishable features that are associated with microstructure.

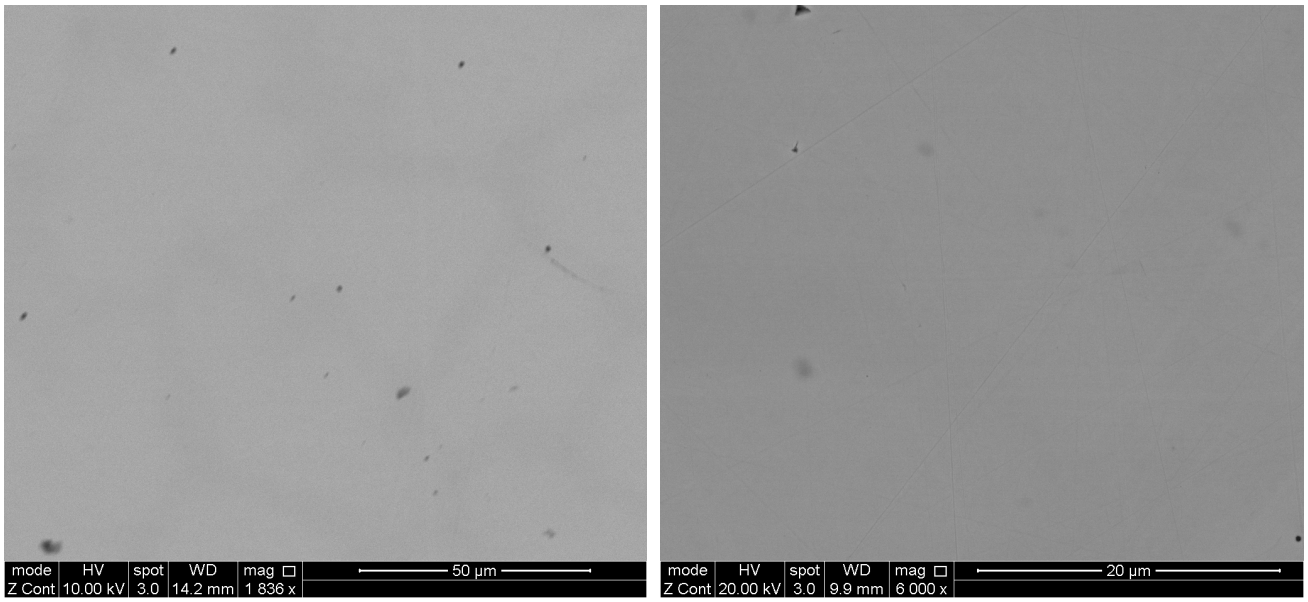

(a) BSE image of as-cast $Pt_5Rh_{20}V_5Ni_{35}Co_{35}$ at ≈1800x magnification

(b) BSE image of as-cast $Pt_5Rh_{20}V_5Ni_{35}Co_{35}$ at 6000x magnification

Figure 6.16: BSE images of as-cast$Pt_5Rh_{20}V_5Ni_{35}Co_{35}$

In figure 6.17 we see an edx map of as-cast $Pt_5Rh_{205}Ni_{35}Co_{35}$. The constituent elements in the alloy appear to be uniformly distributed across the imaged area, however we can see some segregation visible in Pt and V.

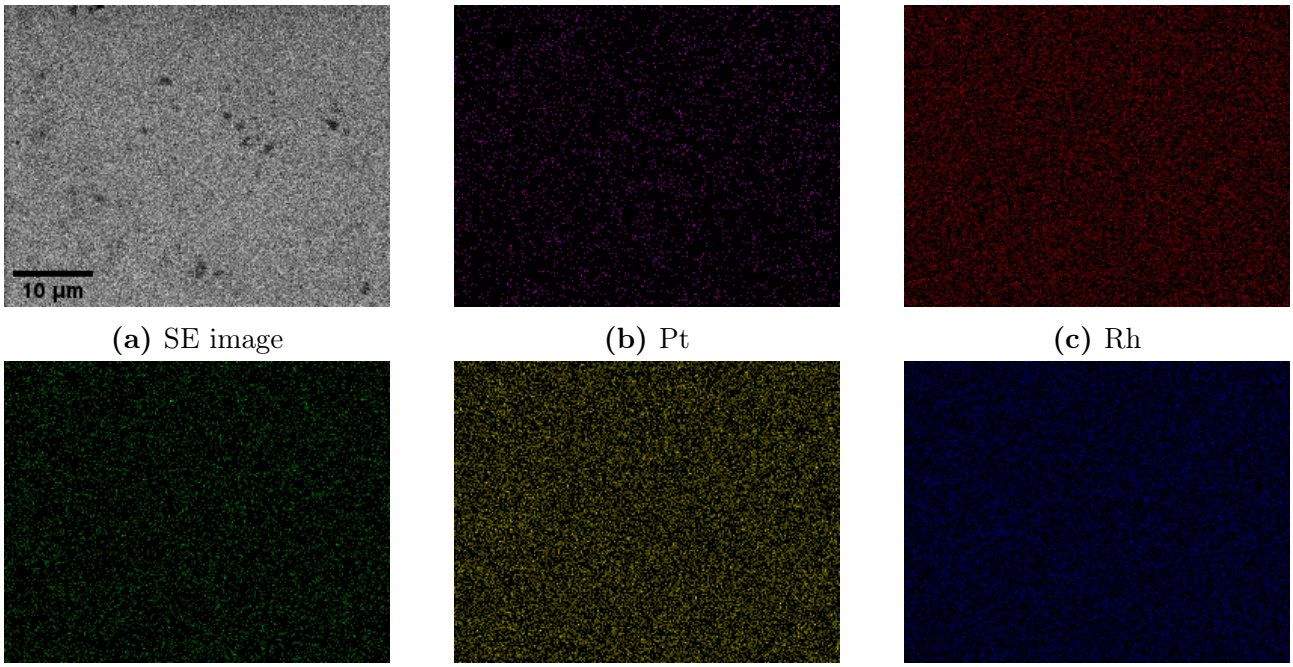

(a) SE image **(b)** Pt **(c)** Rh

(d) V **(e)** Ni **(f)** Co

Figure 6.17: EDX map of as-cast $Pt_5Rh_{20}V_5Ni_{35}Co_{35}$ taken at 6000x magnification

Figures 6.18a and b show bse images of annealed $Pt_5Rh_{205}Ni_{35}Co_{35}$. In both a and b we see a very distinctive regular, cellular dendritic pattern.

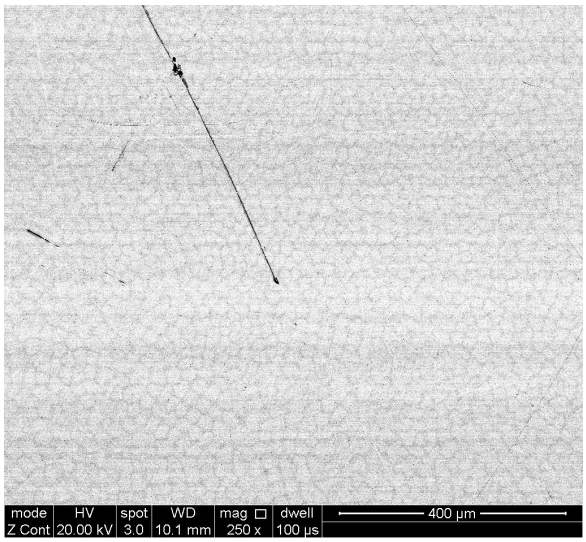

(a) BSE image of annealed $Pt_5Rh_{20}V_5Ni_{35}Co_{35}$ at 250x magnification

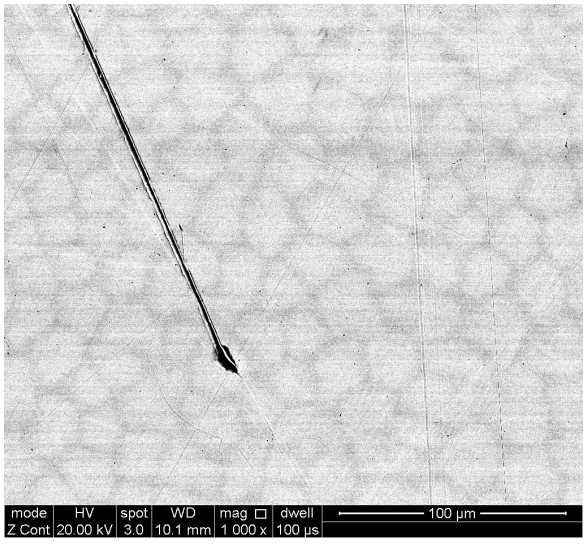

(b) BSE image of annealed $Pt_5Rh_{20}V_5Ni_{35}Co_{35}$ at 1000x magnification

Figure 6.18: BSE images of annealed $Pt_5Rh_{20}V_5Ni_{35}Co_{35}$

The EDX map of annealed $Pt_5Rh_{205}Ni_{35}Co_{35}$ is in figure 6.19. We see the same cellular dendritic pattern in the secondary electron image. We see that there is some segregation in Pt and V compared to the other elements where the distribution is generally more uniform.

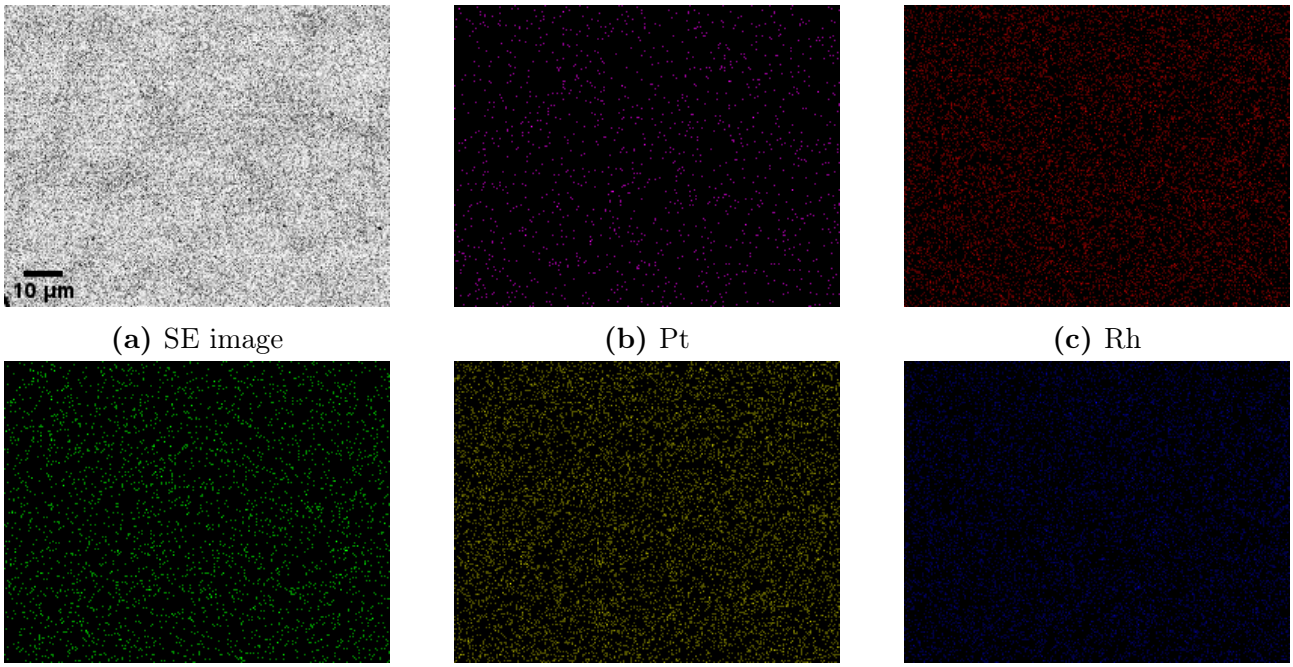

(a) SE image **(b)** Pt **(c)** Rh

(d) V **(e)** Ni **(f)** Co

Figure 6.19: EDX map of annealed $Pt_5Rh_{20}V_5Ni_{35}Co_{35}$ taken at 3000x magnification

Discussion

Both as-cast and annealed samples appear very uniform under SEM-BSE imaging (fig. 6.16 and 6.18). The as-cast samples, in particular, appear to show a very uniform microstructure, although that could also be due to the high magnification used in collecting the data, and the small region observed as a result. However, the annealed sample is displaying a very regular pattern of hive-like matrix, with a crocodile skin pattern where we can see some segregation. There appears to be a higher concentration of heavier elements in the cells and a higher concentration of lighter elements in the matrix between them, as the cells appear lighter in colour in the backscattered electron images. Comparing these observations to the EPMA data we can see that they agree, there is a higher concentration of Ni in the matrix and higher concentration of Rh and Pt in the cells. Likewise, the EDX data for the as-cast sample, displayed in figure 6.17, shows generally uniform distributions of all elements across the imaged surfaces with some segregation observed, particularly in V and Pt. This sparseness in the signal collected for V and Pt might be due to the lower content of V and Pt in the alloy, coupled with the relatively short collection times, as discussed before. Better EDX maps were required to explore the segregation. Longer collection times would produce results with higher confidence, however in this work the assessment of the compositional variation is made based on the EPMA results.

Industrial scale

Figures 6.20 and 6.21 show BSE images of as cast and annealed industry manufactured $Pt_5Rh_{20}V_5Ni_{35}Co_{35}$. We see in figure 6.20 that the dendrites follow a 'tree'-like pattern mixed with a more regular cellular pattern. In figure 6.21 we see can see the grains of the alloy with different contrasts but no dendrites.

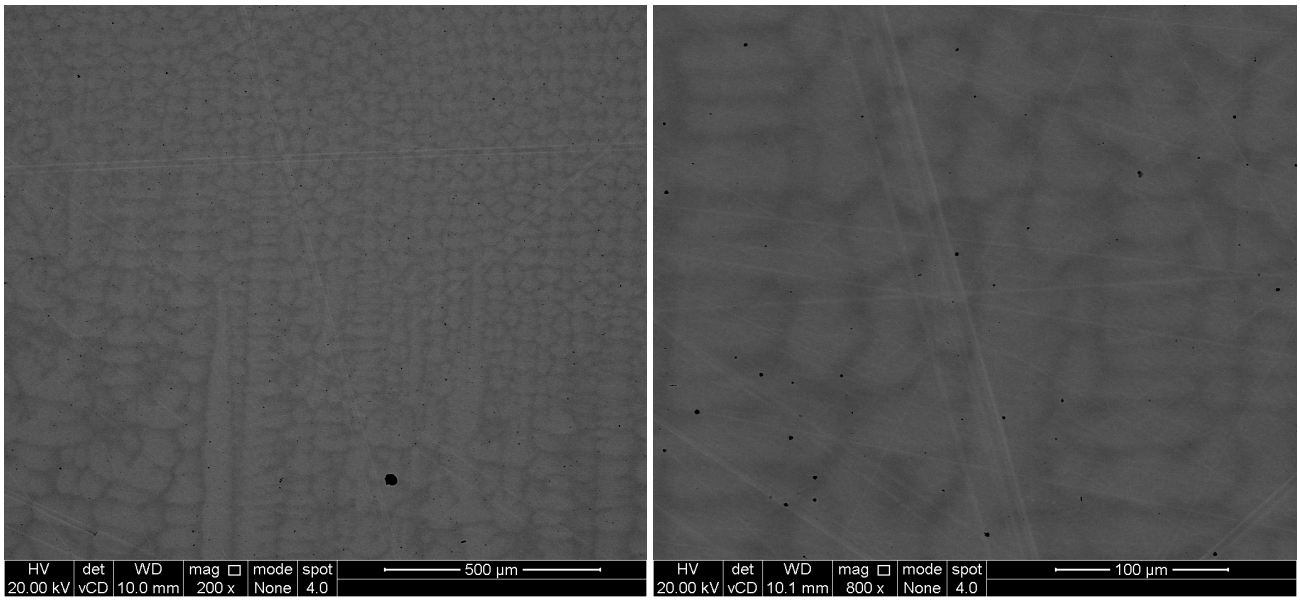

(a) 200x magnification **(b)** 800x magnification

Figure 6.20: As-cast BSE images of industrially manufactured $Pt_5Rh_{20}Vi_5Ni_{35}Co_{35}$

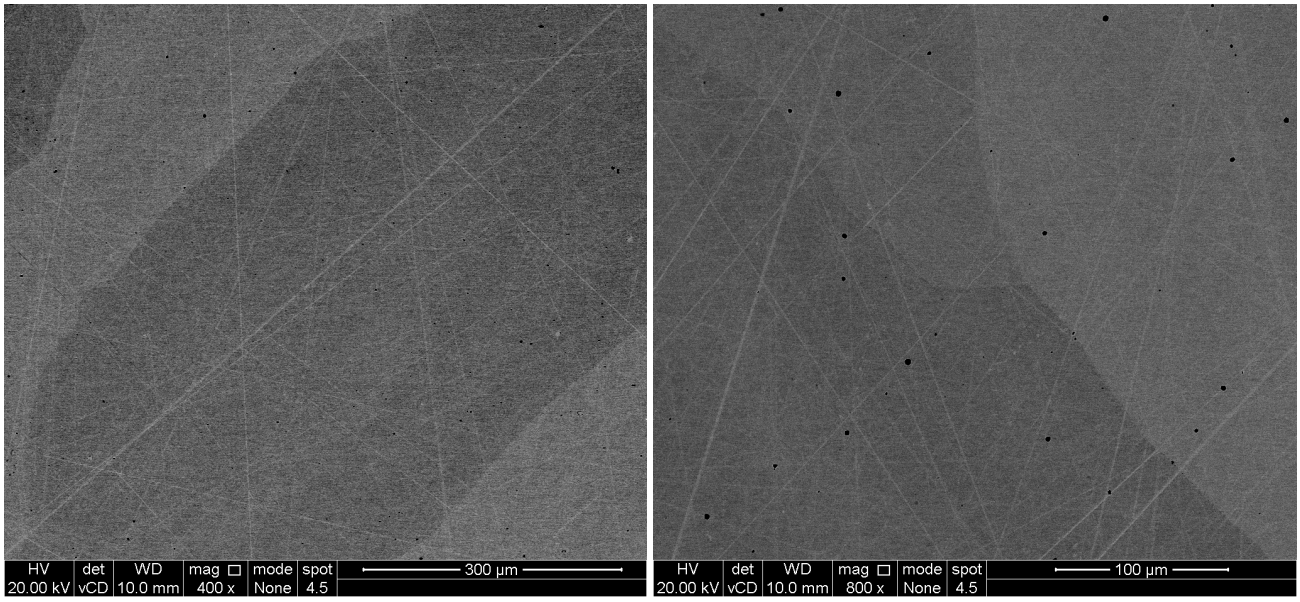

(a) 400x magnification **(b)** 800x magnification

Figure 6.21: Annealed BSE images of industrially manufactured $Pt_5Rh_{20}Vi_5Ni_{35}Co_{35}$

In figure 6.22 we see an EDX map of as-cast industry produced $Pt_5Rh_{20}V_5Ni_{35}Co_{35}$. The elemental distribution in the maps fairly uniform with some very small areas of elemental concentration. Similarly the elemental distribution is very uniform in the EDX map of annealed industry produced $Pt_5Rh_{20}V_5Ni_{35}Co_{35}$ in figure 2.23.

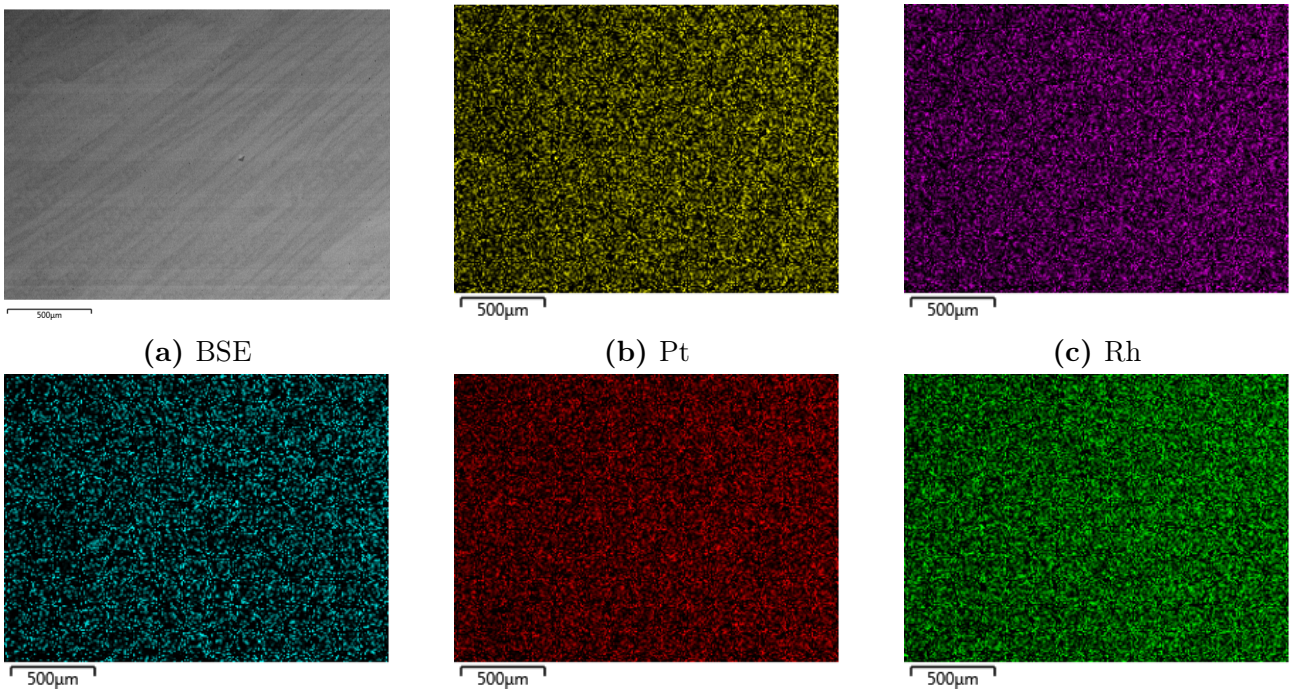

(a) BSE **(b)** Pt **(c)** Rh

(d) V **(e)** Ni **(f)** Co

Figure 6.22: 300x magnification EDX map of as-cast $Pt_5Rh_{20}V_5Ni_{35}Co_{35}$

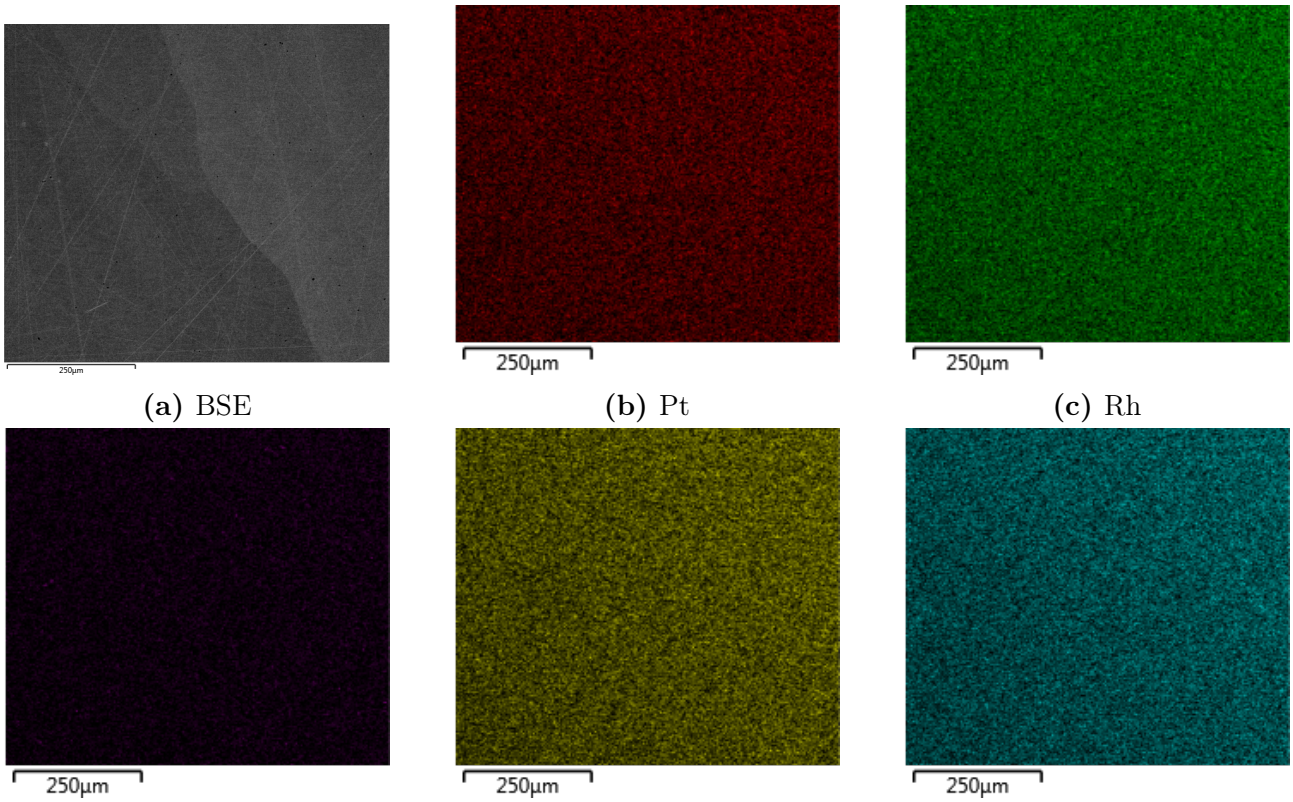

(a) BSE **(b)** Pt **(c)** Rh

(d) V **(e)** Ni **(f)** Co

Figure 6.23: 400x magnification EDX map of annealed $Pt_5Rh_{20}V_5Ni_{35}Co_{35}$

Discussion

SEM-BSE images show microstructural variation in the as-cast sample. The as-cast sample shows dendrites of several different apparent structures, some elongated, some cell-like. This is probably due to the change in cooling rate across the 1 kg ingot with different regions in the image having experienced slightly different thermal histories on cooling. The cell-like dendrite growth on the upper right of figure 6.20a is reminiscent of the growth observed in figure 6.18 of the laboratory scale annealed sample. The cooling rate for the laboratory scale samples would have been higher due to the smaller size so the variation in dendrite growth is likely due to a low cooling rate in such a large ingot. EDX data for the as cast sample shows uniform distribution of elements on the surface imaged. However, the BSE image accompanying the elemental distribution map shows that there are areas of concentration of heavier elements and areas of concentration of lighter elements. Heat treatment appears to have homogenised the composition sufficiently that it has removed the dendrites from the imaged sample, in contrast with the laboratory scale samples where heat treatment made the dendrites more regular, this is likely due to the different heat treatment conditions, due to the choice of different annealing temperatures (700°C for the laboratory sample annealing and 1000°C for the industrial scale sample annealing). This suggests that 1000°C is a better heat treatment temperature for promoting homogeneity, which would be expected as the higher temperature would significantly increase the mobility of atomic species by diffusion. The backscattered images would suggest there is some separation of light and heavy elements in the annealed sample, however, EDX map data indicates otherwise, presenting a very uniform distribution. The differences in what is observed in the EDX maps and the accompanying BSE images is likely to be due to the short measurement time, with the BSE images giving a more accurate representation of the true situation.A longer time of measurement would provide better resolution data.

6.4.2.5 EPMA

EPMA data for the as-cast and annealed samples of the laboratory and industry manufactured alloys are displayed on figures 6.24 and 6.25, and 6.26 and 6.27.

Laboratory scale

Figure 6.24 shows a cellular dendrite structure both at low and high magnification. At low magnification the elements appear to be uniformly distributed across the imaged surface with small degrees of segregation, and a higher degree of segregation in Rh of approximately 1-2%. At high magnification there is more noticeable segregation in Pt, Ni and Rh.

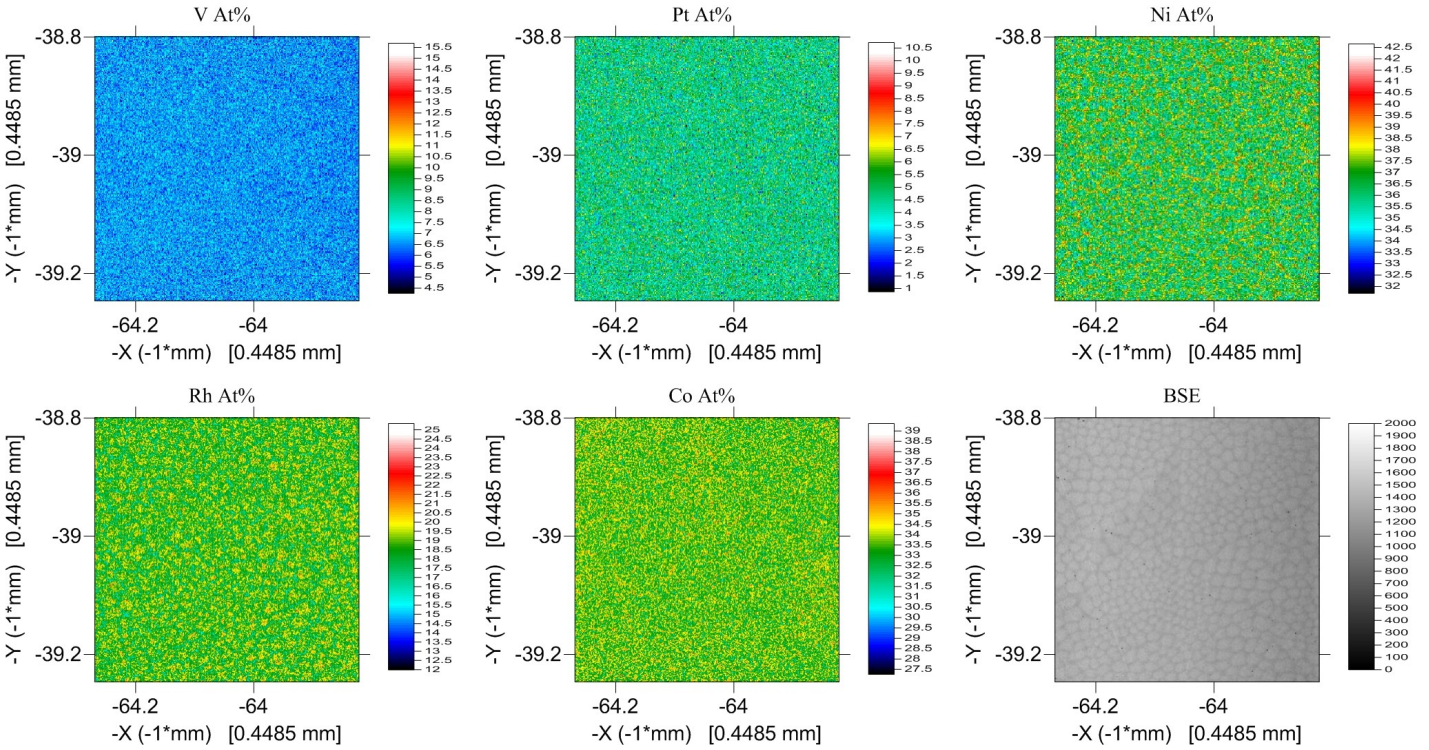

(a) Low magnification

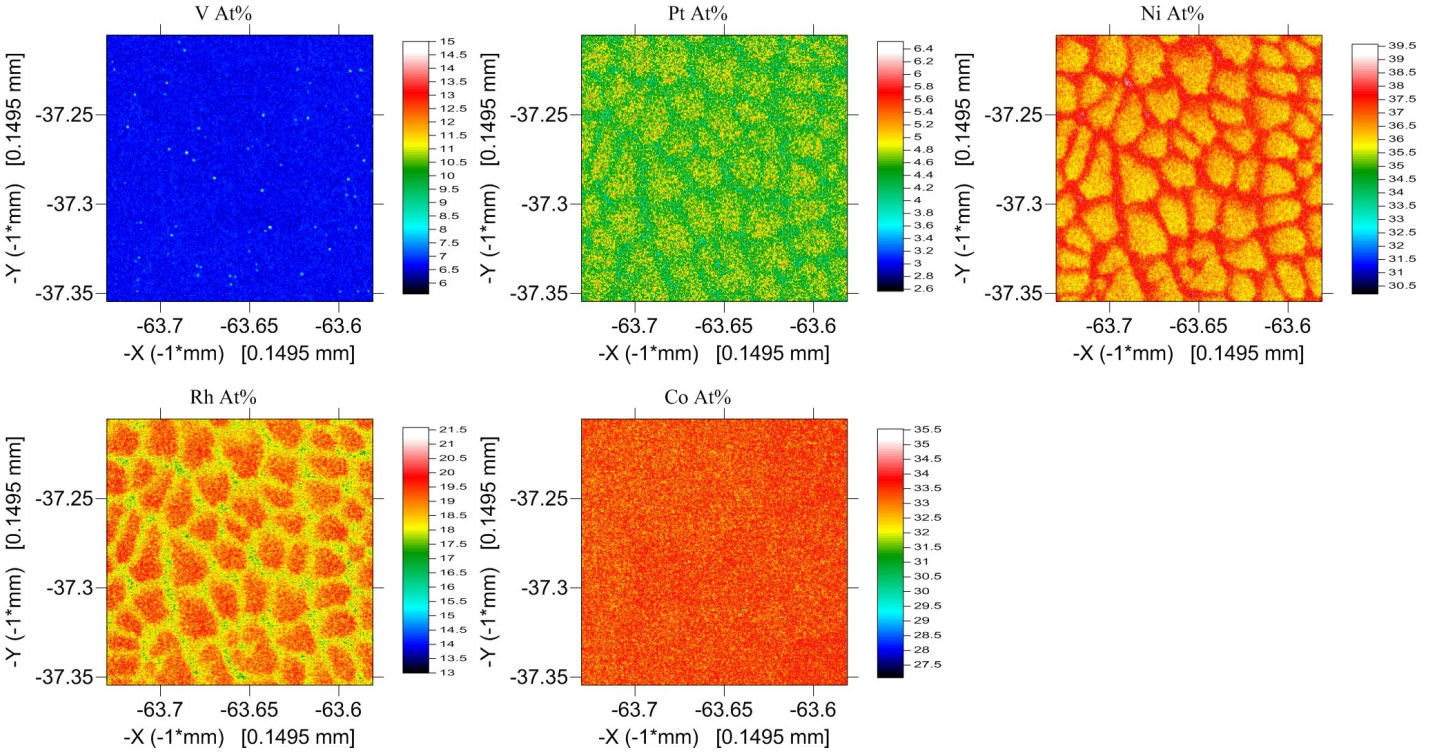

(b) High magnification

Figure 6.24: EPMA of as-cast $Pt_5Rh_{20}V_5Ni_{35}Co_{35}$

Figure 6.25 has a similar cellular dendrite structure, where Co is very uniformly distributed across the imaged surface and Ni is segregating from Pt, Rh and V.

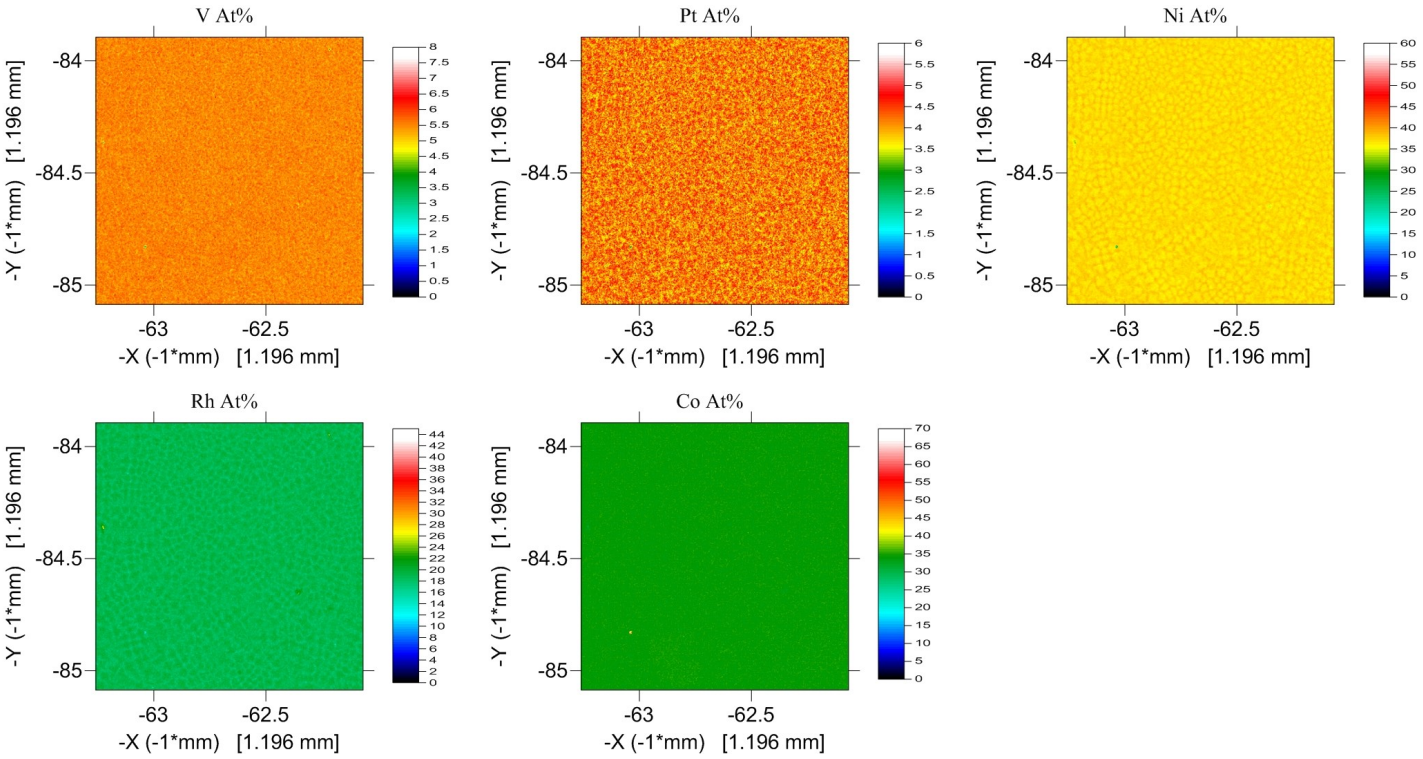

(a) Low magnification

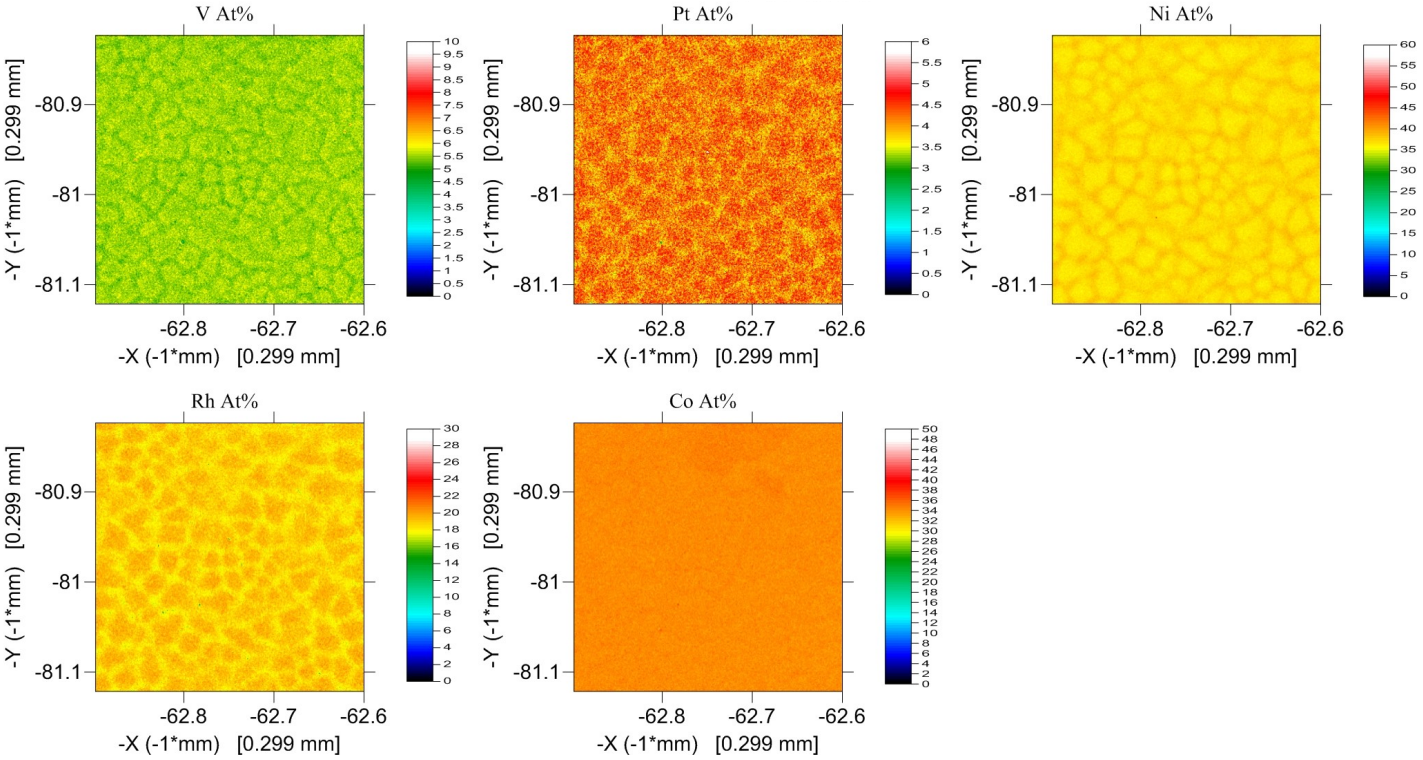

(b) High magnification

Figure 6.25: EPMA of annealed $Pt_5Rh_{20}V_5Ni_{35}Co_{35}$

Industrial scale In figure 6.26, we see that the elemental distribution is fairly uniform across the imaged area both at low and high magnification. Co and V are very uniformly distributed across the imaged surface with no or minimal segregation. We see that Ni is segregating into

the dendrites and away from Pt and Rh which are segregating together out of the dendrites.

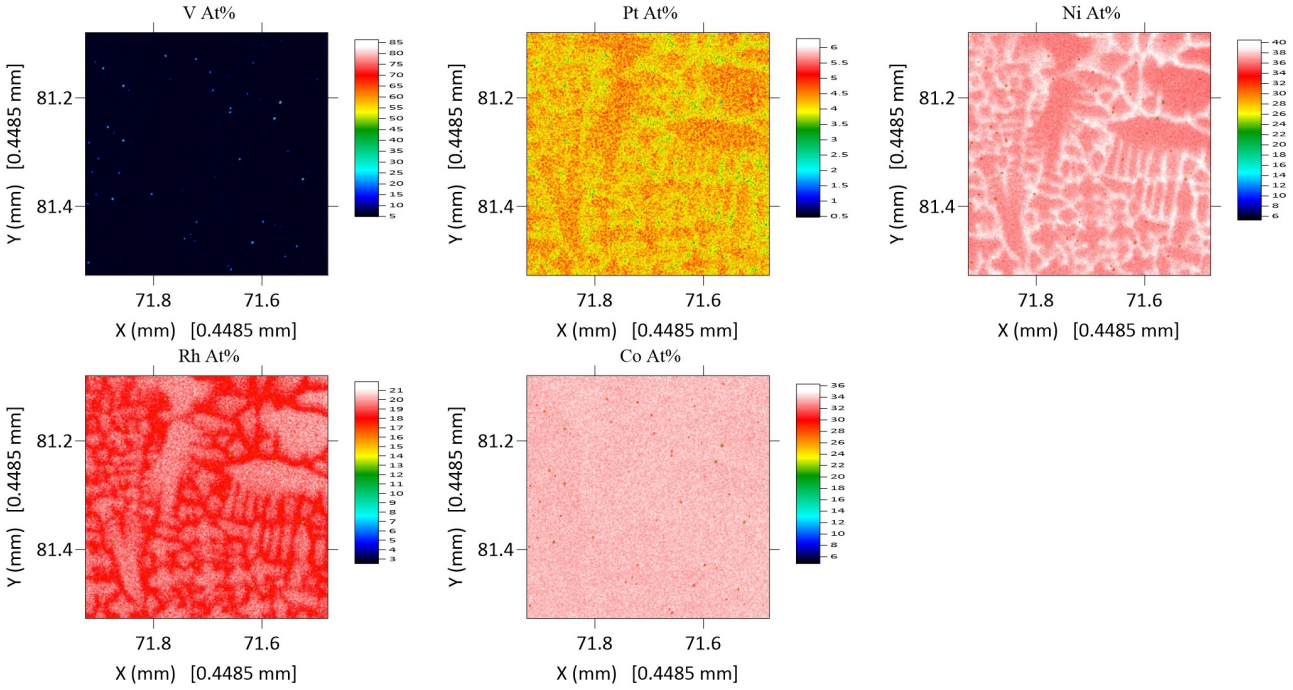

(a) Low magnification

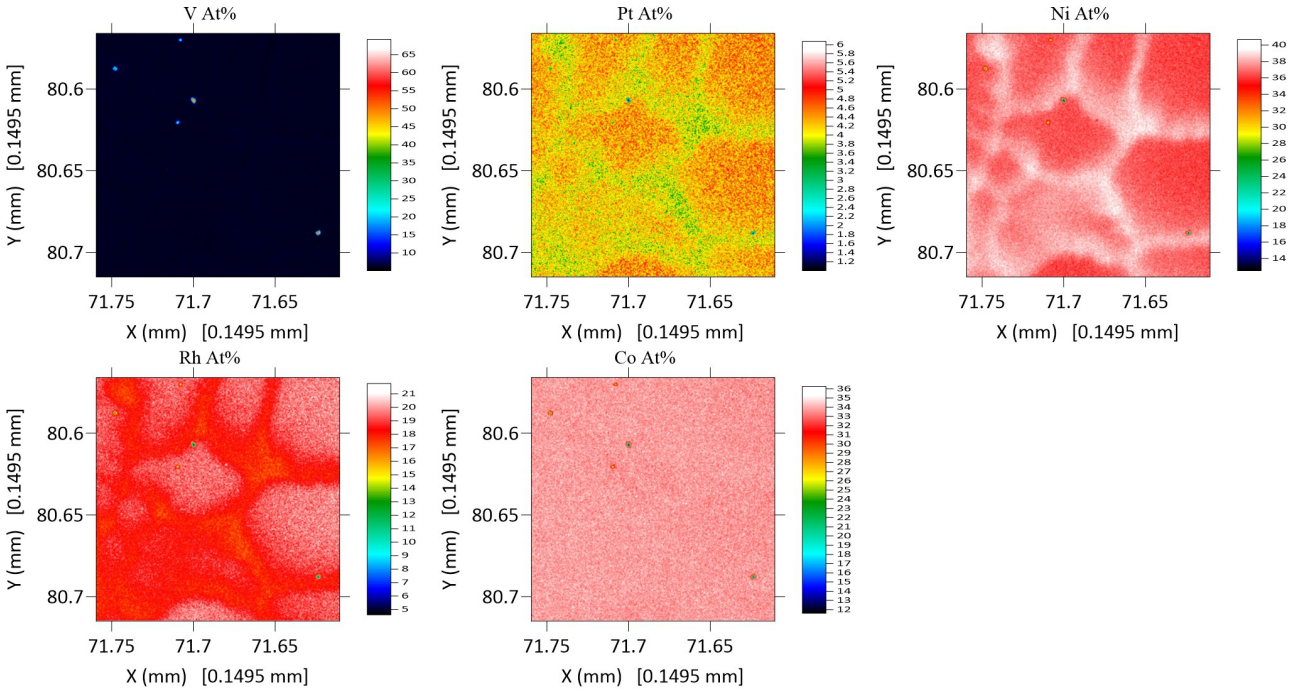

(b) High magnification

Figure 6.26: EPMA of as-cast $Pt_5Rh_{20}V_5Ni_{35}Co_{35}$, samples taken from a 1kg ingot

The elemental distribution in figure 6.27 is uniform across the area imaged at both low and high magnification. There are some noticeable areas of minor unevenness and some fuzziness in Pt, in particular, but overall all elements are uniformly distributed.

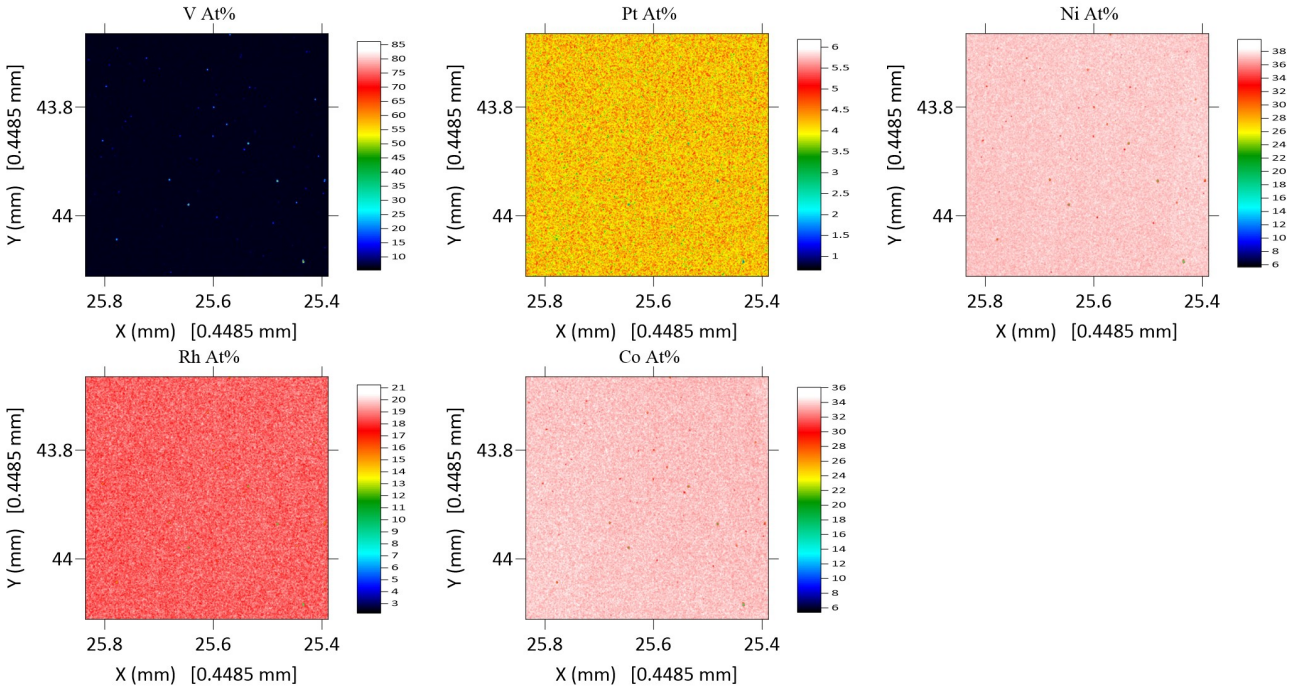

(a) Low magnification

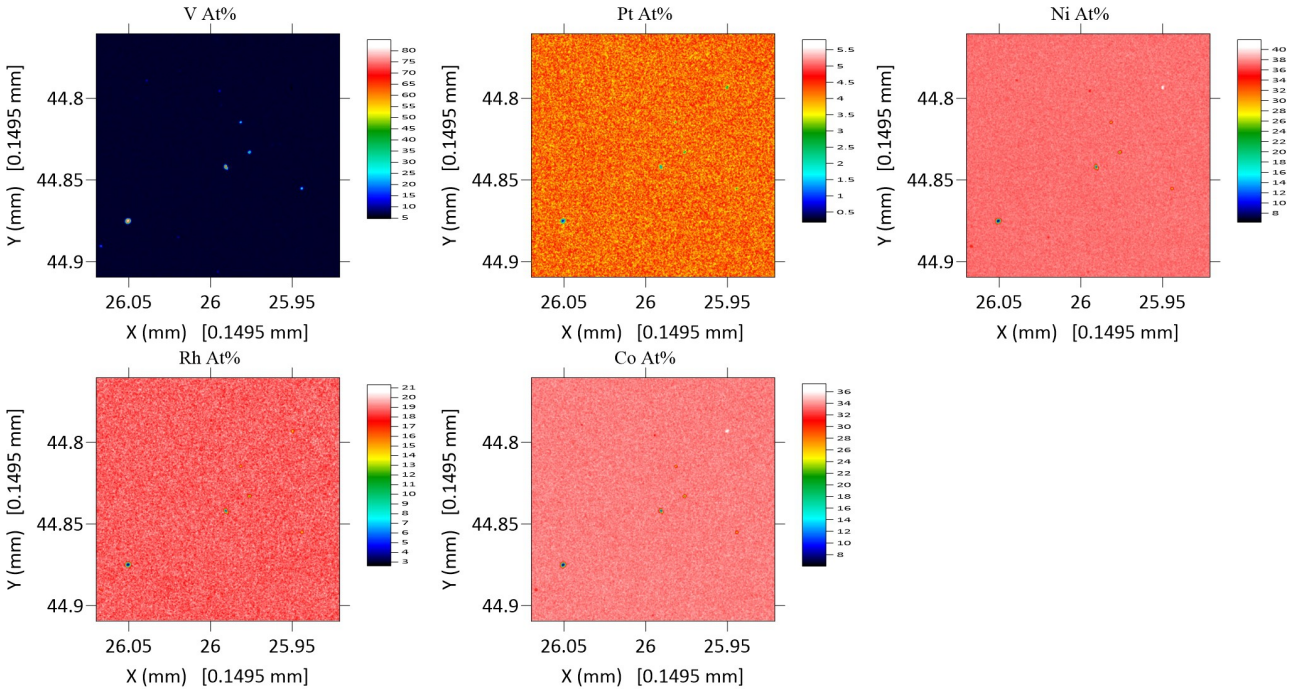

(b) High magnification

Figure 6.27: EPMA of annealed $Pt_5Rh_{20}V_5Ni_{35}Co_{35}$, samples taken from a 1kg ingot

Discussion

For the laboratory manufactured alloys, EPMA data (fig. 6.24 and 6.25) show that there is, indeed, segregation, particularly in Rh out of the dendrites in the as-cast sample, like in $Pt_7Rh_{23}Ni_{35}Co_{35}$. However if we inspect ΔH_{AB} in figure B.1 (section B.1) all ΔH_{AB} for Rh and

the other components is negative. The rejection of Rh from the dendrites is more evident in the high magnification EPMA (Fig. 6.24b). Like with $Pt_7Rh_{23}Ni_{35}Co_{35}$ there seems to be a PtRh phase separating from the Ni, V and Co, which are all very uniformly distributed, however. The EPMA for the annealed sample shows that V is to a small degree being rejected from the dendrites and into the region described by the dendritic matrix, the segregation for Pt, Rh and V is very small 0.5-2 at.%, with Ni being slightly higher at $\approx$ 3at.%. It is evident that annealing at 700°C does little to promote homogenisation and removal of the dendritic structure evident in the elemental distribution. Despite the segregation in the dendrites, the overall elemental distribution across the imaged surface is generally uniform with the segregation observed in the dendrites varying by 3-5at.%.

EPMA data for the industrially manufactured as-cast alloy (fig. 6.26) shows a similar behaviour as with the laboratory manufactured alloys. Pt and Rh are being rejected out of the dendrites on solidification, with Ni being preferentially incorporated into them. In contrast, the annealed EPMA data shows uniform distribution of elements across the area imaged, this might imply that to achieve true uniformity in $Pt_5Rh_{20}V_5Ni_{35}Co_{35}$, the sample needs to be heat treated at temperatures higher than 700°C (laboratory) and closer to 1000°C (industrial). The EPMA data are higher resolution than the EDX data so studies in the heat treatment with EPMA characterisation would illuminate whether the alloy is more uniform after heat treatment at 1000°C.

It is evident that we need to heat treat alloys at a higher temperature to promote homogeneity. The observations made on the heat treated industrially manufactured sample (fig. 6.27)imply that the alloy is very likely to be single phase post heat treatment.

6.4.2.6 Further Discussion of Alloy Structure

DSC results are similar to $Pt_7Rh_{23}Ni_{35}Co_{35}$, and the alloy, $Pt_5Rh_{20}V_5Ni_{35}Co_{35}$, is stable as a solid at 1000°C. TGA, shows that there is more mass gained than in $Pt_7Rh_{23}Ni_{35}Co_{35}$, probably due to the addition of V, and the reactivity of this element with oxygen. Comparing $Pt_5Rh_{20}V_5Ni_{35}Co_{35}$ with $Pt_5Rh_{11}V_{14}Ni_{35}Co_{35}$ which has a higher V content and the highest overall mass gain, it is evident that the presence of V has a linearly positive relationship to the mass gained (fig. 5.7). The mechanical property results show consistency across samples, a minimal rise in the modulus is observed during annealing. The elastic modulus extrapolated from the reduced modulus results are not in agreement with the expected, empirical formulae (ROM) deduced results but that is unsurprising as these calculations are an approximation. Overall, the mechanical data does imply that the alloy is ductile and workable when assessed with the results of the laboratory scale crude manufacturability test.

6.4.3 $Pt_5Rh_{11}V_{14}Ni_{35}Co_{35}$

6.4.3.1 XRD

The lattice parameters for $Pt_5Rh_{11}V_{14}Ni_{35}Co_{35}$ were calculated from the XRD pattern data in figures 6.28 and 6.29. The lattice parameters are displayed on table 6.12.

Manufacture scale	As-cast (Å)	Annealed (Å)
Laboratory	3.607	3.607
Industry	3.623	3.618

Table 6.12: Lattice parameter for $Pt_5Rh_{11}V_{14}Ni_{35}Co_{35}$ obtained from XRD data sets at different stages of manufacture and processing

Discussion

There is very strong agreement in the lattice parameters obtained from the laboratory scale alloys, between different assessments on different samples, and those values are also consistent with those found from samples of alloy made in the scaled up trials. There is a difference between the alloys from the different manufacturing routes of up to 0.1Å. The reason for these small differences might be due to the precision of measuring out the constituent elements. Nevertheless, from the data presented for the lattice parameters we can see that the alloy does scale to industry with semblance to the laboratory scale.

Figures 6.28 and 6.29 show the XRD data collected for the laboratory manufactured samples and industry manufactured samples, respectively. Both figures display the individual data for as-cast and annealed samples and a normalised comparison of the two.

Laboratory scale

In figure 6.28 XRD data for the laboratory manufactured samples of $Pt_5Rh_{11}V_{14}Ni_{35}Co_{35}$ is presented. Figure 6.28 a, b, and c are for the as-cast, annealed, and a normalised comparison of the two, respectively.

In figure 6.28a we see that there is an artefact from the clear resin mounting medium that adds an amorphous hump and background to the data. The data is noisy but relevant peaks, however, are distinguishable as, and consistent with, peaks generally associated with an FCC crystal phase. The same peaks are prominent in figure 6.28b together with some minor peaks.

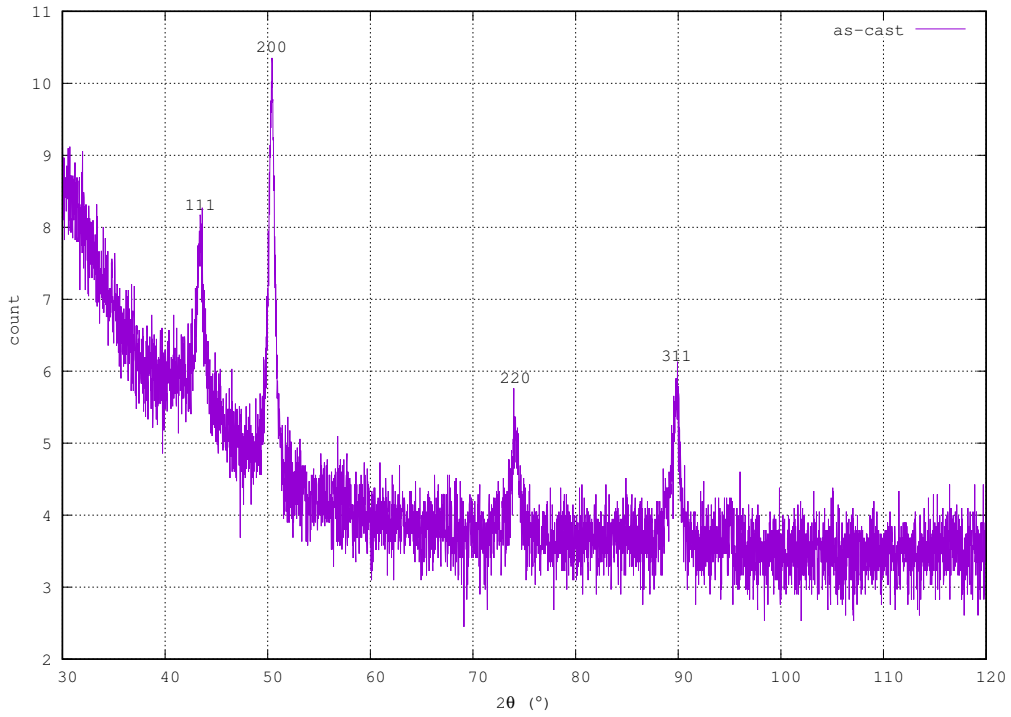

(a) as-cast

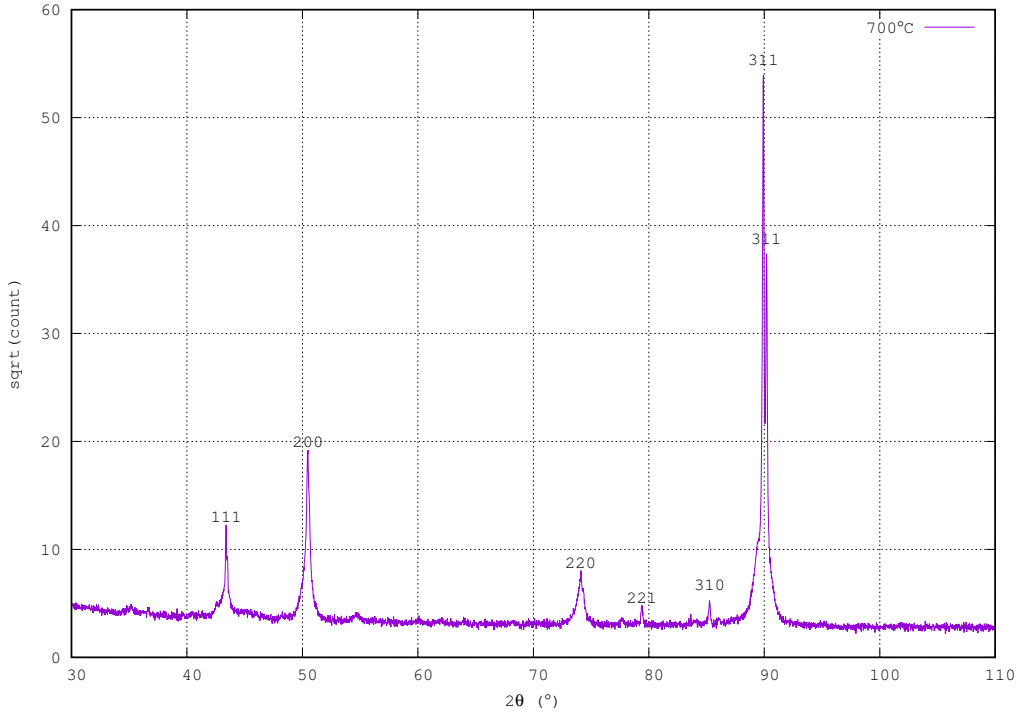

(b) annealed @ 700°C

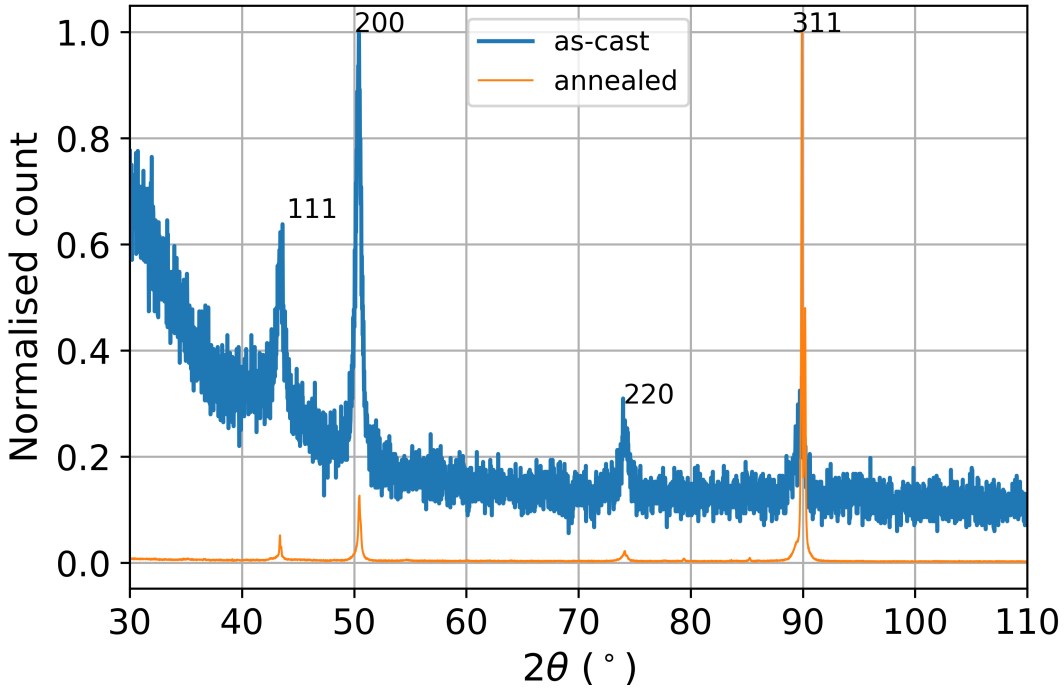

(c) Comparison of normalised XRD data for as-cast and annealed samples

Figure 6.28: XRD of laboratory manufactured $Pt_5Rh_{11}V_{14}Ni_{35}Co_{35}$

Discussion

We observe an amorphous hump and background in the as-cast alloy measurement at 30-40°, this is due to the mounting medium being resin, and this material giving an additional background signal in the measurement. While relatively easy to discount from the analysis, the additional background could have contributed to the distortion of the XRD data and might have hidden some peaks that were due to the sample under analysis. By looking at the clear peaks present in the patterns, have identified peaks that are at angles consistent with an FCC crystal structure.

We can see that the annealed alloy also has peaks corresponding to a FCC crystal structure. However, there are also some unindexed faint peaks which could also be an impurity, or a second phase present in a small amount. Lattice plane (3 1 1) appears to have two peaks. Since the peaks are so close to each other the peaks are very likely to be the result of small scale compositional differences in the examined plane.

Comparing the normalised as-cast and annealed XRD data we can see that the peak positions align with each other. The contribution of the amorphous resin to the as-cast XRD data is making it difficult to discern whether the background and the size of the peaks is due to the alloy or the resin. Overall the alloy does appear FCC but with some of the peaks being observed to split, and the generally high level of the background it is not possible to be confident that there are no other phases present.

Industrial scale

In figure 6.29 XRD data for the industrially manufactured samples of $Pt_5Rh_{11}V_{14}Ni_{35}Co_{35}$ is presented. Figure 6.29 a, b, and c are for the as-cast, annealed, and a normalised comparison of the two, respectively.

The XRD data for the as-cast sample are 3 distinct peaks and do not resemble peaks characteristic of any simple crystal structure. The data for the annealed sample show 2 distinct peaks and a small wider mound tht might be a peak.

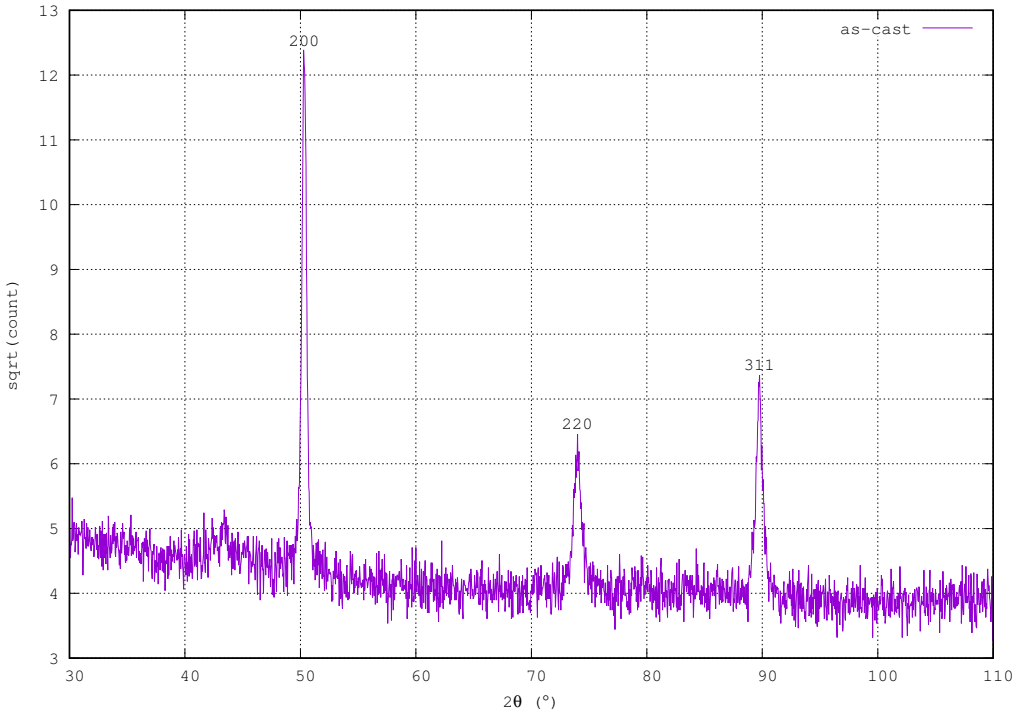

(a) as-cast

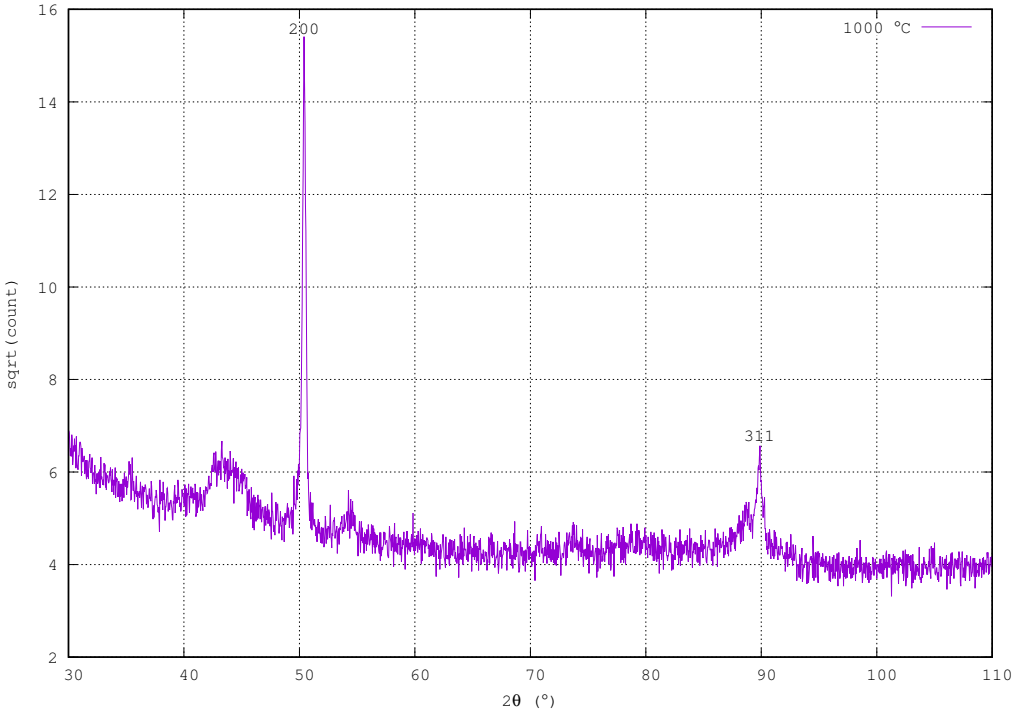

(b) annealed @ 1000°C

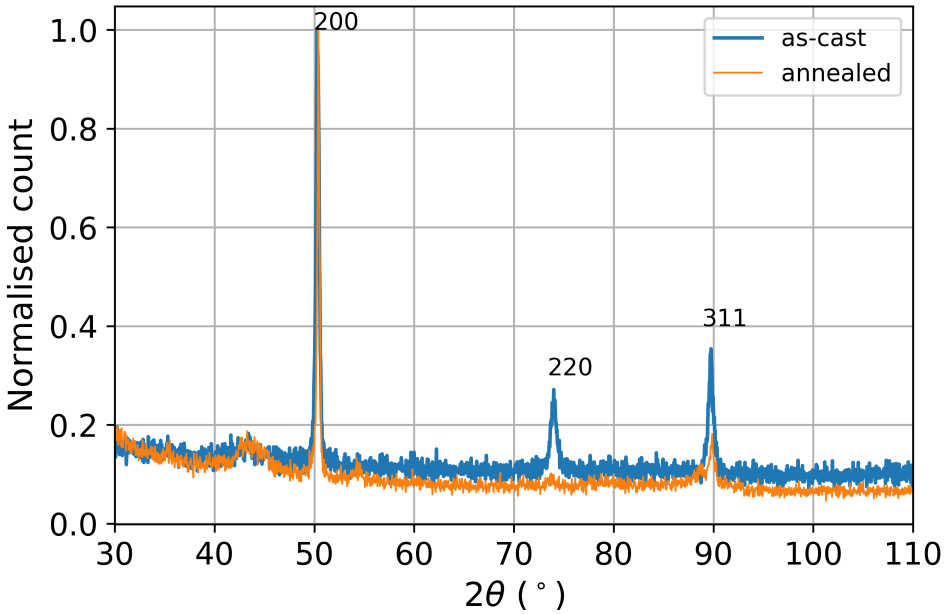

(c) Comparison of normalised XRD data for as-cast and annealed samples

Figure 6.29: XRD of $Pt_5Rh_{11}V_{14}Ni_{35}Co_{35}$ manufactured @ JMNM

Discussion

XRD data for the industrially manufactured alloys are very inconclusive, some peaks are not indexable, indicating the presence of a secondary phase or a complex phase together with

the FCC crystal structure. The presence of peaks also changes post heat treatment, one of the expected peaks is absent and noisier non indexable peaks are more apparent in the scan plot.

Comparing the laboratory manufactured alloy with the industrially manufactured alloy we can see the appearance of similar planes at the same 2θ positions but the data is not sufficient to be able to draw conclusive remarks. This might be due to the uneven cooling of the industrially manufactured samples as both the ingot and the cut-off were much larger than any sample made in the laboratory. Perhaps further heat treatment would either promote the appearance of hidden secondary phases or homogenise the alloy.

6.4.3.2 XRF

The quantitative XRF data for the laboratory manufactured alloys are given in tables 6.13a and 6.13b in the as-cast and annealed states, respectively. Likewise, the XRF data for the industry manufactured alloys are presented in figure 6.14a and b.

Laboratory scale

	XRF (.wt%)	at.%	at.%→wt.%
Pt	13.62	5	14.06
Rh	10.56	11	16.32
V	9.97	14	10.28
Ni	30.18	35	29.61
Co	29.89	35	29.73

(a) As-cast (no absolute error)

	XRF (.wt%)	at.%	at.%→wt.%
Pt	15.70	5	14.06
Rh	11.52	11	16.32
V	8.79	14	10.28
Ni	29.96	35	29.61
Co	34.03	35	29.73

(b) Annealed (no absolute error)

Table 6.13: XRF of laboratory scale manufactured $Pt_5Rh_{11}V_{14}Ni_{35}Co_{35}$

Industrial scale

	XRF (.wt%)	at.%	at.%→wt.%
Pt	13.34±0.7	5	14.06
Rh	8.16±0.5	11	16.32
V	8.61±0.4	14	10.28
Ni	28.58±0.7	35	29.61
Co	28.26±0.8	35	29.73

(a) As-cast

	XRF (.wt%)	at.%	at.%→wt.%
Pt	15.60±0.8	5	14.06
Rh	11.44±0.7	11	16.32
V	10.27±0.5	14	10.28
Ni	30.84±0.7	35	29.61
Co	31.86±0.9	35	29.73

(b) Annealed

Table 6.14: XRF of industrial scale manufactured $Pt_5Rh_{11}V_{14}Ni_{35}Co_{35}$

Discussion

In the laboratory scale manufacture data the results between as-cast and annealed conditions are fairly similar, given the data came from different samples. Both samples have a much lower Rh content than expected. The annealed laboratory sample has a much higher Co content than expected. The same is true for the industrially manufactured alloy, both as-cast and annealed samples exhibit the same Rh depletion. Also, the data between industrial samples indicates that there is a redistribution of elements after heat treatment since some of the element wt.% results are closer to the expected wt.% distribution.

However, comparing the laboratory manufactured samples with the EPMA results they do not agree. The EPMA data for both as-cast and annealed show a higher than expected content of V and a slightly lower but very close to expected content of Rh. The same is true for the industrially manufactured samples.

There is some agreement between XRF and EPMA data but EPMA indicated a more uniformly mixed sample than XRF does. Perhaps, the XRF measurement was affected by external factors we could not control for, or it may be that the differences in these results is due to the different scale they examine; EPMA, looking at a small amount of material, may find one without particular variations away from the expected level, but XRF, which examines at a larger scale, might detect some overall departures from the nominal condition.

6.4.3.3 Optical micrographs

Optical micrographs for $Pt_7Rh_{23}Ni_{35}Co_{35}$ are presented in figure 6.30a and b, respectively. In table 6.15 we present a grain size analysis of the visible grains for figure 6.30a and b, respectively. The grains are fairly large and have an irregular and long shape, dendrites are also noticeable in the images and they appear cellular and bubble-like.

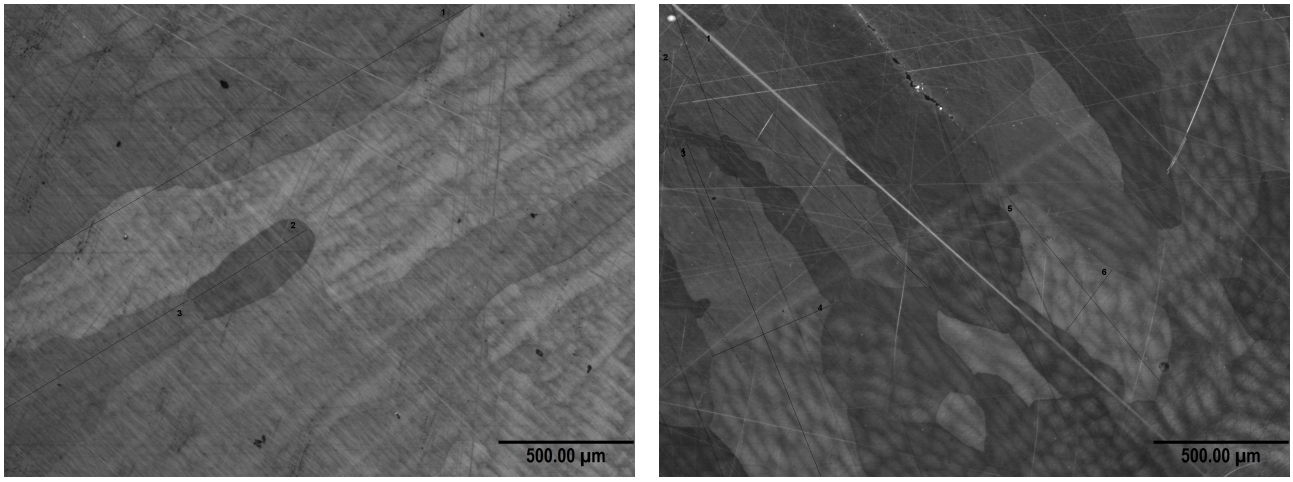

(a) as-cast 5x magnification **(b)** annealed 5x magnification

Figure 6.30: $Pt_5Rh_{11}V_{14}Ni_{35}Co_{35}$ optical images of as-cast and etched and annealed and etched samples

	Length (µm)
1	1975
2	496
3	790

(a) Figure 6.30a grain analysis

	Length (µm)
1	1259
2	1328
3	1340
4	476
5	882
6	282

(b) Figure 6.30b grain analysis

Table 6.15: Grain sizes for the optical micrographs for industrially manufactured $Pt_5Rh_{11}V_{14}Ni_{35}Co_{35}$

Discussion

The optical micrographs (fig. 6.30) show that the grains in the as-cast sample and the annealed sample are generally columnar. After heat treatment, however, we can see that the grains are becoming more equiaxed and larger, but also that this transition does not follow a regular pattern. The reason for the change in grain shape and size is probably the different heat treatment temperatures, allowing different changes to take place, and also the slower, but still uncontrolled, cooling in the furnace after heat treatment.

It is difficult to translate these observations in these images into an understanding of the grain structure change for the whole alloy, and it is also difficult to interpret how these changes may impact the other properties of the material. As a result, we must note that these optical micrographs are presented to give us an idea of the microstructure rather than an extensive and detailed view of it.

6.4.3.4 SEM-EDX

The SEM backscatter data for the as-cast and annealed laboratory and industry manufactured alloys are displayed in figures 6.31a and b, and figures 6.34 and 6.35, respectively.

The EDX data for the laboratory manufactured alloys can be found in figures 6.32 and 6.33, for the as-cast and annealed states, respectively. EDX data for the industry manufactured alloy are displayed in figures 6.36 and 6.37 for as-cast and annealed, respectively.

The images in figure 6.31 show a fairly uniform surface. The grains visible in figure 6.31b are cellular in shape and do not exhibit much size variation.

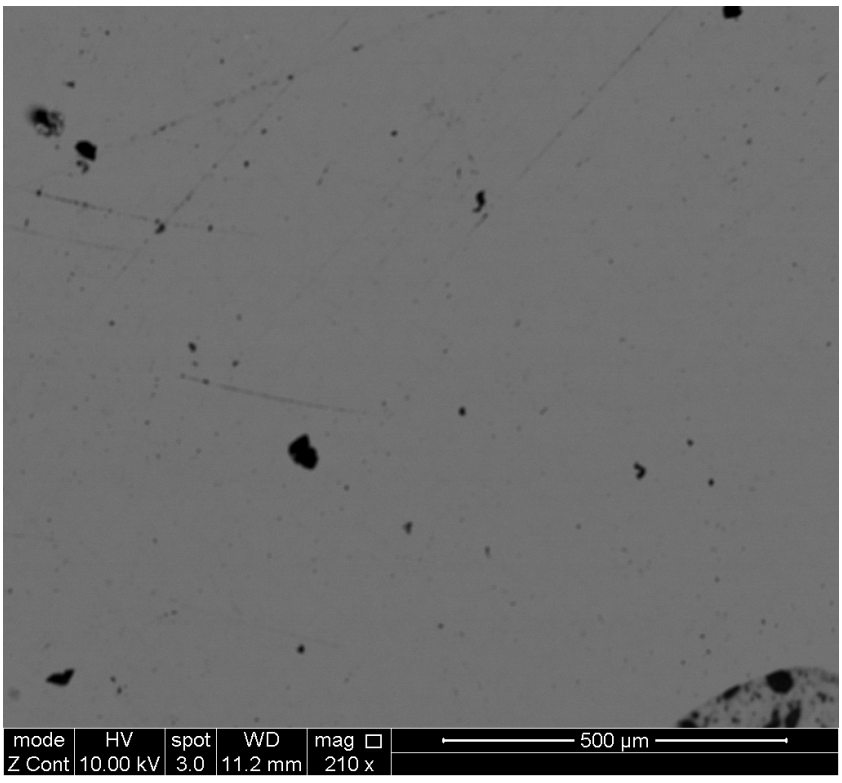

(a) BSE image of as-cast $Pt_5Rh_{11}V_{14}Ni_{35}Co_{35}$ at ≈200x magnification

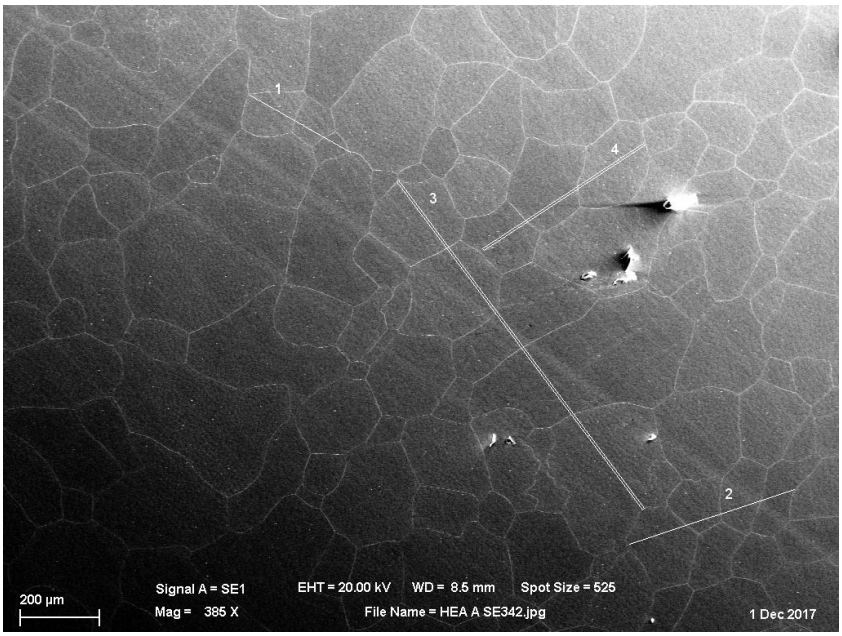

(b) SE image of etched and annealed $Pt_5Rh_{11}V_{14}Ni_{35}Co_{35}$ at ≈400x magnification taken at JMNM by Harry Macpherson

Figure 6.31: SEM of annealed and etched $Pt_5Rh_{11}V_{14}Ni_{35}Co_{35}$ @JMNM

	Distance (µm)	approximate grain size(µm)
1	292	97
2	439	110
3	1035	207
4	486	122

Table 6.16: Figure 6.31b dendrite analysis

The EDX map in figure 6.32 shows a uniform distribution across all constituent elements. Some degree of segregation is noticeable, most prominent in Pt and Co.

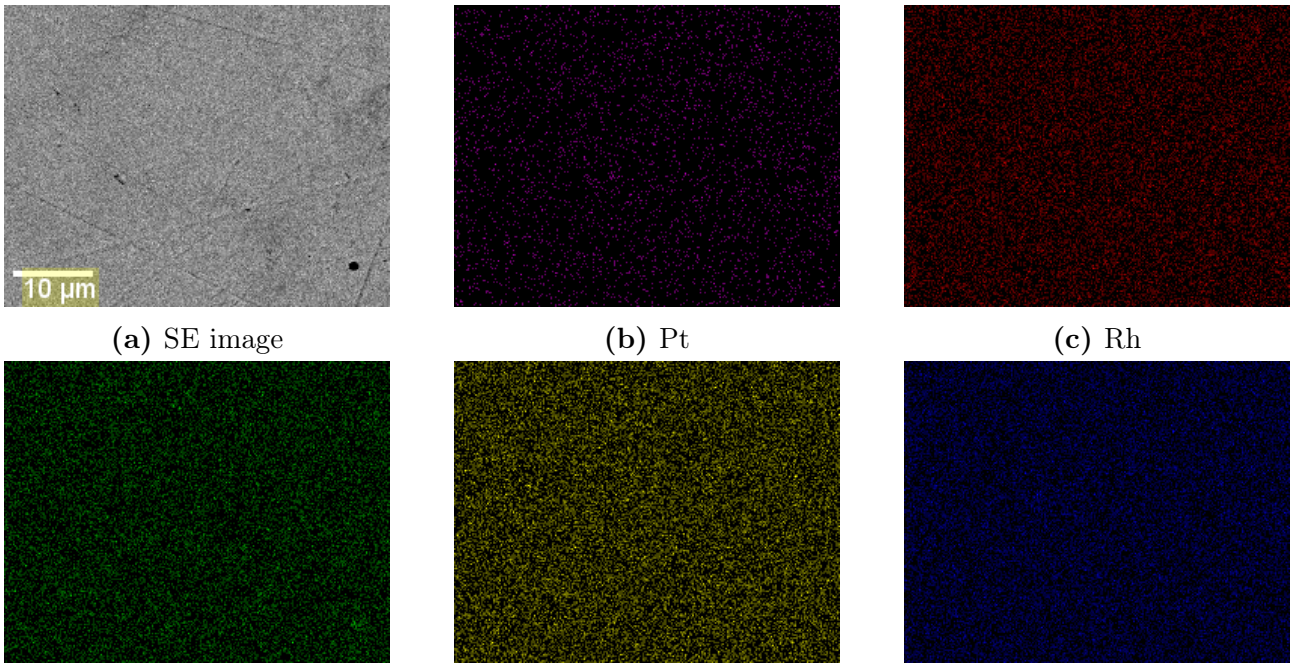

(a) SE image **(b)** Pt **(c)** Rh

(d) V **(e)** Ni **(f)** Co

Figure 6.32: EDX map of as-cast $Pt_5Rh_{11}V_{14}Ni_{35}Co_{35}$ taken at 6000x magnification

Segregation is noticeable in the EDX map in figure 6.33 in Pt. Some small degrees of segregation are exhibited in V, Rh, Ni and Co but these elements are more uniformly distributed across the imaged area.

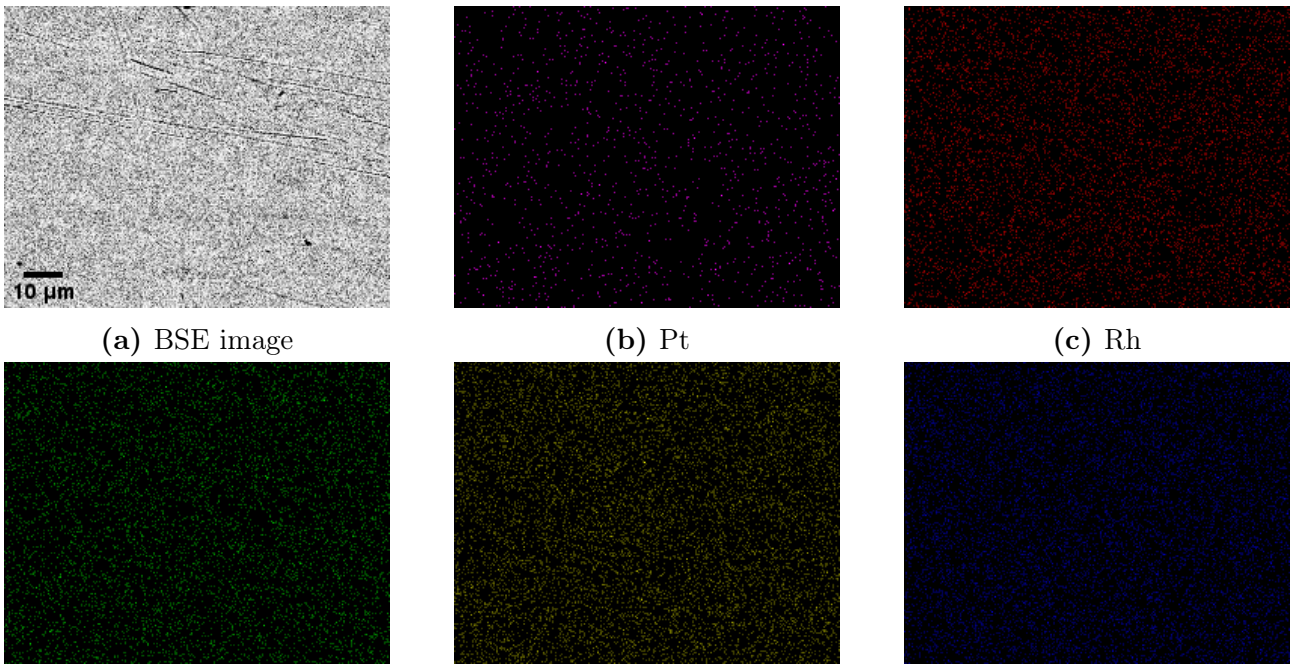

(a) BSE image **(b)** Pt **(c)** Rh

(d) V **(e)** Ni **(f)** Co

Figure 6.33: EDX map of annealed $Pt_5Rh_{11}V_{14}Ni_{35}Co_{35}$ taken at 3000x magnification

The are dendrites visible in both figure 6.34a and 6.34b. The dendrites are a combination

of columnar and cellular bubbles. In figures 6.35a and 6.35b we see similar dendrites, however, they are more laminar in shape.

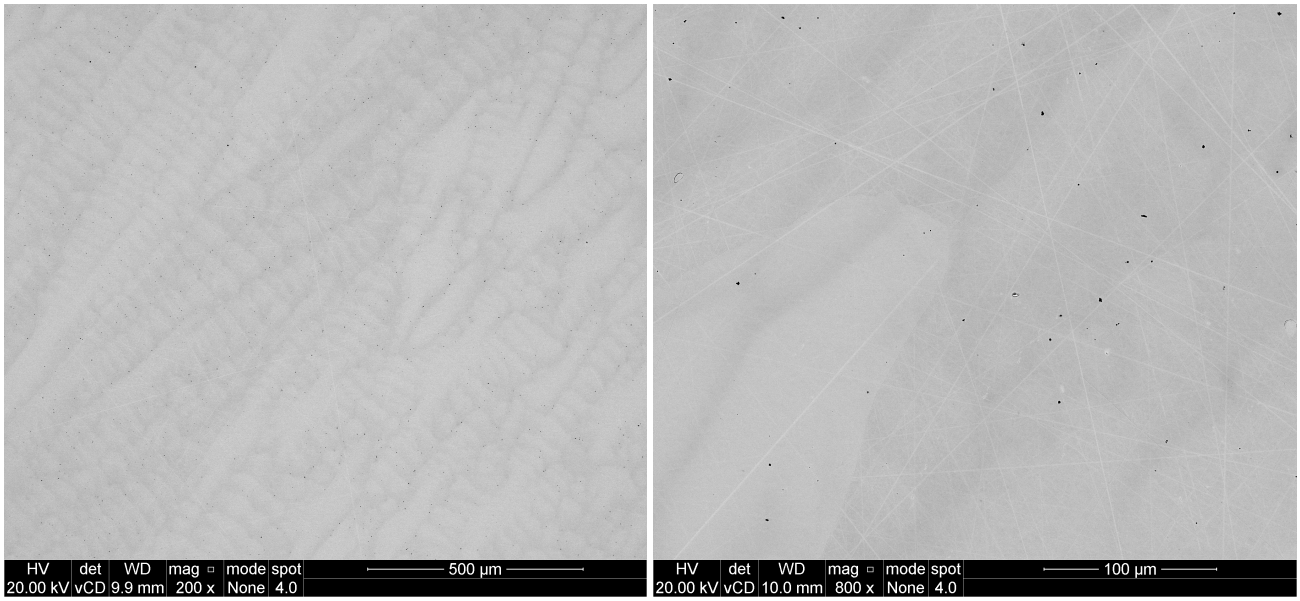

(a) 200x magnification **(b)** 800x magnification

Figure 6.34: BSE images of as-cast $Pt_5Rh_{11}V_{14}Ni_{25}Co_{35}$

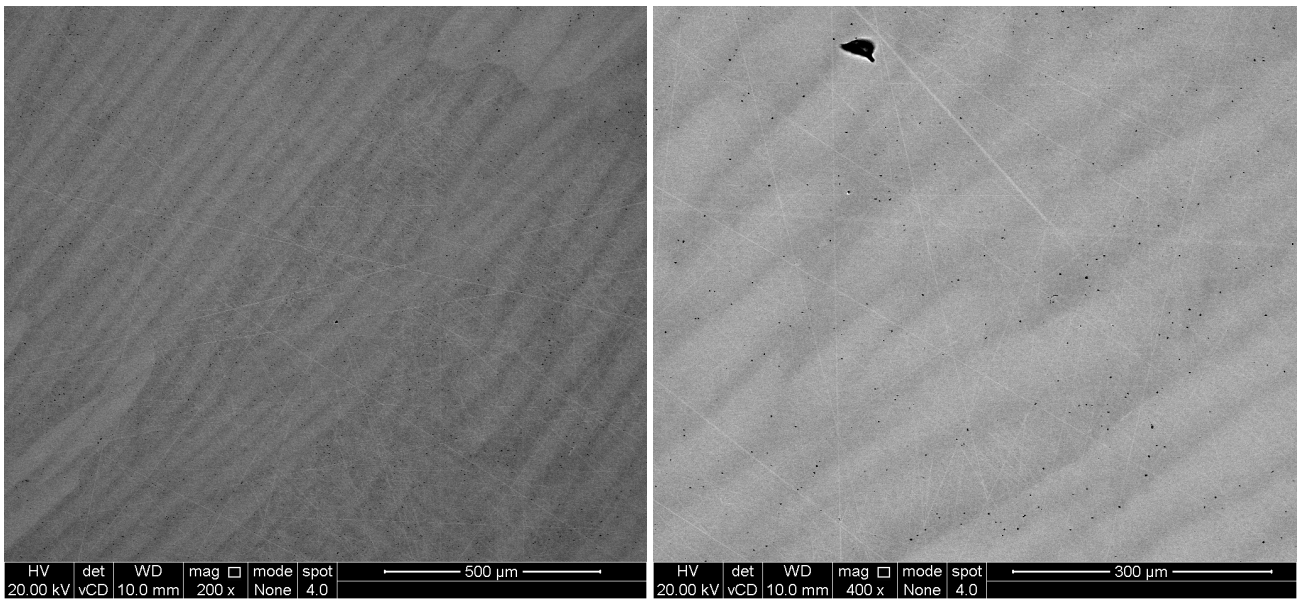

(a) 200x magnification **(b)** 400x magnification

Figure 6.35: BSE images of annealed $Pt_5Rh_{11}V_{14}Ni_{35}Co_{35}$

The elemental distribution in both figures 6.36 and 6.37 is fairly uniform across the imaged surfaces. There are some areas where there is noticeable concentration of elements but there is not visibly stark segregation in any of the elements in either figure.

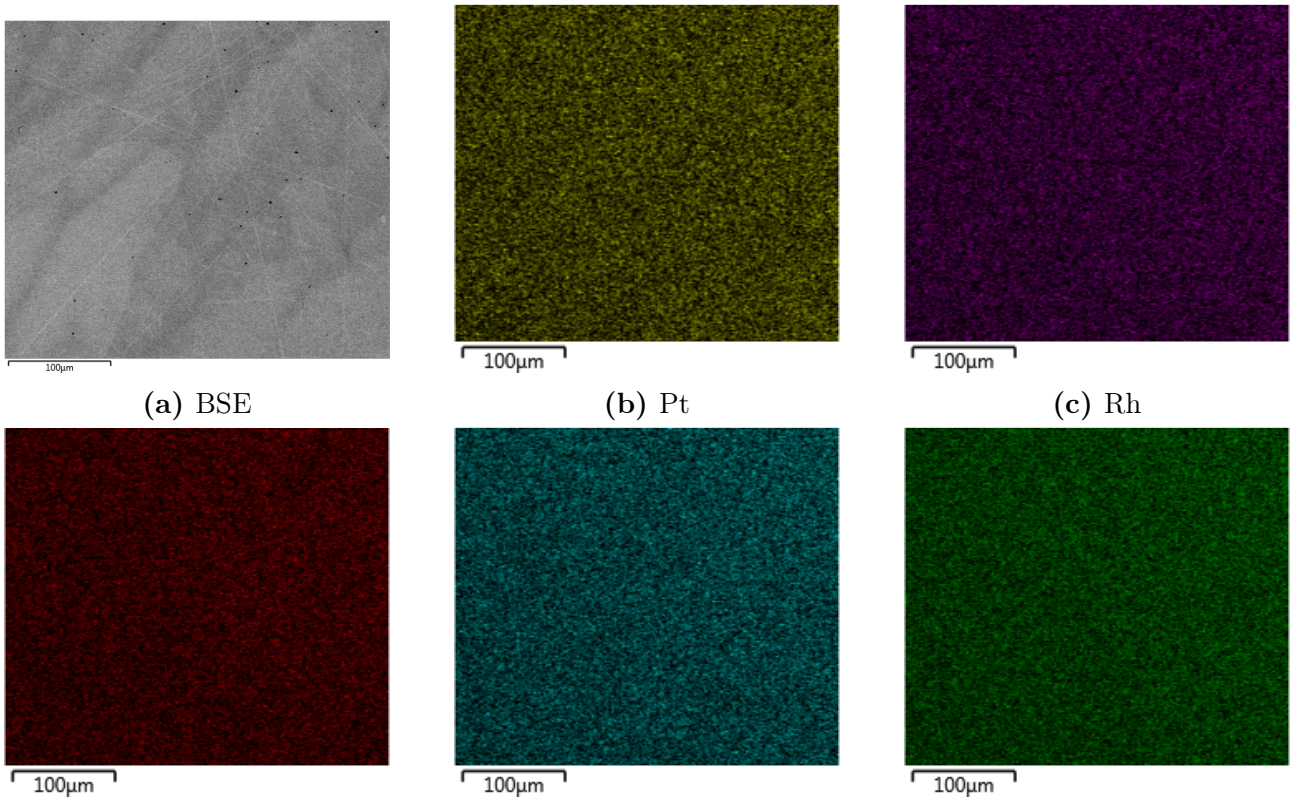

(a) BSE **(b)** Pt **(c)** Rh

(d) V **(e)** Ni **(f)** Co

Figure 6.36: 800x magnification EDX map of as-cast $Pt_5Rh_{11}V_{14}Ni_{35}Co_{35}$

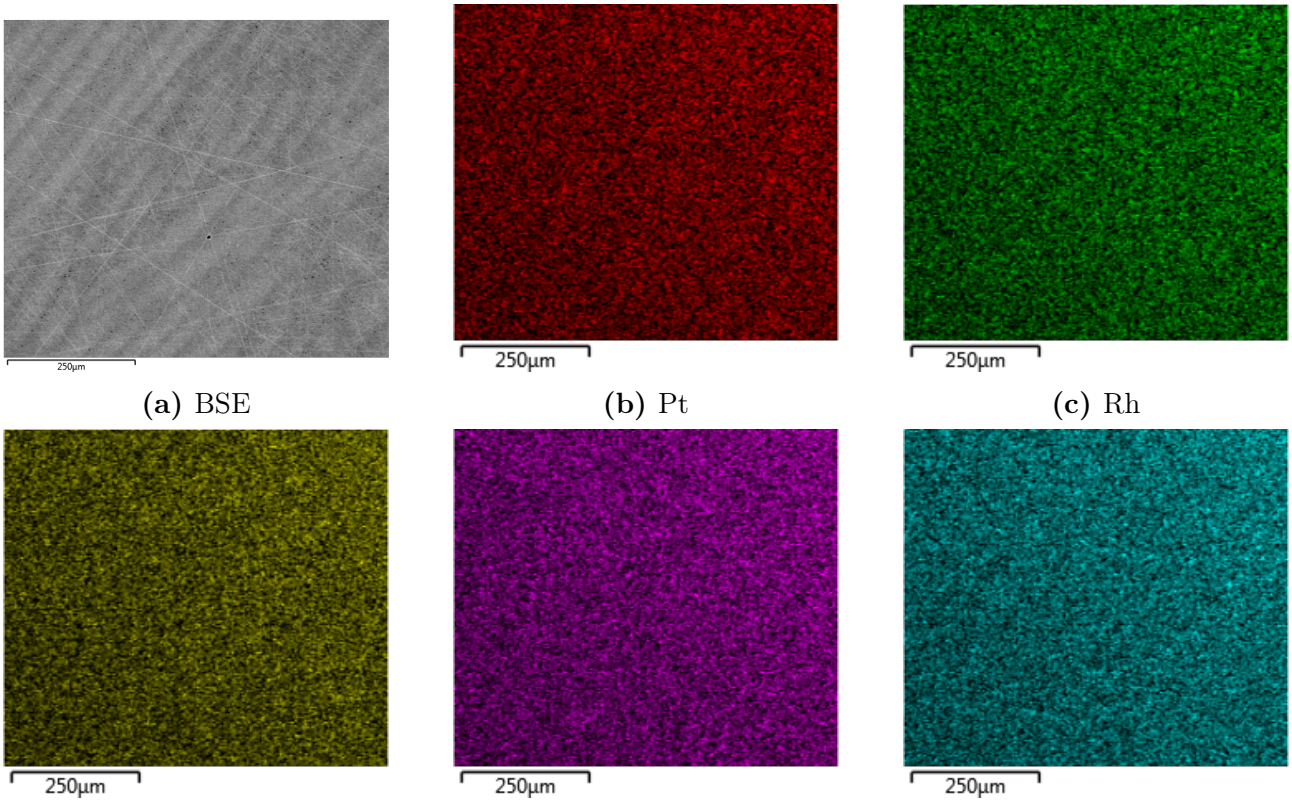

(a) BSE **(b)** Pt **(c)** Rh

(d) V **(e)** Ni **(f)** Co

Figure 6.37: 400x magnification EDX map of annealed $Pt_5Rh_{11}V_{14}Ni_{35}Co_{35}$

Discussion

The SE data shows a crocodile skin-like regular pattern in the annealed laboratory manufactured sample. The grain size appears small, probably due to the size of the sample allowing it to cool relatively rapid, despite the cooling in the furnace.

Laboratory manufactured EDX data shows a very even and uniform distribution of each of the elements, although there appear to be areas of higher Pt distribution, albeit at quite low signal in the images, probably due to the lower at.% of Pt in comparison to the other constituent elements. Comparing it to the EPMA data we can see that most elements are indeed fairly uniformly distributed but Pt is segregating away from V, where Pt is in the dendrite cells and V is rejected from the dendrites as they grow.

The industrially manufactured as-cast BSE images show a laminar dendritic structure, which is also observed in the EPMA maps (fig. 6.40). The structure changes from dendritic and laminar to laminar cells after heat treatment, also observed in the EPMA maps. The presence of cells after heat treatment might indicate that the alloy needs a higher temperature for full heat treatment homogenisation. The industrially manufactured alloy EDX maps are even throughout with no discernable clustering or segregation. This is probably due to the fast EDX collection process (5min duration for the whole image to be collected). Were the collection time for EDX longer we might be able to observe the segregation and clustering we observe in the laboratory data and in the EPMA data.

6.4.3.5 EPMA

EPMA data for the as-cast and annealed samples of the laboratory and industry manufactured alloys are displayed in figures 6.38 and 6.39, and 6.40 and 6.41.

The EPMA data displayed in figure 6.38 shows a cellular dendrite structure at low and high magnification. Ni is uniformly and evenly distributed across the imaged surface. There is some noticeable granularity in the evenness of the distribution of Rh but it is also uniformly distributed. V is diffusing into the dendrites while Co and Pt appear to be diffusing out of the dendrites.

The EPMA of the annealed $Pt_5Rh_{11}V_{14}Ni_{35}Co_{35}$ sample in figure 6.39 shows a very uniform distribution at low magnification. At high magnification it appears that there is a cellular dendrite structure present with some minor segregation into and out of the dendrites. Ni and Rh are evenly distributed and V appears to be more present in the dendrites while Co and Pt are more concentrated in the cells.

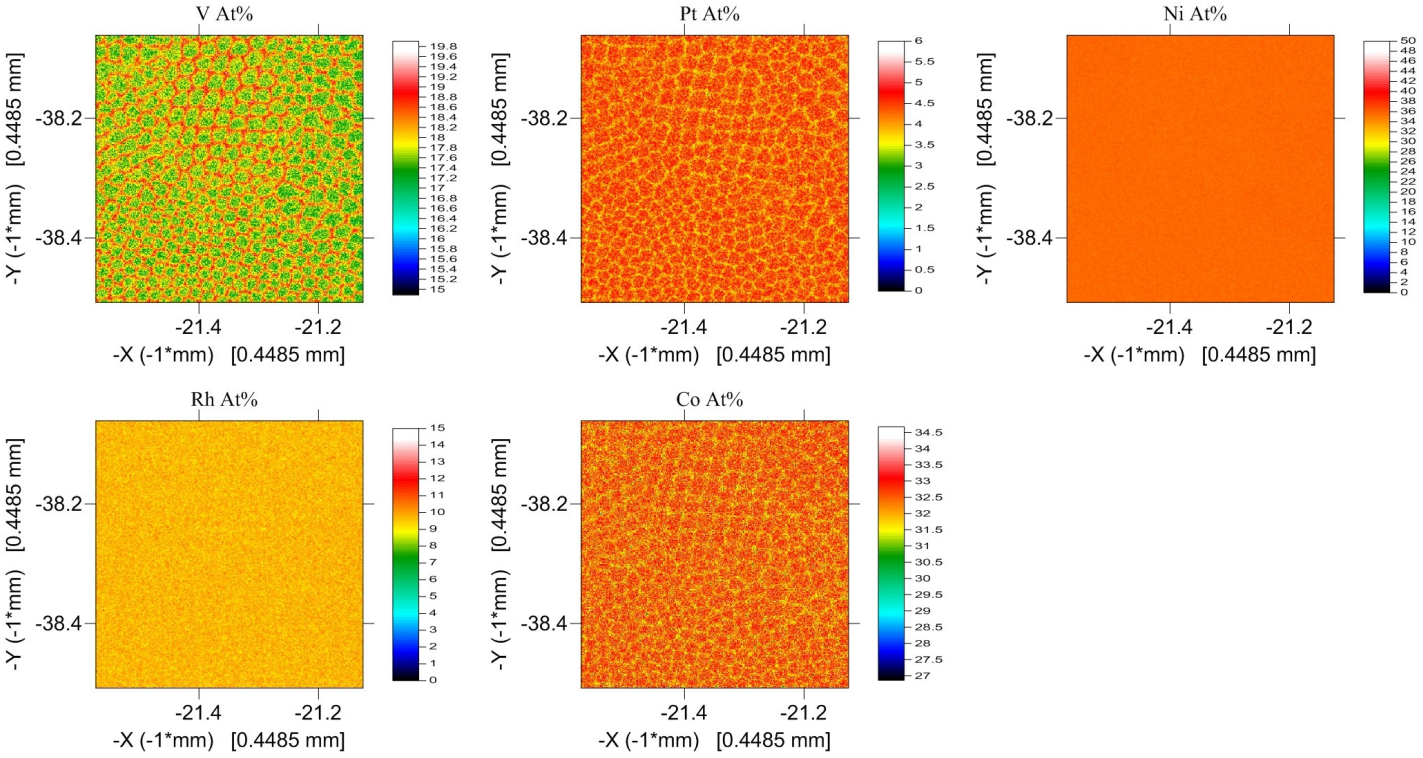

(a) Low magnification

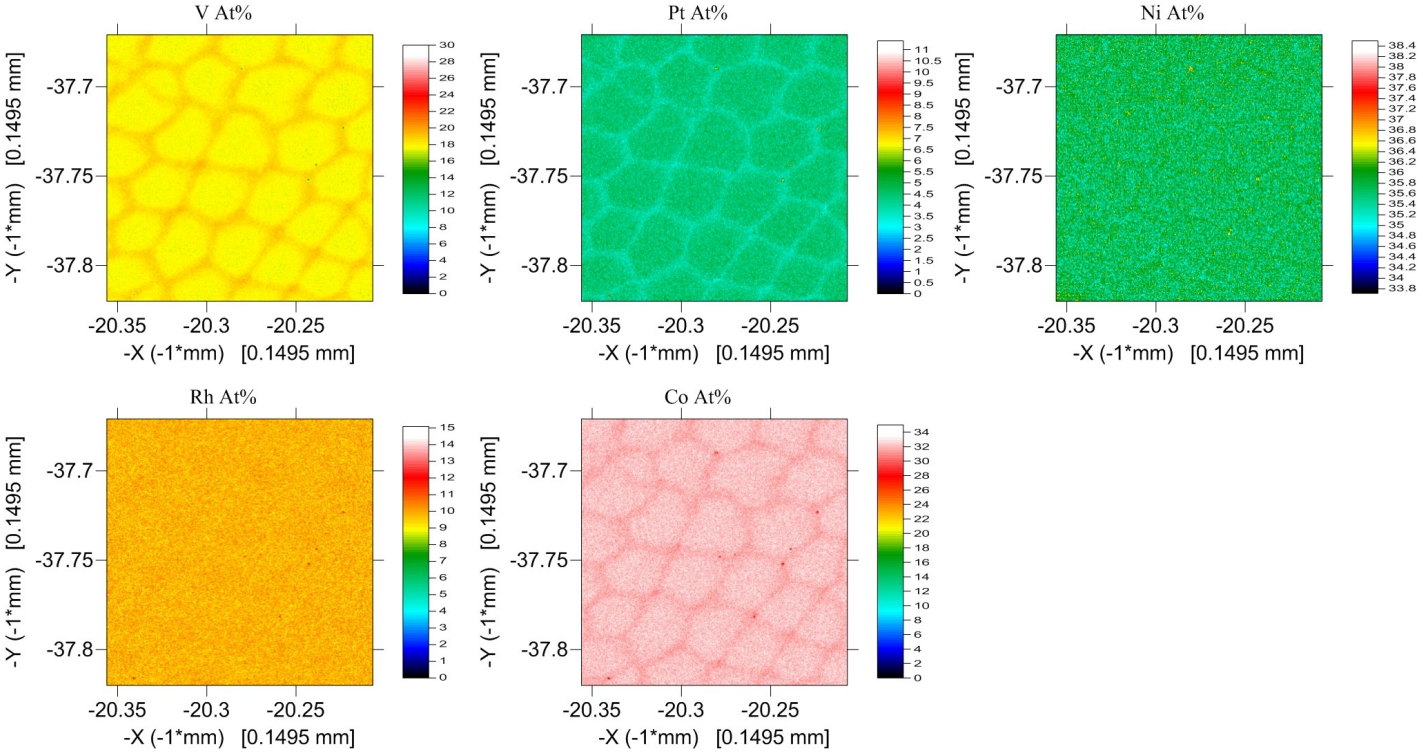

(b) High magnification

Figure 6.38: EPMA of as-cast $Pt_5Rh_{11}V_{14}Ni_{35}Co_{35}$

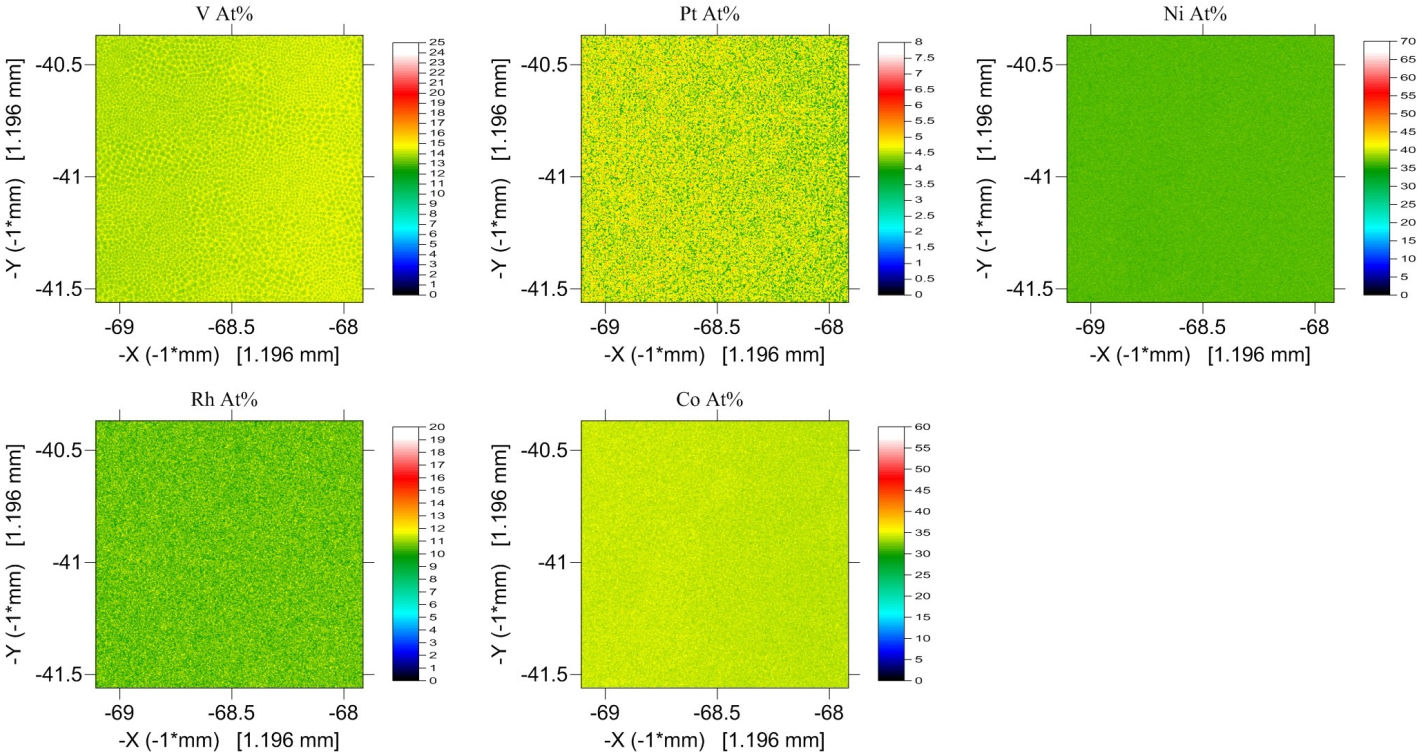

(a) Low magnification

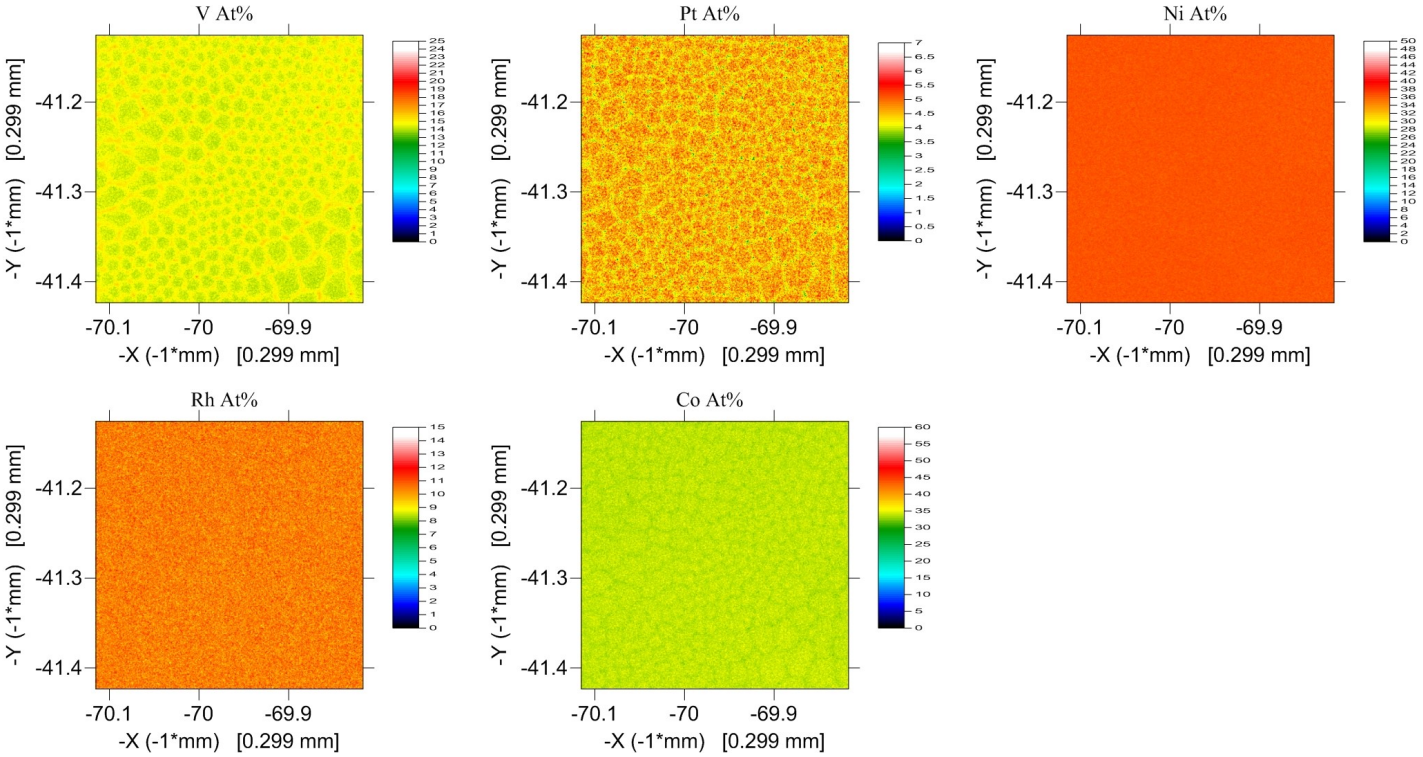

(b) High magnification

Figure 6.39: EPMA of annealed $Pt_5Rh_{11}V_{14}Ni_{35}Co_{35}$

In figure 6.40 we see that at low magnification Ni and Rh are very uniformly distributed. At high magnification, though, there is some noticeable minor segregation in Ni and Rh. Both at low and high magnification, Pt and Co are diffusing out of the dendrites and V is diffusing

into the dendrites.

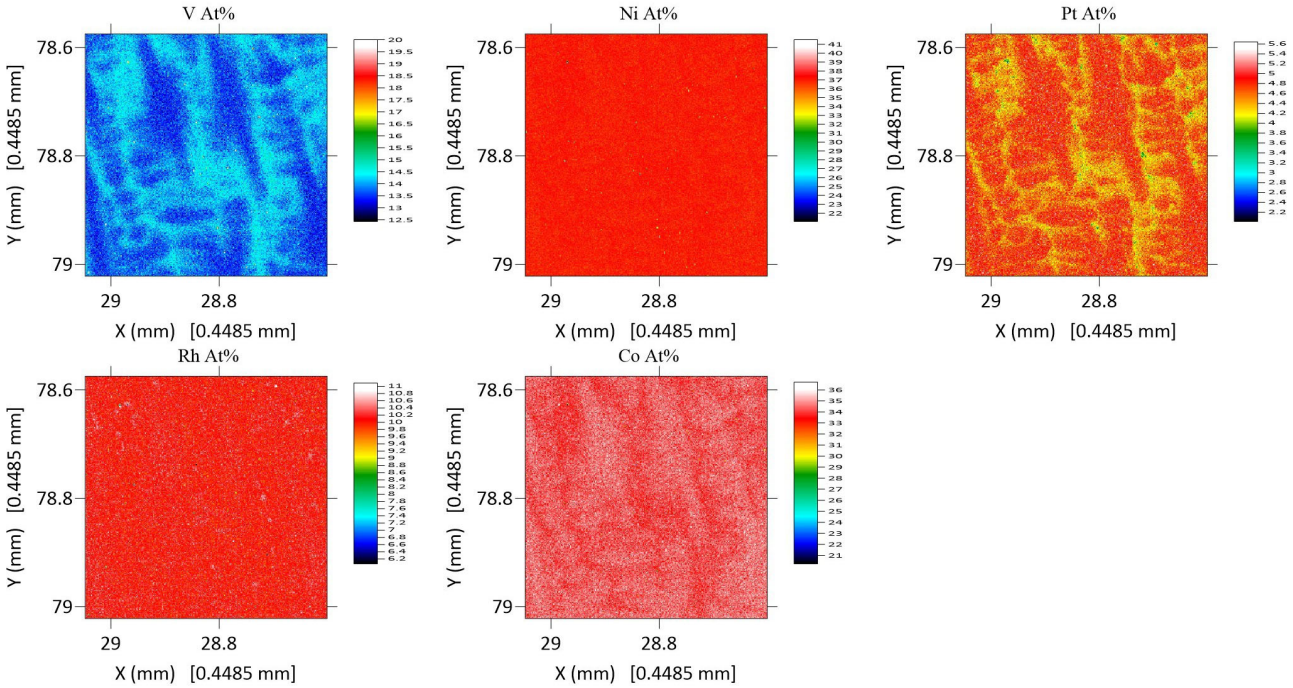

(a) Low magnification

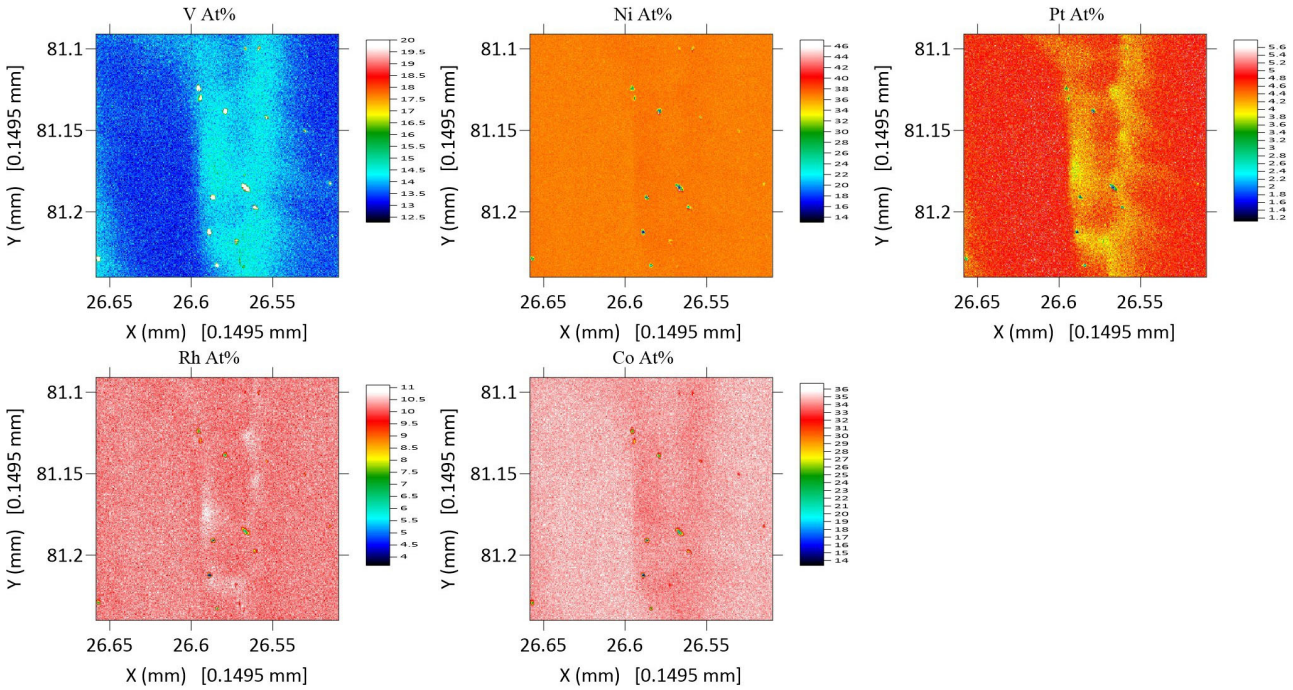

(b) High magnification

Figure 6.40: EPMA of as-cast $Pt_5Rh_{11}V_{14}Ni_{35}Co_{35}$, samples taken from a 1kg ingot

The EPMA image of the annealed $Pt_5Rh_{11}V_{14}Ni_{35}Co_{35}$ sample displayed in figure 6.41 shows an elongated, cellular dendrite structure. At low magnification Co is very uniformly distributed across the imaged area, as is Rh even though theres is some minor segregation into the dendrites.

At low magnification Co is more present out of the dendrites and Rh diffuses into the dendrites at a small degree. At low and high magnification we see that V and Ni are diffusing into the dendrites while Pt is diffusing out of the dendrites.

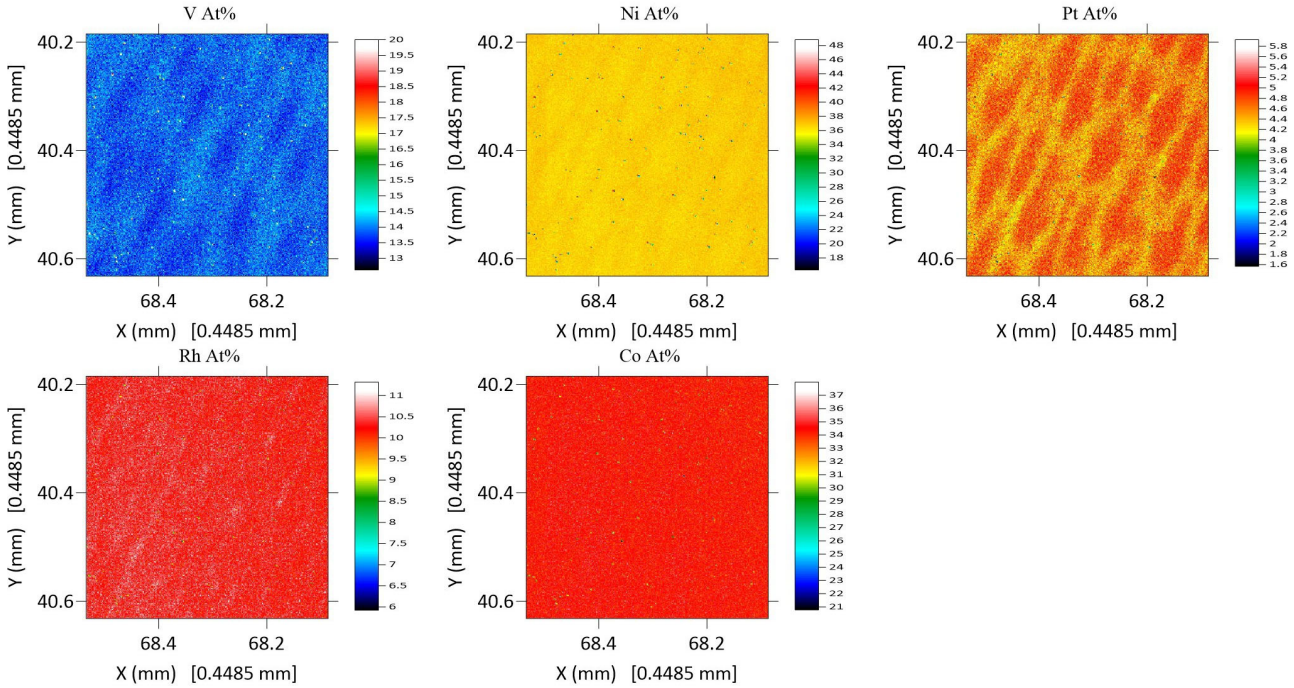

(a) Low magnification

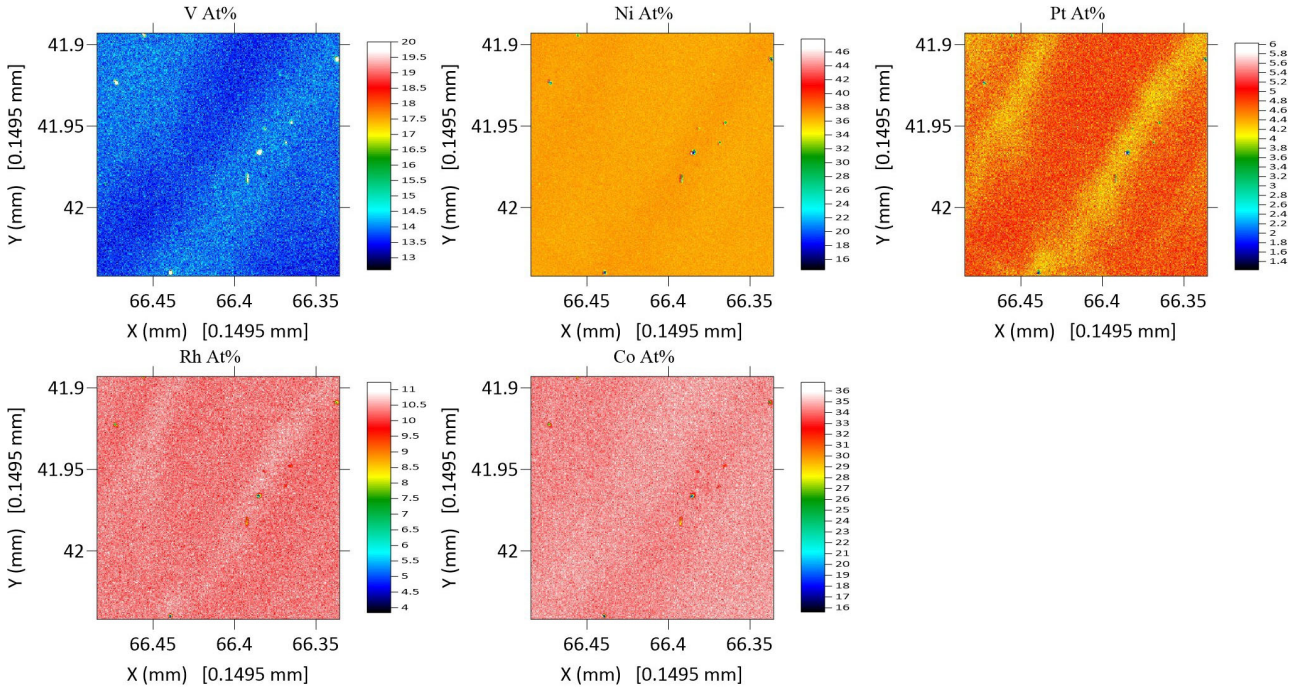

(b) High magnification

Figure 6.41: EPMA of annealed $Pt_5Rh_{11}V_{14}Ni_{35}Co_{35}$, samples taken from a 1kg ingot

Discussion

Laboratory scale EPMA shows segregation between V and PtCo, into the dendrites and out of the dendrites respectively. Also, the at.% of V in the imaged region is higher than expected indicating uneven mixing. Ni is uniform throughout and not separating from Rh or Pt as was observed in $Pt_7Rh_{23}Ni_{35}Co_{35}$ and $Pt_5Rh_{20}V_5Ni_{35}Co_{35}$.

The same is evident in the annealed sample but the elemental distribution is better aligned to what is expected of the intended composition, as is overall more homogeneous.

The ΔH_{AB} for all pairs in the alloy is negative, and some of these indicate the formation of very stable binary compounds is possible (i.e. $\Delta H_{\mathrm{PtV}} = -45$ $\Delta H_{\mathrm{VRh}} = -29$). It would, therefore, be expected that if there is segregationclustering particular elements together, that the strong binary enthalpy pairs would form intermetallic phases but V is very evenly distributed and is not observed clustering with Pt or Rh.

The same is observed in the industrially manufactured samples, with Pt and Co separating from V, in the as-cast and annealed samples. A high magnification inspection shows that Ni is to a very small degree present in the same areas that V is, as is Rh. Overall, the elemental distribution is very even, though.

6.4.3.6 Further Discussion of Alloy Structure

As with the other two PtRh based alloys, the results for the manufacturability trial on $Pth_5Rh_{11}V_{14}Ni_{35}co_{35}$ indicate that it is to some extent ductile and can be worked, this is consistent with observations made during the collection of data from the mechanical trials on the industrially manufactured samples as the as-cast and annealed samples were indented with ease and without cracks. The hardness data, as with $Pt_5Rh_{23}Ni_{35}Co_{35}$ and $Pt_5Rh_{20}V_5Ni_{35}Co_{35}$, indicates that the alloy can be deformed, when compared against standard data[221, 224]. There is some increase in modulus between as-cast and annealed samples (≈10GPa)s but the results are consistent when compared and indicate homogeneous mixing in the alloy overall. The DSC data shows that the alloy responds to heating similarly to $Pt_7Rh_{23}Ni_{35}Co_{35}$ and $Pt_5Rh_{20}V_5ni_{35}Co_{35}$. However, it shows the highest amount of weight gain in TGA in air; this is probably due to the high V content. TGA shows the weight gain follows a similar pattern to $Pt_5Rh_{20}V_5Ni_{35}Co_{35}$, the rate of weight gain is steady and increases at ≈170min. The performance of the alloy when heated in air is not ideal and the performance is even worse when considering the mass gain during the 1h hold at 1000°C. Overall, the alloy gains the most mass per unit surface area of any of these alloys and there appears to be a trend indicating a directly proportional relationship of increasing mass gain per unit surface area to increasing V content when comparing $Pt_7Rh_{23}Ni_{35}Co_{35}$, $Pt_5Rh_{20}V_5Ni_{35}Co_{35}$ and $Pt_5Rh_{11}V_{14}Ni_{35}Co_{35}$ (fig. 5.7).

6.4.4 $Ir_{35}Rh_{35}Co_5Ni_5Pt_{20}$

6.4.4.1 XRD

The lattice parameters for $Ir_{35}Rh_{35}Co_5Ni_5Pt_{20}$ were calculated from the data presented in figures 6.42 and 6.43, and are presented on table 6.17.

Manufacture scale	As-cast (Å)	Annealed (Å)
Laboratory	3.827	N/A
Industry	3.814	3.812

Table 6.17: Lattice parameter for $Ir_{35}Rh_{35}Co_5Ni_5Pt_{20}$ obtained from XRD data sets at different stages of manufacture and processing

Discussion

The lattice parameter for the laboratory manufactured sample and the industrially manufactured ingot cut offs, displayed on table 6.17, is very close. The lattice parameter for the industrially manufactured samples for as-cast and annealed are virtually identical at 0.002Å difference, this might indicate homogeneous mixing in the sample manufacture process. The lattice parameters for both the laboratory manufactured sample and industrially manufactured samples are both within the range between the lattice parameters for Rh and Ir, 3.803Å and 3.839Å, respectively. This is probably due to Rh and Ir being the elements present at the highest at.% content.

Figure 6.42 shows the XRD data collected for the laboratory manufactured sample (the industrial manufacture of the selected alloys was expedited so there was no heat treatment performed on the composition at this stage). Figure 6.43 displays the industry manufactured samples. The individual data for as-cast and annealed samples and a normalised comparison of the two are displayed in the figure.

There are 5 peaks present in figure 6.42, the peaks are consistent with the what is characteristic of an FCC crystal structure.

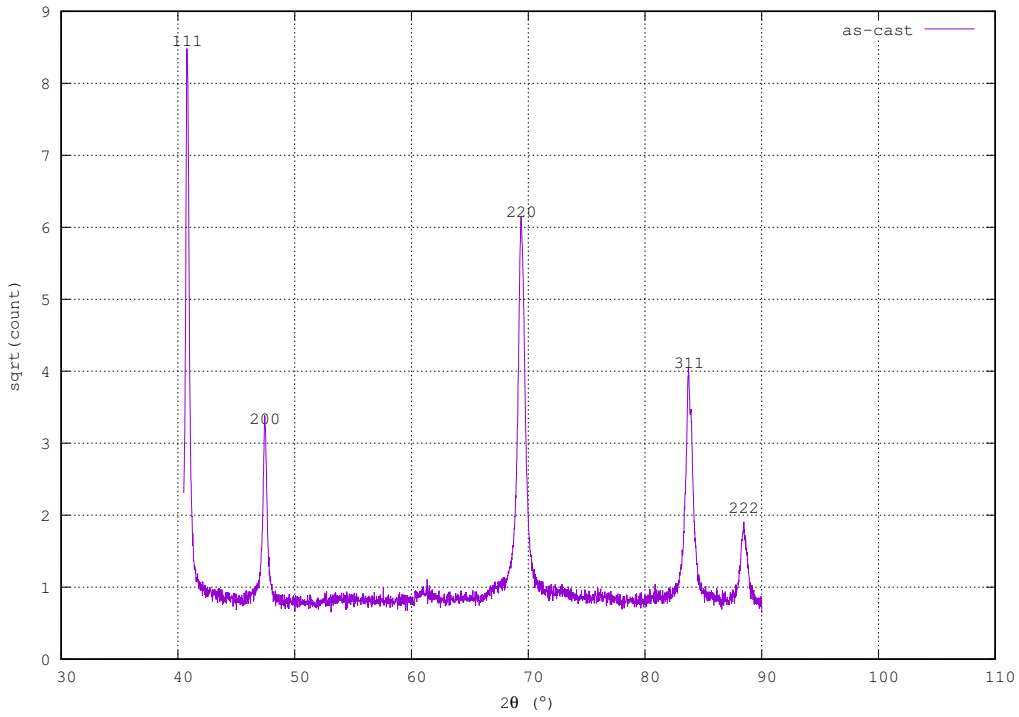

Figure 6.42: XRD of laboratory manufactured as-cast $Ir_{35}Rh_{35}Co_5Ni_5Pt_{20}$

There are 6 peaks and 5 peaks which agree with an FCC crystal structure in as-cast and annealed industry manufactured $Ir_{35}Rh_{35}Co_5Ni_5Pt_{20}$, respectively. Both as-cast and annealed share minor peaks and a wide mound at $\approx 42°$.

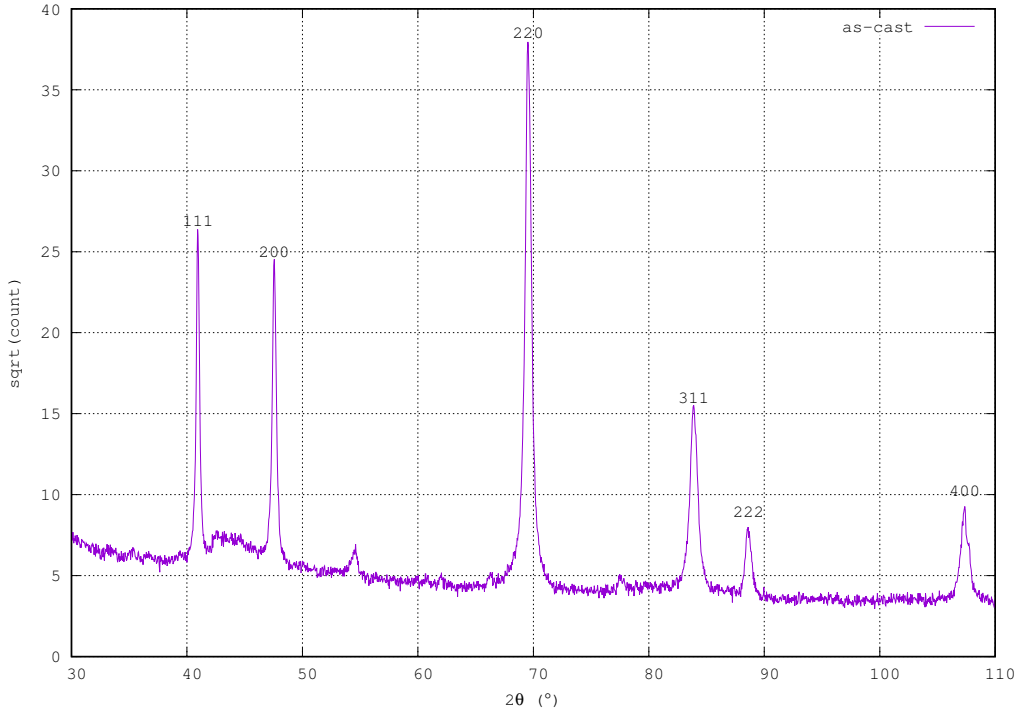

(a) as-cast

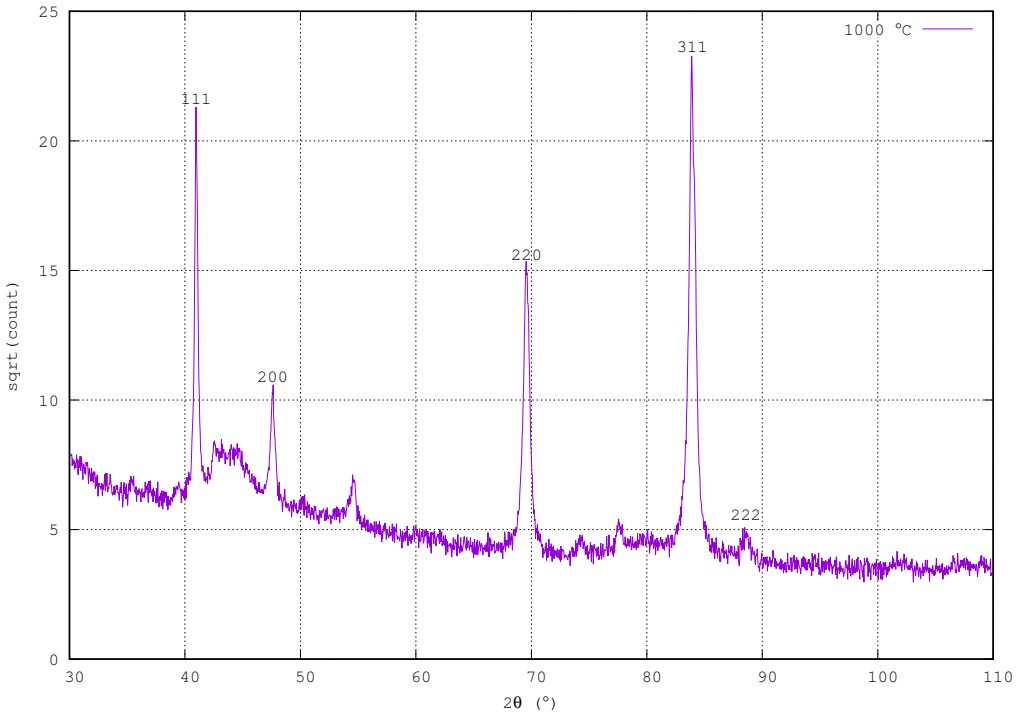

(b) annealed @ 1000°C

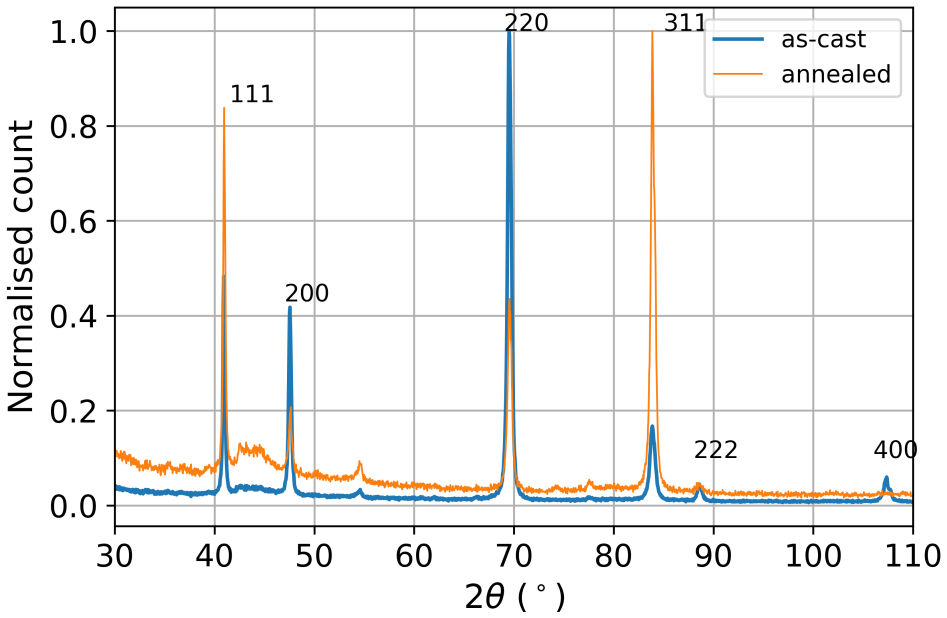

(c) Comparison of normalised XRD data for as-cast and annealed samples

Figure 6.43: XRD of $Ir_{35}Rh_{35}Co_5Ni_5Pt_{20}$ manufactured @ JMNM

Discussion

Inspecting the XRD data for the laboratory as-cast $Ir_{35}Rh_{35}Co_5Ni_5Pt_{20}$ (fig. 6.42) it appears that there is no strong indication of any intermetallic phases, the indexed peaks are sharp and narrow compared to the background. The peak positions and indexed peaks indicate an FCC

crystal phase but whether the alloy is single phase or multiphase is inconclusive due to some noise in the data and unindexed peaks.

The data for the industrially manufactured samples shows that they are in agreement with each other, exhibiting the consistent peaks in consistent positions. There is a peak in both at ≈55° and some small peaks between 70° and 80° that cannot be indexed, possibly minor secondary phases or artifacts due to surface impurities or impurities present in the casting crucible. Both share a hump between 40° and 50°, which might be due to the background rather than secondary phases. The annealed alloy does not show a visible peak corresponding to (4 0 0) lattice planes and the background noise is stronger.

We can see that the peak intensity changeswhich may be due to changes in the local orientations or textures examined, as discussed before for other alloys. From the optical micrographs we can see that the as-cast sample does exhibit a grain size variation, as does the annealed sample but at different grain size magnitudes.

Overall, the data agree with an FCC crystal structure as the main phase in this alloy.

6.4.4.2 XRF

The quantitative XRF data for the industry manufactured alloys are given in tables 6.18a and 6.18b in the as-cast and annealed states, respectively.

Note that XRF data was not collected for the laboratory manufactured alloy due to the decision to expedite the industrial manufacture.

	XRF (.wt%)	at.%	at.%→wt.%
Ir	51.01±1.0	35	45.40
Rh	18.56±1.0	35	24.30
Co	1.89±0.2	5	1.99
Ni	2.33±0.2	5	1.98
Pt	25.92±1.0	20	26.33

(a) As-cast

	XRF (.wt%)	at.%	at.%→wt.%
Ir	52.31±1.0	35	45.40
Rh	15.09±1.0	35	24.30
Co	1.81±0.2	5	1.99
Ni	1.71±0.2	5	1.98
Pt	28.18±1.0	20	26.33

(b) Annealed

Table 6.18: XRF of industrial scale manufactured $Ir_{35}Rh_{35}Co_5Ni_5Pt_{20}$

Discussion

XRF data for the industrially manufactured as-cast and annealed alloy samples show some differences, of the order of several percent. There are significant differences in the wt.% content of Rh across the two samples. Moreover, the sample wt.% content is very different from the nominal in the amount of both Ir and Rh.

Comparing with the EPMA data (fig. 6.51, 6.52), however, we can see that the Ir is close to the expected content but we can see that the Rh is indeed lower than expected, as with the XRF data. We can see that Rh is segregating from Ir in both as-cast and annealed samples. Examination of the Rh-Ir phase diagram shows that, although they show mutual solid solubility at high temperatures, below about 1500°C there is a miscibility gap, and the two elements show little solid solubility at room temperature. This is very similar to what we observe with the XRF data, where the Ir content is higher than expected and the Rh is lower than expected. Since the data came from sample cut offs, we would expect so see high variation in mixing and inhomogeneity across the 1kg ingot.

6.4.4.3 Optical micrographs

Optical micrographs for $Pt_7Rh_{23}Ni_{35}Co_{35}$ are presented in figure 6.44a and b, respectively. In table 6.19 we present a grain size analysis of the visible grains for figure 6.44a and b, respectively.

Note that figures 6.44a and b were obtained using different data acquisition equipment and software, hence the variation in image quality, resolution and magnification.

In figure 6.44a we see that the grain structure is irregular. Some grains are small and equiaxed while others are large and elongated. The different types of grain appear to be separated into their own areas rather than being spread around. In fugure 6.44b we see that the grains are more regular in size.

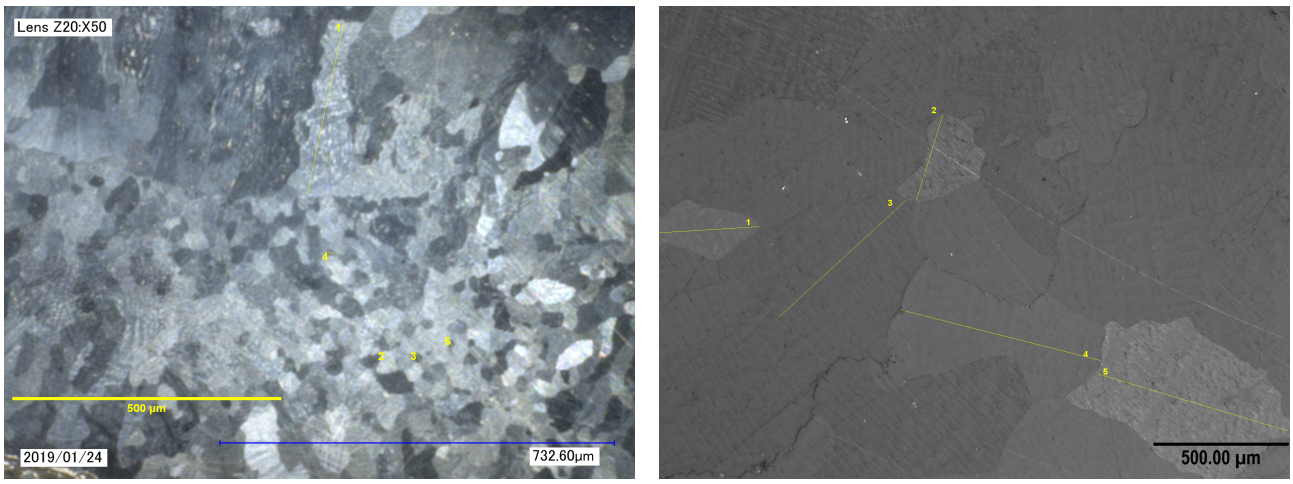

(a) as-cast **(b)** annealed 5x magnification

Figure 6.44: $Ir_{35}Rh_{35}Co_5Ni_5Pt_{20}$ optical images of as-cast and etched and annealed and etched samples

	Length (µm)
1	326
2	41
3	18
4	16
5	10

(a) Figure 6.44a grain analysis

	Distance (µm)
1	1440
2	953
3	1802

(b) Figure 6.44b grain analysis

Table 6.19: Grain sizes for the optical micrographs for industrially manufactured $Ir_{35}Rh_{35}Co_5Ni_5Pt_{20}$

Discussion

The grain growth in the alloy is uneven which is to be expected given the rate of change of the cooling rate across the 1kg ingot. In contrast to the as-cast alloy, the annealed alloy does appear to have a more even grain size across most of the sample, it also looks a lot like the grains revealed under BSE SEM in the laboratory manufactured alloy (fig. 6.45a). A similar grain structure is apparent in fig. 6.48, while the as-cast alloy (fig. 6.47) shows uneven grain growth consistent with a difference in cooling rate across the sample, which would result from the size of the ingot in the case of a 1kg melt, with the first material to solidify cooling rapidly, but the solidification rate decreasing towards the ingot centre.

Comparing the microscopy data with the XRD data, we can see that the change in grain structure could be the reason behind the shift in peak intensities in the annealed sample XRD data (fig. 6.43). As elastic behaviour is not strongly dependent on grains the difference in grain size is not seen to affect the modulus of elasticity.

Again, we cannot draw firm conclusions using just the presented images but having compared them with the XRD data and the elastic modulus change we can see what the microstructure tends to be like in this alloy.

6.4.4.4 SEM-EDX

The EDX map data for the as-cast sample of the laboratory manufactured alloy of $Ir_{35}Rh_{35}Co_5Ni_5Pt_{20}$ are displayed on figures 6.45 and 6.46. Note that no annealed samples were produced due to the industrial scale manufacture being expedited.

The backscatter SEM images of the industry manufactured alloy are displayed on figures 6.47 and 6.48 for as-cast and annealed, respectively. Likewise, the EDX map data for the samples are displayed in figures 6.49 and 6.50.

Laboratory scale

In figures 6.45 and 6.46 we see that all elements are uniformly spread across the imaged surface. However, there is noticeable segregating in and out of the dendrites, this is more visible in figure 6.46 in Ir, Co, Ni and Pt.

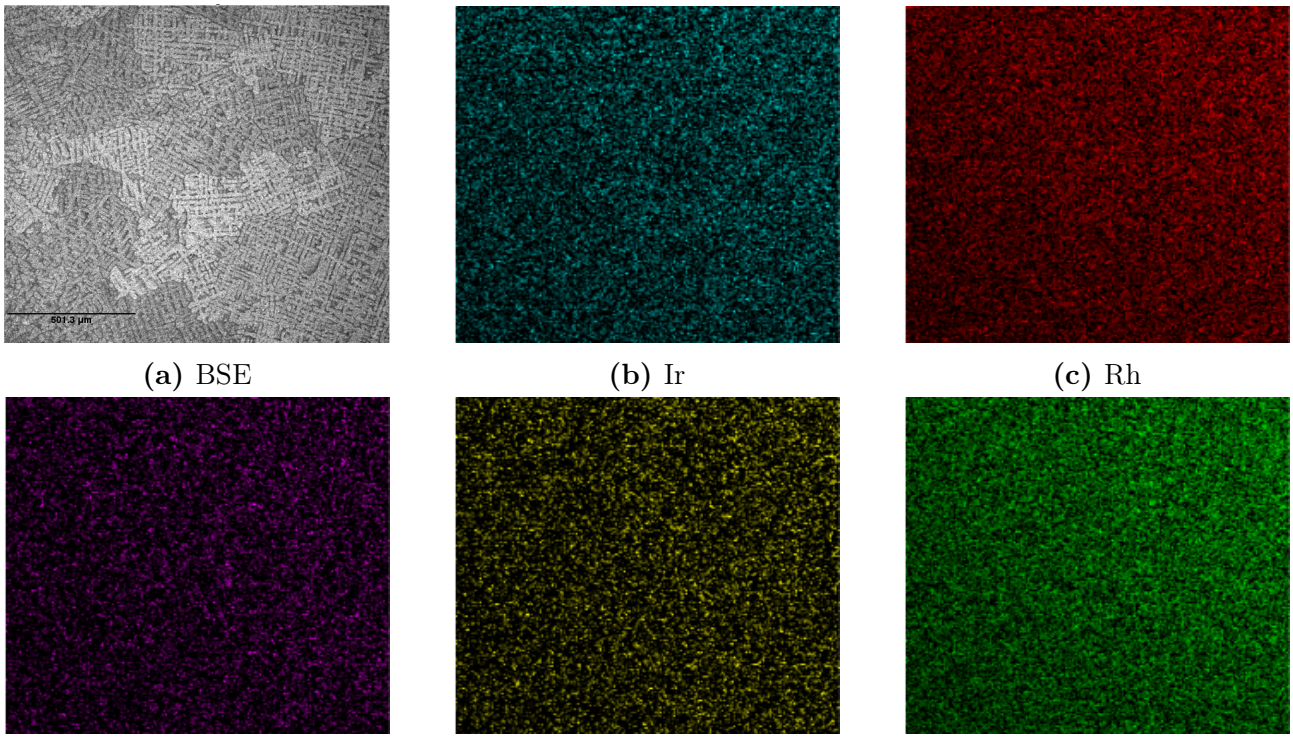

(a) BSE **(b)** Ir **(c)** Rh

(d) Co **(e)** Ni **(f)** Pt

Figure 6.45: EDX map of as-cast $Ir_{35}Rh_{35}Co_5Ni_5Pt_{20}$ taken at 200x magnification

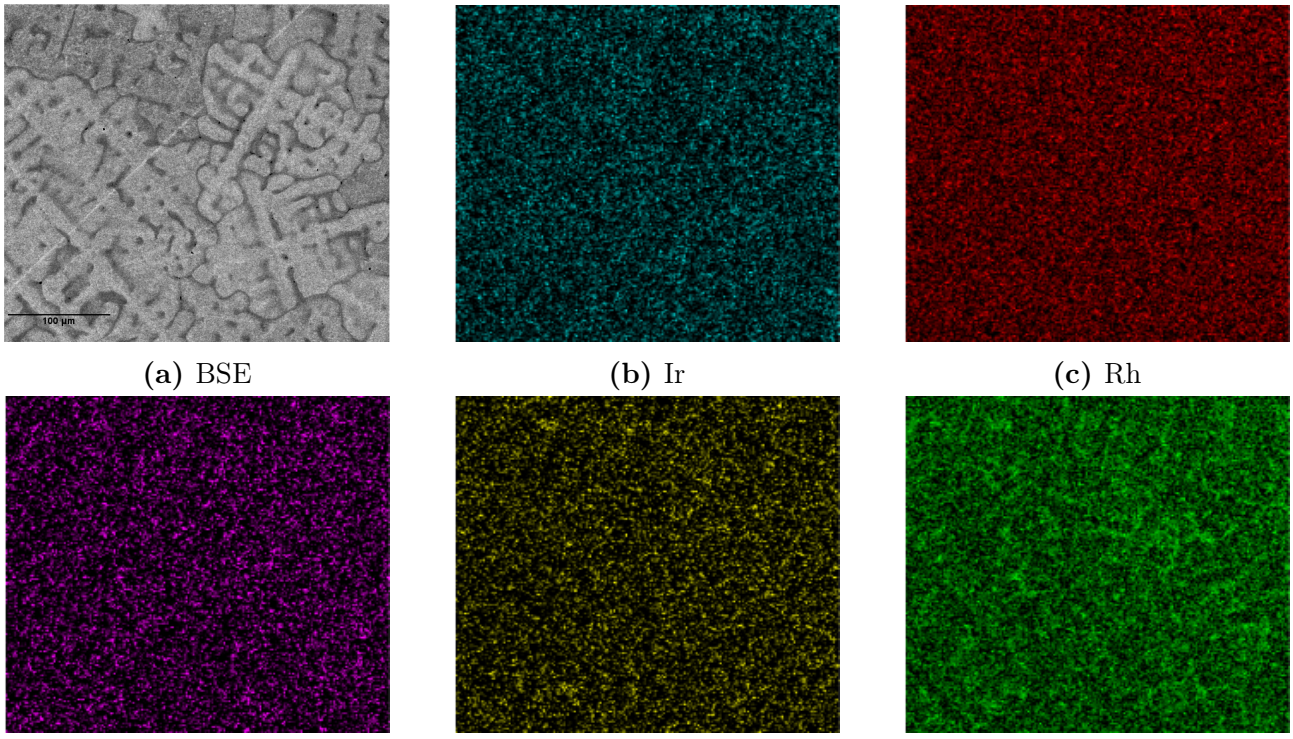

(a) BSE **(b)** Ir **(c)** Rh

(d) Co **(e)** Ni **(f)** Pt

Figure 6.46: EDX map of as-cast $Ir_{35}Rh_{35}Co_5Ni_5Pt_{20}$ taken at 800x magnification at a grain interface

Discussion

EDX maps (fig. 6.45, 6.46) show the elemental distribution with some areas of segregation evident, particularly in Pt, and with this being more prominent in the annealed map (fig. 6.46). The grain and dendritic growth appears regular in the BSE images, probably due to the fast cooling rates given the small size of the laboratory manufactured alloy sample.

In the as-cast alloy, the distribution of Co, Ni and Ir appears uneven, with some spotting in the map, which correlates in general terms with the underlying dendritic structure revealed by the BSE image. This is very likely to be due to segregation of these elements during solidification.

In fig. 6.46 there appears to be some uneven deposition of Pt, with it being present at higher concentration in the interdendritic regions. Ir and Co are seen to favour the interior of the dendrites. Ni appears to be segregating away from Ir, Co and Pt, while Rh has a very uniform distribution. Above the scale of the dendrites however the overall distribution of the elements appears even, indicating that suitable mixing of the elements took place.

Industrial scale The as-cast sample in figure 6.47 does not appear to have a regular grain pattern or dendrite structure. Figure 6.48 We see that the dendrite structure is more regular and that the grains appear to not have a specific shape but are of similar size.

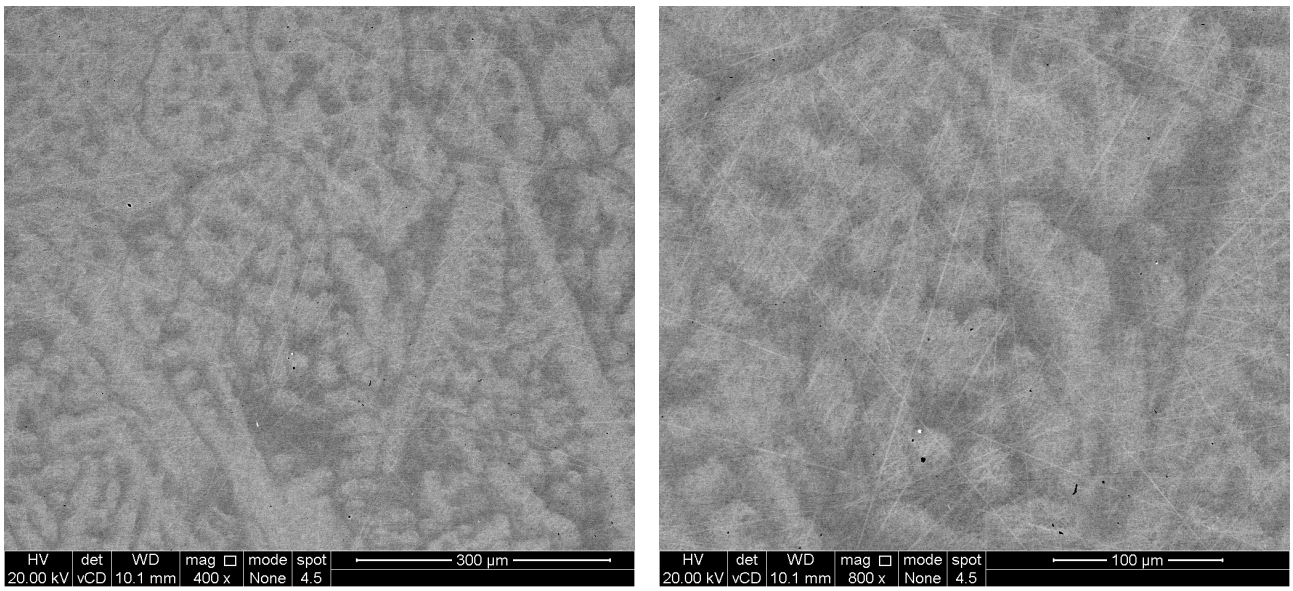

(a) 400x magnification **(b)** 800x magnification

Figure 6.47: BSE images of as-cast $Ir_{35}Rh_{35}Co_5Ni_5Pt_{20}$

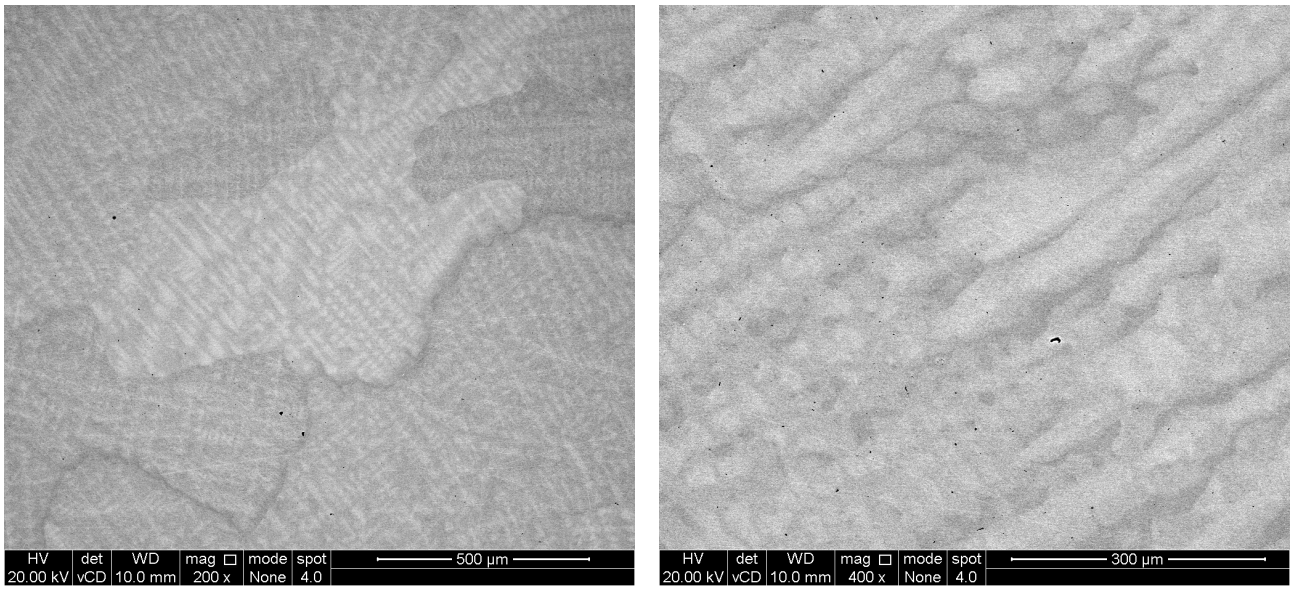

(a) 200x magnification **(b)** 400x magnification

Figure 6.48: BSE images of annealed $Ir_{35}Rh_{35}Co_5Ni_5Pt_{20}$

Discussion

We can see the presence of different types (principally delineated by different scales and degrees of branching) of dendritic growth across the as-cast sample. This is probably due to the difference in cooling rate across the sample due to the large size of the 1kg ingot.

The heat treatment has not done much to remove the evidence of dendritic growth but the dendritic structure may appear more even and regular. The heat treatment temperature probably needed to be higher to fully homogenise the sample.

In figure 6.49 we see that all elements are uniformly distributed across the imaged surface but that there is some segregation, particularly in Ir, Co, Ni and Pt. There is some diffusion in and out of the dendrites, most noticeable in Ir and Pt.

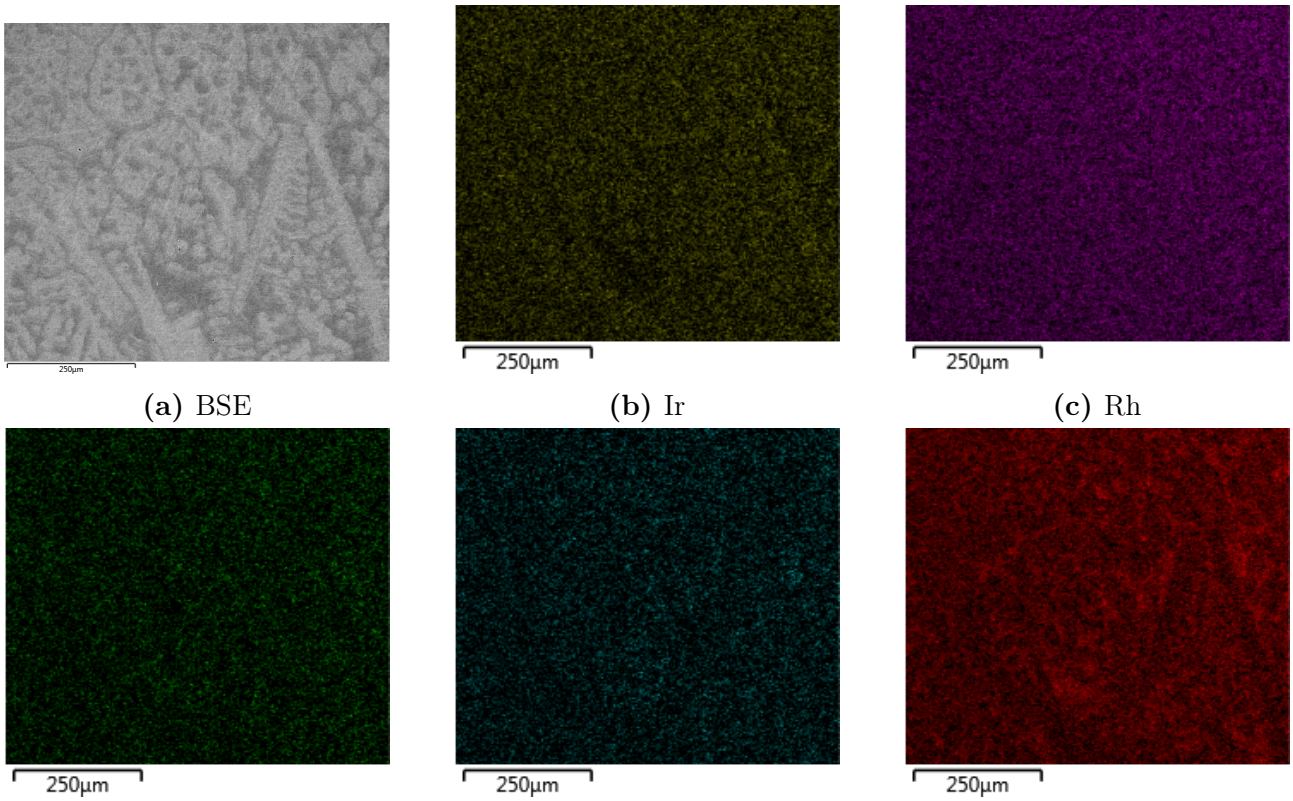

(a) BSE **(b)** Ir **(c)** Rh

(d) Co **(e)** Ni **(f)** Pt

Figure 6.49: 400x magnification EDX map of as-cast $Ir_{35}Rh_{35}Co_5Ni_5Pt_{20}$

We see that the elements are uniformly distributed in figure 6.50 but with some segregation. The segregation is more noticeable in Pt, Ni and Co, in particular.

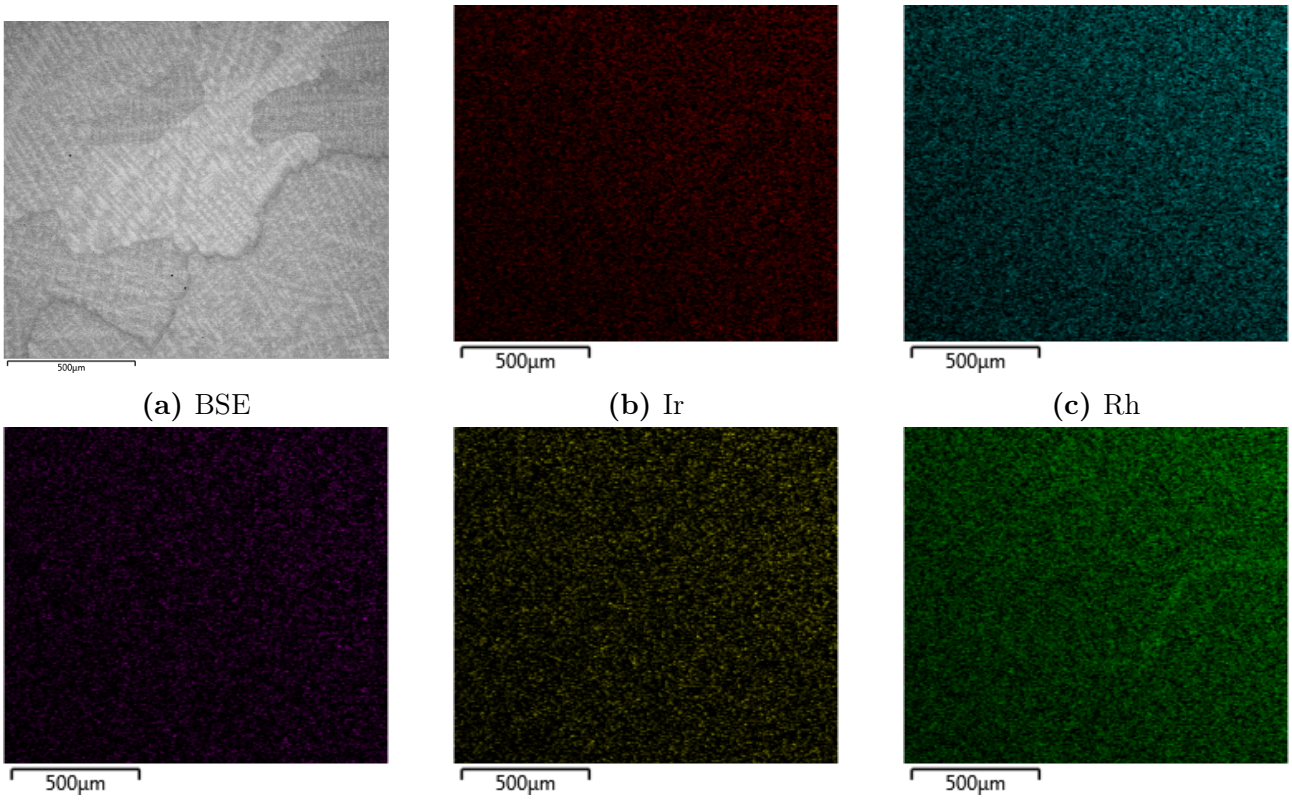

(a) BSE **(b)** Ir **(c)** Rh

(d) Co **(e)** Ni **(f)** Pt

Figure 6.50: 200x magnification EDX map of annealed $Ir_{35}Rh_{35}Co_5Ni_5Pt_{20}$

Discussion

EDX data (fig. 6.49, 6.50) is rather faint, but does show similar segregation of Pt as with the laboratory scale alloy. Pt seems to be segregating from Ir in both as-cast and annealed samples but more starkly in the as-cast sample. There is noticeable segregation in all elements in both as-cast and annealed samples that, from the correspondence with the dendritic structure, looks like solidification segregation.

The segregation is confirmed in inspecting the EPMA data as there is a stark contrast in the composition of the dendrites and the cells described by the dendrites. The strong compositional differences seen are probably indicative of there being multiple phases, with the main one having an FCC structure.

6.4.4.5 EPMA

EPMA data for the as-cast and annealed samples of the industry manufactured alloys are displayed on figures 6.51 and 6.52.

Industrial scale In figure 6.51 we see that there is segregation and diffusion in and out of the dendrites. Ir is diffusing out of the dendrites and away from the other elements while the other elements are more concentrated in the dendrites. The same is observed in figure 6.52, where Ir is segregating from the other elements.

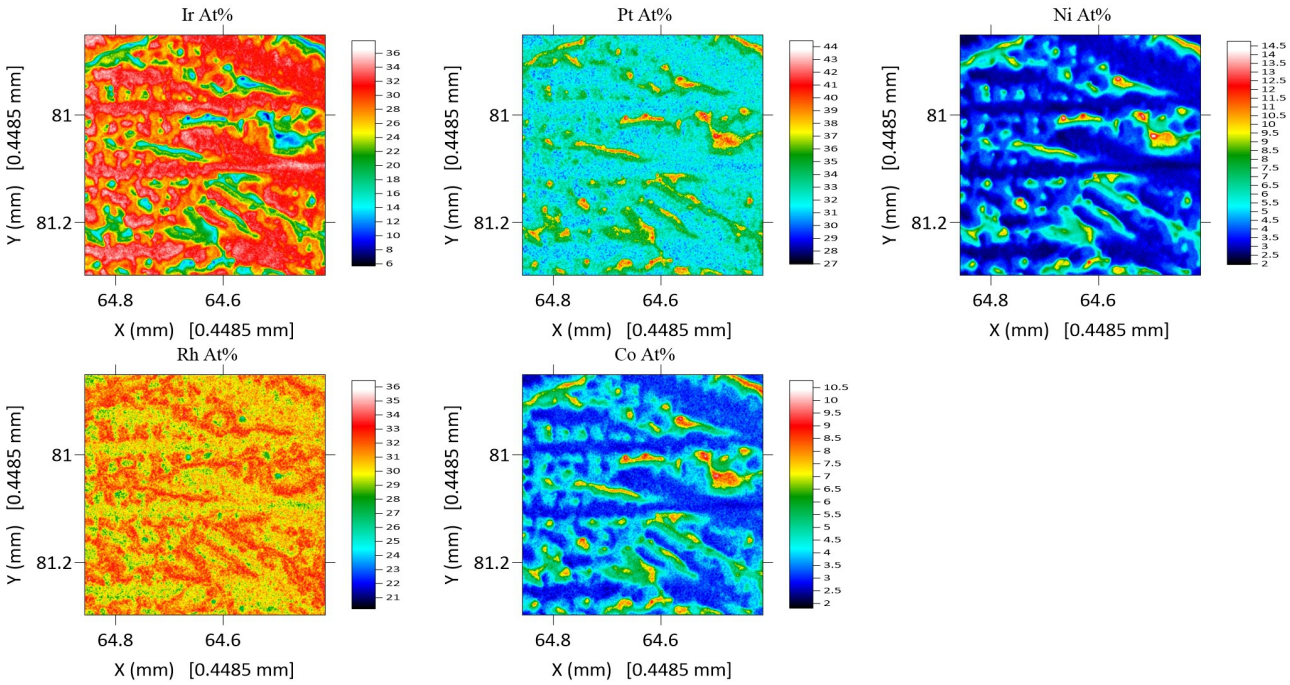

(a) Low magnification

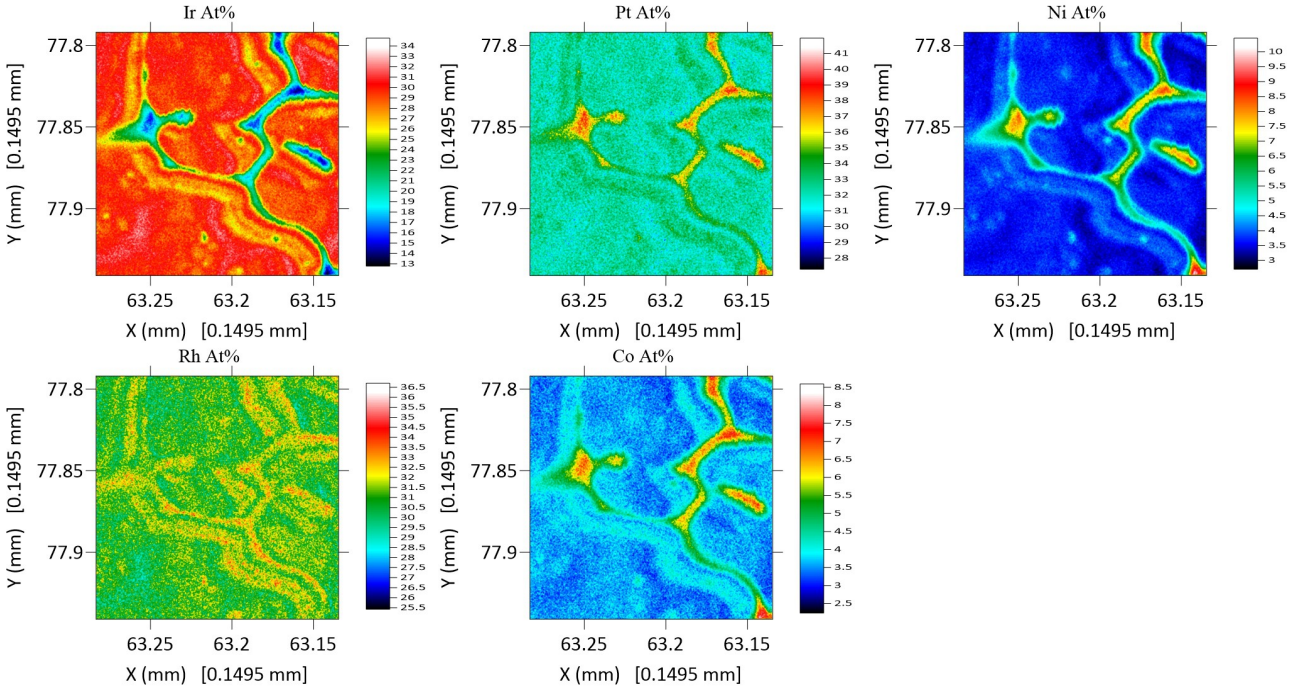

(b) High magnification

Figure 6.51: EPMA of as-cast $Ir_{35}Rh_{35}Co_5Ni_5Pt_{20}$, samples taken from a 1kg ingot

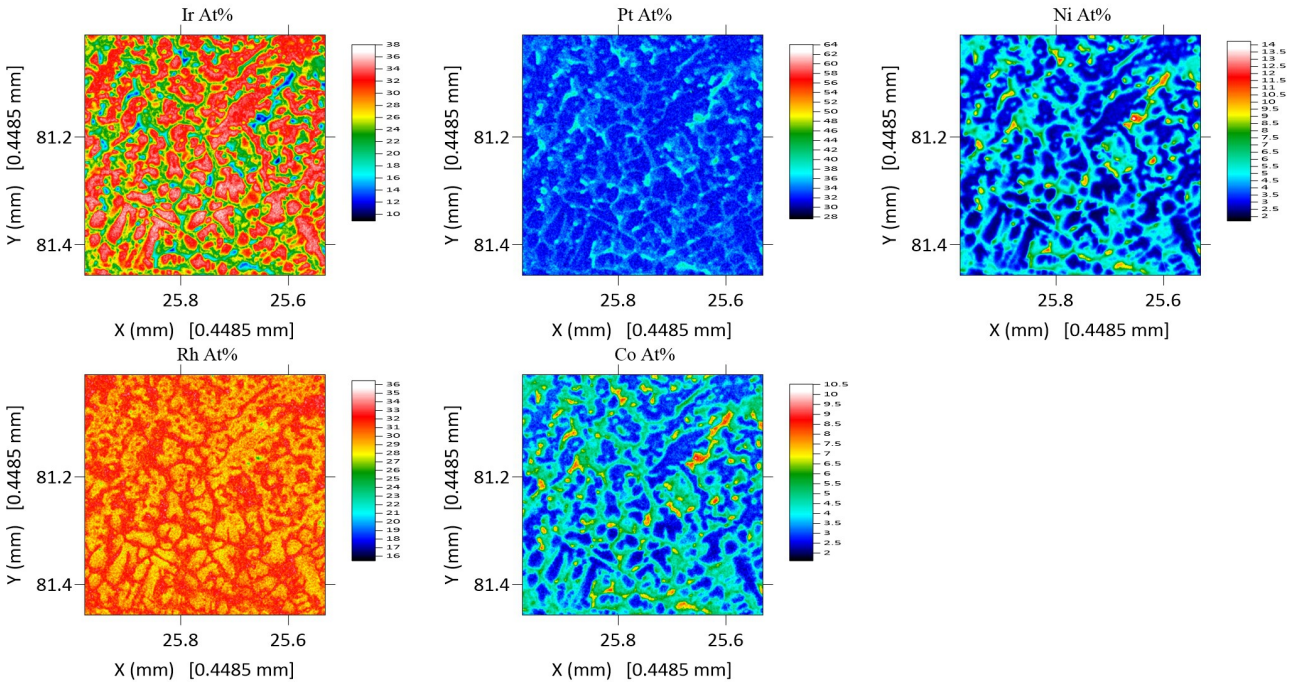

(a) Low magnification

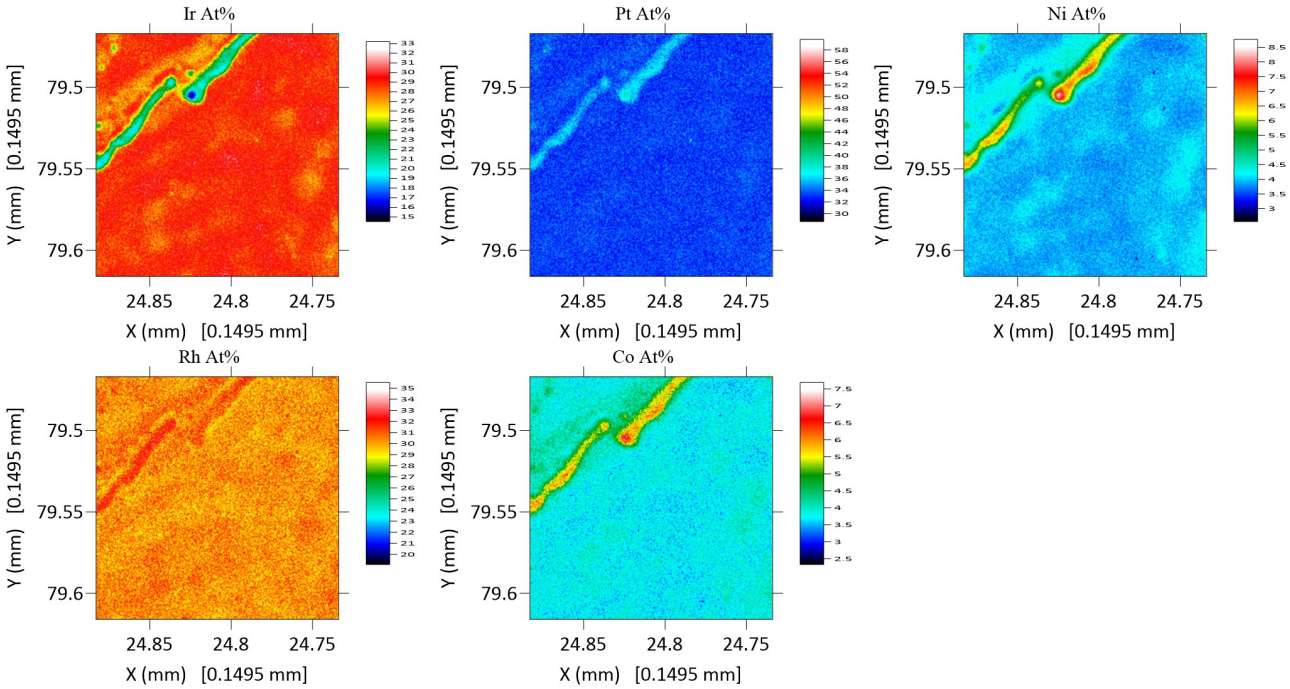

(b) High magnification

Figure 6.52: EPMA of annealed $Ir_{35}Rh_{35}Co_5Ni_5Pt_{20}$, samples taken from a 1kg ingot

Discussion

In the data presented above, the Pt content of the examined region is much higher than the overall nominal composition of the alloy. There could be a number of reasons for this, including human error in weighing the raw materials, uneven mixing of raw materials pre

melting, or uneven mixing during melting. In the as-cast and annealed alloy, it appears that Ir is segregating from the rest of the components. It is evident that Ir might not alloy well with the rest of the components, which would probably be expected as examination of the binary phase diagrams shows that at room temperature the degree of mutual solid solubility is low with all of the components, except for Ni. However, the ΔH_{AB} for most Ir pairs in this alloy does not support this as it is negative. A reason for this might be $\Delta H_{\mathrm{RhIr}} = 1$, which could be introducing the segregation in Ir since areas of high at.% of Rh are depleted in Ir and vice versa (fig. 6.51, fig. 6.52). This coupled with the other elements possibly having a higher affinity for Rh might be the reasons for segregation.

Moreover, the similarity in the segregation in the as cast and annealed alloy samples indicated that the heat treatment temperature was, perhaps, too low to promote homogenisation.

6.4.4.6 Further Discussion of Alloy Structure

DSC data shows that the alloy is very stable to phase transformations and at temperatures up to 1400°C, an incomplete phase transformation, probably tending towards melting is observed between 1150 - 1400°C, however the appropriate equipment to explore this further was not available. Out of all the alloys, $Ir_{35}Rh_{35}Co_5Ni_5Pt_{20}$ responded the best to heating up to 1000°C in air as is evident by the TGA data, gaining virtually no mass per unit surface area. It also performed well in the isothermal part of the study where it appears to have gained no mass from the air. In figure 5.7 it is evident that $Ir_{35}Rh_{35}Co_5Ni_5Pt_{20}$ having a high PGM at.% content does not react with air at temperatures up to 1000°C.

Overall, there is evidence of a simple FCC crystal phase in this alloy, especially in the laboratory manufacture stage, however, the data are inconclusive. In studying the industrially manufactured alloy, there appear to be inconsistencies with what is expected from the intended composition and the composition results from the XRF characterisation in Ir and in Rh, with the characterised surface having a lower wt.% content in Rh by ≈6 - 9wt.% and higher wt.% in Ir at ≈6 - 7wt.%. This might be due to insufficient mixing in melt or due to the positive pairwise enthalpy of RhIr, $\Delta H_{\mathrm{RhIr}} = 1\mathrm{kJ\,mol^{-1}}$, the influence of the pairwise enthalpy on the overall alloying behaviour is discussed further in section 6.6.1

6.4.5 $\mathbf{Ir_{12}Fe_{33}Co_{20}Ni_{30}Pt_5}$

6.4.5.1 XRD

The lattice parameters for the laboratory and industrially manufactured samples were calculate from the data displayed in figures 6.53 and 6.54. The lattice parameters are displayed on table 6.20.

Manufacture scale	As-cast (Å)	Annealed (Å)
Laboratory	3.631	N/A
Industry	3.638	3.637

Table 6.20: Lattice parameter for $Ir_{12}Fe_{33}Co_{20}Ni_{30}Pt_5$ obtained from XRD data sets at different stages of manufacture and processing

Discussion

The lattice parameter for the laboratory manufactured sample and the industrially manufactured samples are in very good agreement with each other. Moreover, the industrially manufactured sample has virtually the same lattice parameter after heat treatment, indicating that the composition is stable. Interestingly, the lattice parameter is close to the lattice parameter of the PGM constituents rather than the more abundant Fe, Co and Ni in the composition[223]. This is probably due to the atoms of Pt and Ir being larger and therefore distorting the lattice.

Figure 6.53 shows the XRD data collected for the laboratory manufactured sample (the industrial manufacture of the selected alloys was expedited so there was no heat treatment performed on the composition at this stage). Figure 6.54 displays the industry manufactured samples. The individual data for as-cast and annealed samples and a normalised comparison of the two are displayed in the figure.

Laboratory scale The XRD data displayer in figure 6.53 is very noisy. Nevertheless, there are two identifiable peaks. In figure 6.54, the peaks present, and their spacing, for both as-cast and annealed samples are consistent with an FCC crystal structure.

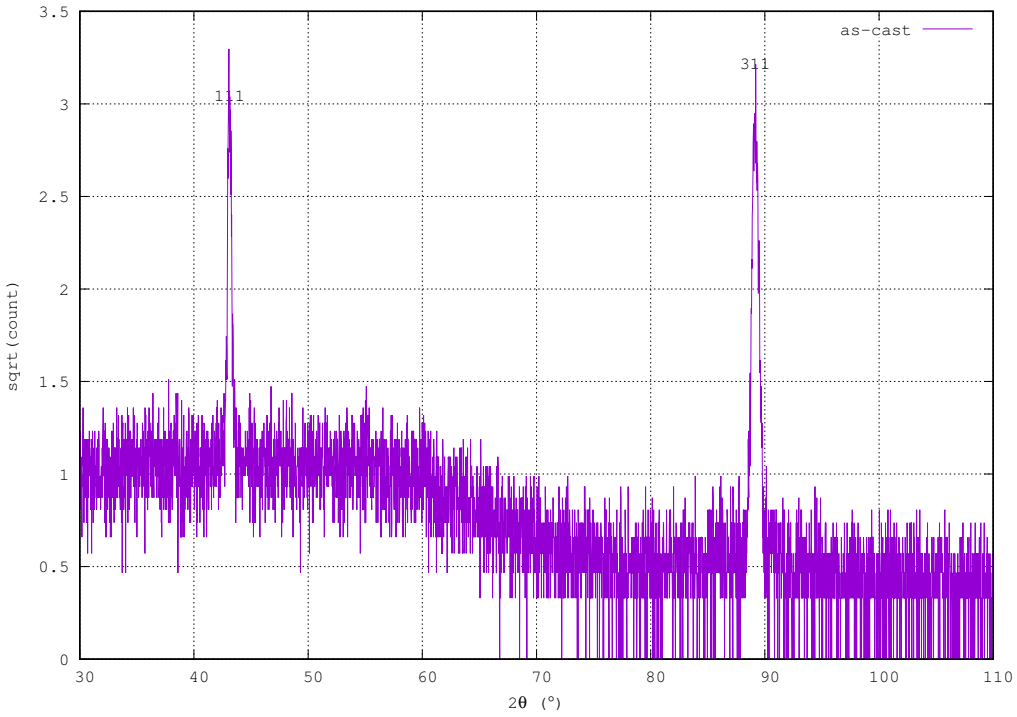

Figure 6.53: XRD of laboratory manufactured as-cast $Ir_{12}F_{33}Co_{20}Ni_{30}Pt_5$

Industrial scale

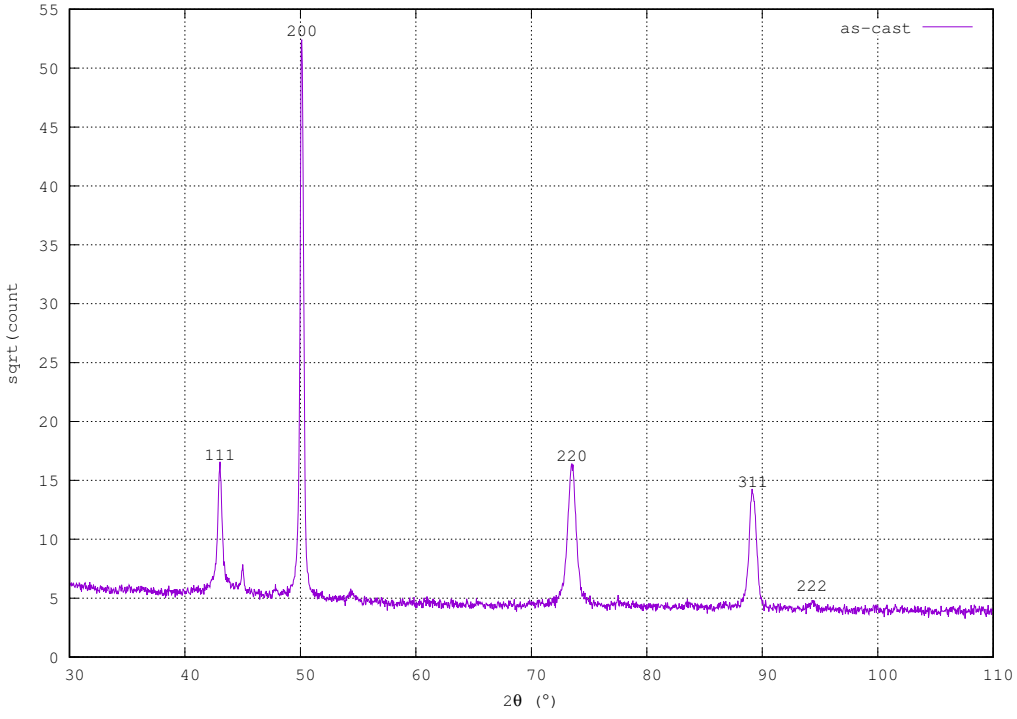

(a) as-cast

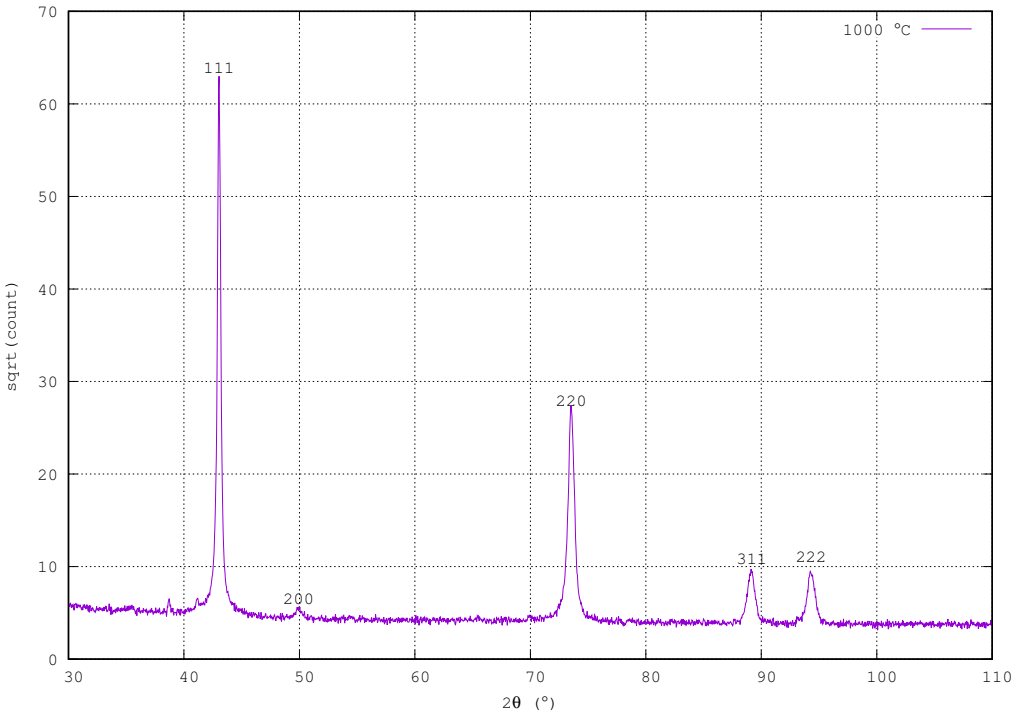

(b) annealed @ 1000°C

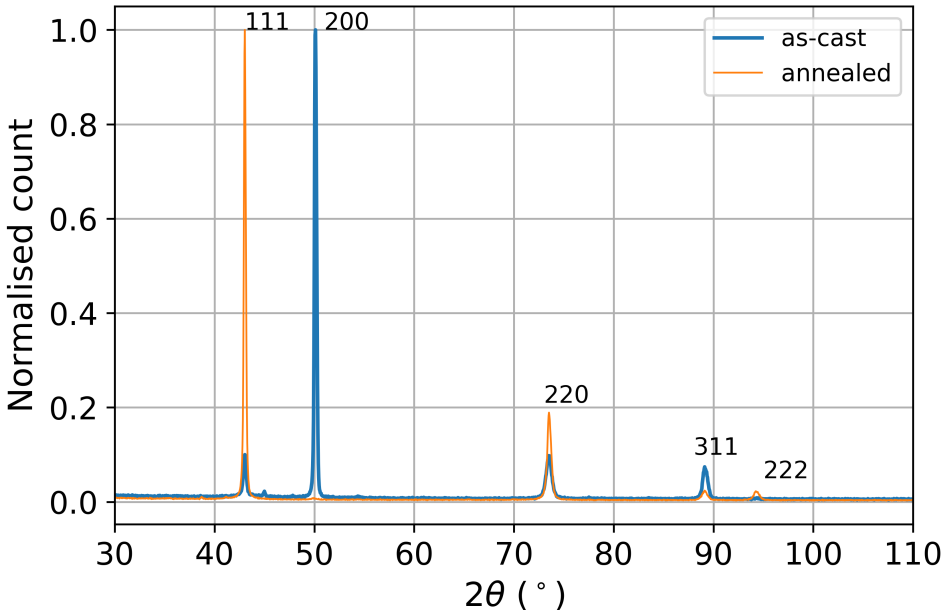

(c) Comparison of normalised XRD data for as-cast and annealed samples

Figure 6.54: XRD of $Ir_{12}Fe_{33}Co_{30}Ni_{30}Pt_5$ manufactured @ JMNM

Discussion

The as-cast laboratory manufactured $Ir_{12}Fe_{33}Co_{20}Ni_{30}Pt_5$ alloy has a very noisy XRD pattern, likely due to the low number of counts collected for the pattern generally, meaning that

the peaks are indistinct (fig. 6.53). However the two peaks (1 1 1) and (3 1 1) and their positions agree with the general peak positions and lattice planes associated with FCC structures.

Comparing the laboratory scale XRD trace with the industrial manufactured XRD traces for as-cast and annealed samples (fig. 6.54), the peaks determined to be corresponding to the (1 1 1) and (3 1 1) lattice planes are in the same 2θ position as with the laboratory scale as-cast alloy. The peak positions in the industrial scale XRD traces and the lattice planes associated with them agree with an FCC crystal structure, however, it is evident that there might be a small presence of other phases.

Comparing the as-cast and annealed industrially manufactured sample we can see that the peaks determined to be corresponding to the (1 1 1) and (2 2 0) lattice planes are more prominent after heat treatment, while the (2 0 0) has become very small. The data indicates that the alloy has relatively large grains, an their orientation is affecting the intensity distribution in the patterns. We have insufficient data from the optical micrographs to compare and confirm this to a high degree of precision, though the grains observed in these alloys generally are large, as would be expected for cast material. If we look at the elastic moduli before and after heat treatment we can see that they are fairly similar, which implies there has not been a radical transformation of the alloy structure on heat treatment, consistent with what is observed.

Heat treatment apears to have removed some unidentifiable peaks from the as-cast to the annealed form of the alloy. Perhaps, the heat treatment homogenised the alloy and removed faint secondary phases.

6.4.5.2 XRF

The quantitative XRF data for the industry manufactured alloys are given in tables 6.21a and 6.21b in the as-cast and annealed states, respectively.

Note that XRF data was not collected for the laboratory manufactured alloy due to the decision to expedite the industrial manufacture.

	XRF (.wt%)	at.%	at.%→wt.%
Ir	28.42±1.0	12	28.60
Fe	20.80±0.7	33	22.85
Co	16.70±0.6	20	14.62
Ni	22.42±0.7	30	21.83
Pt	11.07±0.7	5	12.10

(a) As-cast

	XRF (.wt%)	at.%	at.%→wt.%
Ir	26.74±0.4	12	28.60
Fe	22.46±0.3	33	22.85
Co	16.97±0.2	20	14.62
Ni	21.61±0.2	30	21.83
Pt	12.13±0.2	5	12.10

(b) Annealed

Table 6.21: XRF of industrial scale manufactured $Ir_{12}Fe_{33}Co_{30}Ni_{30}Pt_5$

Discussion

The XRF data presented above indicates that the mixing in the hearth was homogeneous. The as-cast and annealed wt.% distribution for the components only varies by 1-2wt.%. It is possible that if the whole ingot was homogenised then the alloy would present an even better elemental distribution across the bulk.

Comparing the XRF with the EPMA data we can see that they agree with regards to distribution but the EPMA data shows significant segregation across the imaged surface. Of course, XRF will give the elemental distribution of the area sampled, which is at a larger scale than the EPMA analysis, but will not give indication of segregation or otherwise.

Overall, the XRF data shows that the composition solidifies to a stable, homogeneously mixed alloy.

6.4.5.3 Optical micrographs

Optical micrographs for $Pt_7Rh_{23}Ni_{35}Co_{35}$ are presented in figure 6.55a and b, and c and d, respectively. In table 6.22 we present a grain size analysis of the visible grains for figure 6.55d.

In figure 6.55 we see that the as-cast sample exhibits many different types of dendrite structures separated by the grain interfaces. In the annealed sample image in figure 6.55d we can make out more of the grain structure. The grains appear to be small and equiaxed among larger ones.

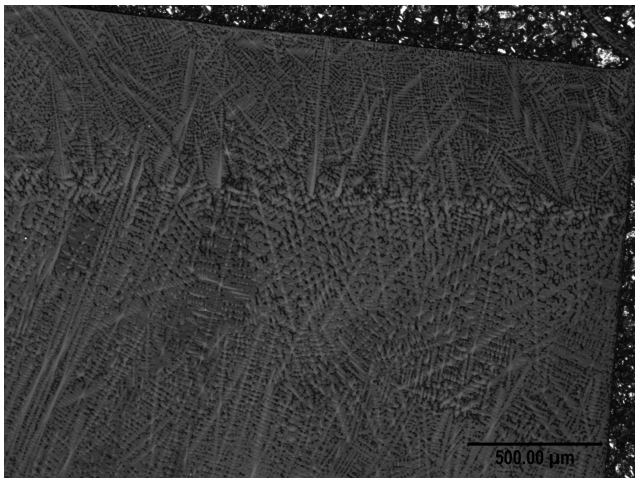

(a) as-cast 5x magnification

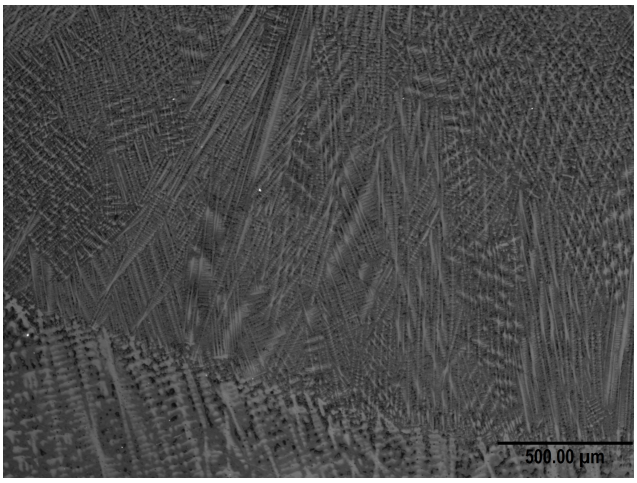

(b) as-cast 5x magnification

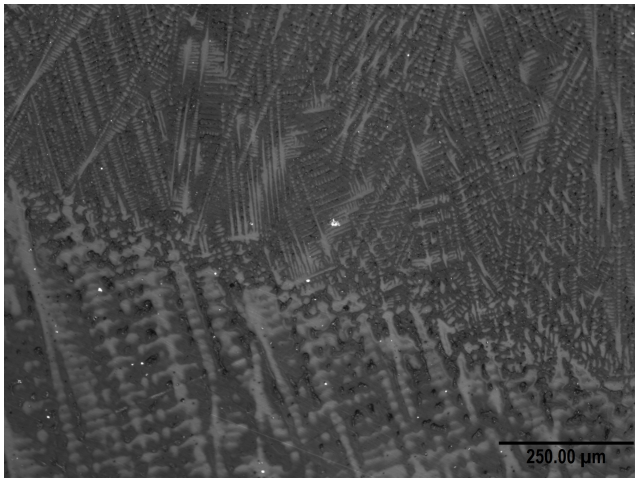

(c) as-cast 10x magnification

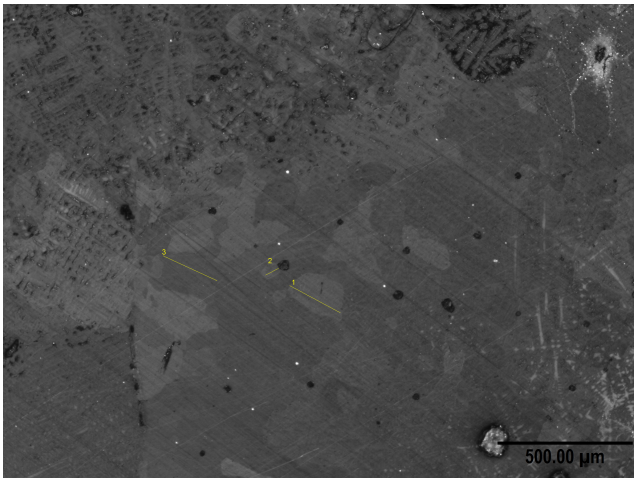

(d) annealed 5x magnification

Figure 6.55: $Ir_{12}Fe_{33}Co_{20}Ni_{30}Pt_5$ optical images of as-cast and etched and annealed and etched samples

	Distance (µm)
1	212
2	54
3	219

Table 6.22: Figure 6.55d grain analysis

Discussion

The optical micrographs reveal stark dendrite interfaces, where dendrites growing with different orientations, and different scales meet. This is probably due to different growth conditions in different regions of the cast, due to cooling rate changes, and also may be affected by

the angle at which the imaged section meets the different dendrites present. Considering the amount of alloy (1kg) manufactured this is a very reasonable assumption to make.

Heat treatment appears to have removed most of the dendrite structure but not all. This indicates that the sample might need to be heat treated for a longer period of time or at a higher temperature to achieve full homogenisation. Evidence of the grain structure is visible in figure 6.55d; this appears to be fairly irregular in size but not vastly different.

6.4.5.4 SEM-EDX

The EDX map data for the as-cast sample of the laboratory manufactured alloy of $Ir_{35}Rh_{35}Co_5Ni_5Pt_{20}$ are displayed on figure 6.56. Note that no annealed samples were produced due to the industrial scale manufacture being expedited.

The backscatter SEM images of the industry manufactured alloy are displayed on figures 6.57 and 6.58 for as-cast and annealed, respectively. Likewise, the EDX map data for the samples are displayed in figures 6.59 and 6.60.

Laboratory scale

The elemental distribution in the EDX Map in figure 6.56 is fairly uniform across the imaged surface without any areas of large segregation. There is some noticeable segregation, though, in every element and in Ir, in particular. Ir seems to be diffusing away from the other elements.

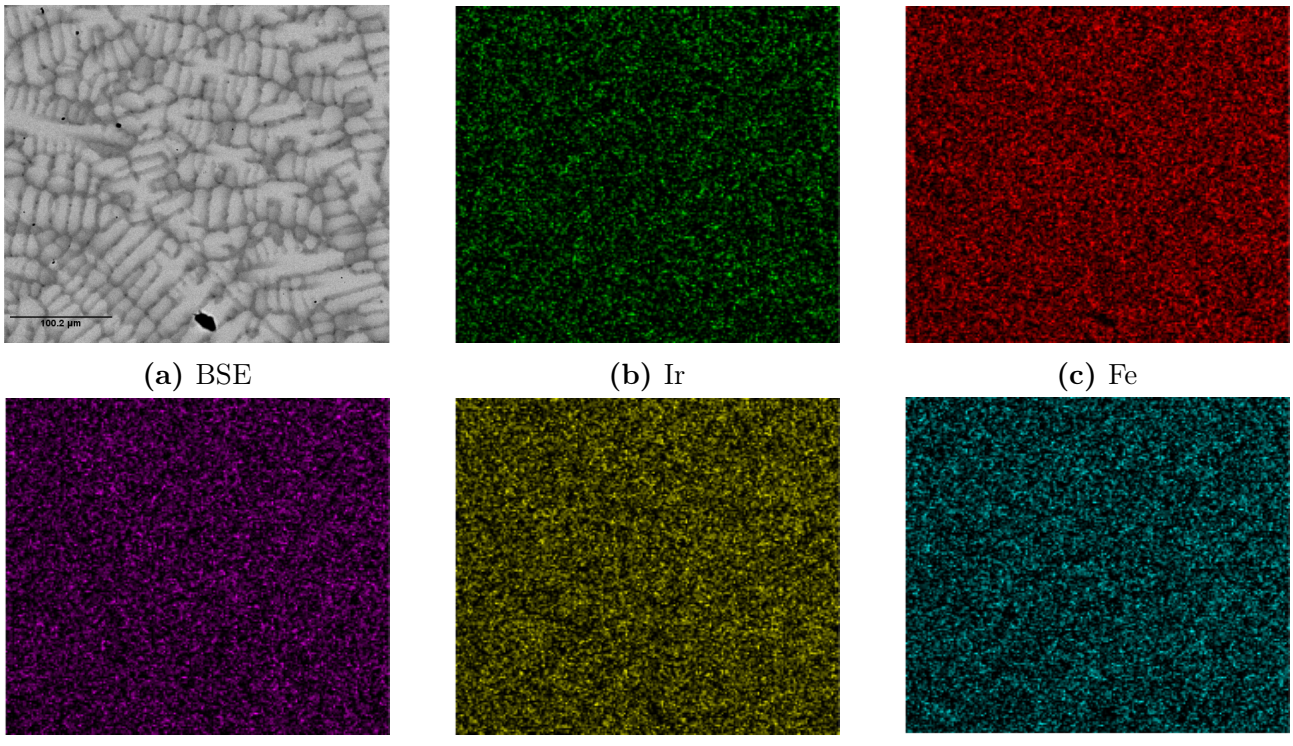

(a) BSE **(b)** Ir **(c)** Fe

(d) Co **(e)** Ni **(f)** Pt

Figure 6.56: EDX map of as-cast $Ir_{12}Fe_{33}Co_{20}Ni_{30}Pt_5$ taken at 800x magnification

Industrial scale In figure 6.57 we see different types of dendrite structures, either thin and

short or wide and long. There is an area of different dendrite growth separated by an interface at the top of figure 5.57a.

The dendrite structure exhibited in figure 6.58 appears more uniform and even. There is some disparity in the thickness and length of the dendrites but the dendrite growth is quite uniform.

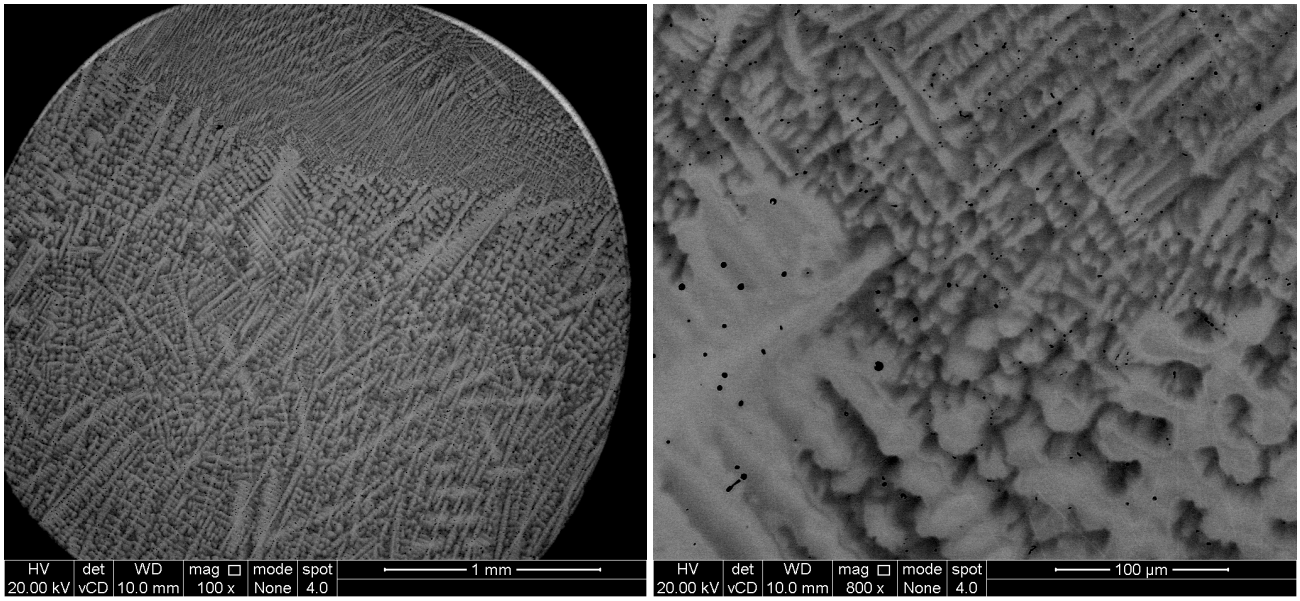

(a) 100x magnification **(b)** 800x magnification

Figure 6.57: BSE images of as-cast $Ir_{12}Fe_{33}Co_{20}Ni_{30}Pt_5$

Both figures 6.59 and 6.60 show uniform distribution of elements across the imaged areas. In both there is some noticeable patches that point to segregation in and out of the dendrites. This is particularly noticeable in Ir.

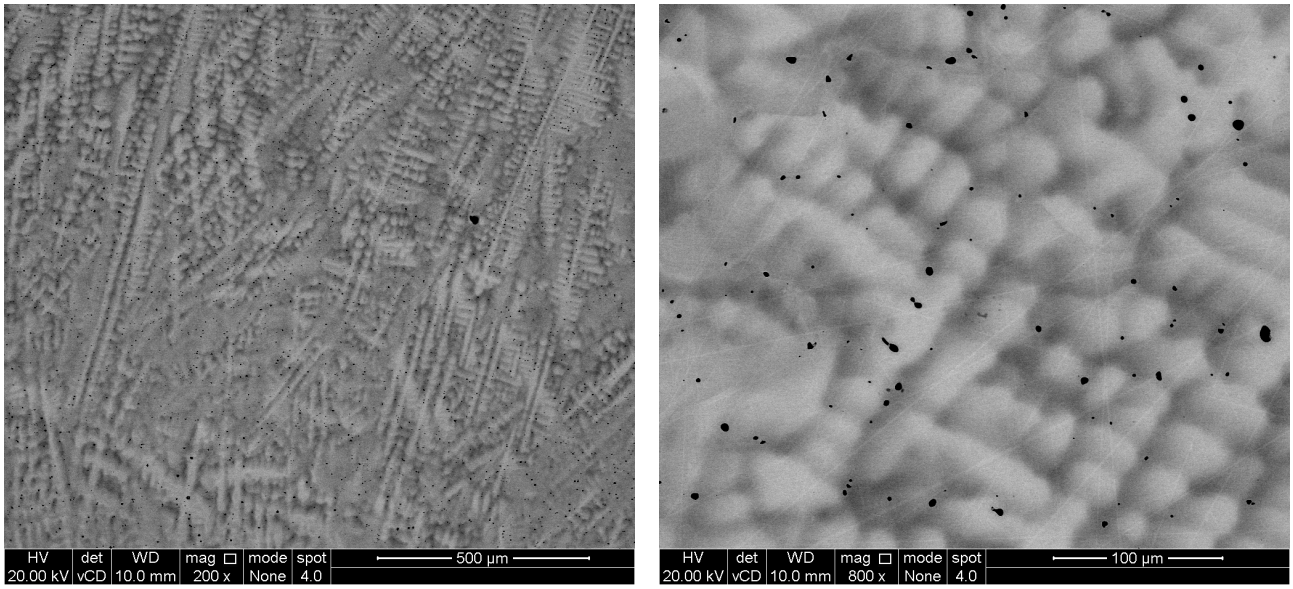

(a) 200x magnification **(b)** 800x magnification

Figure 6.58: BSE images of annealed $Ir_{12}Fe_{33}Co_{20}Ni_{30}Pt_5$

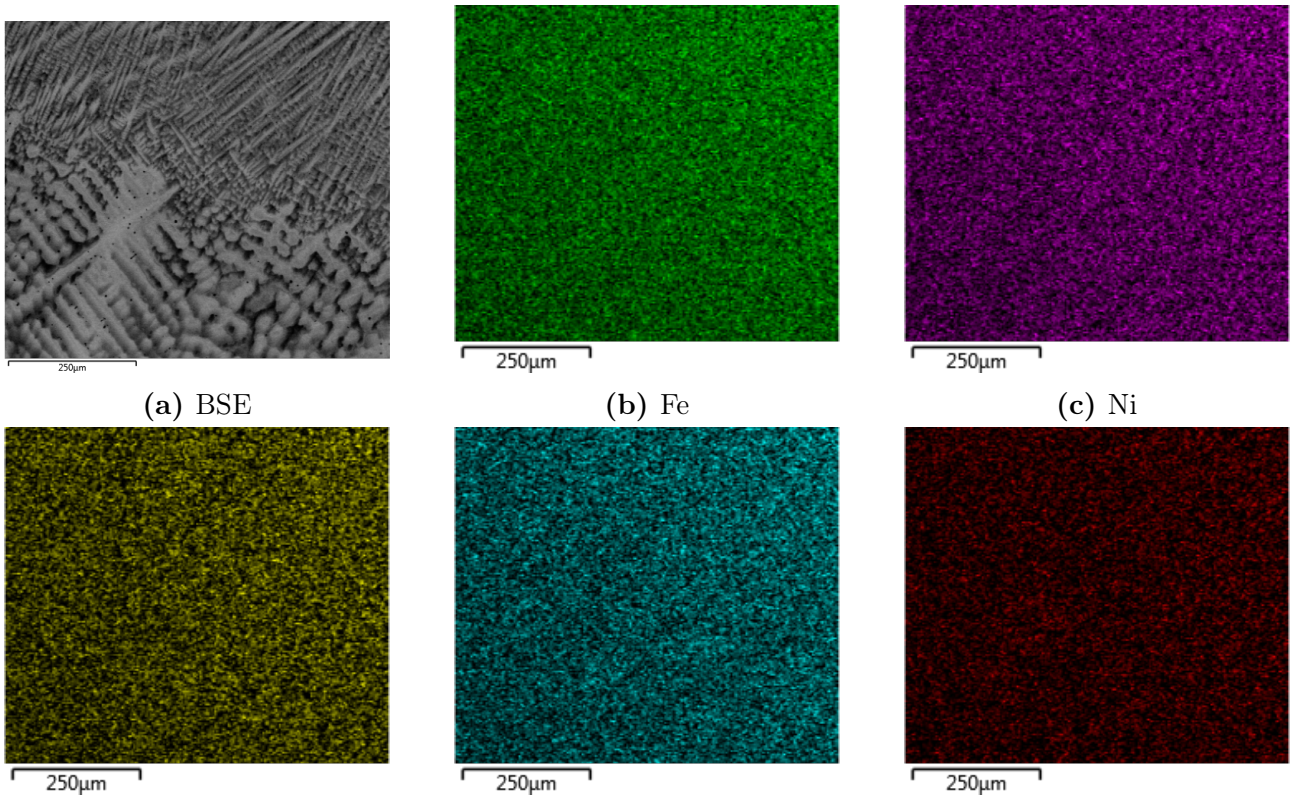

(a) BSE **(b)** Fe **(c)** Ni

(d) Pt **(e)** Co **(f)** Ir

Figure 6.59: 400x magnification EDX map of as-cast $Ir_{12}Fe_{33}Co_{20}Ni_{30}Pt_5$

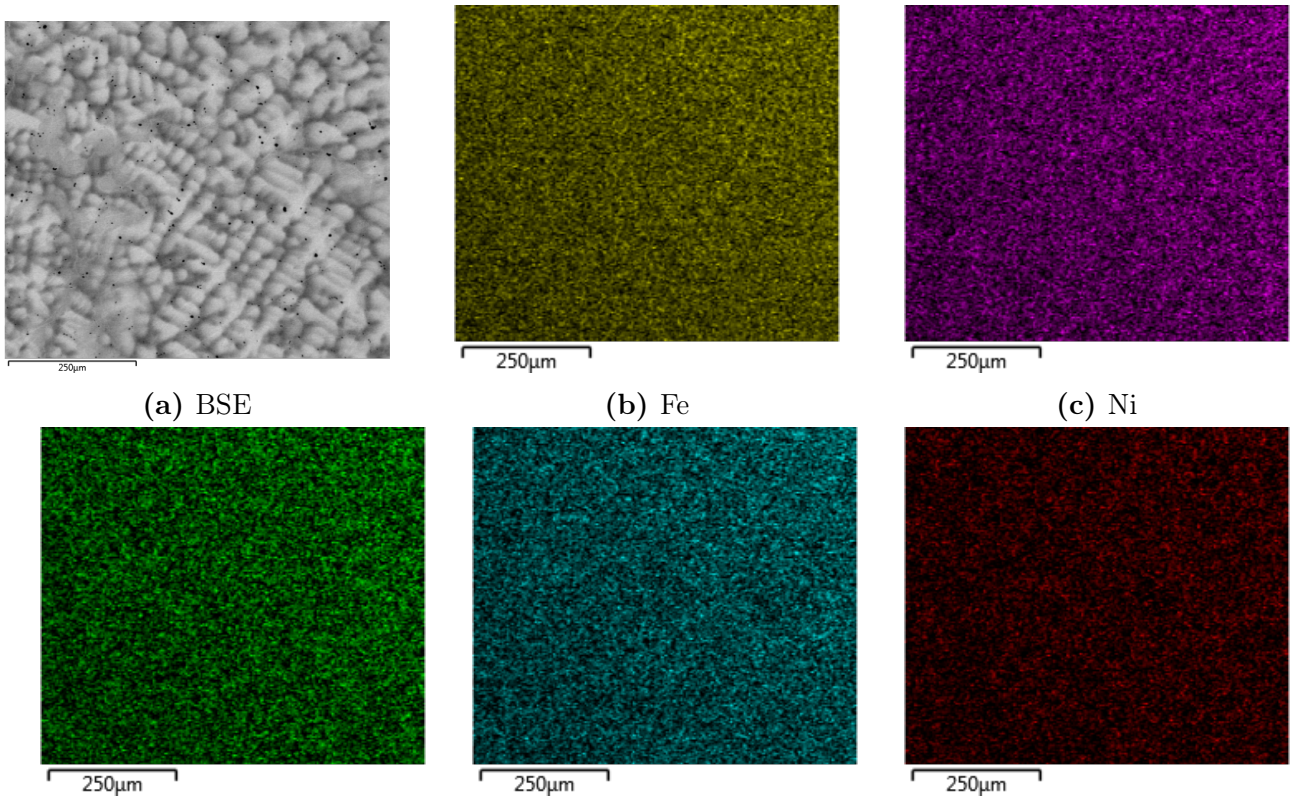

(a) BSE **(b)** Fe **(c)** Ni

(d) Pt **(e)** Co **(f)** Ir

Figure 6.60: 400x magnification EDX map of annealed $Ir_{12}Fe_{33}Co_{20}Ni_{30}Pt_5$

Discussion

The laboratory scale alloy has a fairly uniform elemental distribution as revealed in the EDX map in figure 6.56. Some minor segregation is observed in the laboratory manufactured alloy but the distribution is very uniform. However, the dendritic structure of the BSE image indicates segregation. Perhaps if the measurement time was longer we would have obtained a map that highlights this segregation. The uniform dendritic growth with fine scale revealed by the BSE image indicates that the rate of cooling was high as would be expected given the mass, and consequent size, (5g) of the laboratory produced sample.

The as-cast industrially manufactured sample SEM images (fig. 6.57) further highlight interfaces in dendritic growth. This is probably due to the uneven cooling rate in the hearth and the large size of the ingot. The annealed sample (fig. 6.62) shows a more uniform dendritic growth, similar to the fast cooled as-cast sample. The uniformity in the dendritic growth of the annealed sample may of course be due to the particular locations viewed in the imaging process, but may also be a systematic feature, due to the development of the structure on heat treatment, and the more rapid redistribution of material across the short distances needed where the dendritic structure was at fine scale. However, the continued presence of the dendritic structure indicates that the heat treatment length was too short or the heat treatment temperature was too low. The EDX images of the industrially manufactured alloys are consistent with the results previously discussed, some segregation is apparent in the constituents with lower at.% content, Pt and Ir.

6.4.5.5 EPMA

EPMA data for the as-cast and annealed samples of the industry manufactured alloys are displayed on figures 6.61 and 6.62.

The EPMA map of as-cast industry manufactured $Ir_{12}Fe_{33}Co_{20}Ni_{30}Pt_5$ in figure 6.61 shows that the elements are segregating in and out of the dendrites. This segregation is most stark in Ir and Pt which appear to be segregating away from each other. Co is fairly uniformly distributed across the imaged area, Ni seems to be segregating with Pt to a small degree and Fe appears to be segregating with Ir to a small degree.

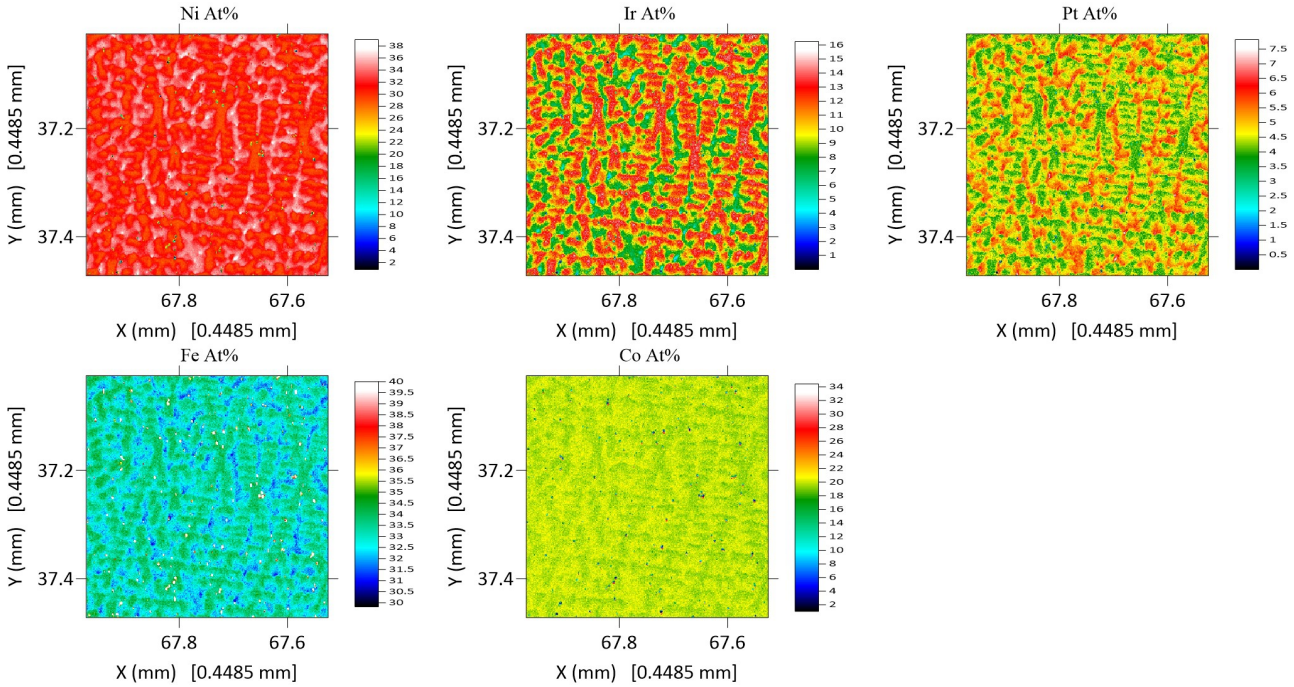

(a) Low magnification

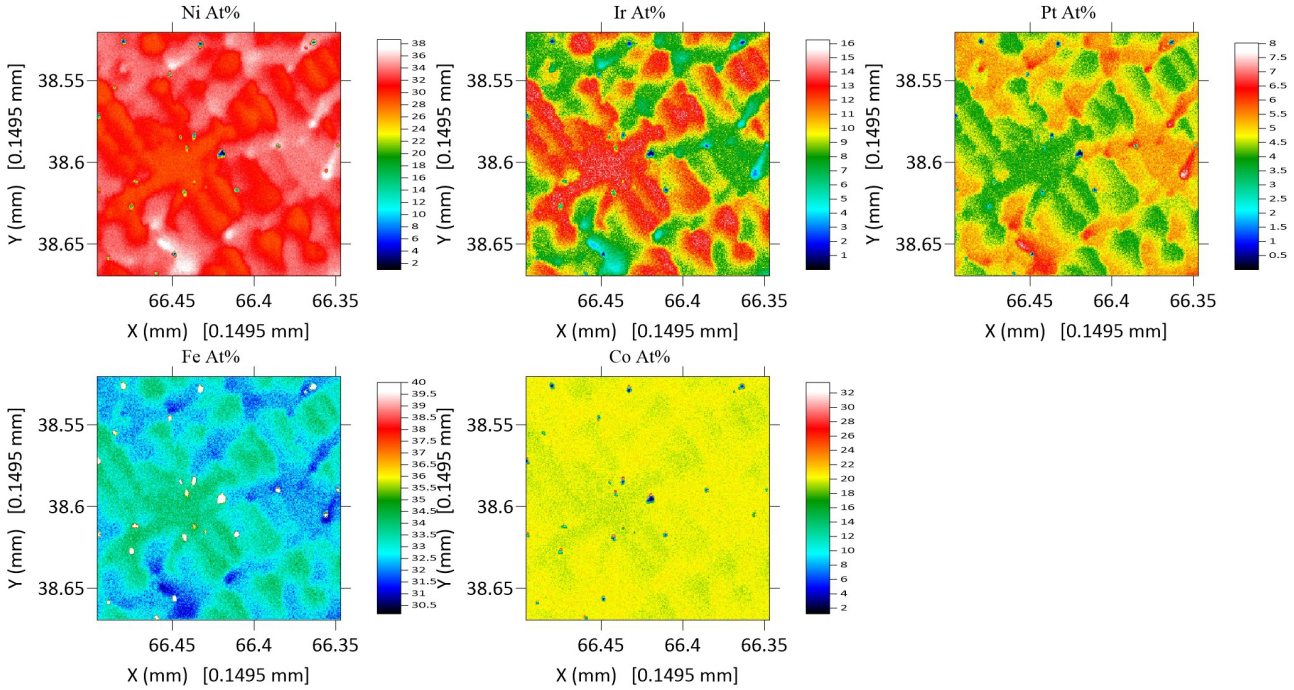

(b) High magnification

Figure 6.61: EPMA of as-cast $Ir_{12}Fe_{33}Co_{20}Ni_{30}Pt_5$, samples taken from a 1kg ingot

Segregation is present in the EPMA map of annealed industry manufactured $Ir_{12}Fe_{33}C_{20}Ni_{30}Pt_5$ figure 6.62. There is a high degree of segregation of Ir and Pt from each other. Fe seems to be segregating with Pt while Ni and Co are segregating with Ir.

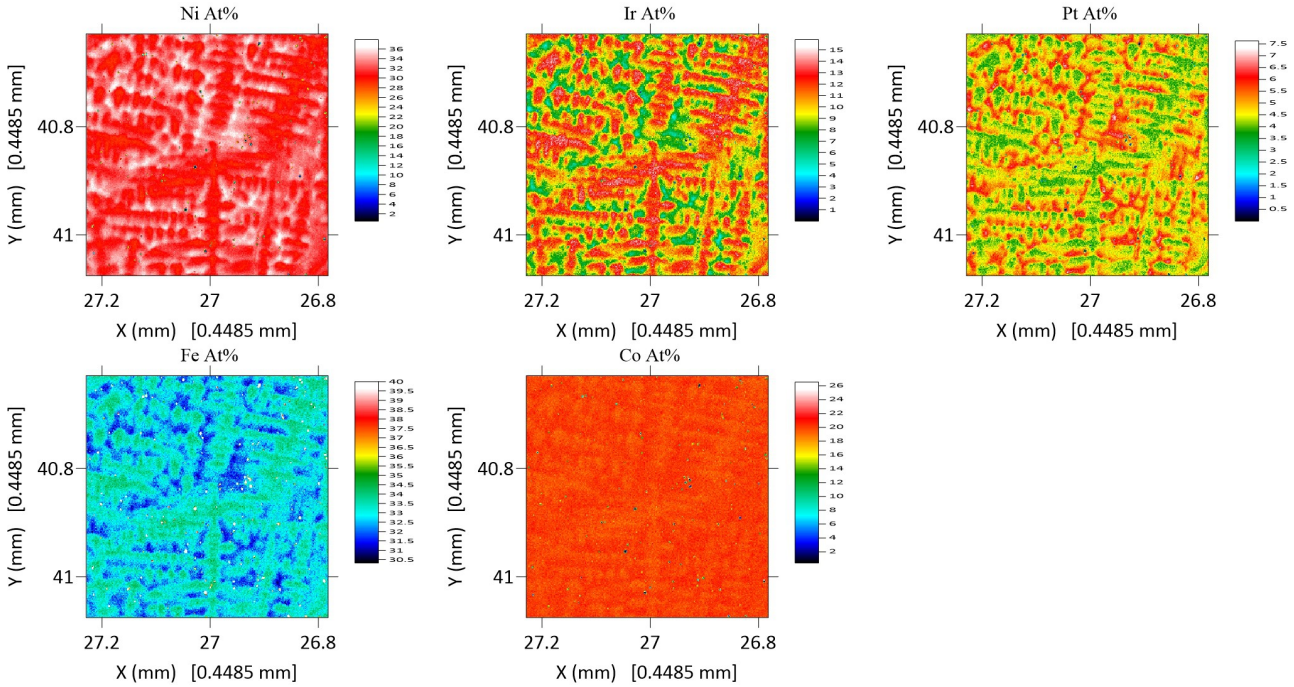

(a) Low magnification

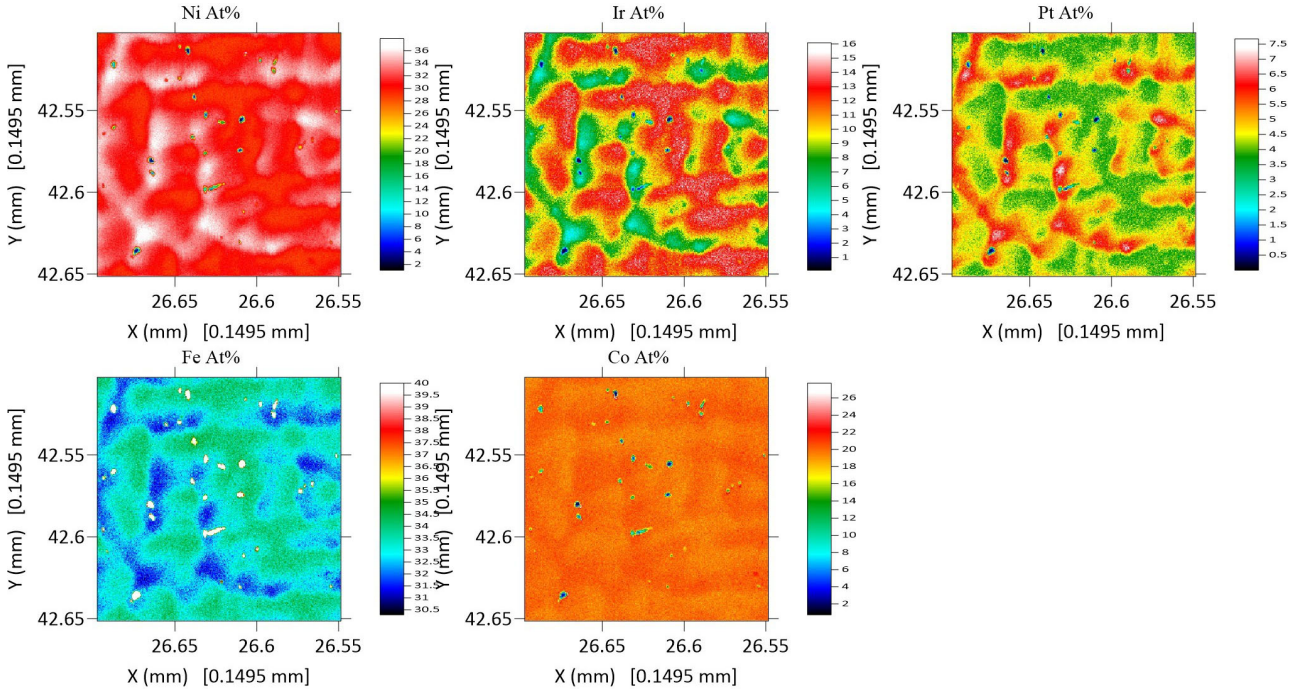

(b) High magnification

Figure 6.62: EPMA of annealed $Ir_{12}Fe_{33}Co_{20}Ni_{30}Pt_5$, samples taken from a 1kg ingot

Discussion

The segregation indicated in the BSE images is very evident in the EPMA elemental distribution maps. The EPMA data for the as-cast industrially manufactured sample (fig. 6.61) reveals that the alloy is homogeneously mixed, as the composition of each element averaged

across the imaged area is consistent with the target composition for the alloy. This is also observed in the XRF data. The segregation in and out of the dendrites at the scale examined by EPMA is very obvious, though. Some elements are segregating away from others, namely there are areas of higher Ir and Fe content and lower Pt and Ni content, and vice versa. Interestingly, Co is very evenly distributed across the whole surface imaged, with <1% difference in at.% between dendrites and interdendritic region.

The same observations are true in the annealed sample(fig. 6.62). This indicates that the heat treatment length was too short or the heat temperature was too low to promote homogenisation, or that this alloy does not tend towards a single phase in its stable form. The absence of structural development towards a clear two phase microstructure also suggests that, even if this is the case, the heat treatment temperature is not sufficiently high. More studies into the appropriate heat treatment temperature are needed.

6.4.5.6 Further Discussion of Alloy Structure

The TGA data reveal that the alloy very readily begins to gain mass in air (oxidise) and continues to steadily gain mass when held at 1000°C. The DSC data for this sample are very different from the rest of the alloys, as it appears that not as much thermal energy is required to produce a phase change in the alloy. The alloy is very likely to be ductile and workable as it indents with ease without any cracks observed, the calculated elastic moduli from the reduced moduli nanoindentation data for as-cast and annealed do agree to an extent with the ROM elastic moduli calculated from the XRF wt.% to at.% conversion and the expected elastic ROM modulus from the at.% content input, there are discrepancies which can be explained by the empirical nature of the methods used to calculate the expected data from the content input at.% and wt.%.

6.5 Silver

In both the design cycles the alloys which contained silver did not alloy to any extent, i.e. did not mix in the molten state in the hearth resulting to samples such as those shown in figure 6.63; these samples do not have the smooth, regular structures of alloys which have formed a homogenous melt, and despite all the elements exceeding their liquidus temperatures and transforming to the molten state, they have regions where different elements or parts of the alloy seem to have remained separate. All this is despite the alloy compositions being within the accepted criteria for HEA formation, and this behaviour is evidently a concern for the alloy design approach. If it is systematically making incorrect predictions with regard to alloys with silver, then it is likely that there is an important factor in the metallurgical nature of silver that contributes to the process, but is not captured by the approach. Further study of silver alloys of the types examined here may help understand what this factor is and perhaps provide improved routes for prediction.

While it helps to ensure melting, the fact that that the argon arc melter can reach temperatures of 3500°C and the reduced pressure of 0.7bar may be one reason why the silver containing alloys to have not been able to form a stable mixture in the melted state. Taking $Pt_{35}Rh_{35}V_5Ag_{25}$ into consideration all element melting and boiling points (table.3.1) are within a suitable range and can be melted together in terms of the temperatures needed under standard conditions, but given the lower pressure in the arc melter silver could have vaporised before forming a stable melt. That is likely the case for compositions such as $Ir_{35}Rh_{28}Pd_{27}Ag_5Pt_5$ where the boiling point of silver is in fact lower than the melting point of iridium. While the dynamic nature of the heat application in the arc melter, and the possibility to physically position the elements in the hearth in ways to minimise such material loss, a better route to alloying compositions such as $Ir_{35}Rh_{28}Pd_{27}Ag_5Pt_5$ would be to create a master alloy. However, this can introduce difficulties with elements that can show volatility, like silver, as it will need to be taken to the molten state multiple times, and can lead to accumulating more significant departures from the nominal composition. Nevertheless, with higher production volumes and established protocols to target the correct composition, this may be a viable route for industrial production of the alloys.

The boiling point change with lower pressure would present some problems in such alloys. However, these would be likely to present as compositional variances with respect to silver, and perhaps failure of alloying due to the evaporated silver impairing the function of the arc melter. Here, where the elements appear to have been molten but not to have mixed, there could be other effects also at play. One consideration is the pairwise enthalpy between constituents in compositions containing silver. From table B.1 we can see that for both example compositions mentioned above silver only has a negative pairwise enthalpy of mixing with palladium and platinum.

Once the pairwise enthalpy criterion was identified as a result of the PtRh and Ir studies, a study was devised to try to identify whether we can alloy silver with some of the selected elements within the full scope of this project (tab. 3.1). The pairwise enthalpy pairs for the selected elements are shown in table 6.23. For the study we selected elements that, according to previous experience with the PtRh and Ir studies should alloy, using a criterion of $\Delta H_{AB} \leq 2\text{kJ}\,\text{mol}^{-1}$ in addition to the general criteria of low δ, $\delta \leq 4\%$, and $-20\text{kJ}\,\text{mol}^{-1} \leq \Delta H_{mix} \leq 10\text{kJ}\,\text{mol}^{-1}$. The alloy compositions manufactured for this study are shown in table 3.4.

	V	Ni	Cu	Rh	Pd	Ag	Re	Ir	Pt	Au
V	x	-18	5	-29	-35	17	-13	-34	-45	-19
Ni	-18	x	4	-1	0	15	2	-2	-5	7
Cu	5	4	x	-2	-14	2	18	0	-12	-9
Rh	-29	-1	-2	x	2	10	1	1	-2	7
Pd	-35	0	-14	2	x	-7	6	6	2	0
Ag	17	15	2	10	-7	x	38	16	-1	-6
Re	-13	2	18	1	6	38	x	-3	-4	20
Ir	-34	-2	0	1	6	16	-3	x	0	13
Pt	-45	-5	-12	-2	2	-1	-4	0	x	4
Au	-19	7	-9	7	0	-6	20	13	4	x

Table 6.23: ΔH_{AB} for element constituents in the alloys summarised on table 3.4, modified from [225]

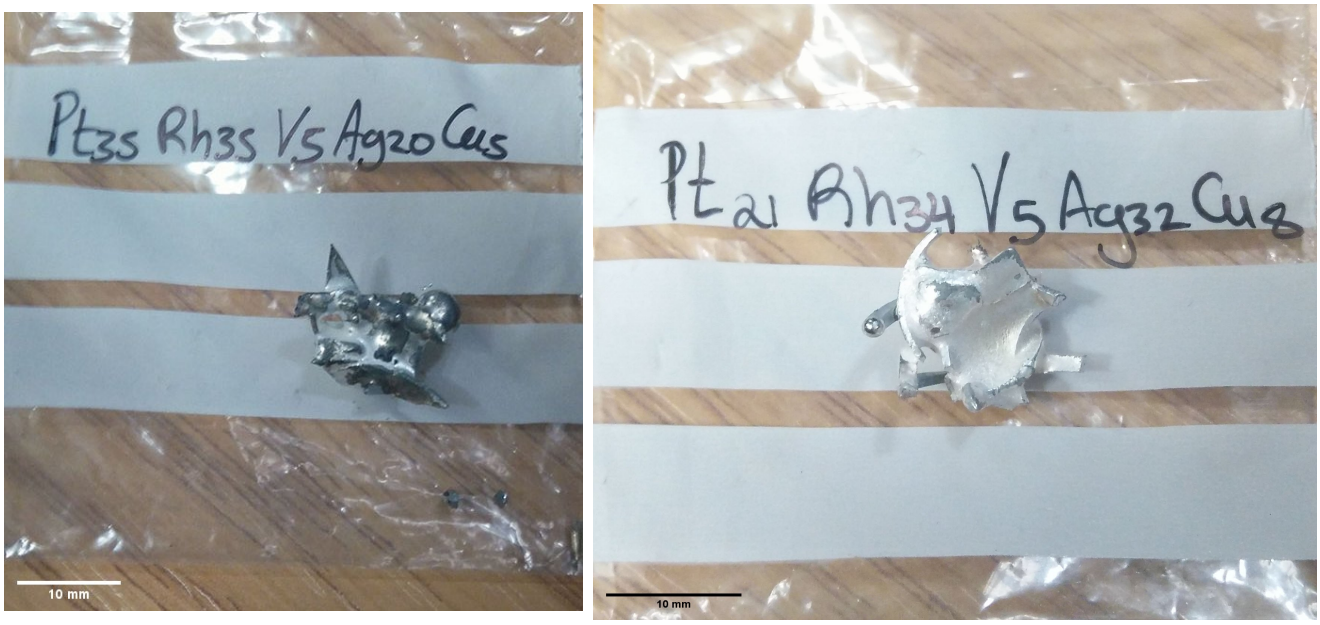

Figure 6.63: Example of the visual appearance of 2 alloys containing Ag

6.5.1 Silver results

Composition
$Ag_{25}Cu_5Pd_{35}Pt_{35}$
$Ag_{30}Pd_{35}Pt_{35}$
$Ag_{35}Pd_5Pt_{25}Au_{35}$
$Ag_{35}Pd_{30}Au_{35}$

Table 6.24: Silver compositions based on the pair elements highlighted in green in table 6.23, as used in a study on the pairwise enthalpy criterion

This subsection concerns a study of testing the pairwise enthalpy criterion by trying to alloy silver successfully. The silver alloy compositions are presented in table 6.24. The sample compositions were a result of taking into consideration the elements which had favourable pairwise enthalpy with silver and with each other, as presented in table 6.23. The study was an effort in ensuring that silver alloyed successfully, in contrast with the results of the previous studies concerning PtRh and IrRh, where the silver containing alloys resulted in structures similar to the ones presented in figure 6.63. When the silver samples designed were being manufactured in the hearth they mixed successfully in the liquid state and formed uniformly shaped masses. The samples were subsequently prepared using the preparation technique described in section 3.3.1. The alloys were visibly uniform so we continued with SEM-BSE and EDX based characterisation to investigate the degree of alloying.

SEM-BSE and EDX were chosen as the only characterisation method for this study. As outlined above, the study was intended to show that if one were to apply binary substitutional alloy formation H-R rules, using the pairwise enthalpy criterion, to HEA formation rules then the resulting alloy would be successfully formed. As the intent was not to create alloys of particular value for end applications, the further characterisation steps were not needed.

Below the EDX maps show that despite the alloys appearing successfully alloyed when prepared for characterisation they did not form single phase materials, and indeed, may not have properly mixed on a fine scale. Heat treatment and homogenisation of these alloys was not performed but if one wanted to assess and investigate that and the mixed stability in the future then it is a worthy task to be pursued.

In figure 6.64 we see that there is some segregation in and out of the dendrites, Ag is diffusing into the dendrites while Pt is mostly uniformly distributed. The distribution of both Pt and Cu is patchy and they are not as present in the imaged area as one would expect from the atomic concentration. Additionally, Pt appears to be segregating in a similar pattern to Ag.

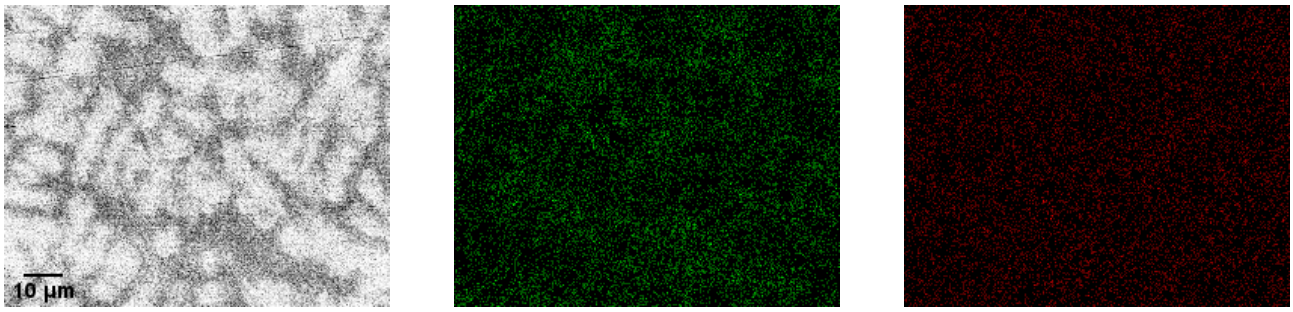

(a) BSE image **(b)** Ag **(c)** Pd

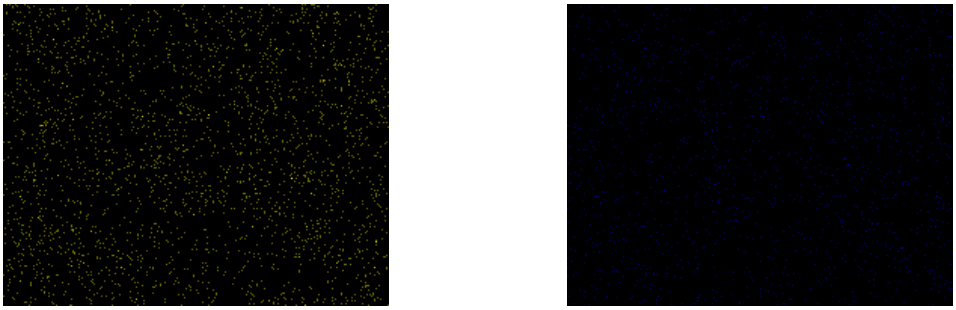

(d) Pt **(e)** Cu

Figure 6.64: EDX map of as-cast $Ag_{25}Cu_5Pd_{35}Pt_{35}$ taken at 3000x magnification

The EDX maps of $Ag_{25}Cu_5Pd_{35}Pt_{35}$ (figs. 6.65, 6.66) show an area where there is stark segregation and an area composed solely of Pt. In figure 6.65 we see that one area is mostly composed of Ag and Pd, with a small degree of both in the other area. Pt has predominantly segregated from Ag and Pd but is present to a small degre in the AgPd area. Cu appears to be uniformly distributed across the imaged area. Figure 6.66 shows an area which is only composed of Pt.

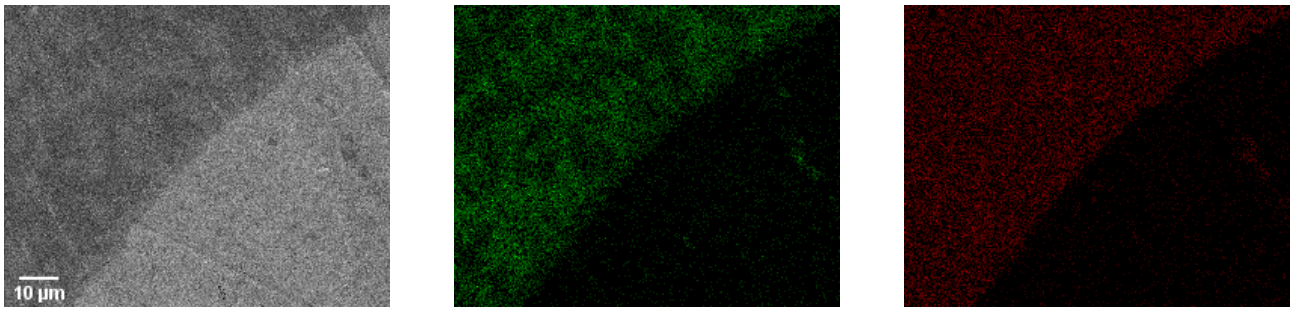

(a) BSE image **(b)** Ag **(c)** Pd

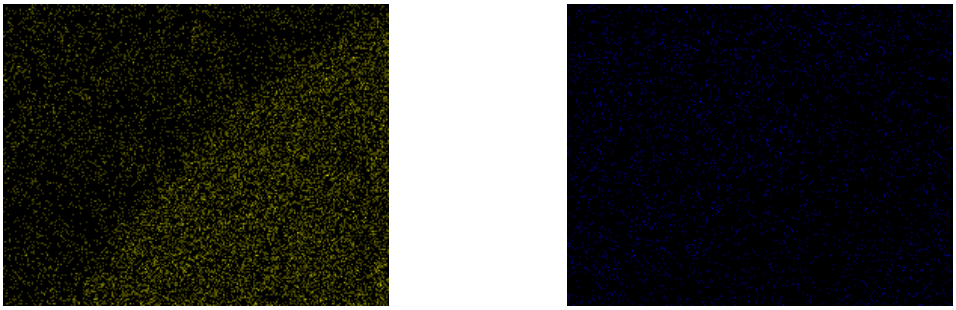

(d) Pt **(e)** Cu

Figure 6.65: EDX map of as-cast $Ag_{25}Cu_5Pd_{35}Pt_{35}$ taken at 3000x magnification

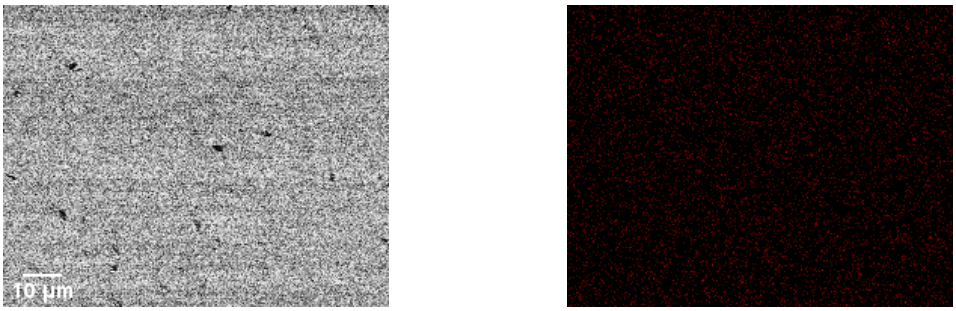

(a) BSE image **(b)** Pt

Figure 6.66: EDX map of as-cast $Ag_{25}Cu_5Pd_{35}Pt_{35}$ taken at 3000x magnification showing an area of the alloy where only Pt is present

The EDX maps of $Ag_{30}Pd_{35}Pt_{35}$ are in figures 6.67, 6.68and 6.69. Figure 6.67 shows an area where there is an interface between a dendrite structure and a heavier element area. Figure 6.68 shows the dendrite structure and figure 6.69 shows an area of only Pt. In figure 6.67 we see that Ag and Pd are diffusing from Pt. In the AgPd area there is further segregation as Ag is segregating from Pd into the dendrites. Pt is fairly evenly distributed across the imaged area.

In figure 6.68 we see a dendrite structure where Ag is segregating into the dendrites and Pd and Pt are unofrmly distributed across the imaged area.

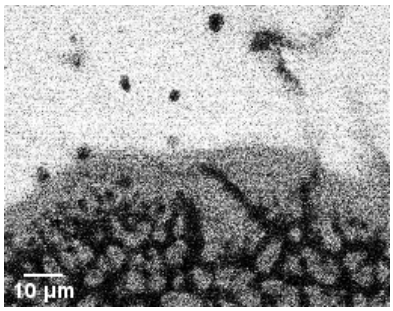

(a) BSE image

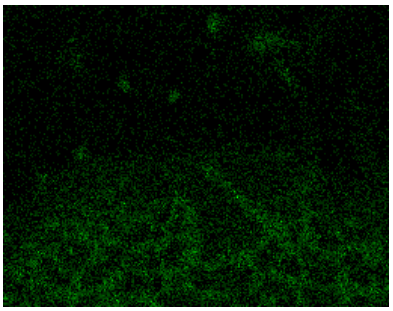

(b) Ag

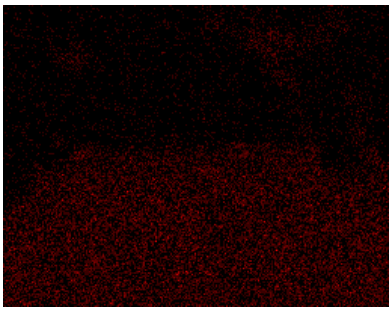

(c) Pd

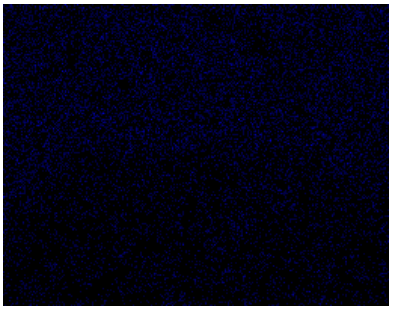

(d) Pt

Figure 6.67: EDX map of as-cast $Ag_{30}Pd_{35}Pt_{35}$ taken at 3000x magnification

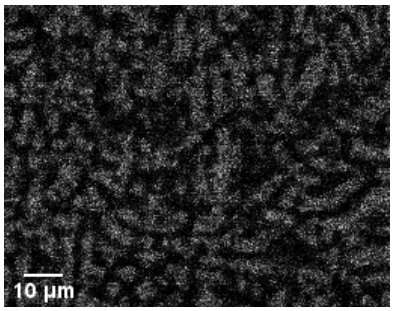

(a) BSE image

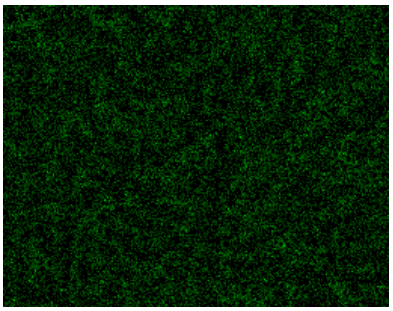

(b) Ag

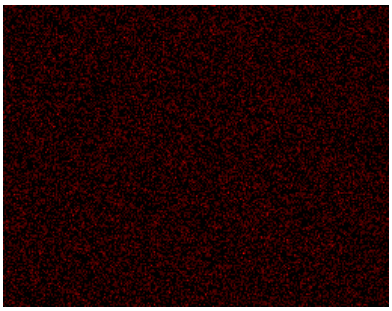

(c) Pd

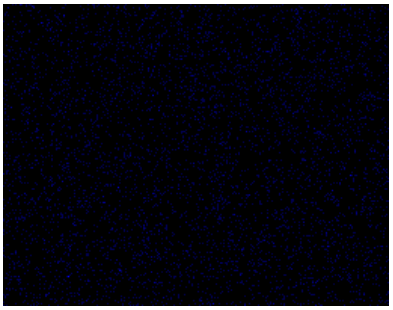

(d) Pt

Figure 6.68: EDX map of as-cast $Ag_{30}Pd_{35}Pt_{35}$ taken at 3000x magnification

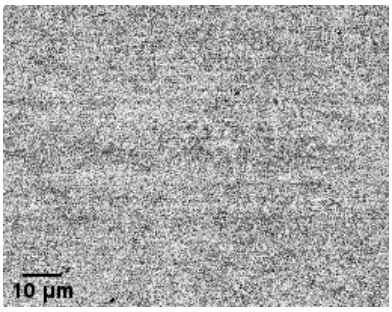

(a) BSE image

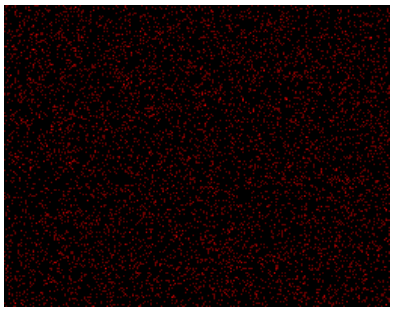

(b) Pt

Figure 6.69: EDX map of as-cast $Ag_{30}Pd_{35}Pt_{35}$ taken at 3000x magnification showing an area of the alloy where only Pt is present

Figures 6.70, 6.71 and 6.72 show the EDX maps of $Ag_{35}Pd_5Pt_{25}Au_{35}$. We see areas of stark segregation in figure 6.70 and 6.72. In figure 6.70 We see that Ag, Pd and Au are segregating from Pd. Similarly, in 6.72 Pd is segregating to an area and there is no Pt present. In figure 6.71 we see a fairly even and uniform distribution but without the expected count from some of the elements.

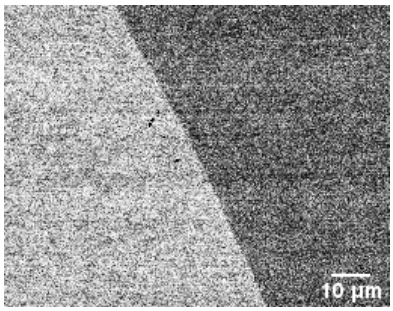

(a) BSE image

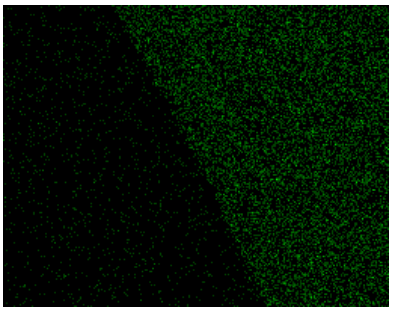

(b) Ag

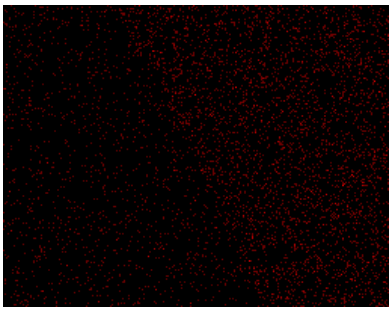

(c) Pd

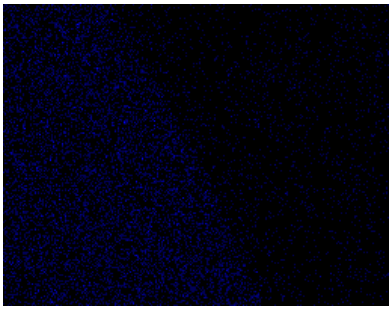

(d) Pt

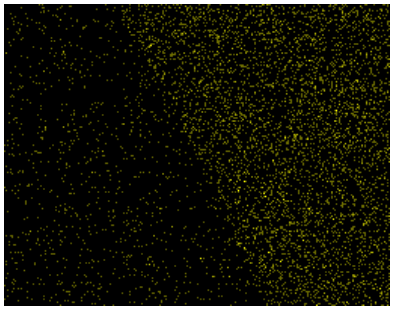

(e) Au

Figure 6.70: EDX map of as-cast $Ag_{35}Pd_5Pt_{25}Au_{35}$ taken at 3000x magnification

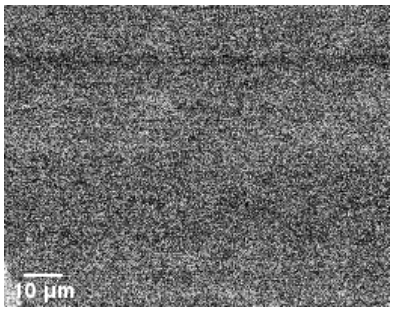

(a) BSE image

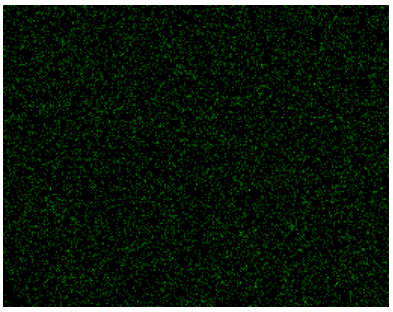

(b) Ag

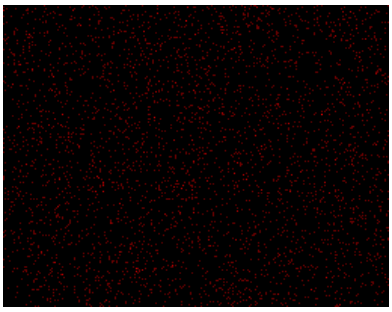

(c) Pd

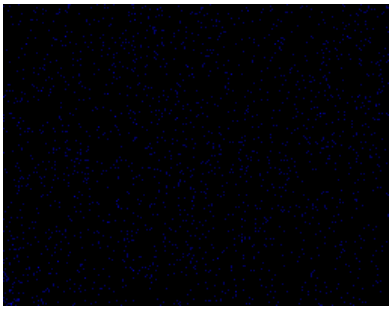

(d) Pt

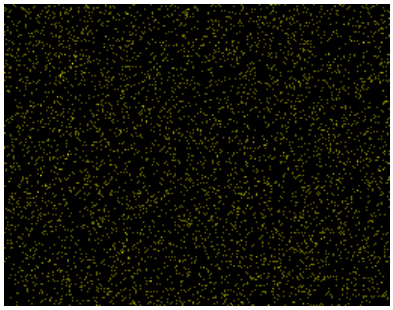

(e) Au

Figure 6.71: EDX map of as-cast $Ag_{35}Pd_5Pt_{25}Au_{35}$ taken at 3000x magnification

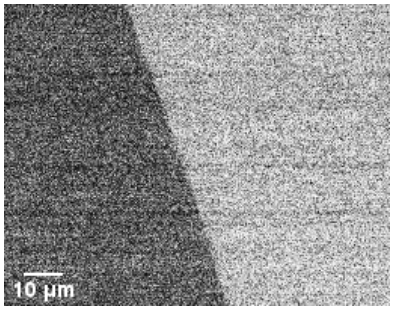

(a) BSE image

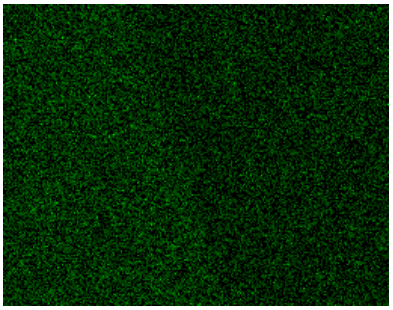

(b) Ag

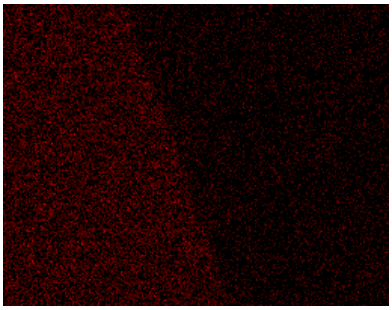

(c) Pd

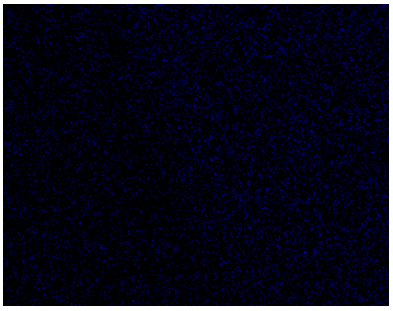

(d) Au

Figure 6.72: EDX map of as-cast $Ag_{35}Pd_{30}Au_{35}$ taken at 3000x magnification

6.5.2 Discussion

It should be noted that the Ag alloys explored in this section (formed from the elements in green in table 6.23) are different from those explored in Section 5.2, and that the discussion below relates to the particular series of Ag alloys developed under the new criteria (table 6.24).

The alloys presented in figures 6.64-6.72 are a stark contrast to the inhomogeneous, not alloyed masses of material presented in figure. 6.63. This indicates that the improved criteria have avoided some fundamental incompatibilities in the behaviour of some of these elements. It is clear that such incompatibility can exist; examination of the Ag-Ni phase diagram for example, shows the formation of immiscible liquids. However, single phase alloys (as encountered in some of the other systems explored earlier) do not seem to have formed as can be seen in figures 6.65, 6.66, 6.67, 6.69, 6.70 and 6.72. Although some of these images (e.g. 6.65 or 6.70) show structures which could be multiphase alloys or segregation, as seen before, many show, as the scale examined, clear separation. This could be due to the formation of two phase microstructures with a scale on the order of hundreds of microns, or incomplete mixing in the liquid state, on a fine scale. Particularly, Pt is found not to homogenise well with the other elements. Inspecting figure 6.72 it is evident that $Ag_{35}Pd_{30}Au_{35}$ is the most promising composition in terms of homogeneity across the sample and the most likely candidate of those studied to be able to form a fully homogeneous alloy at equilibrium given the correct heat treatment.

There are several potential reason for the inhomogeneity. Firstly, the $\Delta H_{AB} \leq 2$ criterion employed in the selection process might need to be stricter, for example, $\Delta H_{AB} \leq 0$ as with the H-R rules for binary alloys; the ΔH_{AB} values for Ag binaries are presented on table 6.23. In the case of $Ag_{25}Cu_5Pd_{35}Pt_{35}$ the origin of the separation could be the big differences in ΔH_{AB} of CuPd and CuPt binaries in comparison with AgCu and PdPt. Another reason could be the rapid speed of the process, as, while fast cooling could aid retention of a mixed structure, if the alloy lacks fluidity (as could be the case with the high temperature components of the alloys), it may be that proper mixing in the liquid state was not achieved. Other refinements of the criteria used could include, the melting point and boiling point overlap effects at pressures lower than ambient pressure. Another source of uncertainty is the melting procedure, where there is no direct control over the temperature, heat is generated by completing the circuit between arc tip and constituent elements.

A further study of this exploring the suggested additional design factors and a study exploring the homogenisation of these alloys is necessary. This could be achieved by using different alloying techniques to argon arc melting or using a master alloy which is closer to the melting point of silver and ensures no overlap between melting and boiling point.

6.6 Alloy prediction methods

6.6.1 Empirical prediction criteria

We know that the binary systems of the PGM are very well studied and proven in the majority of cases to dissolve easily and readily with each other[225]. PGM ore is usually made of different naturally occurring binary PGM alloys[1, 9]. With this information it was important

to try to alloy them into multiprincipal component alloys given the resources provided to us by JMNM.

With the PtRh) based alloys we have identified 3, $Pt_7Rh_{23}Ni_{35}Co_{35}$, $Pt_5Rh_{20}V_5Ni_{35}Co_{35}$, $Pt_5Rh_{11}V_{14}Ni_{35}Co_{35}$, very interesting alloys that are virtually single phase as-cast and after heat treatment at 700°C and 1000°C, found using the H-R extrapolation criteria outlined in section 2.2.2 and section 3.1.1. The compositions were identified without any adjustments to the criteria, and $\frac{3}{17}$ compositions, $\approx 18\%$, $\frac{10}{17}$, $\approx 59\%$, alloyed to a uniform mass. Considering that the compositions that did not form uniform masses were the Ag containing compositions, the original unmodified criteria seem able to identify with a reasonable chance of success interesting compositions that will alloy. If we probe the ΔH_{AB} of the binaries (fig. B.1, section B.1) in the successfully synthesised compositions apart from VCu, CoCu and NiCu which are slightly positive, all other pair enthalpies are negative. All the pair enthalpies in the industrially scaled single phase candidates are negative but not extremely apart from the V pair enthalpies. The other successfully synthesised alloys that are not single phase have Cu as a common component. A reason for the successful synthesis may be that while the Cu pair enthalpies are positive they are still under $10\text{kJ}\,\text{mol}^{-1}$ and it has been reported by Miracle *et al.* [63] that high entropy alloys might be best defined at high temperatures in melt. It is noteworthy that Cu addition also introduces second phase into other HEA systems, such as in CoCrFeNiCu, as observed, for example, by Otto *et al.* [98], Lin *et al.* [226], Munitz *et al.* [227], and Shang *et al.* [228]. It is likely that this also occurs due to the more positive pair enthalpies of mixing with the other elements. For the Ag containing compositions, it is evident that there is a strong connection between successful synthesis and small pair enthalpies, especially pair enthalpies below 0.

The modified criteria for the Ir containing alloys involved requiring ΔH_{AB} between all pairs of the components of compositions to be under a certain value (usually 2-$10\text{kJ}\,\text{mol}^{-1}$) before the criteria of $\delta \leq 4\%$ and $-10\text{kJ}\,\text{mol}^{-1} \leq \Delta H_{mix} \leq 5\text{kJ}\,\text{mol}^{-1}$ were applied. The desired result would be that all alloy compositions would melt into a homogeneous mass and that some if not most of the alloys would be single phase post heat treatment. However, the Ag containing alloys once again did not melt homogeneously. Alloys with VCu, CoCu, FeCu and NiCu did alloy into homogeneous masses but were visibly not well mixed when cut. The Pd containing alloy, $Ir_{35}Rh_{35}Pd_{20}Pt_{10}$, did melt well but was not single phase, probably due to the pair enthalpies between Pd and the other components being positive, $\Delta H_{\text{RhPd}} = 2\text{kJ}\,\text{mol}^{-1}$, $\Delta H_{\text{PdIr}} = 6\text{kJ}\,\text{mol}^{-1}$, $\Delta H_{\text{PdPt}} = 2\text{kJ}\,\text{mol}^{-1}$. $Ir_{35}Rh_{35}Co_5Ni_5Pt_{20}$ and $Ir_{12}Fe_{33}Co_{20}Ni_{30}Pt_5$ did melt well and appeared to be single phase when analysed by SEM-EDX at laboratory scale, however the industrial scale results, which experience slower cooling rates due to larger ingot sizes, show that the alloys both exhibit an FCC crystal phase with some extra peaks in the XRD signal. Also, the EPMA data show segregation in and out of the dendrites, this is further discussed in section 6.4.4.6 and section 6.4.5.6. Particularly for $Ir_{35}Rh_{35}Co_5Ni_5Pt_{20}$ where regions of high Rh at.% are depleted in Ir, interestingly regions of high Ir at.% are not without Rh but the Rh is lower. The pair enthalpy of RhIr is positive, $\Delta H_{RhIr} = 1\text{kJ}\,\text{mol}^{-1}$, in

$Ir_{35}Rh_{35}Co_5Ni_5Pt_{20}$ and could be the reason for this and this can be supported in figures 6.51 and 6.52 where areas of high Ir at.% are low in Rh and vice versa. For $Ir_{12}Fe_{33}Co_{20}Ni_{30}Pt_5$ all pair enthalpies are negative so the pair enthalpies indicate towards a single phase. The EPMA data (fig. 6.61, fig. 6.62) that the segregation is minimal, ≈1 - 2%, for Ni, Co, Fe, and Pt, with Ir having a segregation of ≈1 - 4%, so the presence of unexpected peaks in the XRD could be due to insufficient mixing and insufficient heat treatment duration or temperature to allow sufficient mobility of the atoms.

Using $\Delta H \leq 2\text{kJ}\,\text{mol}^{-1}$ as a criterion, Ag containing ternary and quaternary alloy compositions were identified and manufactured at laboratory scale. In comparison to previous laboratory trials these alloy compositions did alloy to uniform masses so the criterion did work successfully in achieving the desired result. The alloys appear uniformly mixed but not completely alloyed, which might be due to insufficient liquid state mixing of the melt in the hearth or the positive ΔH_{AB} of CuAg, $\Delta H_{\text{CuAg}} = 2\text{kJ}\,\text{mol}^{-1}$. Both reasons are evidenced by how well alloyed $Ag_{30}Pd_{35}Pt_{35}$ appears under SEM-EDX (fig.6.69) but there appears to be a region of solely Pt which is most likely due to uneven fluid mixing in the hearth. The previous failed attempts at alloying with silver were most likely due to the pairwise enthalpy factor not being considered at that earlier stage, or not applied at the right level for those systems, rather than another factor for those alloys.

The alloys $Pt_5Rh_{20}V_5Ni_{35}Co_{35}$ and $Pt_5Rh_{11}V_{14}Ni_{35}Co_{35}$, mix uniformly, however they have the most stark difference in the pairwise enthalpy, where $\Delta H_{PtRh} = -2$, $\Delta H_{PtV} = -45$, $\Delta H_{PtNi} = -5$, $\Delta H_{PtCo} = -7$, $\Delta H_{RhV} = -29$, $\Delta H_{RhNi} = -1$, $\Delta H_{RhCo} = -2$, $\Delta H_{VNi} = -18$, $\Delta H_{VCo} = -14$, $\Delta H_{NiCo} = 0$. There is a $45\text{kJ}\,\text{mol}^{-1}$ difference between the highest pairwise enthalpy and the lowest pairwise enthalpy. So we cannot suggest a lower limit, however we do suggest that when inspecting pairwise enthalpies to be aware of such stark differences. As an estimate, we will suggest that pairwise enthalpies not differ by $50\text{kJ}\,\text{mol}^{-1}$ or more, which makes the lower limit -$50\text{kJ}\,\text{mol}^{-1}$, however the lower limit could be at a higher enthalpy and requires further investigation to find a precise value, or indeed determine if the identification of a precise value is possible.

We have shown that if $\Delta H_{AB} \leq 0$ for all pairs in a composition then the resulting alloy will tend to want to mix uniformly and tend to a single phase crystal structure, provided good fluid mixing in the melt during manufacture and a small δ are achieved. This is also supported in the paper of Sohn *et al.* [229] where they found that ΔH_{AB} does play a role in phase formation in similar alloys. Ref.[229] did focus on PGM based HEA as did we so we cannot be certain that this criterion will work for other systems, however the evidence overwhelmingly supports it since most the alloys that were scaled for industrial manufacture had only relatively small additions of PGM in comparison to the other components. However, we can compare with what we know of single phase high entropy alloys. CoCrFeMnNi is virtually single phase in most cases, although breaks down in some conditions, such as long term heat treatments at moderate temperature[94]. Looking at the pairwise enthalpies for the constituents of CoCrFeMnNi we

can see that $\Delta H_{\mathrm{CrMn}} = 2\mathrm{kJ\,mol^{-1}}$, $\Delta H_{\mathrm{CrFe}} = -1\mathrm{kJ\,mol^{-1}}$, $\Delta H_{\mathrm{CrCo}} = -4\mathrm{kJ\,mol^{-1}}$, $\Delta H_{\mathrm{CrNi}} = -7\mathrm{kJ\,mol^{-1}}$, $\Delta H_{\mathrm{MnFe}} = 0\mathrm{kJ\,mol^{-1}}$, $\Delta H_{\mathrm{MnCo}} = -5\mathrm{kJ\,mol^{-1}}$, $\Delta H_{\mathrm{MnNi}} = -8\mathrm{kJ\,mol^{-1}}$, $\Delta H_{\mathrm{FeCo}} = -1\mathrm{kJ\,mol^{-1}}$, $\Delta H_{\mathrm{FeNi}} = -2\mathrm{kJ\,mol^{-1}}$ and $\Delta H_{\mathrm{CoNi}} = 0\mathrm{kJ\,mol^{-1}}$. The data for CoCrFeMnNi does agree with our proposed pairwise criterion as do the data from Ref[229]. Moreover, as with the alloys developed in this work, which exhibit a main phase of FCC crystal structure, sometimes accompanied by secondary phases, the CoCrFeNiMnNi alloy has been shown to exhibit precipitation due to heat treatment[94]. Of course, we do suggest that the criterion be explored in many other systems to confirm validity, but conclude that this is the optimum approach for alloy design of this type. Furthermore, as ΔH_{AB} is insensitive to composition, and the overall δ and molten metal flow properties which influence mixing in the liquid state are relatively weakly influenced by stoichiometric changes, the inference would be that alloys found by this method are likely to be stable over a moderate range of compositions, rather than being a very specific ratio with narrow margins of error. This opens the possibility of further iterations of alloy development after the initial search and verification step, where relatively minor (of the order of a few percent) adjustments to compositions are made to fine tune the properties to match requirements.

6.6.2 Predictive power of DFT

We have seen that DFT is a very powerful prediction tool, able to show trends that align with physical results. In these studies we used DFT to calculate the ground state energy of PtRh and PtNi and showed that, assuming a random lattice arrangement of atoms on an FCC lattice, the more the ratios of atoms tended to equiatomic the more energetically favoured they were, as would be expected for ideal mixing. This agrees with the accepted phase diagram for PtRh, which is complete solid solubility, but not for PtNi, where intermetallic compounds are known to form. This of course derives from the fact that in DFT alternative structures need to be explicitly considered. By repeating calculations for ordered structures, we also showed that known ordered phases of PtNi are more energetically favoured than the disordered lattice arrangements at those atomic ratios. The DFT results did agree with the phase diagrams constructed from physical data so we can trust the validity of DFT as implemented here in being a powerful screening tool.

Using DFT we calculated the ground state energy for 30 disordered lattice arrangements of $Pt_7Rh_{23}Ni_{35}Co_{35}$ on a 108 atom FCC lattice and 3 ordered phases. We saw by comparison of random structures with possible ordered forms that the disordered phases tended to be more energetically favoured. If we compare the results to physical data we see that the alloy $Pt_7Rh_{23}Ni_{35}Co_{35}$ does mix well into a homogeneous alloy, showing only minor segregation provided it is mixed well in the melt. Therefore, DFT is potentially a powerful tool to determine whether an alloy will tend to mix or not, though the factor of the time required to undertake the calculations needs to be considered.

Additional criteria that could be added to DFT for screening HEA are screening of ordered arrangements, which we do in this study and addition of known intermetallic phases to an otherwise disordered lattice. Efforts should be made towards screening $4 \times 4 \times 4$ supercells (i.e. 256 for an FCC lattice). Also, we have shown how to calculate the energy of a cleaved surface. Efforts should be put towards relaxing these surfaces and performing reaction calculations such as oxygen adsorption for oxidation characteristics.

6.7 Laboratory vs. industrial manufacture

Where the laboratory scale EPMA data show minimal segregation, 1-2at.% on the imaged surfaces in alloys $Pt_7Rh_{23}Ni_{35}Co_{35}$, $Pt_5Rh_{20}V_5Ni_{35}Co_{35}$ and $Pt_5Rh_{11}V_{14}Ni_{35}Co_{35}$. The segregation in the industrially manufactured alloys is in the range of 1-6at.% when imaged with EPMA. Where we can compare directly, that is the PtRh alloys, this is a difference of $\approx$ 5at.%. Considering the difference is between 5g and 1000g of material, that is the laboratory manufactured alloys are 0.5% the mass of the industrially manufactured alloys and that they will have had very different casting and solidification conditions as a result, this difference is not very significant. The uniformity in the mixing of the alloy is established when the melted components mix, therefore the minor segregation on the scale of the casting could be due to uneven mixing in the arc melter in both cases, the amount of material in the 1000g ingot amplifying the necessity for mixing.

Heat treatment of the laboratory manufactured alloys does not appear to change the alloys towards more uniformity. Overall, the industrially manufactured alloys do not appear very different from the as-cast ingot after heat treatment at 1000°C, although we have observed homogenisation in some of the alloys after heat treatment at 1000°C, most successfully with $Pt_5Rh_{20}V_5Ni_{35}Co_{35}$ Given that these are high melting point alloys, it could be that heat treatment at higher temperatures might be needed to allow for rearrangement of the distribution of the elements towards a more uniform distribution. For heat treatment to have a rapid effect on the structure the accepted standard is to heat treat at 0.75-0.8T_m, table 6.25 suggests such heat treatment temperatures based on a rule of mixtures estimated T_m from equation 2.9. The heat treatment is intended to homogenise the structure so should be performed either in a vacuum furnace or a controlled inert atmosphere such as Ar, and may be required to have a duration of several hours to have the proper effect.

	ROM T_m(K)	$0.8T_m$(K)	$0.8T_m$(°C)	Indicative heat treatment temperature (°C)
$Pt_7Rh_{23}Ni_{35}Co_{35}$	1881	1505	1232	1250
$Pt_5V_5Ni_{35}Co_{35}$	1882	1506	1233	1250
$Pt_5Rh_{11}V_{14}Ni_{35}Co_{35}$	1877	1502	1229	1250
$Ir_{35}Rh_{35}Co_5Ni_5Pt_{20}$	2325	1860	1587	1600
$Ir_{12}Fe_{33}Co_{20}Ni_{30}Pt_5$	1900	1520	1247	1250

Table 6.25: ROM calculated temperatures from equation 2.9 and suggested heat treatment temperatures based on industry standard of 0.75-0.8T_m for annealing in vacuum or Ar

Overall, the evidence does show that all 5 of the alloys can be combined to uniform mixtures provided the appropriate measures are taken during manufacture and that the conclusions reached on the small 5g laboratory samples are consistent with the 1kg industrially produced material.

6.8 Potential for application

All alloys taken forward for industrial scale manufacture show indications of ductility in mechanical tests, and therefore there is a basis to anticipate that these alloys could be drawn at room temperature. Nevertheless, the degree of plastic deformation that would have to be supported for a wire drawing operation is very high, and the simple hammering test is not able to capture behaviour under equivalent circumstances, so further investigation, for example by compression tests of samples, would be needed. DSC data show that all 5 alloys perform well during heating up to 1400°C in an inert, Ar, atmosphere, and do not go through melting below 1200°C Of the 5 alloys, 3 perform very well in terms of oxidation behaviour when heated to 1000°C in air and very well when held at that temperature for 1h. These 3 alloys are therefore very suitable based on this criteria for high temperature uses. Such applications might include thermocouples, for the higher PGM content alloys, ignition spark plugs, and use in glass manufacture, specifically as $Ir_{12}Fe_{33}Co_{20}Ni_{30}Pt_5$ which at least in terms of oxidation shows good resistance, and is heavily thrifted compared to a pure PGM alloy has a comparable T_m to pure Pt (fig. 3.1). Further tests, commencing with plastic deformation trials to lead to wire drawing, could be used to investigate these further. Due to the oxidation, and indeed the nature of the oxides which could be potentially formed, there would be less desirability in using the vanadium-containing alloys for applications where oxidation was a risk. The $Ir_{12}Fe_{33}Co_{20}Ni_{30}Pt_5$ alloy specifically could find applications where reduced cost (due to the more heavily thrifted PGM) would be desirable. Pending further investigation, we would

suggest that $Pt_7Rh_{23}Ni_{35}Co_{35}$ and $Ir_{35}Rh_{35}Co_5Ni_5Pt_{20}$ only be considered for high temperature applications in air or oxygen heavy atmospheres as they responded the best to heating in air.

Chapter 7

Conclusions

We designed alloys with the following criteria:

- high temperature application compatibility
- simple crystal structure
- cold workability
- lower PGM content than conventional PGM alloys

to achieve these criteria we chose elements that had high melting points to include in our high throughput composition investigation. We used two design rules from the HEA extrapolated Hume-Rothery rules:

- $\delta \leq 4\%$
- $-22\text{kJ mol}^{-1} \leq \Delta H_{mix} \leq 10\text{kJ mol}^{-1}$

Throughout our investigation these design rules were continually revised according to observations made upon characterisation of certain alloy compositions which had resulted from employing these rules. We explored 29 alloys in this work in ternary, quaterary and quinary PGM containing systems, 25 of which were identified as candidates for industrial scale manufacture. We have identified a factor that influences single crystal phase formation, and an be used to guide alloy design, as, $\Delta H_{AB} \leq 0$, and tested it by manufacturing Ag based alloys at laboratory scale with some success. The phase formation criterion is also assessed in the alloys chosen to be manufactured at industrial scale and found to be successful, and note that the same criteria seems effective in some other alloys of the HEA type. We suggest that the phase formation criterion be explored further in systems not based on PGM.

Of the alloys identified, 5 were deemed of industrial interest and were scaled to industrial quantities (which is castings of around a kilogram for alloys of this type). The alloys were found to be single phase FCC even at industrial scale. Of the 5 alloys, 4 alloys fully obeyed the novel

phase formation criterion we identified as $-50\text{kJ}\,\text{mol}^{-1} \leq \Delta H_{AB} \leq 0$, that is a 16% success rate considering the 25 alloys which were designed for the possibility of industrial interest. The alloys appear single phase, or at least to consist of a dominant phase with some minor phases or segregation, when characterised in both laboratory and industrial scale.

Of the 5 alloys, all 5 alloys are promising for high temperature uses in controlled atmospheres, based on the properties assessed here, and 3 of the 5 alloys are very promising for high temperature uses in air, due to their resistance to oxidation.

We further confirmed the validity of DFT as a screening tool by demonstrating the agreement between experimental and simulated results, both in well-established binary alloys, and one of the novel multicomponent alloys developed here. We explored and suggested methods and parameters of treating HEA compositions via DFT as a screening tool before manufacture and of creating surface slabs for reaction calculations. DFT is a good tool for trend based analysis and computational screening is a good tool for physical resource management and reduction, provided an appropriate balance can be struck between the accuracy needed and the computational time and resources required.

Chapter 8

Future Work

The binary enthalpy contribution to influencing the formation and stabilisation of PGM HEA is discussed in sections 6.5, 6.3, 6.5.2 and supported by observations made by Freudenberger *et al.* [49]. There is more work to be done in confirming that the binary enthalpy terms, and a balancing of the binary enthalpy terms, does stabilise the alloy as it would a binary alloy. Studies should be expanded to include non-PGM containing systems as both our studies and the one by Freudenberger *et al.* [49] were exclusively on purely PGM or PGM based systems.

The work performed in these studies has provided a holistic view of design, development and investigations into PGM HEA, however it has left the investigators with a few questions. As mentioned in section 4.3 the simulated surface slabs show that the as-cast $Pt_7Rh_{23}Ni_{35}Co_{35}$ does not exhibit a favouring of any plane. This observation can be taken further, adopting a mixed simulation-experimental characterisation approach, and expanded beyond PGM HEA. For the preliminary work we propose that samples of $Pt_7Rh_{23}Ni_{35}Co_{35}$ be made up at small scale (≈5-20g), those samples should be divided to as-cast and annealed. The annealing process should follow the one described in section 3.1.2.3, and should allow the surface to adopt energetically-favoured orientations (it would therefore need to be done under a very clean vacuum, and have a long duration). Samples should should then be characterised by EBSD. This investigation will be complemented by further DFT simulations on the surface slabs of the alloy, including geometry optimisation and cleaving slabs from different bulk lattice arrangements. Once the geometry of each slab is optimised by DFT, annealing should be simulated using a static, force-field, atomistic simulation based approach, however, it should be noted that parametrising a force field for an HEA is not a simple process and requires extensive data on the particular HEA. The study can include efforts towards simulating the as-cast alloy and the annealed alloy at room temperature. The methods and workflows developed in the suggested project should be expanded to include other systems. This should be extended to larger systems of the order of 1000s of atoms.

The EBSD investigation could also be combined with XRD data analysis to investigate further how grain orientations and texture are translated into peak intensity.

Also, the investigations performed in this project and suggested above could and should be expanded to alloys not containing PGM. This is to investigate the criterion of ΔH_{AB} proposed in this study for combining elements into single phase high entropy alloys, and whether it works well on non-PGM containing combinations. The simulations of surface slabs should be performed on other systems as well.

We have shown that the HEA bulk cells and surface slabs can be simulated reliably as 108 atom lattice systems. The systems should be expanded to larger sets of atoms and the simulations benchmarked for performance. The systems should also be scaled to classical dynamics based simulation approaches and beyond. Further, the reliable simulation of surface slabs means we can adopt a mixed simulations-experimental characterisation based approach to oxidation by performing surface slab adsoprtion of O_2 complemented by TGA investigations in alloys.

Efforts should be taken towards a mixed simulations-experimental approach to designing, identifying, and exploring alloys with certain properties for intended uses and as replacement materials for conventional critical materials. The need for reducing the use of, and finding alternatives to, critical materials is discussed in section 2.1.2, a mixed modelling-experimental approach not only addresses the need to reduce the consumption of the alloys but addresses it head-on by reducing the amount of resources required as part of the investigation.

Finally, a more extensive study into the effect of heat treatment on these alloys should be performed. We have seen that the heat treatment length and temperature affect all these alloys differently so they should also all be studied individually. Extensive care should be taken in the parameters for the design of experiment, and the study should also be targeted and informed by the identification of specific target applications for each alloy.

References

[1] G. Gunn, "Platinum-group metals", in *Critical Metals Handbook*, G. Gunn, Ed., 2014, ch. 12, pp. 284–311.

[2] P. Sinisalo and M. Lundström, "Refining Approaches in the Platinum Group Metal Processing Value Chain—A Review", *Metals*, vol. 8, no. 4, p. 203, 2018.

[3] M. Balcerzak, "Noble Metals, Analytical Chemistry of', *Encyclopedia of Analytical Chemistry*, pp. 1–29, 2015.

[4] Johnson Matthey, *Applications - PMM*, 2015.

[5] G. Raykhtsaum, "Platinum Alloys", in *The Santa Fe Symposium*, 2011.

[6] IPA - International Platinum Group Metals Association, *PGM Facts*.

[7] L. Osmieri, L. Pezzolato, and S. Specchia, *Recent trends on the application of PGM-free catalysts at the cathode of anion exchange membrane fuel cells*, 2018.

[8] S. Lu and Z. Zhuang, "Electrocatalysts for hydrogen oxidation and evolution reactions", *Science China Materials*, vol. 59, no. 3, pp. 217–238, 2016.

[9] G. Raykhtsaum, "Platinum 2012 Interim Review"", *Platinum Metals Review*, vol. 57, no. 3, pp. 202–213, 2013.

[10] R. Seymour, "Platinum group metals patent analysis and mapping", *Platinum Metals Review*, vol. 52, no. 4, pp. 231–240, 2008.

[11] IPA - International Platinum Group Metals Association, *PGM applications*, 2015.

[12] T. Pradeep and Anshup, "Noble metal nanoparticles for water purification: A critical review", *Thin Solid Films*, vol. 517, no. 24, pp. 6441–6478, 2009.

[13] G. Gunn, *Critical Metals Handbook*. Hoboken: American Geophysical Union, 2014.

[14] C. N. Mpinga, J. J. Eksteen, C Aldrich, and L Dyer, "Direct leach approaches to Platinum Group Metal (PGM) ores and concentrates: A review", *Minerals Engineering*, vol. 78, pp. 93–113, 2015.

[15] A. R. Köhler, *Material Scarcity: A Reason for Responsibility in Technology Development and Product Design*, 2013.

[16] L. Grandell, A. Lehtilä, M. Kivinen, T. Koljonen, S. Kihlman, and L. S. Lauri, "Role of critical metals in the future markets of clean energy technologies", *Renewable Energy*, vol. 95, pp. 53–62, 2016.

[17] R. S. Pell, F. Wall, X. Yan, and G. Bailey, "Applying and advancing the economic resource scarcity potential (ESP) method for rare earth elements", *Resources Policy*, vol. 62, pp. 472–481, 2019.

[18] U. Bardi and S. Caporali, "Precious metals in automotive Technology: An unsolvable depletion problem?", *Minerals*, vol. 4, no. 2, pp. 388–398, 2014.

[19] M. Liu, F. Li, Z. Sun, L. Ma, L. Xu, and Y. Wang, "Noble-metal-free photocatalysts MoS 2 -graphene/CdS mixed nanoparticles/nanorods morphology with high visible light efficiency for H 2 evolution", *Chemical Communications*, vol. 50, no. 75, pp. 11 004–11 007, 2014.

[20] Z. Zhuang, J. Huang, Y. Li, L. Zhou, and L. Mai, "The Holy Grail in Platinum-Free Electrocatalytic Hydrogen Evolution: Molybdenum-Based Catalysts and Recent Advances", *ChemElectroChem*, pp. 3570–3589, 2019.

[21] Y. Yan, B. Y. Xia, B. Zhao, and X. Wang, "A review on noble-metal-free bifunctional heterogeneous catalysts for overall electrochemical water splitting", *Journal of Materials Chemistry A*, vol. 4, no. 45, pp. 17 587–17 603, 2016.

[22] T. N. Murakami, S. Ito, Q. Wang, M. K. Nazeeruddin, T. Bessho, I. Cesar, P. Liska, R. Humphry-Baker, P. Comte, P. Péchy, and M. Grätzel, "Highly efficient dye-sensitized solar cells based on carbon black counter electrodes", *Journal of the Electrochemical Society*, vol. 153, no. 12, A2255, 2006.

[23] H. M. Barkholtz and D. J. Liu, *Advancements in rationally designed PGM-free fuel cell catalysts derived from metal-organic frameworks*, 2017.

[24] S. S. Yi, J. M. Yan, B. R. Wulan, S. J. Li, K. H. Liu, and Q. Jiang, "Noble-metal-free cobalt phosphide modified carbon nitride: An efficient photocatalyst for hydrogen generation", *Applied Catalysis B: Environmental*, vol. 200, pp. 477–483, 2017.

[25] W. Xia, A. Mahmood, Z. Liang, R. Zou, and S. Guo, *Earth-Abundant Nanomaterials for Oxygen Reduction*, 2016.

[26] X. Zhu, T. Zhang, Z. Sun, H. Chen, J. Guan, X. Chen, H. Ji, P. Du, and S. Yang, "Black Phosphorus Revisited: A Missing Metal-Free Elemental Photocatalyst for Visible Light Hydrogen Evolution", *Advanced Materials*, vol. 29, no. 17, p. 1 605 776, 2017.

[27] S. Singh, N. Wanderka, B. S. Murty, U. Glatzel, and J. Banhart, "Decomposition in multi-component AlCoCrCuFeNi high-entropy alloy", *Acta Materialia*, vol. 59, no. 1, pp. 182–190, 2011.

[28] X. Zou and Y. Zhang, "Noble metal-free hydrogen evolution catalysts for water splitting", *Chemical Society Reviews*, vol. 44, no. 15, pp. 5148–5180, 2015.

[29] C. Lv, C. Yan, G. Chen, Y. Ding, J. Sun, Y. Zhou, and G. Yu, "An Amorphous Noble-Metal-Free Electrocatalyst that Enables Nitrogen Fixation under Ambient Conditions", *Angewandte Chemie - International Edition*, vol. 57, no. 21, pp. 6073–6076, 2018.

[30] M. Wu and T. Ma, *Platinum-free catalysts as counter electrodes in dye-sensitized solar cells*, 2012.

[31] C. Hu and L. Dai, *Carbon-Based Metal-Free Catalysts for Electrocatalysis beyond the ORR*, 2016.

[32] H. T. Chung, D. A. Cullen, D. Higgins, B. T. Sneed, E. F. Holby, K. L. More, and P. Zelenay, "Direct atomic-level insight into the active sites of a high-performance PGM-free ORR catalyst", *Science*, vol. 357, no. 6350, pp. 479–484, 2017.

[33] D. Liu, L. Tao, D. Yan, Y. Zou, and S. Wang, "Recent Advances on Non-precious Metal Porous Carbon-based Electrocatalysts for Oxygen Reduction Reaction", *ChemElectroChem*, vol. 5, no. 14, pp. 1775–1785, 2018.

[34] L. Lin, Q. Zhu, and A. W. Xu, "Noble-metal-free Fe-N/C catalyst for highly efficient oxygen reduction reaction under both alkaline and acidic conditions", *Journal of the American Chemical Society*, vol. 136, no. 31, pp. 11 027–11 033, 2014.

[35] A. Morozan, B. Jousselme, and S. Palacin, *Low-platinum and platinum-free catalysts for the oxygen reduction reaction at fuel cell cathodes*, 2011.

[36] T. Löffler, H. Meyer, A. Savan, P. Wilde, A. Garzón Manjón, Y. T. Chen, E. Ventosa, C. Scheu, A. Ludwig, and W. Schuhmann, "Discovery of a Multinary Noble Metal–Free Oxygen Reduction Catalyst", *Advanced Energy Materials*, vol. 8, no. 34, p. 1 802 269, 2018.

[37] M. Shao, Q. Chang, J. P. Dodelet, and R. Chenitz, *Recent Advances in Electrocatalysts for Oxygen Reduction Reaction*, 2016.

[38] J. Wang, F. Xu, H. Jin, Y. Chen, and Y. Wang, "Non-Noble Metal-based Carbon Composites in Hydrogen Evolution Reaction: Fundamentals to Applications", *Advanced Materials*, vol. 29, no. 14, 2017.

[39] Y. Zhan, J. Huang, Z. Lin, X. Yu, D. Zeng, X. Zhang, F. Xie, W. Zhang, J. Chen, and H. Meng, "Iodine/nitrogen co-doped graphene as metal free catalyst for oxygen reduction reaction", *Carbon*, vol. 95, pp. 930–939, 2015.

[40] A. Piontek, E. Bisz, and M. Szostak, "Iron-Catalyzed Cross-Couplings in the Synthesis of Pharmaceuticals: In Pursuit of Sustainability", *Angewandte Chemie - International Edition*, vol. 57, no. 35, pp. 11 116–11 128, 2018.

[41] B. Cantor, I. T. H. Chang, P. Knight, and a. J. B. Vincent, "Microstructural development in equiatomic multicomponent alloys", *Materials Science and Engineering A*, vol. 375-377, no. 1-2 SPEC. ISS. Pp. 213–218, 2004.

[42] J. W. Yeh, S. K. Chen, S. J. Lin, J. Y. Gan, T. S. Chin, T. T. Shun, C. H. Tsau, and S. Y. Chang, "Nanostructured high-entropy alloys with multiple principal elements: Novel alloy design concepts and outcomes", *Advanced Engineering Materials*, vol. 6, no. 5, pp. 299–303+274, 2004.

[43] J. W. Yeh, S. K. Chen, J. Y. Gan, S. J. Lin, T. S. Chin, T. T. Shun, C. H. Tsau, and S. Y. Chang, "Formation of simple crystal structures in Cu-Co-Ni-Cr-Al-Fe-Ti-V alloys with multiprincipal metallic elements", *Metallurgical and Materials Transactions A: Physical Metallurgy and Materials Science*, vol. 35 A, no. 8, pp. 2533–2536, 2004.

[44] J.-W. Yeh, "Alloy Design Strategies and Future Trends in High-Entropy Alloys", *JOM*, vol. 65, no. 12, pp. 1759–1771, 2013.

[45] M.-H. Tsai and J.-W. Yeh, "High-entropy alloys: A critical review", *Materials Research Letters*, vol. 2, no. 3, pp. 107–123, 2014.

[46] E. J. Pickering and N. G. Jones, "High-entropy alloys: a critical assessment of their founding principles and future prospects", *International Materials Reviews*, vol. 61, no. 3, pp. 183–202, 2016.

[47] S Ranganathan, "Alloyed pleasures: Multimetallic cocktails", *Current Science*, vol. 85, no. 10, pp. 1404–1406, 2003.

[48] J. W. Yeh, *Physical Metallurgy of High-Entropy Alloys*, 2015.

[49] J. Freudenberger, D. Rafaja, D. Geissler, L. Giebeler, C. Ullrich, A. Kauffmann, M. Heilmaier, and K. Nielsch, "Face Centred Cubic Multi-Component Equiatomic Solid Solutions in the Au-Cu-Ni-Pd-Pt System", *Metals*, vol. 7, no. 4, p. 135, 2017.

[50] M. S. Lucas, G. B. Wilks, L. Mauger, J. A. Muñoz, O. N. Senkov, E. Michel, J. Horwath, S. L. Semiatin, M. B. Stone, D. L. Abernathy, and E. Karapetrova, "Absence of long-range chemical ordering in equimolar FeCoCrNi", *Applied Physics Letters*, vol. 100, no. 25, p. 251 907, 2012.

[51] O. N. Senkov, G. B. Wilks, D. B. Miracle, C. P. Chuang, and P. K. Liaw, "Refractory high-entropy alloys", *Intermetallics*, vol. 18, no. 9, pp. 1758–1765, 2010.

[52] O. Senkov, J. Scott, S. Senkova, D. Miracle, and C. Woodward, "Microstructure and room temperature properties of a high-entropy TaNbHfZrTi alloy", *Journal of Alloys and Compounds*, vol. 509, no. 20, pp. 6043–6048, 2011.

[53] O. Senkov, G. Wilks, J. Scott, and D. Miracle, "Mechanical properties of Nb25Mo25Ta25W25 and V20Nb20Mo20Ta20W20 refractory high entropy alloys", *Intermetallics*, vol. 19, no. 5, pp. 698–706, 2011.

[54] M. Feuerbacher, M. Heidelmann, and C. Thomas, "Hexagonal High-entropy Alloys", *Materials Research Letters*, vol. 3, no. 1, pp. 1–6, 2014.

[55] A. Takeuchi, K. Amiya, T. Wada, K. Yubuta, and W. Zhang, "High-Entropy Alloys with a Hexagonal Close-Packed Structure Designed by Equi-Atomic Alloy Strategy and Binary Phase Diagrams", *Jom*, vol. 66, no. 10, pp. 1984–1992, 2014.

[56] K. V. Yusenko, S. Riva, P. A. Carvalho, M. V. Yusenko, S. Arnaboldi, A. S. Sukhikh, M. Hanfland, and S. A. Gromilov, "First hexagonal close packed high-entropy alloy with outstanding stability under extreme conditions and electrocatalytic activity for methanol oxidation", *Scripta Materialia*, vol. 138, pp. 22–27, 2017.

[57] R. Soler, A. Evirgen, M. Yao, C. Kirchlechner, F. Stein, M. Feuerbacher, D. Raabe, and G. Dehm, "Microstructural and mechanical characterization of an equiatomic YGdTb-DyHo high entropy alloy with hexagonal close-packed structure", *Acta Materialia*, vol. 156, pp. 86–96, 2018.

[58] J. W. Qiao, M. L. Bao, Y. J. Zhao, H. J. Yang, Y. C. Wu, Y. Zhang, J. A. Hawk, and M. C. Gao, "Rare-earth high entropy alloys with hexagonal close-packed structure", *Journal of Applied Physics*, vol. 124, no. 19, p. 195 101, 2018.

[59] X. F. Wang, Y. Zhang, Y. Qiao, and G. L. Chen, "Novel microstructure and properties of multicomponent CoCrCuFeNiTix alloys", *Intermetallics*, vol. 15, no. 3, pp. 357–362, 2007.

[60] L. Liu, J. B. Zhu, C. Zhang, J. C. Li, and Q. Jiang, "Microstructure and the properties of FeCoCuNiSn x high entropy alloys", *Materials Science and Engineering A*, vol. 548, pp. 64–68, 2012.

[61] C. J. Tong, M. R. Chen, S. K. Chen, J. W. Yeh, T. T. Shun, S. J. Lin, and S. Y. Chang, "Mechanical performance of the AlxCoCrCuFeNi high-entropy alloy system with multi-principal elements", in *Metallurgical and Materials Transactions A: Physical Metallurgy and Materials Science*, vol. 36, Springer-Verlag, 2005, pp. 1263–1271.

[62] J. M. Zhu, H. M. Fu, H. F. Zhang, A. M. Wang, H. Li, and Z. Q. Hu, "Microstructures and compressive properties of multicomponent AlCoCrFeNiMo x alloys", *Materials Science and Engineering A*, vol. 527, no. 26, pp. 6975–6979, 2010.

[63] D. B. Miracle, J. D. Miller, O. N. Senkov, C. Woodward, M. D. Uchic, and J. Tiley, "Exploration and Development of High Entropy Alloys for Structural Applications", *Entropy*, vol. 16, pp. 494–525, 2014.

[64] E. Fazakas, V. Zadorozhnyy, L. K. Varga, A. Inoue, D. V. Louzguine-Luzgin, F. Tian, and L. Vitos, "Experimental and theoretical study of Ti20Zr20Hf 20Nb20X20 (X = v or Cr) refractory high-entropy alloys", *International Journal of Refractory Metals and Hard Materials*, vol. 47, pp. 131–138, 2014.

[65] W. H. Liu, Y. Wu, J. Y. He, Y. Zhang, C. T. Liu, and Z. P. Lu, "The Phase Competition and Stability of High-Entropy Alloys", *JOM*, vol. 66, no. 10, pp. 1973–1983, 2014.

[66] Y. Zou, S. Maiti, W. Steurer, and R. Spolenak, "Size-dependent plasticity in an Nb25Mo25Ta 25W25 refractory high-entropy alloy", *Acta Materialia*, vol. 65, pp. 85–97, 2014.

[67] G. F. Ma, Z. K. Li, H. Ye, C. L. He, H. F. Zhang, and Z. Q. Hu, "Wetting and interface phenomena in the molten Sn/CuFeNiCoCr high-entropy alloy system", *Applied Surface Science*, vol. 356, pp. 460–466, 2015.

[68] X. Ji, H. Duan, H. Zhang, and J. Ma, "Slurry Erosion Resistance of Laser Clad NiCoCr-FeAl3 High-Entropy Alloy Coatings", *Tribology Transactions*, vol. 58, no. 6, pp. 1119–1123, 2015.

[69] W. H. Liu, Z. P. Lu, J. Y. He, J. H. Luan, Z. J. Wang, B. Liu, Y. Liu, M. W. Chen, and C. T. Liu, "Ductile CoCrFeNiMox high entropy alloys strengthened by hard intermetallic phases", *Acta Materialia*, vol. 116, pp. 332–342, 2016.

[70] K. V. Yusenko, S. Riva, W. A. Crichton, K. Spektor, E. Bykova, A. Pakhomova, A. Tudball, I. Kupenko, A. Rohrbach, S. Klemme, F. Mazzali, S. Margadonna, N. P. Lavery, and S. G. Brown, "High-pressure high-temperature tailoring of High Entropy Alloys for extreme environments", *Journal of Alloys and Compounds*, vol. 738, pp. 491–500, 2018.

[71] L. Zhang, D. Zhou, and B. Li, "Anomalous microstructure and excellent mechanical properties of Ni35Al21.67Cr21.67Fe21.67 high-entropy alloy with BCC and B2 structure", *Materials Letters*, vol. 216, pp. 252–255, 2018.

[72] Y. J. Zhou, Y. Zhang, Y. L. Wang, and G. L. Chen, "Microstructure and compressive properties of multicomponent Al x (TiVCrMnFeCoNiCu) 100-x high-entropy alloys", *Materials Science and Engineering A*, vol. 454-455, pp. 260–265, 2007.

[73] ——, "Solid solution alloys of AlCoCrFeNiTix with excellent room-temperature mechanical properties", *Applied Physics Letters*, vol. 90, no. 18, p. 181 904, 2007.

[74] C.-J. Tong, Y.-L. Chen, J.-W. Yeh, S.-J. Lin, S.-K. Chen, T.-T. Shun, C.-H. Tsau, and S.-Y. Chang, "Microstructure characterization of Al x CoCrCuFeNi high-entropy alloy system with multiprincipal elements", *Metallurgical and Materials Transactions A*, vol. 36, no. 4, pp. 881–893, 2005.

[75] B. Gludovatz, A. Hohenwarter, D. Catoor, E. H. Chang, E. P. George, and R. O. Ritchie, "A fracture-resistant high-entropy alloy for cryogenic applications", *Science*, vol. 345, no. 6301, pp. 1153–1158, 2014.

[76] M. Liu, Z. Zhang, F. Okejiri, S. Yang, S. Zhou, and S. Dai, "Entropy-Maximized Synthesis of Multimetallic Nanoparticle Catalysts via a Ultrasonication-Assisted Wet Chemistry Method under Ambient Conditions", *Advanced Materials Interfaces*, vol. 6, no. 7, p. 1 900 015, 2019.

[77] H. J. Qiu, G. Fang, Y. Wen, P. Liu, G. Xie, X. Liu, and S. Sun, "Nanoporous high-entropy alloys for highly stable and efficient catalysts", *Journal of Materials Chemistry A*, vol. 7, no. 11, pp. 6499–6506, 2019.

[78] G. Zhang, K. Ming, J. Kang, Q. Huang, Z. Zhang, X. Zheng, and X. Bi, "High entropy alloy as a highly active and stable electrocatalyst for hydrogen evolution reaction", *Electrochimica Acta*, vol. 279, pp. 19–23, 2018.

[79] Y. Yao, Z. Huang, P. Xie, S. D. Lacey, R. J. Jacob, H. Xie, F. Chen, A. Nie, T. Pu, M. Rehwoldt, D. Yu, M. R. Zachariah, C. Wang, R. Shahbazian-Yassar, J. Li, and L. Hu, "Carbothermal shock synthesis of high-entropy-alloy nanoparticles", *Science*, vol. 359, no. 6383, pp. 1489–1494, 2018.

[80] Z. Y. Lv, X. J. Liu, B. Jia, H. Wang, Y. Wu, and Z. P. Lu, "Development of a novel high-entropy alloy with eminent efficiency of degrading azo dye solutions", *Scientific Reports*, vol. 6, no. 1, p. 34 213, 2016.

[81] W. Dai, T. Lu, and Y. Pan, "Novel and promising electrocatalyst for oxygen evolution reaction based on MnFeCoNi high entropy alloy", *Journal of Power Sources*, vol. 430, pp. 104–111, 2019.

[82] S. kai Wu, Y. Pan, N. Wang, T. Lu, and W. ji Dai, "Azo dye degradation behavior of AlFeMnTiM (M = Cr, Co, Ni) high-entropy alloys", *International Journal of Minerals, Metallurgy and Materials*, vol. 26, no. 1, pp. 124–132, 2019.

[83] Y. Brif, M. Thomas, and I. Todd, "The use of high-entropy alloys in additive manufacturing", *Scripta Materialia*, vol. 99, no. February, pp. 93–96, 2015.

[84] H. Dobbelstein, M. Thiele, E. L. Gurevich, E. P. George, and A. Ostendorf, "Direct metal deposition of refractory high entropy alloy MoNbTaW", in *Physics Procedia*, vol. 83, 2016, pp. 624–633.

[85] H. Shiratori, T. Fujieda, K. Yamanaka, Y. Koizumi, K. Kuwabara, T. Kato, and A. Chiba, "Relationship between the microstructure and mechanical properties of an equiatomic AlCoCrFeNi high-entropy alloy fabricated by selective electron beam melting", *Materials Science and Engineering A*, vol. 656, pp. 39–46, 2016.

[86] J. Joseph, N. Stanford, P. Hodgson, and D. M. Fabijanic, "Tension/compression asymmetry in additive manufactured face centered cubic high entropy alloy", *Scripta Materialia*, vol. 129, pp. 30–34, 2017.

[87] T. Fujieda, H. Shiratori, K. Kuwabara, M. Hirota, T. Kato, K. Yamanaka, Y. Koizumi, A. Chiba, and S. Watanabe, "CoCrFeNiTi-based high-entropy alloy with superior tensile strength and corrosion resistance achieved by a combination of additive manufacturing using selective electron beam melting and solution treatment", *Materials Letters*, vol. 189, pp. 148–151, 2017.

[88] R. Zhou, Y. Liu, C. Zhou, S. Li, W. Wu, M. Song, B. Liu, X. Liang, and P. K. Liaw, "Microstructures and mechanical properties of C-containing FeCoCrNi high-entropy alloy fabricated by selective laser melting", *Intermetallics*, vol. 94, pp. 165–171, 2018.

[89] H. Dobbelstein, E. L. Gurevich, E. P. George, A. Ostendorf, and G. Laplanche, "Laser metal deposition of a refractory TiZrNbHfTa high-entropy alloy", *Additive Manufacturing*, vol. 24, pp. 386–390, 2018.

[90] J. Guo, M. Goh, Z. Zhu, X. Lee, M. L. S. Nai, and J. Wei, "On the machining of selective laser melting CoCrFeMnNi high-entropy alloy", *Materials and Design*, vol. 153, pp. 211–220, 2018.

[91] R. Li, P. Niu, T. Yuan, P. Cao, C. Chen, and K. Zhou, "Selective laser melting of an equiatomic CoCrFeMnNi high-entropy alloy: Processability, non-equilibrium microstructure and mechanical property", *Journal of Alloys and Compounds*, vol. 746, pp. 125–134, 2018.

[92] P. Niu, R. Li, T. Yuan, S. Zhu, C. Chen, M. Wang, and L. Huang, "Microstructures and properties of an equimolar AlCoCrFeNi high entropy alloy printed by selective laser melting", *Intermetallics*, vol. 104, pp. 24–32, 2019.

[93] Y. Zhuang, H. Xue, Z. Chen, Z. Hu, and J. He, "Effect of annealing treatment on microstructures and mechanical properties of FeCoNiCuAl high entropy alloys", *Materials Science and Engineering: A*, vol. 572, pp. 30–35, 2013.

[94] E. Pickering, R. Muñoz-Moreno, H. Stone, and N. Jones, "Precipitation in the equiatomic high-entropy alloy CrMnFeCoNi", *Scripta Materialia*, vol. 113, pp. 106–109, 2016.

[95] G. Laplanche, S. Berglund, C. Reinhart, A. Kostka, F. Fox, and E. George, "Phase stability and kinetics of σ-phase precipitation in CrMnFeCoNi high-entropy alloys", *Acta Materialia*, vol. 161, pp. 338–351, 2018.

[96] F Otto, A Dlouhý, K. G. Pradeep, M. Kuběnová, D Raabe, G Eggeler, and E. P. George, "Decomposition of the single-phase high-entropy alloy CrMnFeCoNi after prolonged anneals at intermediate temperatures", *Acta Materialia*, vol. 112, pp. 40–52, 2016.

[97] N. Park, B.-J. Lee, and N. Tsuji, "The phase stability of equiatomic CoCrFeMnNi high-entropy alloy: Comparison between experiment and calculation results", *Journal of Alloys and Compounds*, vol. 719, pp. 189–193, 2017.

[98] F. Otto, Y. Yang, H. Bei, and E. P. George, "Relative effects of enthalpy and entropy on the phase stability of equiatomic high-entropy alloys", *Acta Materialia*, vol. 61, no. 7, pp. 2628–2638, 2013.

[99] M. G. Poletti and L Battezzati, "Electronic and thermodynamic criteria for the occurrence of high entropy alloys in metallic systems", *Acta Materialia*, vol. 75, pp. 297–306, 2014.

[100] B. Murty, J. Yeh, and S. Ranganathan, *High-Entropy Alloys*, 1st. Butterworth-Heinemann, 2014.

[101] M. C. Gao, J.-W. Yeh, P. K. Liaw, and Y. Zhang, Eds., *High-Entropy Alloys: Fundamental and Applications*, 1st. Springer, 2016.

[102] M. Laurent-Brocq, L. Perrière, R. Pirès, and Y. Champion, "From high entropy alloys to diluted multi-component alloys: Range of existence of a solid-solution", *Materials and Design*, vol. 103, pp. 84–89, 2016.

[103] S. Guo, C. Ng, J. Lu, and C. T. Liu, "Effect of valence electron concentration on stability of fcc or bcc phase in high entropy alloys", *Intermetallics*, 2015.

[104] D. King, S. Middleburgh, A. McGregor, and M. Cortie, "Predicting the formation and stability of single phase high-entropy alloys", *Acta Materialia*, no. 104, pp. 172–179, 2016.

[105] H.-H. Yang, W.-T. Tsai, J.-C. Kuo, and C.-C. Yang, "Solid/liquid interaction between a multicomponent FeCrNiCoMnAl high entropy alloy and molten aluminum", *Journal of Alloys and Compounds*, vol. 509, no. 32, pp. 8176–8182, 2011.

[106] J. W. Yeh, Y. L. Chen, S. J. Lin, and S. K. Chen, "High-entropy alloys - A new era of exploitation", in *Materials Science Forum*, vol. 560, 2007, pp. 1–9.

[107] D. Miracle and O. Senkov, "A critical review of high entropy alloys and related concepts", *Acta Materialia*, vol. 122, pp. 448–511, 2017. arXiv: `arXiv:1507.02142v2`.

[108] M. G. Poletti, S Branz, G Fiore, B. A. Szost, W. A. Crichton, and L Battezzati, "Equilibrium high entropy phases in X-NbTaTiZr (X $\frac{1}{4}$ Al,V,Cr and Sn) multiprincipal component alloys", *Journal of Alloys and Compounds*, vol. 655, pp. 138–146, 2016.

[109] Y. Zhang, Y. J. Zhou, J. P. Lin, G. L. Chen, and P. K. Liaw, "Solid-solution phase formation rules for multi-component alloys", *Advanced Engineering Materials*, vol. 10, no. 6, pp. 534–538, 2008.

[110] U. Mizutani, *Hume-Rothery rules for structurally complex alloy phases*. CRC Press, 2011.

[111] S. Guo, C. Ng, J. Lu, and C. T. Liu, "Effect of valence electron concentration on stability of fcc or bcc phase in high entropy alloys", *Journal of Applied Physics*, vol. 109, no. 10, p. 103 505, 2011.

[112] T. B. Massalski, *Comments concerning some features of phase diagrams and phase transformations*, 2010.

[113] S. Guo and C. Liu, "Phase stability in high entropy alloys: Formation of solid-solution phase or amorphous phase", *Progress in Natural Science: Materials International*, vol. 21, no. 6, pp. 433–446, 2011.

[114] U. Mizutani, H. Sato, M. Inukai, Y. Nishino, and E. S. Zijlstra, "Electrons per atom ratio determination and hume-rothery electron concentration rule for p-based polar compounds studied by FLAPW-fourier calculations", *Inorganic Chemistry*, vol. 54, no. 3, pp. 930–946, 2015.

[115] Y. Zhang, T. T. Zuo, Z. Tang, M. C. Gao, K. A. Dahmen, P. K. Liaw, and Z. P. Lu, "Microstructures and properties of high-entropy alloys", *Progress in Materials Science*, vol. 61, no. October 2013, pp. 1–93, 2014.

[116] Y. F. Ye, Q. Wang, J. Lu, C. T. Liu, and Y. a. Yang, "High-entropy alloy: Challenges and prospects", *Materials Today*, 2016.

[117] Y. Zhang, X. Yang, and P. K. Liaw, "Alloy Design and Properties Optimization of High-Entropy Alloys", *JOM Journal of the Minerals Metals and Materials Society*, vol. 64, no. 7, pp. 830–838, 2012.

[118] R. Kozak, A. Sologubenko, and W. Steurer, "Single-phase high-entropy alloys – an overview", *Z. Kristallogr*, vol. 230, no. 1, pp. 55–68, 2015.

[119] S. Guo and C. Liu, "Phase stability in high entropy alloys: Formation of solid-solution phase or amorphous phase", *Progress in Natural Science: Materials International*, vol. 21, no. 6, pp. 433–446, 2011.

[120] Z. Wang, W. Qiu, Y. Yang, and C. T. Liu, "Atomic-size and lattice-distortion effects in newly developed high-entropy alloys with multiple principal elements", *Intermetallics*, vol. 64, pp. 63–69, 2015.

[121] B. A. Parkinson, J. Ren, and M. H. Whangbo, "Relationship of STM and AFM images to the local density of states in the valence and conduction bands of rhenium selenide (ReSe2)", *Journal of the American Chemical Society*, vol. 113, no. 21, pp. 7833–7837, 1991.

[122] H. Duan, S. D. Hudson, G. Ungar, M. N. Holerca, and V. Percec, "Definitive support by transmission electron microscopy, electron diffraction, and electron density maps for the formation of a BCC lattice from poly{N-[3,4,5-tris(n-dodecan-l-yloxy)benzoyl]ethyleneimine}", *Chemistry - A European Journal*, vol. 7, no. 19, pp. 4134–4141, 2001.

[123] E. Merzbacher, *Quantum mechanics*. J. Wiley, 1970, p. 621.

[124] M. Born and R. Oppenheimer, "Zur Quantentheorie der Molekeln", *Annalen der Physik*, vol. 389, no. 20, pp. 457–484, 1927.

[125] J. Kohanoff, *Electronic Structure Calculations for Solids and Molecules*. Cambridge: Cambridge University Press, 2006.

[126] D. R. Hartree, "The Wave Mechanics of an Atom with a Non-Coulomb Central Field Part I Theory and Methods", *Mathematical Proceedings of the Cambridge Philosophical Society*, vol. 24, no. 1, pp. 89–110, 1928.

[127] ——, "The Wave Mechanics of an Atom with a Non-Coulomb Central Field Part II Some Results and Discussion", *Mathematical Proceedings of the Cambridge Philosophical Society*, vol. 24, no. 1, pp. 111–132, 1928.

[128] ——, "The Wave Mechanics of an Atom with a non-Coulomb Central Field. Part III. Term Values and Intensities in Series in Optical Spectra", *Mathematical Proceedings of the Cambridge Philosophical Society*, vol. 24, no. 3, pp. 426–437, 1928.

[129] D. S. Sholl and J. A. Steckel, *Density Functional Theory*. Hoboken, NJ, USA: John Wiley & Sons, Inc., 2009.

[130] J. C. Slater, "The theory of complex spectra", *Physical Review*, vol. 34, no. 10, pp. 1293–1322, 1929.

[131] P. Hohenberg and W. Kohn, "Inhomogeneous electron gas", *Physical Review*, vol. 136, no. 3B, B864–B871, 1964.

[132] W. Kohn and L. J. Sham, "Self-consistent equations including exchange and correlation effects", *Physical Review*, vol. 140, no. 4A, A1133–A1138, 1965.

[133] W. A.W. A. Harrison, *Electronic structure and the properties of solids : the physics of the chemical bond*. Dover Publications, 1989, p. 586.

[134] P. Ziesche, S. Kurth, and J. P. Perdew, "Density functionals from LDA to GGA", *Computational Materials Science*, vol. 11, no. 2, pp. 122–127, 1998.

[135] A. Zunger and J. P. Perdew, "Self-interaction correction to density-functional approximations for many-electron systems", *Physical Review B*, vol. 23, no. 10, pp. 5048–5079, 1981.

[136] U von Barth and L. Hedin, "A local exchange-correlation potential for the spin polarized case: I", *Journal of Physics C: Solid State Physics*, vol. 5, no. 13, pp. 1629–1642, 1972.

[137] J. P. Perdew, K. Burke, and M. Ernzerhof, "Generalized Gradient Approximation Made Simple", *Physical Review Letters*, vol. 77, no. 18, pp. 3865–3868, 1996. arXiv: 0927-0256(96)00008 [10.1016].

[138] J. P. Perdew, A. Ruzsinszky, G. I. Csonka, O. A. Vydrov, G. E. Scuseria, L. A. Constantin, X. Zhou, and K. Burke, "Restoring the Density-Gradient Expansion for Exchange in Solids and Surfaces", *Physical Review Letters*, vol. 100, no. 13, p. 136 406, 2008. arXiv: 0707.2088.

[139] Y. Umeno, T. Shimada, Y. Kinoshita, and T. Kitamura, "Methodology of Quantum Mechanics/Atomic Simulations", in, ser. Nanostructure Science and Technology, Tokyo: Springer Japan, 2017, pp. 5–34.

[140] P. Schwerdtfeger, "The Pseudopotential Approximation in Electronic Structure Theory", *ChemPhysChem*, vol. 12, no. 17, pp. 3143–3155, 2011.

[141] D. R. Hamann, M. Schlüter, and C. Chiang, "Norm-Conserving Pseudopotentials", *Physical Review Letters*, vol. 43, no. 20, pp. 1494–1497, 1979.

[142] A. T. Zayak, "A first-principles investigation of the magnetic, structural and dynamical properties of Ni2MnGa", PhD thesis, University of Duisburg-Essen, 2003.

[143] D. Vanderbilt, "Soft self-consistent pseudopotentials in a generalized eigenvalue formalism", *Physical Review B*, vol. 41, no. 11, pp. 7892–7895, 1990.

[144] C. Freeman, "Computational Studies of Solid Solutions and Interfaces", University of Bristol, 2005.

[145] S. Clark, "Complex Structures In Tetrahedrally Bonded Semiconductors", PhD thesis, 1994.

[146] M. C. Gibson, "Implementation and application of advanced density functionals", 2006.

[147] F. Tian, L. K. Varga, N. Chen, J. Shen, and L. Vitos, "Ab initio design of elastically isotropic TiZrNbMoVx high-entropy alloys", *Journal of Alloys and Compounds*, vol. 599, pp. 19–25, 2014.

[148] G. Bonny, D. Chakraborty, S. Pandey, A. Manzoor, N. Castin, S. R. Phillpot, and D. S. Aidhy, "Classical interatomic potential for quaternary Ni-Fe-Cr-Pd solid solution alloys", *Modelling and Simulation in Materials Science and Engineering*, vol. 26, no. 6, 2018.

[149] G Anand, R Goodall, and C. L. Freeman, "Role of configurational entropy in body-centred cubic or face-centred cubic phase formation in high entropy alloys", *Scripta Materialia*, vol. 124, pp. 90–94, 2016.

[150] W. P. Huhn and M. Widom, "Prediction of A2 to B2 phase transition in the high-entropy alloy Mo-Nb-Ta-W", *JOM*, vol. 65, no. 12, pp. 1772–1779, 2013.

[151] I. Toda-Caraballo, J. S. Wróbel, S. L. Dudarev, D. Nguyen-Manh, and P. E. Rivera-Díaz-Del-Castillo, "Interatomic spacing distribution in multicomponent alloys", *Acta Materialia*, vol. 97, pp. 156–169, 2015.

[152] D. J. King, P. A. Burr, E. G. Obbard, and S. C. Middleburgh, "DFT study of the hexagonal high-entropy alloy fission product system", *Journal of Nuclear Materials*, vol. 488, pp. 70–74, 2017.

[153] D. J. King, S. T. Cheung, S. A. Humphry-Baker, C. Parkin, A. Couet, M. B. Cortie, G. R. Lumpkin, S. C. Middleburgh, and A. J. Knowles, "High temperature, low neutron cross-section high-entropy alloys in the Nb-Ti-V-Zr system", *Acta Materialia*, vol. 166, pp. 435–446, 2019.

[154] R. Wei, H. Zhang, H. Wang, C. Chen, T. Wang, F. Li, S. Guan, T. Zhang, T. Hu, and Y. Dong, "Phase transitions and magnetic properties of Fe 30 Co 29 Ni 29 Zr 7 B 4 Cu 1 high-entropy alloys", *Journal of Alloys and Compounds*, vol. 789, pp. 762–767, 2019.

[155] B. Yin and W. A. Curtin, "First-principles-based prediction of yield strength in the RhIrPdPtNiCu high-entropy alloy", *npj Computational Materials*, vol. 5, no. 1, 2019.

[156] N. E. Koval, J. I. Juaristi, R. Díez Muiño, and M. Alducin, "Elastic properties of the TiZrNbTaMo multi-principal element alloy studied from first principles", *Intermetallics*, vol. 106, pp. 130–140, 2019.

[157] Y. Tong, S. Zhao, K. Jin, H. Bei, J. Y. Ko, Y. Zhang, and F. X. Zhang, "A comparison study of local lattice distortion in Ni80Pd20 binary alloy and FeCoNiCrPd high-entropy alloy", *Scripta Materialia*, vol. 156, pp. 14–18, 2018.

[158] T. Zuo, M. C. Gao, L. Ouyang, X. Yang, Y. Cheng, R. Feng, S. Chen, P. K. Liaw, J. A. Hawk, and Y. Zhang, "Tailoring magnetic behavior of CoFeMnNiX (X = Al, Cr, Ga, and Sn) high entropy alloys by metal doping", *Acta Materialia*, vol. 130, pp. 10–18, 2017.

[159] M. Calvo-Dahlborg, J. Cornide, J. Tobola, D. Nguyen-Manh, J. S. Wróbel, J. Juraszek, S. Jouen, and U. Dahlborg, "Interplay of electronic, structural and magnetic properties as the driving feature of high-entropy CoCrFeNiPd alloys", *Journal of Physics D: Applied Physics*, vol. 50, no. 18, 2017.

[160] W. Chen, X. Ding, Y. Feng, X. Liu, K. Liu, Z. P. Lu, D. Li, Y. Li, C. T. Liu, and X. Q. Chen, "Vacancy formation enthalpies of high-entropy FeCoCrNi alloy via first-principles calculations and possible implications to its superior radiation tolerance", *Journal of Materials Science and Technology*, vol. 34, no. 2, pp. 355–364, 2018.

[161] C. G. Schön, T. Duong, Y. Wang, and R. Arróyave, "Probing the entropy hypothesis in highly concentrated alloys", *Acta Materialia*, vol. 148, pp. 263–279, 2018.

[162] ——, "A proof of concept: Thermodynamics of aluminum – transition metal highly concentrated alloys", *Journal of Alloys and Compounds*, vol. 781, pp. 595–605, 2019.

[163] P. K. Sarswat, S. Sarkar, A. Murali, W. Huang, W. Tan, and M. L. Free, "Additive manufactured new hybrid high entropy alloys derived from the AlCoFeNiSmTiVZr system", *Applied Surface Science*, vol. 476, pp. 242–258, 2019.

[164] S. Ener, M. Fries, F. Hammerath, I. Opahle, E. Simon, P. Fritsch, S. Wurmehl, H. Zhang, and O. Gutfleisch, "Magnetic and magnetocaloric properties of the Co2-xMnxB system by experiment and density functional theory", *Acta Materialia*, vol. 165, pp. 270–277, 2019.

[165] A. Zunger, S.-H. Wei, L. G. Ferreira, and J. E. Bernard, "Special quasirandom structures", *Physical Review Letters*, vol. 65, no. 3, pp. 353–356, 1990.

[166] T. A. Batchelor, J. K. Pedersen, S. H. Winther, I. E. Castelli, K. W. Jacobsen, and J. Rossmeisl, "High-Entropy Alloys as a Discovery Platform for Electrocatalysis", *Joule*, vol. 3, no. 3, pp. 834–845, 2019.

[167] F. Körmann, D. Ma, D. D. Belyea, M. S. Lucas, C. W. Miller, B. Grabowski, and M. H. Sluiter, ""Treasure Maps" for Magnetic High-Entropy-Alloys From Theory and Experiment", *Applied Physics Letters*, vol. 107, no. 14, 2015.

[168] WebElements, [Online]. Available: `https://www.webelements.com` (visited on Jun. 27, 2019).

[169] Compact Arc Melter MAM-1, [Online]. Available: `https://www.edmund-buehler.de/en/materials-science/arc-melting/compact-arc-melter-mam-1/` (visited on Apr. 23, 2019).

[170] P. Mahoney, *MAM-1 Usage Protocol*.

[171] S. J. Clark, M. D. Segall, C. J. Pickard, P. J. Hasnip, M. J. Probert, K. Refson, and M. Payne, "First principles methods using CASTEP", *Z. Kristall.*, vol. 220, pp. 567–570, 2005.

[172] P. Hohenberg and W. Kohn, "Inhomogeneous electron gas", *Phys. Rev.*, vol. 136, B864–B871, 1964.

[173] W. Kohn and L. J. Sham, "Self-consistent equations including exchange and correlation effects", *Phys. Rev.*, vol. 140, A1133–A1138, 1965.

[174] G. P. Francis and M. C. Payne, "Finite basis set corrections to total energy pseudopotential calculations", *J. Phys.-Condes. Matter*, vol. 2, pp. 4395–4404, 1990.

[175] H. J. Monkhorst and J. D. Pack, "Special points for Brillouin-zone integrations", *Phys. Rev. B*, vol. 13, pp. 5188–5192, 1976.

[176] M. C. Payne, M. P. Teter, D. C. Allan, T. Arias, and J. D. Joannopoulos, "Iterative minimization techniques for ab initio total-energy calculations - molecular-dynamics and conjugate gradients", *Rev. Mod. Phys.*, vol. 64, pp. 1045–1097, 1992.

[177] W. T. Cahyanto, W. Widanarto, M. Effendi, and H. Kasai, "Stability of atomic oxygen chemisorption on Pt-alloy surfaces", *Surface and Interface Analysis*, vol. 48, no. 4, pp. 181–185, 2016.

[178] M. Xu, X.-L. Huai, and H. Liu, "Role of Keto–Enol Isomerization on Surface Chemistry and Hydrogenation of Acetone on Pt(111): A DFT study", *Industrial & Engineering Chemistry Research*, vol. 53, no. 13, pp. 5451–5454, 2014.

[179] J. Scaranto and M. Mavrikakis, "HCOOH decomposition on Pt(111): A DFT study", *Surface Science*, vol. 648, pp. 201–211, 2016.

[180] A. Trinchero, A. Hellman, and H. Grönbeck, "Methane oxidation over Pd and Pt studied by DFT and kinetic modeling", *Surface Science*, vol. 616, pp. 206–213, 2013.

[181] S. Sharma, M. N. Groves, J. Fennell, N. Soin, S. L. Horswell, and C. Malardier-Jugroot, "Carboxyl group enhanced CO tolerant GO supported Pt catalysts: DFT and electrochemical analysis", *Chemistry of Materials*, vol. 26, no. 21, pp. 6142–6151, 2014.

[182] M. A. Quiroga, "Growth of carbon structured over Pd, Pt and Ni: A comparative DFT study", *Applied Surface Science*, vol. 268, pp. 11–15, 2013.

[183] E. Sosa and H. Liu, "Oxygen adsorption on Pt-Pd nanoclusters by DFT and ab initio atomistic thermodynamics", *Journal of Alloys and Compounds*, vol. 735, pp. 643–653, 2018.

[184] M. Lee, "Advanced pseudopotentials for large scale electronic structure calculations with application to a study of weakly ordered material - gamma-Al2O3.", PhD thesis, 1996.

[185] P. Pulay, "Convergence acceleration of iterative sequences. the case of scf iteration", *Chemical Physics Letters*, vol. 73, no. 2, pp. 393–398, 1980.

[186] G. Kresse and J. Furthmüller, "Efficiency of ab-initio total energy calculations for metals and semiconductors using a plane-wave basis set", *Computational Materials Science*, vol. 6, no. 1, pp. 15–50, 1996.

[187] E. G. Moshopoulou, R. M. Ibberson, J. L. Sarrao, J. D. Thompson, and Z. Fisk, "Structure of Ce_2RhIn_8: An example of complementary use of high-resolution neutron powder diffraction and reciprocal-space mapping to study complex materials", *Electrochemical and Solid-State Letters*, vol. 9, no. 5, pp. 173–189, 2006.

[188] R. T. Downs and M. Hall-Wallace, "The american mineralogist crystal structure database", *American Mineralogist*, vol. 88, pp. 247–250, 2003.

[189] S. Gražulis, D. Chateigner, R. T. Downs, A. F. T. Yokochi, M. Quirós, L. Lutterotti, E. Manakova, J. Butkus, P. Moeck, and A. Le Bail, "Crystallography Open Database – an open-access collection of crystal structures", *Journal of Applied Crystallography*, vol. 42, no. 4, pp. 726–729, 2009.

[190] S. Gražulis, A. Daškevič, A. Merkys, D. Chateigner, L. Lutterotti, M. Quirós, N. R. Serebryanaya, P. Moeck, R. T. Downs, and A. Le Bail, "Crystallography open database (cod): An open-access collection of crystal structures and platform for world-wide collaboration", *Nucleic Acids Research*, vol. 40, no. D1, pp. D420–D427, 2012. eprint: `http://nar.oxfordjournals.org/content/40/D1/D420.full.pdf+html`.

[191] S. Gražulis, A. Merkys, A. Vaitkus, and M. Okulič-Kazarinas, "Computing stoichiometric molecular composition from crystal structures", *Journal of Applied Crystallography*, vol. 48, no. 1, pp. 85–91, 2015.

[192] A. Merkys, A. Vaitkus, J. Butkus, M. Okulič-Kazarinas, V. Kairys, and S. Gražulis, "*COD::CIF::Parser*: an error-correcting CIF parser for the Perl language", *Journal of Applied Crystallography*, vol. 49, no. 1, 2016.

[193] "The structure of crystals. By R. W. G. Wyckoff. American Chemical Society Monograph Series. 2nd edition. Pp. 497. New York: Chemical Catalog Co., 1931. 37.50", *Journal of the Society of Chemical Industry*, vol. 50, no. 44, p. 877, 1931.

[194] C. H. Johansson and J. O. Linde, "Röntgenographische und elektrische Untersuchungen des CuAu-Systems", *Annalen der Physik*, vol. 417, no. 1, pp. 1–48, 1936.

[195] H. Okamoto, "Pt-Rh (Platinum-Rhodium)", *Journal of Phase Equilibria and Diffusion*, vol. 34, no. 2, pp. 176–177, 2013.

[196] ——, "Ni-Pt (Nickel-Platinum)", *Journal of Phase Equilibria and Diffusion*, vol. 31, no. 3, p. 322, 2010.

[197] M. J. Rutter, "C2x: A tool for visualisation and input preparation for CASTEP and other electronic structure codes", *Computer Physics Communications*, vol. 225, pp. 174–179, 2018.

[198] G. W. Watson, E. T. Kelsey, N. H. De Leeuw, D. J. Harris, and S. C. Parker, "Atomistic simulation of dislocations, surfaces and interfaces in MgO", *Journal of the Chemical Society - Faraday Transactions*, vol. 92, no. 3, pp. 433–438, 1996.

[199] N. Marzari, D. Vanderbilt, and M. C. Payne, "Ensemble Density-Functional Theory for Ab Initio Molecular Dynamics of Metals and Finite-Temperature Insulators", *Physical Review Letters*, vol. 79, no. 7, pp. 1337–1340, 1997.

[200] M. Ramamoorthy, D. Vanderbilt, and R. D. King-Smith, "First-principles calculations of the energetics of stoichiometric TiO_2 surfaces", *Physical Review B*, vol. 49, no. 23, pp. 16 721–16 727, 1994.

[201] R. L. Harlow and E. I. Dupont De Nemours, "Single Crystal X-Ray Diffraction", in *ASM Handbook,Volume 10: Materials Characterizations*, ASM International, 1986, pp. 344–356.

[202] A. Chatterjee, "X-Ray Diffraction", in *Handbook of Analytical Techniques in Concrete Science and Technology*, Elsevier, 2001, pp. 275–332.

[203] ICDD, *PDF-4+ 2019 (Database)*, D. S. Kabekkodu, Ed. Newtown Square, PA, USA: International Centre for Diffraction Data, 2018.

[204] B. Cullity and S. Stock, *Elements of X-ray Diffraction, Third Edition*, English (US). Prentice-Hall, 2001.

[205] Manual Indexing of Diffraction Data, [Online]. Available: `https://www.youtube.com/watch?v=9n1u8ymc8aw` (visited on Sep. 18, 2019).

[206] M. H. Mendenhall, A. Henins, L. T. Hudson, C. I. Szabo, D. Windover, and J. P. Cline, "High-precision measurement of the x-ray Cu K α spectrum", *Journal of Physics B: Atomic, Molecular and Optical Physics*, vol. 50, no. 11, p. 115 004, 2017.

[207] D. E. Leyden, "X-Ray Spectrometry", in *ASM Handbook,Volume 10: Materials Characterizations*, ASM International, 1986, pp. 82–101.

[208] M. Haschke, *Laboratory Micro-X-Ray Fluorescence Spectroscopy: Instrumentation and Applications*. 2014, p. 356.

[209] E. Marguí and R. v. R. Grieken, *X-ray fluorescence spectrometry and related techniques : an introduction*. Momentum Press, 2013, p. 142.

[210] Sheffield X-ray Diffraction SRF, *PANalytical Zetium Standard Operating Procedures*.

[211] S. J. B. Reed, *Electron microprobe analysis and scanning electron microscopy in geology*. Cambridge University Press, 2005, p. 189.

[212] H. Schatten, *Scanning electron microscopy for the life sciences*. Cambridge University Press, 2013.

[213] H. Exner and S. Weinbruch, "Scanning Electron Microscopy", in *Metallography and Microstructures*, ASM International, 2004, pp. 355–367.

[214] "Probe analyzer pinpointed by JEOL", *Materials Today*, vol. 7, no. 11, p. 69, 2004.

[215] ASTM International, "E92-17 Standard Test Methods for Vickers Hardness and Knoop Hardness of Metallic Materials.", *ASTM International*, pp. 1–27, 2017.

[216] R. L. Smith and G. E. Sandland, "An Accurate Method of Determining the Hardness of Metals, with Particular Reference to Those of a High Degree of Hardness", *Proceedings of the Institution of Mechanical Engineers*, vol. 102, no. 1, pp. 623–641, 1922.

[217] W. C. Oliver and G. M. Pharr, "An improved technique for determining hardness and elastic modulus using load and displacement sensing indentation experiments", *Journal of Materials Research*, vol. 7, no. 6, pp. 1564–1583, 1992.

[218] D. Migas, G. Moskal, M. Mikuśkiewicz, and T. Maciąg, "Thermogravimetric investigations of new γ-γ' cobalt-based superalloys", *Journal of Thermal Analysis and Calorimetry*, vol. 134, no. 1, pp. 119–125, 2018.

[219] W. D. Callister and D. G. Rethwisch, *Materials science and engineering*. Wiley, 2011.

[220] D. Ma, W. O. Chung, J. Liu, and J. He, "Determination of Young's modulus by nanoindentation", *Science in China Series E*, vol. 47, no. 4, p. 398, 2004.

[221] The PGM Database, [Online]. Available: `http://www.pgmdatabase.com/jmpgm/index.jsp` (visited on Sep. 19, 2019).

[222] X.-W. Cheng, Z.-Y. Jiang, B. J. Monaghan, R. J. Longbottom, D.-B. Wei, A. C. Hee, and L.-Z. Jiang, "Degradation of ferritic stainless steels at 1200 °C in air", *Materials and Corrosion*, vol. 69, no. 1, pp. 63–75, 2018.

[223] M. Winter. The periodic table, [Online]. Available: `www.webelements.com`.

[224] Young's Modulus - Tensile and Yield Strength for common Materials, [Online]. Available: `https://www.engineeringtoolbox.com/young-modulus-d_417.html` (visited on Sep. 18, 2019).

[225] A. Takeuchi and A. Inoue, "Metallic Glasses By Atomic Size Difference, Heat of Mixing and Period of Constituent Elements and Its Application To Characterization of the Main Alloying Element", *Materials Transactions*, vol. 46, no. 12, pp. 2817–2829, 2005.

[226] C.-M. Lin and H.-L. Tsai, "Effect of annealing treatment on microstructure and properties of high-entropy FeCoNiCrCu0.5 alloy", *Materials Chemistry and Physics*, vol. 128, no. 1-2, pp. 50–56, 2011.

[227] A. Munitz, M. Kaufman, and R. Abbaschian, "Liquid phase separation in transition element high entropy alloys", *Intermetallics*, vol. 86, pp. 59–72, 2017.

[228] C. Shang, E. Axinte, W. Ge, Z. Zhang, and Y. Wang, "High-entropy alloy coatings with excellent mechanical, corrosion resistance and magnetic properties prepared by mechanical alloying and hot pressing sintering", *Surfaces and Interfaces*, vol. 9, no. April 2016, pp. 36–43, 2017.

[229] S. Sohn, Y. Liu, J. Liu, P. Gong, S. Prades-Rodel, A. Blatter, B. E. Scanley, C. C. Broadbridge, and J. Schroers, "Noble metal high entropy alloys", *Scripta Materialia*, vol. 126, pp. 29–32, 2017.

Appendix A

Supplementary information on simulations

A.1 Mean nearest neighbours analysis

Pt	
Arrangement 2	Pt has 1.14 Pt 2.71 Rh 5.57 Ni and 2.57 Co nearest neighbours on average
Arrangement 25	Pt has 0.86 Pt 1.57 Rh 4.29 Ni and 5.29 Co nearest neighbours on average
Arrangement 17	Pt has 0.57 Pt 2.00 Rh 4.86 Ni and 4.57 Co nearest neighbours on average
Arrangement 1	Pt has 0.57 Pt 2.57 Rh 4.29 Ni and 4.57 Co nearest neighbours on average
Arrangement 5	Pt has 0.29 Pt 2.57 Rh 4.29 Ni and 4.86 Co nearest neighbours on average
Arrangement 21	Pt has 0.86 Pt 2.57 Rh 4.57 Ni and 4.00 Co nearest neighbours on average
Arrangement 28	Pt has 1.14 Pt 2.29 Rh 3.57 Ni and 5.00 Co nearest neighbours on average
Arrangement 8	Pt has 1.43 Pt 2.57 Rh 5.00 Ni and 3.00 Co nearest neighbours on average
Arrangement 9	Pt has 0.00 Pt 2.86 Rh 4.71 Ni and 4.43 Co nearest neighbours on average
Arrangement 18	Pt has 0.86 Pt 2.14 Rh 4.43 Ni and 4.57 Co nearest neighbours on average
Arrangement 3	Pt has 2.00 Pt 2.14 Rh 4.57 Ni and 3.29 Co nearest neighbours on average
Arrangement 27	Pt has 0.29 Pt 2.57 Rh 4.14 Ni and 5.00 Co nearest neighbours on average
Arrangement 19	Pt has 0.57 Pt 3.00 Rh 4.71 Ni and 3.71 Co nearest neighbours on average
Arrangement 11	Pt has 1.14 Pt 2.71 Rh 4.14 Ni and 4.00 Co nearest neighbours on average
Arrangement 24	Pt has 0.86 Pt 2.29 Rh 4.71 Ni and 4.14 Co nearest neighbours on average
Arrangement 14	Pt has 0.29 Pt 3.00 Rh 4.43 Ni and 4.29 Co nearest neighbours on average
Arrangement ordered 3	Pt has 1.71 Pt 4.57 Rh 2.86 Ni and 2.86 Co nearest neighbours on average
Arrangement 6	Pt has 0.57 Pt 2.43 Rh 4.57 Ni and 4.43 Co nearest neighbours on average
Arrangement 20	Pt has 0.29 Pt 2.57 Rh 5.43 Ni and 3.71 Co nearest neighbours on average
Arrangement 4	Pt has 0.29 Pt 2.14 Rh 5.00 Ni and 4.57 Co nearest neighbours on average
Arrangement 23	Pt has 0.86 Pt 3.14 Rh 4.43 Ni and 3.57 Co nearest neighbours on average
Arrangement 13	Pt has 1.43 Pt 2.86 Rh 3.29 Ni and 4.43 Co nearest neighbours on average
Arrangement 29	Pt has 0.29 Pt 2.57 Rh 4.86 Ni and 4.29 Co nearest neighbours on average

Arrangement 0	Pt has 0.29 Pt 2.57 Rh 4.29 Ni and 4.86 Co nearest neighbours on average
Arrangement 16	Pt has 0.57 Pt 2.29 Rh 4.14 Ni and 5.00 Co nearest neighbours on average
Arrangement 15	Pt has 0.86 Pt 3.29 Rh 3.43 Ni and 4.43 Co nearest neighbours on average
Arrangement 22	Pt has 0.29 Pt 2.86 Rh 4.00 Ni and 4.86 Co nearest neighbours on average
Arrangement 26	Pt has 0.86 Pt 2.86 Rh 4.14 Ni and 4.14 Co nearest neighbours on average
Arrangement 12	Pt has 0.86 Pt 3.00 Rh 4.71 Ni and 3.43 Co nearest neighbours on average
Arrangement 10	Pt has 0.57 Pt 3.00 Rh 4.57 Ni and 3.86 Co nearest neighbours on average
Arrangement ordered 2	Pt has 3.14 Pt 5.43 Rh 0.57 Ni and 2.86 Co nearest neighbours on average
Arrangement ordered 1	Pt has 3.71 Pt 3.71 Rh 1.00 Ni and 3.57 Co nearest neighbours on average

Table A.1: Mean nearest neighbours analysis for Pt for 32 arrangements of $Pt_7Rh_{23}Ni_{35}Co_{35}$

Rh	
Arrangement 2	Rh has 0.76 Pt 2.40 Rh 4.12 Ni and 4.72 Co nearest neighbours on average
Arrangement 25	Rh has 0.44 Pt 2.64 Rh 4.40 Ni and 4.52 Co nearest neighbours on average
Arrangement 17	Rh has 0.56 Pt 3.12 Rh 4.32 Ni and 4.00 Co nearest neighbours on average
Arrangement 1	Rh has 0.72 Pt 2.64 Rh 4.00 Ni and 4.64 Co nearest neighbours on average
Arrangement 5	Rh has 0.72 Pt 2.88 Rh 4.00 Ni and 4.40 Co nearest neighbours on average
Arrangement 21	Rh has 0.72 Pt 2.80 Rh 4.28 Ni and 4.20 Co nearest neighbours on average
Arrangement 28	Rh has 0.64 Pt 3.04 Rh 4.68 Ni and 3.64 Co nearest neighbours on average
Arrangement 8	Rh has 0.72 Pt 2.80 Rh 3.68 Ni and 4.80 Co nearest neighbours on average
Arrangement 9	Rh has 0.80 Pt 3.04 Rh 4.40 Ni and 3.76 Co nearest neighbours on average
Arrangement 18	Rh has 0.60 Pt 3.20 Rh 4.08 Ni and 4.12 Co nearest neighbours on average
Arrangement 3	Rh has 0.60 Pt 2.88 Rh 4.48 Ni and 4.04 Co nearest neighbours on average
Arrangement 27	Rh has 0.72 Pt 3.84 Rh 3.96 Ni and 3.48 Co nearest neighbours on average
Arrangement 19	Rh has 0.84 Pt 3.04 Rh 3.84 Ni and 4.28 Co nearest neighbours on average
Arrangement 11	Rh has 0.76 Pt 3.44 Rh 4.20 Ni and 3.60 Co nearest neighbours on average
Arrangement 24	Rh has 0.64 Pt 3.04 Rh 3.96 Ni and 4.36 Co nearest neighbours on average
Arrangement 14	Rh has 0.84 Pt 2.48 Rh 4.16 Ni and 4.52 Co nearest neighbours on average
Arrangement ordered 3	Rh has 1.28 Pt 4.16 Rh 4.32 Ni and 2.24 Co nearest neighbours on average
Arrangement 6	Rh has 0.68 Pt 2.72 Rh 4.16 Ni and 4.44 Co nearest neighbours on average
Arrangement 20	Rh has 0.72 Pt 2.56 Rh 4.48 Ni and 4.24 Co nearest neighbours on average
Arrangement 4	Rh has 0.60 Pt 2.56 Rh 4.48 Ni and 4.36 Co nearest neighbours on average
Arrangement 23	Rh has 0.88 Pt 2.40 Rh 4.40 Ni and 4.32 Co nearest neighbours on average
Arrangement 13	Rh has 0.80 Pt 2.96 Rh 4.40 Ni and 3.84 Co nearest neighbours on average
Arrangement 29	Rh has 0.72 Pt 2.64 Rh 4.20 Ni and 4.44 Co nearest neighbours on average
Arrangement 0	Rh has 0.72 Pt 3.44 Rh 3.92 Ni and 3.92 Co nearest neighbours on average
Arrangement 16	Rh has 0.64 Pt 3.12 Rh 4.28 Ni and 3.96 Co nearest neighbours on average
Arrangement 15	Rh has 0.92 Pt 2.24 Rh 4.32 Ni and 4.52 Co nearest neighbours on average

Arrangement 22	Rh has 0.80 Pt 2.72 Rh 4.32 Ni and 4.16 Co nearest neighbours on average
Arrangement 26	Rh has 0.80 Pt 2.56 Rh 4.40 Ni and 4.24 Co nearest neighbours on average
Arrangement 12	Rh has 0.84 Pt 2.56 Rh 3.84 Ni and 4.76 Co nearest neighbours on average
Arrangement 10	Rh has 0.84 Pt 2.08 Rh 4.32 Ni and 4.76 Co nearest neighbours on average
Arrangement ordered 2	Rh has 1.58 Pt 4.00 Rh 2.67 Ni and 3.75 Co nearest neighbours on average
Arrangement ordered 1	Rh has 1.04 Pt 6.00 Rh 2.72 Ni and 2.24 Co nearest neighbours on average

Table A.2: Mean nearest neighbours analysis for Rh for 32 arrangements of $Pt_7Rh_{23}Ni_{35}Co_{35}$

Ni	
Arrangement 2	Ni has 1.03 Pt 2.71 Rh 4.00 Ni and 4.26 Co nearest neighbours on average
Arrangement 25	Ni has 0.79 Pt 2.89 Rh 4.11 Ni and 4.21 Co nearest neighbours on average
Arrangement 17	Ni has 0.89 Pt 2.84 Rh 3.84 Ni and 4.42 Co nearest neighbours on average
Arrangement 1	Ni has 0.79 Pt 2.63 Rh 4.26 Ni and 4.32 Co nearest neighbours on average
Arrangement 5	Ni has 0.79 Pt 2.63 Rh 4.47 Ni and 4.11 Co nearest neighbours on average
Arrangement 21	Ni has 0.84 Pt 2.82 Rh 3.79 Ni and 4.55 Co nearest neighbours on average
Arrangement 28	Ni has 0.66 Pt 3.08 Rh 4.00 Ni and 4.26 Co nearest neighbours on average
Arrangement 8	Ni has 0.92 Pt 2.42 Rh 4.16 Ni and 4.50 Co nearest neighbours on average
Arrangement 9	Ni has 0.87 Pt 2.89 Rh 4.05 Ni and 4.18 Co nearest neighbours on average
Arrangement 18	Ni has 0.82 Pt 2.68 Rh 4.21 Ni and 4.29 Co nearest neighbours on average
Arrangement 3	Ni has 0.84 Pt 2.95 Rh 3.63 Ni and 4.58 Co nearest neighbours on average
Arrangement 27	Ni has 0.76 Pt 2.61 Rh 3.89 Ni and 4.74 Co nearest neighbours on average
Arrangement 19	Ni has 0.87 Pt 2.53 Rh 3.89 Ni and 4.71 Co nearest neighbours on average
Arrangement 11	Ni has 0.76 Pt 2.76 Rh 4.05 Ni and 4.42 Co nearest neighbours on average
Arrangement 24	Ni has 0.87 Pt 2.61 Rh 4.37 Ni and 4.16 Co nearest neighbours on average
Arrangement 14	Ni has 0.82 Pt 2.74 Rh 4.37 Ni and 4.08 Co nearest neighbours on average
Arrangement ordered 3	Ni has 0.53 Pt 2.84 Rh 4.26 Ni and 4.37 Co nearest neighbours on average
Arrangement 6	Ni has 0.84 Pt 2.74 Rh 4.05 Ni and 4.37 Co nearest neighbours on average
Arrangement 20	Ni has 1.00 Pt 2.95 Rh 3.89 Ni and 4.16 Co nearest neighbours on average
Arrangement 4	Ni has 0.92 Pt 2.95 Rh 3.37 Ni and 4.76 Co nearest neighbours on average
Arrangement 23	Ni has 0.82 Pt 2.89 Rh 3.95 Ni and 4.34 Co nearest neighbours on average
Arrangement 13	Ni has 0.61 Pt 2.89 Rh 4.37 Ni and 4.13 Co nearest neighbours on average
Arrangement 29	Ni has 0.89 Pt 2.76 Rh 3.95 Ni and 4.39 Co nearest neighbours on average
Arrangement 0	Ni has 0.79 Pt 2.58 Rh 4.53 Ni and 4.11 Co nearest neighbours on average
Arrangement 16	Ni has 0.76 Pt 2.82 Rh 4.26 Ni and 4.16 Co nearest neighbours on average
Arrangement 15	Ni has 0.63 Pt 2.84 Rh 4.79 Ni and 3.74 Co nearest neighbours on average
Arrangement 22	Ni has 0.74 Pt 2.84 Rh 3.95 Ni and 4.47 Co nearest neighbours on average
Arrangement 26	Ni has 0.76 Pt 2.89 Rh 3.95 Ni and 4.39 Co nearest neighbours on average
Arrangement 12	Ni has 0.87 Pt 2.53 Rh 4.32 Ni and 4.29 Co nearest neighbours on average

Arrangement 10	Ni has 0.84 Pt 2.84 Rh 4.05 Ni and 4.26 Co nearest neighbours on average
Arrangement ordered 2	Ni has 0.11 Pt 1.73 Rh 6.32 Ni and 3.84 Co nearest neighbours on average
Arrangement ordered 1	Ni has 0.19 Pt 1.84 Rh 7.46 Ni and 2.51 Co nearest neighbours on average

Table A.3: Mean nearest neighbours analysis for Ni for 32 arrangements of $Pt_7Rh_{23}Ni_{35}Co_{35}$

Co	
Arrangement 2	Co has 0.47 Pt 3.11 Rh 4.26 Ni and 4.16 Co nearest neighbours on average
Arrangement 25	Co has 0.97 Pt 2.97 Rh 4.21 Ni and 3.84 Co nearest neighbours on average
Arrangement 17	Co has 0.84 Pt 2.63 Rh 4.42 Ni and 4.11 Co nearest neighbours on average
Arrangement 1	Co has 0.84 Pt 3.05 Rh 4.32 Ni and 3.79 Co nearest neighbours on average
Arrangement 5	Co has 0.89 Pt 2.89 Rh 4.11 Ni and 4.11 Co nearest neighbours on average
Arrangement 21	Co has 0.74 Pt 2.76 Rh 4.55 Ni and 3.95 Co nearest neighbours on average
Arrangement 28	Co has 0.92 Pt 2.39 Rh 4.26 Ni and 4.42 Co nearest neighbours on average
Arrangement 8	Co has 0.55 Pt 3.16 Rh 4.50 Ni and 3.79 Co nearest neighbours on average
Arrangement 9	Co has 0.82 Pt 2.47 Rh 4.18 Ni and 4.53 Co nearest neighbours on average
Arrangement 18	Co has 0.84 Pt 2.71 Rh 4.29 Ni and 4.16 Co nearest neighbours on average
Arrangement 3	Co has 0.61 Pt 2.66 Rh 4.58 Ni and 4.16 Co nearest neighbours on average
Arrangement 27	Co has 0.92 Pt 2.29 Rh 4.74 Ni and 4.05 Co nearest neighbours on average
Arrangement 19	Co has 0.68 Pt 2.82 Rh 4.71 Ni and 3.79 Co nearest neighbours on average
Arrangement 11	Co has 0.74 Pt 2.37 Rh 4.42 Ni and 4.47 Co nearest neighbours on average
Arrangement 24	Co has 0.76 Pt 2.87 Rh 4.16 Ni and 4.21 Co nearest neighbours on average
Arrangement 14	Co has 0.79 Pt 2.97 Rh 4.08 Ni and 4.16 Co nearest neighbours on average
Arrangement ordered 3	Co has 0.53 Pt 1.47 Rh 4.37 Ni and 5.63 Co nearest neighbours on average
Arrangement 6	Co has 0.82 Pt 2.92 Rh 4.37 Ni and 3.89 Co nearest neighbours on average
Arrangement 20	Co has 0.68 Pt 2.79 Rh 4.16 Ni and 4.37 Co nearest neighbours on average
Arrangement 4	Co has 0.84 Pt 2.87 Rh 4.76 Ni and 3.53 Co nearest neighbours on average
Arrangement 23	Co has 0.66 Pt 2.84 Rh 4.34 Ni and 4.16 Co nearest neighbours on average
Arrangement 13	Co has 0.82 Pt 2.53 Rh 4.13 Ni and 4.53 Co nearest neighbours on average
Arrangement 29	Co has 0.79 Pt 2.92 Rh 4.39 Ni and 3.89 Co nearest neighbours on average
Arrangement 0	Co has 0.89 Pt 2.58 Rh 4.11 Ni and 4.42 Co nearest neighbours on average
Arrangement 16	Co has 0.92 Pt 2.61 Rh 4.16 Ni and 4.32 Co nearest neighbours on average
Arrangement 15	Co has 0.82 Pt 2.97 Rh 3.74 Ni and 4.47 Co nearest neighbours on average
Arrangement 22	Co has 0.89 Pt 2.74 Rh 4.47 Ni and 3.89 Co nearest neighbours on average
Arrangement 26	Co has 0.76 Pt 2.79 Rh 4.39 Ni and 4.05 Co nearest neighbours on average
Arrangement 12	Co has 0.63 Pt 3.13 Rh 4.29 Ni and 3.95 Co nearest neighbours on average
Arrangement 10	Co has 0.71 Pt 3.13 Rh 4.26 Ni and 3.89 Co nearest neighbours on average
Arrangement ordered 2	Co has 0.50 Pt 2.25 Rh 3.55 Ni and 5.70 Co nearest neighbours on average
Arrangement ordered 1	Co has 0.64 Pt 1.44 Rh 2.38 Ni and 7.54 Co nearest neighbours on average

Table A.4: Mean nearest neighbours analysis for Co for 32 arrangements of $Pt_7Rh_{23}Ni_{35}Co_{35}$

Appendix B

Supplementary material

B.1 Pairwise Enthalpy

(b) \ (a)	1	3	4	5	6	7	11	12	13	14	15	19	20	21	22	23	24	25	26	27	28	29	30	31	32	33	37	38	39	40	41	42	43	44	45	46	(a) \ (b)
	H	Li	Be	B	C	N	Na	Mg	Al	Si	P	K	Ca	Sc	Ti	V	Cr	Mn	Fe	Co	Ni	Cu	Zn	Ga	Ge	As	Rb	Sr	Y	Zr	Nb	Mo	Tc	Ru	Rh	Pd	
46 Pd	-27	40	-8	24	-32	-62	-15	-40	-46	-55	-36.5	-9	-63	-86	-65	-35	-15	-23	-4	-1	0	-14	-33	-42	-43.5	-36	-9	-61	-84	-91	-53	-15	4	6	2		Pd 46
47 Ag	-10	-16	6	5	-32	-94	0	-10	-4	-20	-18.5	7	-28	-28	-2	17	27	13	28	19	15	2	-4	-5	-17.5	-8	7	-27	-29	-20	16	37	24	23	10	-7	Ag 47
48 Cd	-6	-13	11	13	-27	-91	-3	-6	3	-13	-11.5	1	-32	-30	-8	9	17	2	17	6	2	6	1	1	-14.5	-4	1	-33	-35	-26	11	28	10	9	-6	-26	Cd 48
49 In	-6	-12	16	18	-27	-98	-5	-4	7	-10	-10.5	-4	-35	-30	-5	12	20	3	19	7	2	10	3	3	-13.5	-3	-4	-37	-36	-25	15	33	11	10	-8	-31	In 49
50 Sn	-4	-18	15	18	-23	-90	-8	-9	4	-11	-7.5	-7	-45	-45	-21	-1	10	-7	11	0	-4	7	1	1	-12.5	-1	-7	-46	-51	-43	-1	20	5	4	-13	-34	Sn 50
51 Sb	-1	-28	18	23	-13	-74	-20	-16	2	-8	2.5	-22	-62	-61	-33	-8	7	-11	10	2	-1	7	-1	-1	-10.5	3	-24	-66	-68	-50	-11	17	8	9	-8	-28	Sb 51
55 Cs	-16	16	29	29	-43	-155	3	25	26	-3	-24.5	0	19	70	104	103	97	71	85	58	48	28	15	14	-19.5	-12	0	14	62	101	135	128	89	64	34	-9	Cs 55
56 Ba	-49	0	-10	-19	-90	-212	-3	-4	-20	-52	-85.5	6	1	28	57	57	50	29	37	11	0	-9	-23	-30	-63.5	-66	9	0	20	52	81	73	11	6	-21	-62	Ba 56
57 La	-60	6	-29	-47	-116	-235	24	-7	-38	-73	-112.5	46	8	2	20	22	17	3	5	-17	-27	-21	-31	-41	-73.5	-81	52	14	0	13	36	31	-23	-28	-50	-82	La 57
58 Ce	-61	7	-30	-48	-116	-234	25	-7	-38	-73	-112.5	47	9	2	18	20	15	1	3	-18	-28	-21	-31	-41	-73.5	-81	53	15	0	12	34	29	-25	-30	-52	-83	Ce 58
59 Pr	-61	7	-31	-49	-117	-233	26	-6	-38	-73	-112.5	49	10	1	17	18	13	0	1	-20	-30	-22	-31	-41	-72.5	-81	55	16	0	10	32	26	-27	-32	-53	-83	Pr 59
60 Nd	-61	7	-31	-49	-116	-235	26	-6	-38	-73	-112.5	49	10	2	17	18	13	0	1	-20	-30	-22	-31	-40	-101.5	-80	55	16	0	10	32	26	-27	-32	-53	-83	Nd 60
61 Pm	-61	8	-33	-51	-118	-233	28	-6	-39	-74	-114.5	51	11	1	15	16	10	-2	-2	-23	-32	-23	-32	-41	-73.5	-81	57	18	0	9	29	23	-30	-35	-56	-86	Pm 61
62 Sm	-61	8	-32	-50	-117	-202	28	-6	-38	-74	-113.5	50	11	1	15	17	11	-1	-1	-22	-31	-22	-31	-40	-72.5	-80	56	17	0	9	30	24	-29	-34	-54	-84	Sm 62
63 Eu	-46	-1	-12	-19	-87	-231	0	-5	-19	-49	-79.6	10	0	21	48	49	43	23	30	7	-3	-10	-21	-27	-58.5	-60	13	0	14	42	69	63	6	2	-24	-61	Eu 63
64 Gd	-61	8	-32	-50	-117	-232	28	-6	-39	-73	-113.5	50	11	1	15	17	11	-1	-1	-22	-31	-22	-31	-40	-72.5	-80	56	17	0	9	30	24	-29	-34	-54	-84	Gd 64
65 Tb	-61	9	-33	-51	-118	-232	29	-6	-39	-74	-113.5	52	12	1	14	15	9	-3	-3	-23	-32	-23	-31	-40	-72.5	-80	58	18	0	8	28	22	-30	-35	-56	-85	Tb 65
66 Dy	-61	9	-32	-51	-117	-231	29	-6	-38	-74	-112.5	51	12	1	14	15	9	-3	-3	-23	-32	-22	-31	-40	-71.5	-80	58	18	0	8	27	22	-30	-35	-55	-84	Dy 66
67 Ho	-60	8	-32	-50	-116	-229	28	-6	-38	-73	-111.5	51	11	1	14	16	10	-2	-2	-22	-31	-22	-30	-39	-71.5	-79	57	18	0	9	28	22	-29	-34	-54	-83	Ho 67
68 Er	-61	9	-33	-52	-118	-230	30	-5	-38	-74	-113.5	53	13	0	13	14	8	-4	-5	-24	-34	-23	-31	-40	-71.5	-79	59	20	0	7	26	20	-32	-37	-57	-85	Er 68
69 Tm	-61	9	-33	-52	-117	-229	30	-5	-38	-74	-112.5	52	13	0	12	13	8	-4	-5	-24	-34	-23	-30	-39	-71.5	-79	59	20	0	7	25	19	-32	-37	-56	-85	Tm 69
70 Yb	-46	-1	-14	-22	-88	-199	2	-6	-20	-51	-80.6	12	0	16	41	43	37	19	25	2	-7	-12	-21	-27	-58.5	-59	16	1	10	36	61	55	1	-4	-28	-62	Yb 70
71 Lu	-61	10	-35	-54	-119	-231	31	-5	-39	-75	-114.5	55	14	0	11	11	5	-6	-7	-27	-36	-24	-31	-40	-71.5	-80	61	21	0	6	23	17	-35	-40	-59	-87	Lu 71
72 Hf	-63	30	-37	-66	-123	-218	63	10	-39	-77	-117.5	92	39	5	0	-2	-9	-12	-21	-35	-42	-17	-24	-34	-65.5	-75	98	50	11	0	4	-4	-47	-52	-63	-80	Hf 72
73 Ta	-46	48	-24	-54	-101	-173	89	30	-19	-56	-89.5	119	60	16	1	-1	-7	-4	-15	-24	-29	2	-3	-10	-37.5	-45	125	73	27	3	0	-5	-36	-39	-45	-52	Ta 73
74 W	-24	30	-3	-31	-60	-103	97	38	-2	-31	-46.5	124	57	9	-6	-1	1	6	0	-1	-3	22	15	11	-7.5	-9	129	70	24	-9	-8	0	-7	-10	-9	-6	W 74
75 Re	-18	29	0	-25	-42	-72	73	21	-9	-31	-32.5	95	28	-17	-25	-13	-4	-1	0	2	2	18	8	3	-7.5	-6	98	39	-4	-35	-26	-7	0	-1	1	6	Re 75
76 Os	-19	11	-2	-24	-35	-60	52	5	-18	-36	-29.5	70	4	-39	-41	-23	-11	-9	-4	0	1	10	-1	-7	-14.5	-11	72	13	-28	-55	-39	-14	0	0	2	8	Os 76
77 Ir	-20	-9	-5	-26	-32	-54	28	-13	-30	-43	-30.5	42	-23	-62	-57	-34	-18	-18	-9	-3	-2	0	-13	-21	-24.5	-19	44	-16	-53	-76	-53	-21	-2	-1	1	6	Ir 77
78 Pt	-24	-33	-10	-28	-30	-62	-1	-35	-44	-53	-34.5	9	-55	-89	-74	-45	-24	-28	-13	-7	-5	-12	-29	-38	-37.5	-31	9	-50	-83	-100	-67	-28	-3	-1	-2	2	Pt 78
79 Au	-8	-37	0	-2	-20	-58	-14	-32	-22	-30	-13.5	-9	-60	-74	-47	-19	0	-11	8	7	7	-9	-16	-19	-21.5	-11	-10	-59	-74	-74	-32	3	14	15	7	0	Au 79
80 Hg	-3	-19	15	19	-20	-81	-11	-10	4	-10	-4.5	-10	-43	-37	-10	10	21	4	22	12	8	8	1	1	-11.5	0	-11	-45	-43	-31	11	32	18	18	2	-18	Hg 80
81 Tl	-3	-15	23	27	-19	-91	-11	-3	11	-4	-1.5	-13	-40	-28	2	22	31	11	31	18	13	15	6	6	-9.5	3	-14	-44	-35	-19	26	46	25	24	5	-21	Tl 81
82 Pb	-1	-21	25	30	-13	-82	-18	-8	10	-2	4.5	-21	-52	-40	-8	15	28	7	29	17	13	15	5	5	-7.5	6	-23	-56	-48	-33	17	42	26	25	6	-18	Pb 82
83 Bi	0	-23	26	31	-12	-80	-20	-10	10	-2	5.5	-24	-56	-46	-14	10	24	3	26	14	10	15	4	4	-7.5	7	-26	-61	-54	-40	12	38	23	23	3	-21	Bi 83
90 Th	-61	14	-37	-57	-123	-237	39	3	-40	-77	-119.5	65	19	0	8	9	2	-8	-11	30	-39	-24	-30	-39	-72.5	-82	72	27	1	4	20	13	-39	-45	-63	-91	Th 90
92 U	-53	30	-27	-54	-105	-189	65	14	-30	-66	-98.5	93	37	3	0	1	-3	-5	-11	-23	-29	-7	-15	-25	-52.5	-60	99	48	11	-3	4	2	-31	-36	-46	-59	U 92
94 Pu	-54	21	-25	-50	-102	-188	49	6	-33	-66	-95.5	72	24	-1	2	4	2	-4	-6	-19	-25	-9	-20	-29	-56.5	-62	77	33	4	-3	9	8	-26	-30	-42	-58	Pu 94
(b) \ (a)	H	Li	Be	B	C	N	Na	Mg	Al	Si	P	K	Ca	Sc	Ti	V	Cr	Mn	Fe	Co	Ni	Cu	Zn	Ga	Ge	As	Rb	Sr	Y	Zr	Nb	Mo	Tc	Ru	Rh	Pd	(b) \ (a)
	1	3	4	5	6	7	11	12	13	14	15	19	20	21	22	23	24	25	26	27	28	29	30	31	32	33	37	38	39	40	41	42	43	44	45	46	

(a) Part 1

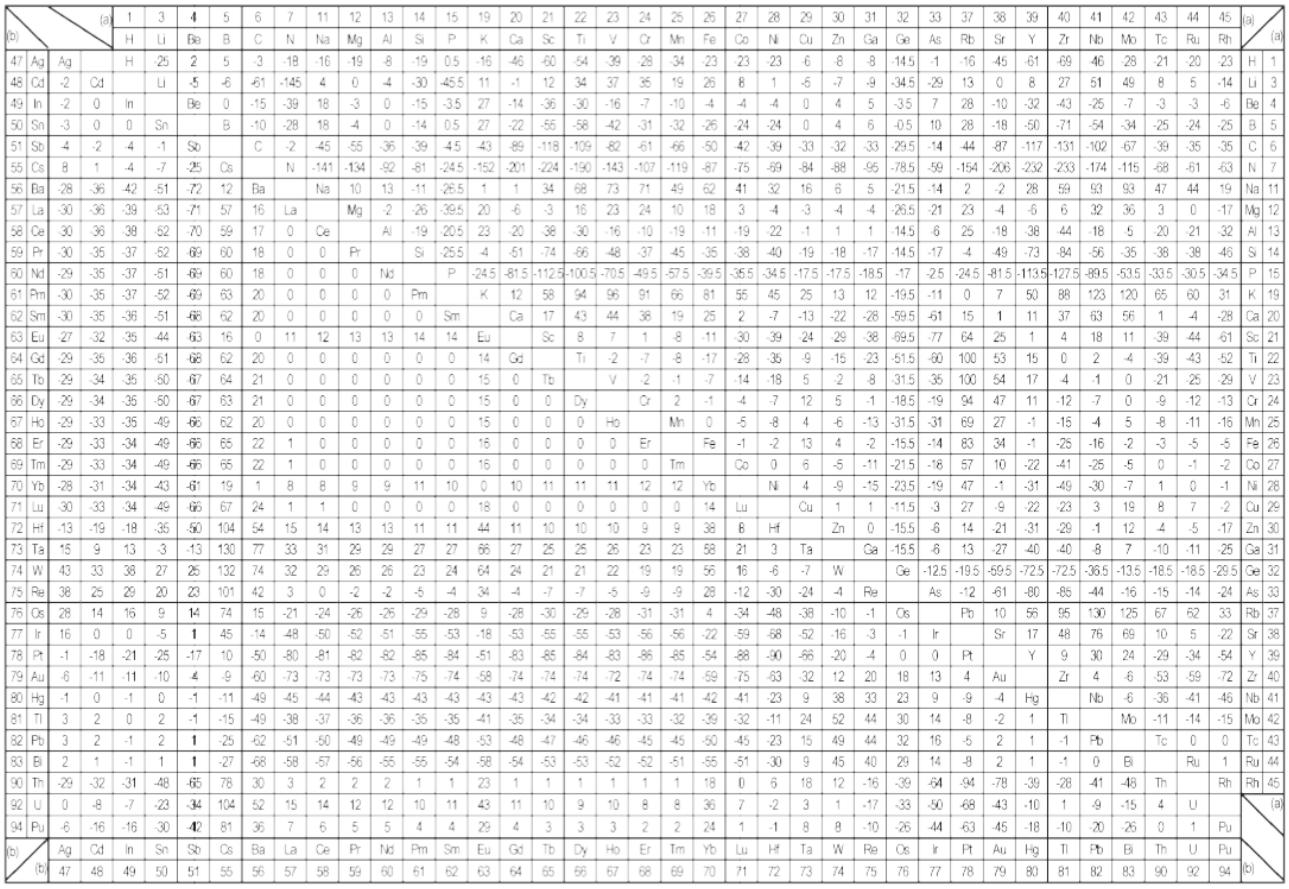

(b) Part 2

Figure B.1: Binary enthalpy of mixing table from ref. [225]